A STUDY ON INNOVATIVE WAYS OF INCORPORATING RADIATIVE COOLING WITH SOLAR ENERGY APPLICATION IN BUILDINGS

Suhendri MSc

Student ID: 14316717

Supervisors: Prof. Yuehong Su, Prof. Jo Darkwa, Dr. Mingke Hu

A thesis submitted to the University of Nottingham
for the degree of Doctor of Philosophy

September 2023

Acknowledgements

Bismillah. Alhamdulillah. Was salatu was salamu ‘ala Rasoolillah. Amma ba’d.

I would not have completed this thesis without the guidance of my supervisors. Thus, first and foremost, I would like to express my sincere gratitude to Prof. Yuehong Su, my principal supervisor. Prof. Su has taught me valuable lessons, specifically about my PhD topic, and more importantly about how to be a good researcher. I would like to also thank Dr. Mingke Hu for his continuous support and assistance in understanding the technical aspects of my research. Dr. Hu is such a dedicated and patience academic mentor. Additionally, I would like to extend my gratitude to Prof. Jo Darkwa my second supervisor for his input on my research and his insights about research in sustainable buildings in general.

Moreover, the help and support from staff, technicians, and fellow students of the Department of Architecture and Built Environment (DABE), at the University of Nottingham are also important for me in completing this thesis. Hence, I would like to thank them, especially Tony Gospel, Daniel Cooper, and Carson Cheng, the technicians who helped me in my experiment. Also, to fellow students of DABE, Cagri Kutlu who helped me settle in on the early days of my PhD, and Muna Alsukkar who is, despite all the difficulties, always persistent.

I also would like to acknowledge the financial support from my sponsor, the Indonesia Endowment Fund for Education (LPDP). I will try to be a good educator and researcher in the university where I work as my gratitude to LPDP.

Support from my family and friends has also been crucial in my PhD journey. I am grateful to have my lovely wife and daughter with me here in Nottingham. The journey would be so depressing for me if they were not by my side. I would also give thanks to my fellow Indonesian friends in Nottingham who are like my second family far from home. Last but not least, thanks to my family in Indonesia, who constantly send prayers to me and who are always in my prayers.

Suhendri

August 2023

Abstract

Solar energy technologies for sustainable building heating have been widely established. But most populated regions on earth need both heating and cooling for their buildings. Providing both heating and cooling sustainably for building in one device is particularly challenging since, like solar technologies, the established passive cooling technologies only serve one function. In the recently revived passive cooling mechanism, namely radiative sky cooling or radiative cooling, one may find a solution to tackle this problem. This is possible because the radiative cooling mechanism is a kind of the reverse of solar absorption.

Research on radiative cooling itself is rejuvenated after the breakthrough in passive daytime radiative cooling almost a decade ago. Since then, researchers in the field have been pursuing the real-world application of radiative cooling, besides also enhancing the optical and mechanical properties of the material. Interested in tackling the abovementioned problem and motivated by the revival of the radiative cooling research field, this thesis aims to find innovative ways to use radiative cooling in buildings. Along with radiative cooling as the passive cooling mechanism, the passive heating mechanism investigated in this thesis comes from the sun. Hence, the research investigates strategies to effectively combine radiative cooling with solar energy applications in buildings.

Reviewing previous research on similar topics, there are at least three common themes of how radiative cooling can be combined with solar technologies. Firstly, the radiative cooling mechanism can be used to enhance the performance of existing solar technologies. Secondly, radiative cooling can be used to extend the working time of solar technologies. Also, still related to the second theme, radiative cooling can alternatingly work with solar energy technologies to provide cooling and heating in the respective seasons.

This thesis offers four novel strategies to combine the two technologies in diverse ways. Computational fluid dynamics (CFD) simulations and experiments were conducted to evaluate the proposed concepts. The discussion on the proposed concepts is presented from a fully passive strategy such as radiative cooling combination with

solar chimney ventilation to a fully active strategy such as its combination with photovoltaics/thermal module.

The first proposed design is a fully passive solar chimney-radiative cooling (SC-RC) ventilation, as discussed in Chapter 3. The SC-RC ventilation can increase the average daily ventilation flow rate of a conventional solar chimney to 1.2 air change per hour, an increase of 0.2 air change per hour. Also, the SC-RC ventilation can cool the inlet air to be more than 3 °C lower than the room air temperature.

Modified from the SC-RC ventilation strategy to accommodate passive heating into the system and make it a multi-seasonal device, the second proposed design employs a switchable absorber/emitter surface on the ventilation air channel. Unlike the previous SC-RC ventilation that is fully passive, this so-called Switchable SC-RC ventilation also introduces a fan to deliver the ventilation. In the annual term, the Switchable SC-RC ventilation can reduce the total unmet hours, and thus provide a more thermally comfortable room than the conventional ventilation. Annually, the unmet hours of the Switchable SC-RC ventilation case are 429 hours fewer than the base case.

Furthermore, the third design proposed to combine a solar air heater with radiative cooling. Changes were made in the spectral properties of a solar absorber and the cover of the collector to allow more thermal emission in the atmospheric window band. This so-called photothermal-radiative cooling (PT-RC) collector collects heating during the day and cooling during the night. When installed as part of an HVAC system, the fully active device has the potential to save up to 32.7% of energy from heating and cooling in the Mediterranean climate.

Moreover, the PT-RC collector design can be more developed into a PVT-RC collector. The difference between them is if the PT-RC collector is a modified solar collector, the PVT-RC, however, is a modified PV module. Hence, the PVT-RC has one additional function which is to generate electricity. Also, the PVT-RC design uses two fluids (i.e., water and air) to collect the heating and cooling energy. The bi-fluid PVT-RC collector is estimated to have a total efficiency of 72% in the daytime. In optimal conditions at night, the bi-fluid PVT-RC collector can provide up to 45 W/m2 cooling power.

To conclude, the proposed radiative cooling combination designs have been shown capable of improving the performance and/or extending the working time of the solar

technologies, hence saving energy from heating and cooling. Also, how radiative cooling is integrated with solar energy technologies can be done in a fully passive or fully active way. Nonetheless, further studies still need to be done especially for studying the use of thermal storage mechanisms or for appraising the economic viability of the designs.

Keywords: *radiative cooling, solar energy, combination, buildings, energy saving*

List of Publications

1. Suhendri, Hu, M., Su, Y., Darkwa, J., Riffat, S. Implementation of passive radiative cooling technology in buildings: A review. (2020) Buildings, 10 (12), art. no. 215, pp. 1-28.

2. Suhendri, S., Hu, M., Su, Y., Darkwa, J., Riffat, S. Performance evaluation of combined solar chimney and radiative cooling ventilation. (2022) Building and Environment, 209.

3. Suhendri, S., Hu, M., Su, Y., Darkwa, J., Riffat, S. Parametric study of a novel combination of solar chimney and radiative cooling cavity for natural ventilation enhancement in residential buildings. (2022) Building and Environment, 225.

4. Suhendri, S., Hu, M., Dan, Y., Su, Y., Zhao, B., Riffat, S. Building Energy-saving Potential of a Dual-functional Solar Heating and Radiative Cooling System. (Under review in Energy and Buildings)

5. Hu, M., Zhao, B., Ao, X., Suhendri, Cao, J., Wang, Q., Riffat, S., Su, Y., Pei, G. An analytical study of the nocturnal radiative cooling potential of typical photovoltaic/thermal module. (2020) Applied Energy, 277.

6. Hu, M., Guo, C., Zhao, B., Ao, X., Suhendri, Cao, J., Wang, Q., Riffat, S., Su, Y., Pei, G. A parametric study on the performance characteristics of an evacuated flat-plate photovoltaic/thermal (PV/T) collector. (2021) Renewable Energy, 167, pp. 884-898.

7. Hu, M., Zhao, B., Ao, X., Suhendri, Cao, J., Wang, Q., Riffat, S., Su, Y., Pei, G. Performance analysis of a novel bifacial solar photothermic and radiative cooling module. (2021) Energy Conversion and Management, 236.

8. Hu, M., Suhendri, Zhao, B., Ao, X., Cao, J., Wang, Q., Riffat, S., Su, Y., Pei, G. Effect of the spectrally selective features of the cover and emitter combination on radiative cooling performance. (2021) Energy and Built Environment, 2 (3), pp. 251-259.

9. Hu, M., Zhao, B., Suhendri, Cao, J., Wang, Q., Riffat, S., Su, Y., Pei, G. Feasibility of realizing daytime solar heating and radiative cooling simultaneously with a novel structure. (2021) Sustainable Cities and Society, 74.

10. Hu, M., Zhao, B., Suhendri, S., Cao, J., Wang, Q., Riffat, S., Yang, R., Su, Y., Pei, G. Experimental study on a hybrid solar photothermic and radiative cooling collector equipped with a rotatable absorber/emitter plate. (2022) Applied Energy, 306.
11. Hu, M., Zhao, B., Suhendri, Ao, X., Cao, J., Wang, Q., Riffat, S., Su, Y., Pei, G. Applications of radiative sky cooling in solar energy systems: Progress, challenges, and prospects. (2022) Renewable and Sustainable Energy Reviews, 160.
12. Hu, M., Zhao, B., Suhendri, Cao, J., Wang, Q., Riffat, S., Su, Y., Pei, G. Extending the operation of a solar air collector to nighttime by integrating radiative sky cooling: A comparative experimental study. (2022) Energy, 251.
13. Hu, M., Zhao, B., Suhendri, Cao, J., Wang, Q., Riffat, S., Su, Y., Pei, G. Quantitative characterization of the effect of inclination angle on flat-plate radiative cooling performance in buildings. (2022) Journal of Building Engineering, 59.
14. Hu, M., Zhao, B., Suhendri, Cao, J., Wang, Q., Riffat, S., Su, Y., Pei, G. Effect of vacuum scheme on radiative sky cooling performance. (2023) Applied Thermal Engineering, 219.

Table of Contents

List of Figures

List of Tables

Nomenclature

A	area (m²)
c_p	specific heat capacity ($J \cdot kg^{-1} \cdot K^{-1}$)
E	energy (J or kWh)
$\vec{F}$	external body forces (N)
F	inclination angle factor
g	gravitational acceleration ($9.81\ m \cdot s^{-2}$)
H	solar irradiance (W·m-2)
h	heat transfer coefficient ($W \cdot m^{-2} \cdot K^{-1}$)
k_{eff}	effective thermal conductivity ($W \cdot m^{-2} \cdot K^{-1}$)
$\dot{m}$	mass flow rate ($kg \cdot s^{-1}$)
P	fan power (W)
p	pressure (Pa)
P_v	water vapour pressure (mbar)
q	heat flux ($W \cdot m^{-1}$)
$\dot{Q}$	volume flow rate ($m^3 \cdot s^{-1}$)
q	heat flux (W·m-2)
S_m	mass source term ($kg \cdot s^{-1}$)
S_h	energy source term (W)
T	temperature (°C)
t	time (s)
U	thermal transmittance ($W \cdot m^{-2} \cdot K^{-1}$)
v	wind speed ($m \cdot s^{-1}$)
z	vertical distance (m)

Greek letters

α	absorptivity
ΔP	pressure difference (Pa)
ΔT	temperature difference (°C)
ε	emissivity

η	efficiency (%)
ρ	density (kg·m^{-3})
σ	Stefan-Boltzmann constant (5.67×10-8 W·m^{-2}·K^{-4})
τ	transmissivity
$\bar{\bar{\tau}}$	stress tensor

Abbreviations

ACH	air change per hour
CFD	computational fluid dynamics
DO	discrete ordinates
NV	naturally-ventilated
OPF	overhang projection factor
PCM	phase change material
PE	polyethylene
PT	photothermal
PT-RC	photo-thermal-radiative cooling
PV	photovoltaics
PVT-RC	photovoltaic/thermal-radiative cooling
RC	radiative cooling
RMSD	root mean square deviation
SC	solar chimney
SH	solar heater
STC	standard test conditions
TMY	typical meteorological year
UDF	user-defined function

Subscript

a/e	absorber/emitter
abs	absorber
ad	air duct
ag	air gap

amb	ambient
cond	conduction
conv	convection
cov	cover
dp	dew point
el	electrical
emit	RC emitter
env	building envelope
ext	exterior side
ind	indoor
int	interior side
ins	insulation
rad	radiation
sol	solar
surf	building’s surface
th	thermal

Chapter 1 Introduction

1.1 Research Background

Building cooling demands have risen significantly in the past two decades. It is projected that by 2050, the number of global HVAC stocks will reach over 1 billion units (IEA, 2016). This increase is partly due to global warming, and, for people who live in urban areas, also due to urban heat island phenomenon. In both phenomena, anthropogenic heat is the main contributor. Ironically, part of the anthropogenic heat comes from the air conditioning unit used to cool buildings.

The abovementioned dilemma urges architects and building researchers to find alternatives for building cooling under the broad research area of *passive cooling*. There are three general strategies of passive cooling, namely heat protection, heat modulation, and heat dissipation (Geetha and Velraj, 2012; Bhamare, Rathod and Banerjee, 2019).

Heat protection strategy, as the term suggests, protects the building interior from external heat gain. It mostly manifests in the form of solar protection in building openings, i.e., glazing and shading devices, or microclimate modification using water and vegetation. Shading devices used to be static, and their dimension (depth and length) is defined accordingly, to maximise the amount of blocked solar radiation (Valladares-Rendón, Schmid and Lo, 2017; Kirimtat *et al.*, 2019). Nowadays, there is also the dynamic shading system that responds to the sun's position (van Moeseke, Bruyère and De Herde, 2007). Al-Masrani et al. (Al-Masrani and Al-Obaidi, 2019) argued that dynamic solar shading is an effective passive cooling strategy in terms of energy savings and thermal comfort. Even Kirimtat et al. (Kirimtat *et al.*, 2016) proposed that the integration of shading devices into buildings in the future should prioritise movable types.

Nonetheless, a current practice favoured static shading devices over dynamic ones due to design simplicity, easy installation, cost-effectiveness, low maintenance rate, and passive practice (Al-Masrani *et al.*, 2018). However, the performance of the static shading devices still needs to be improved. Unlike dynamic shading devices, the quantity and quality of penetrating daylight cannot respond to the dynamic nature of solar angles and varying sky conditions. This leads to research in the parametric design of shading devices, which tries to optimise the dimension and shape of shading devices according to the site's condition (Valladares-Rendón, Schmid and Lo, 2017). The parametric approach in designing shading devices is also preferred by architects because it assists their creativity in façade design.

Water and vegetation are used either on the roof or wall. Despite the passive cooling classification considering them as a heat protection strategy, water and vegetation are seen as heat modulation and dissipation techniques by researchers (Sodha *et al.*, 1981; Wu and Lei, 2016; Seyam, 2019). Water can work as heat storage or thermal mass for buildings, while greeneries provide heat dissipation via evapotranspiration.

Nevertheless, in some applications, vegetation does work as merely heat protection, especially when used as a green wall or façade (Pérez *et al.*, 2011; Chun, Nyuk and Kardinal, 2014; Pan and Chu, 2016; Haggag and Hassan, 2017; Serra *et al.*, 2017; Pan, Wei and Chu, 2018). Green façade studies show various rates of cooling, measured by temperature reduction from 1.4 ℃ (Pérez *et al.*, 2011), 4 ℃ (Serra *et al.*, 2017), to 12 ℃ (Haggag and Hassan, 2017). In addition to indoor temperature reduction, a green façade and green roof can also benefit the surroundings and are very suitable to be implemented in a densely populated area (Chun, Nyuk and Kardinal, 2014; Pan and Chu, 2016).

In energy-saving terms, green roofs have the potential for 5-16 % cooling load reduction, depending on the climate condition (Feng and Hewage, 2014; Schweitzer and Erell, 2014; Cascone *et al.*, 2019). However, Feng & Hewage (Feng and Hewage, 2014) argued that vegetation on green roof and wall are not cost-effective, and they are also not favourable for the heating season (Gabriel *et al.*, 2016). Another drawback of greenery attached to buildings is the risk of excessive amounts of moisture content due to precipitation Instead of cooling, too much moisture content can add an unwanted latent heat to the building (Seyam, 2019). There is also a structural consideration when implementing a green roof or wall because the components add a substantial amount of weight to the building (Lee and Jim, 2018).

The heat modulation technique minimises heat gain by enhancing the thermal properties of the building materials. The most common methods are thermal mass and phase change material (PCM). Some research also utilises desiccant materials to modulate heat and moisture inside the building (Asim *et al.*, 2019).

Thermal mass is arguably beneficial for almost all climate conditions, especially in combination with insulation material (Verbeke and Audenaert, 2018). Insulation and thermal mass can be named as prerequisites for low-energy building. However, more climate-specific studies state that thermal mass is more beneficial where there is a significant difference between diurnal and nocturnal outdoor temperatures (Balaras, 1996; Yang and Li, 2008; Zhu *et al.*, 2009; Williamson, 2011). Cheng et al. (Cheng, Ng and Givoni, 2005) emphasised that to really benefit from thermal mass, its application should consider the building's mode of operation and occupancy pattern. They also found that the colour of the building envelope impacts the thermal mass performance. Also, thermal mass performs well within a protective insulated envelope (Gregory *et al.*, 2008; Rodrigues, Sougkakis and Gillott, 2016).

Furthermore, some requirements in thermal mass application are mentioned in the literature. Firstly, the selection of material must be appropriate to the building function and architectural consideration. Secondly, the thermal mass should be positioned accordingly. Thirdly, the application of thermal mass must be accompanied by other passive cooling strategies such as insulation, night ventilation, and shading devices to avoid overheating and night (Kendrick *et al.*, 2012). Al-Sanea et al. (Al-Sanea, Zedan and Al-Hussain, 2013) suggested a general hint for thermal mass materials which are materials with heavier mass (i.e., higher heat capacity) and smaller surface absorptivity.

Currently, research on thermal mass in combination with other passive techniques is getting more attention. One study in a hot humid climate region claimed that thermal mass and natural ventilation combination can reduce indoor temperature by 3-6 ℃ (Shaviv, Yezioro and Capeluto, 2001). La Roche & Milne (Roche and Milne, 2004) stated that a higher air change rate provided by ventilation increases the amount of heat released from a thermal mass building. Rodrigues et al. (Rodrigues, Sougkakis and Gillott, 2016) combined thermal mass with PCM. The furthest idea even mentioned in a study is that thermal mass can be made as an active system by controlling its thermal properties electrically (Olsthoorn *et al.*, 2017).

Another common technology to use as a heat modulator is PCM. PCM is usually installed in buildings in three different ways: impregnation, integration, or in combination with other cooling strategies such as Trombe walls and solar chimneys (Zeinelabdein, Omer and Gan, 2018). Impregnated PCM is easier to install and has been proposed by many researchers. It can be put into a wall (Feldman, Banu and Hawes, 1995; Banu, Feldman and Hawes, 1998; Voelker, Kornadt and Ostry, 2008; Karaipekli, Sarı and Biçer, 2016), ceiling (Koschenz and Lehmann, 2004; Voelker, Kornadt and Ostry, 2008; Karaipekli, Sarı and Biçer, 2016), or roof (Pasupathy and Velraj, 2008). Whereas the integrated PCM is mainly applied as a wall, ceiling, or floor. Both techniques are not too different in cooling performance.

Further, some issues related to the deployment of PCM are durability, fire resistance, long-term thermal behaviour, and contact of the PCM with building elements (Feldman, Banu and Hawes, 1995; Voelker, Kornadt and Ostry, 2008; Hasse *et al.*, 2011; Memon, 2014). Gypsum, as one of the most used materials for PCM impregnation is a flammable material. Hence, researchers are now using other materials such as concrete and wallboard (Feldman, Banu and Hawes, 1995; Darkwa and Kim, 2004; Hunger *et al.*, 2009; Kuznik and Virgone, 2009). PCM wallboards are also thought to have the ability to enhance the natural convection inside the room (Kuznik and Virgone, 2009).

One of the emerging technologies to overcome the issue of thermal behaviour is microencapsulated PCM (MPCM) (Hunger *et al.*, 2009; Lai, Chen and Lin, 2010; Memon, 2014). It can increase the amount of stored heat. Another promising technique is shape-stabilised PCM (Xu *et al.*, 2005; Zhang *et al.*, 2006; Memon, 2014). Shape-stabilised phase change material (PCM) is a kind of novel PCM. It has large specific heat for phase change temperature region, lower thermal conductivity, and does not need a container for installation (Xu *et al.*, 2005; Zhang *et al.*, 2006). This technique helps to overcome the problem of contact factors between PCM and building elements. Also, an interesting approach was made by Hasse et al. (2011) by creating a honeycomb panel as the container of PCM to enlarge the contact area of the PCM substance. They claimed that the honeycomb panel significantly increased the thermal inertia of the PCM.

Nevertheless, there are some drawbacks to PCM technologies mentioned in the literature. Inadequate heat transfer and overall reduction in thermal conductivities during energy recovery are identified as the main barriers of PCM material, especially for wallboard PCM (Darkwa and Kim, 2004). PCM also has a very long payback period (14 ½ years) (Panayiotou, Kalogirou and Tassou, 2016).

In this heat dissipation mechanism, excessive heat from the building is rejected to the suitable environmental heat sink at a lower temperature. Available environmental heat sinks are ambient air, water, and sky. Based on the available environmental heat sink, this technique is further classified as convective cooling, evaporative cooling, and radiative cooling.

Evaporative cooling can be divided into two basic types, direct evaporative cooling, and indirect evaporative cooling. In direct evaporative cooling, a reduction of temperature is followed by an increase in moisture content, making the wet bulb temperature its lowest possible temperature reduction. This makes direct evaporative cooling effective in hot humid climates. On the other hand, the indirect system does not increase the air humidity because evaporative cooling is delivered across a heat exchanger, which keeps the cool moist air separated from the room (Santamouris and Kolokotsa, 2013).

Indirect evaporative cooling is an active system since it uses at least some type of pump of fan to circulate the working fluid. Some direct evaporative cooling techniques are also active systems, but there are passive strategies as well. Yet, direct and indirect evaporative cooling is usually applied to enhance the air conditioning system (Cuce and Riffat, 2016; Yang, Cui and Lan, 2019).

One of the attempts to passively utilise direct evaporative cooling is using a roof pond (Sodha, Kaushik and Nayak, 1981). Roof pond is available in various kind of techniques such as open roof ponds, ponds with movable insulations, and ventilated roof ponds. Modification of the roof pond techniques done by Cheikh & Bouchair (Ben Cheikh and Bouchair, 2004), with namely evapo-reflective roof. Roof ponds are effective in arid, as well as temperate climates (Sharifi and Yamagata, 2015a). They also have advantages such as being independent of building orientation, keeping humidity outside the building, and the potential to be used for stormwater management, the stored water can also be used for fire-extinguishing purposes as well (Sharifi and Yamagata, 2015a).

However, there are also some disadvantages of roof ponds. Roof pond systems can only be installed atop flat roofs and affect the accessibility of the roof for other uses. Roof ponds also increase the weight of the building construction, and if not properly maintained, leakage and water contamination may occur. Most variants can only provide indoor comfort in one- or two-story buildings (Sharifi and Yamagata, 2015a).

Another passive evaporative cooling technique is passive downdraught evaporative cooling (PDEC). PDEC is actually a technique to enhance the cooling performance of the wind catcher (Givoni, 1993; Bowman *et al.*, 1997; Belarbi, Ghiaus and Allard, 2006; Kamal, 2012). Water is sprayed inside the wind catcher, so the incoming air is humidified and thus cooled down. Kamal (Kamal, 2012) stated that this system can reduce the temperature in the Torrent Research Centre in Ahmedabad to 13 ℃ lower than outside. However, the performance of the PDEC system depends on the controlled flow rate of the water spray (Bahadori, 1985; Belarbi, Ghiaus and Allard, 2006) Similar principle to the windcatcher PDEC has also been applied in the solar chimney, and wall, and façade element. Al Touma et al. (al Touma *et al.*, 2016) measured a decrease in the space load by 19.8% using PDEC for solar chimneys. Passive evaporative cooling wall (PECW) was studied and found to be effective in reducing temperature by several degrees during summer daytime (He and Hoyano, 2010; He, 2011).

Classifying the passive cooling strategy in the abovementioned way hints at heat dissipation as the optimum way of cooling that a building can use. This is because the heat dissipation strategy does not only prevent or regulate heat from outside from entering the indoor environment (which is done in heat protection and modulation strategies) but also releases heat from the building to the heat sink. The heat dissipation strategy has more varied and flexible mechanisms than the other strategies since it uses any kind of possible heat transfer phenomena. Figure 1-1 illustratively describes the available ways to cool the built environment against the many sources of heat. Among the heat dissipation mechanisms, there is a revival in the research on the use of radiative cooling. As its name suggests, radiative cooling (RC) is a cooling mechanism via radiation to space as the heat sink (Hossain and Gu, 2016; B. Zhao, Hu, Ao, Chen and Pei, 2019). Radiation from the surface of the earth can escape to space because the atmosphere is transparent to certain wavelengths of radiation, namely the atmospheric window band (8-13 μm).

This cooling via radiation to the sky has made it possible for ancient people to make ice (Mahdavinejad and Javanrudi, 2012). As for application in buildings, it is mostly used for *nocturnal* cooling, starting since the mid-20th century (Lu *et al.*, 2016). Yet, the revival of the radiative cooling field has not been started since passive *daytime* radiative cooling was observed in 2014 (Raman *et al.*, 2014). Thanks to the advancement in material sciences, the mechanism that is limited to the nighttime only is now being pursued by various sectors.

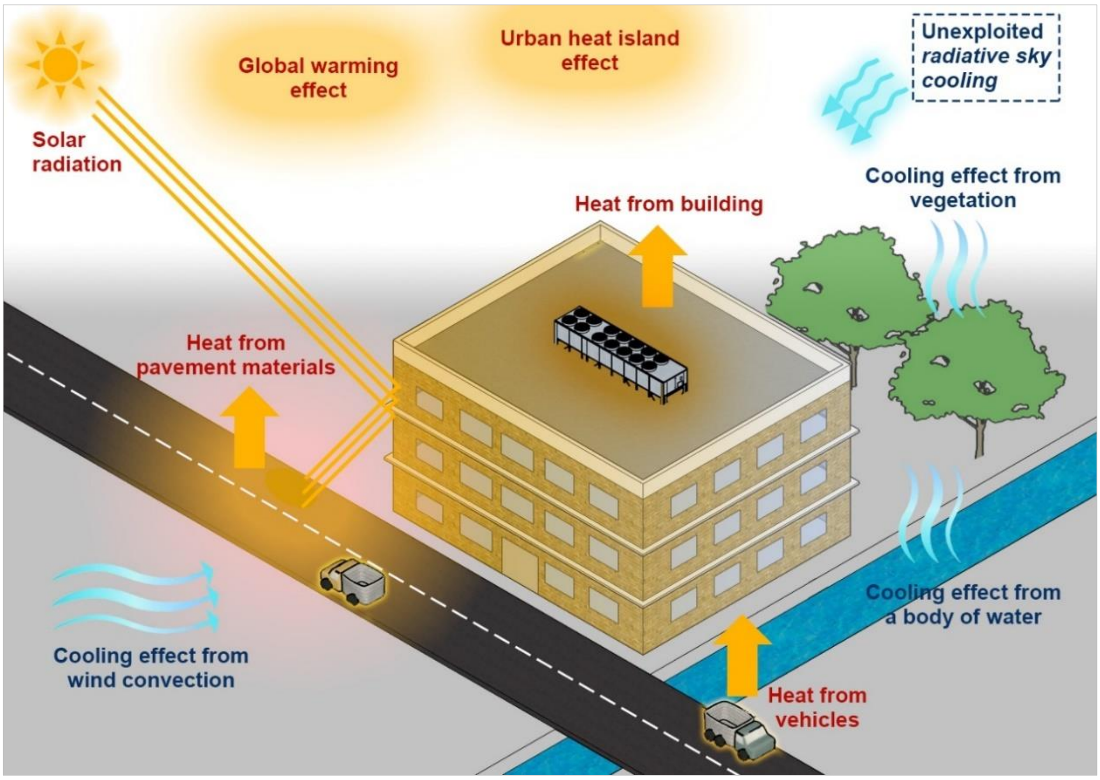

Figure 1-1 Illustration of the heat loads to the built-environment and the potential cooling sources.

As a newly revived passive cooling strategy, radiative sky cooling has much potential to be exploited for building cooling, and yet the challenges to utilise it are still limiting its application. This thesis offers to address some of the challenges mentioned in the literature. One of the technical problems is related to the low cooling power of a radiative cooling emitter compared to buildings' cooling load, the sophisticated material technology to produce the emitter, the complicated systems in implementations to building, the durability of some of the materials involved, and the maintenance issues (Li *et al.*, 2019). Moreover, like many other passive and renewable energy sources, the time in which radiative cooling energy is available mismatches the time when the cooling demand occurs. The highest radiative cooling power occurs at night while building occupants require cooling mostly in the daytime (Ahmad, Jarimi and Riffat, 2019; B. Zhao, Hu, Ao, Chen and Pei, 2019). This means that some kind of cooling energy storage should be involved in the utilisation of radiative sky cooling in buildings.

Moreover, to overcome those challenges, one of the earliest and easiest ways is to integrate radiative cooling fully passively in buildings by using radiative cooling coating on a flat roof (Khedari *et al.*, 2000). However, there might still be many mismatches in supply-demand times with this strategy. The more modern fully passive ways are combining radiative cooling emitter with thermo-regulating materials such as thermal mass (Etzion and Erell, 1991) or phase change materials (PCM) (He *et al.*, 2019; Shen, Yu and Wang, 2020; Yu *et al.*, 2021). These two strategies can overcome the mismatch between the cooling supply and demand.

When active or mechanical devices are involved, the utilisation of radiative cooling for building become more creative. Radiative cooling can be combined with solar collectors (Hu *et al.*, 2019), photovoltaics (PV) (Hu, Zhao, Ao, Zhao, *et al.*, 2018), or even air conditioning (AC) systems (Bergman, 2018). These combinations of radiative cooling with some active, established, technologies can be the solutions to many of the problems mentioned previously. The combination of radiative cooling with an AC system, for example, overcomes the problem of the low cooling power of radiative because it is only used as supplementary cooling. Also, because radiative cooling is added to a well-established system, it is less complicated and arguably cheaper than developing a new standalone radiative cooling system.

1.2 Motivation and Objectives

Motivated by the challenges in radiative cooling utilisation in buildings, this research wants to contribute some proposals on this topic. Notice that most of the aforementioned ideas of implementing radiative cooling in buildings come in the form of a combination with other passive or active systems. This is realistic in terms of state-of-the-art radiative cooling research since developing a new stand-alone radiative cooling device that caters for most of the building cooling demand would take a long time to do. Such a device might be eventually available, but in the meantime, a combination strategy is more feasible.

In this study, the possible combination of radiative cooling is limited to the combination with solar technologies in buildings. This is first because solar technologies have a wide variety of applications in buildings, from fully passive to advanced mechanical devices, from the utilisation for ventilation purposes to space heating and cooling, as well as from the architecturally integrated to separate features.

This wide application of solar energy technologies in buildings opens the possibilities for radiative cooling to be combined with various other purposes besides cooling. Also, most global climates have both heating and cooling season, and thus incorporating radiative cooling with solar technologies make it possible for a dual-functional heating-cooling device. Figure 1-2 illustrates some widely used solar energy technologies in buildings and where radiative cooling can play a role in improving them. Therefore, the research field of radiative cooling in combination with solar technologies is still good for novel ideas to grow.

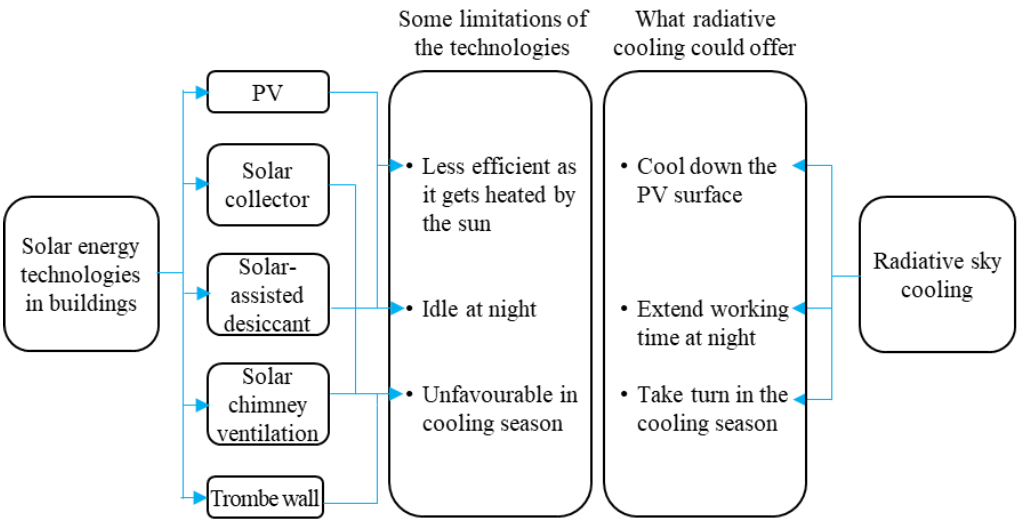

Figure 1-2 Various solar energy technologies in buildings and potential improvements provided by radiative sky cooling.

The research question is then *how to best use the radiative cooling mechanism to passively cool buildings, especially when combined with solar energy applications*. This thesis aims to tackle the question by developing some innovative ways of integrating radiative cooling with solar technologies in buildings. To fulfil that objective, the thesis involves some processes as follows.

a. Reviewing application and integration of radiative cooling with solar technologies in buildings.

This stage reviews all relevant research on the application of radiative cooling in buildings that has previously been done. From the review of the literature, themes or patterns in how previous researchers have incorporated radiative cooling are summarised.

b. Developing concepts of radiative cooling in combination with several solar technologies in buildings.

The proposed concepts are developed from the findings in the previous review process. Also, this thesis offers a variety of concepts to implement radiative cooling in buildings from combination with a fully passive solar energy application in buildings to a fully active solar energy technology.

c. Testing the performance of the concepts according to their proposed function with computer simulation.

All the proposed designs are then evaluated, mainly with the assistance of computational fluid dynamics (CFD) simulations. In the analysis of the energy-saving potential of the proposed design, especially the active ones, EnergyPlus simulations are also involved.

d. Summarising some recommendations for the application of radiative cooling in buildings.

Given the findings from the evaluation of the proposed designs, some insights can be summarised. The advantages and disadvantages of each proposed design are discussed. Limitations in the methods to evaluate the performance of the proposed design are also elaborated.

These processes indicate the smaller goals to obtain the thesis objective. They are also the basis of the structure of this thesis as well. The flow diagram of the objectives is shown in Figure 1-3 below. Chapters in this thesis are arranged according to the structure in Figure 1-3. The main chapters (Chapters 3-6) about the proposed concepts of radiative cooling combination with solar technologies in buildings are sequenced based on the level of active device involvement in the design. This means the proposed concepts in this thesis are available in a fully passive to a fully active system. This diversity opens the possibility of consideration for using radiative cooling in any stage of building design. For instance, architects in their early stages of building design can start to think of a fully passive building-integrated radiative cooling system, whereas HVAC engineers might introduce active radiative cooling systems in the later stage of building design.

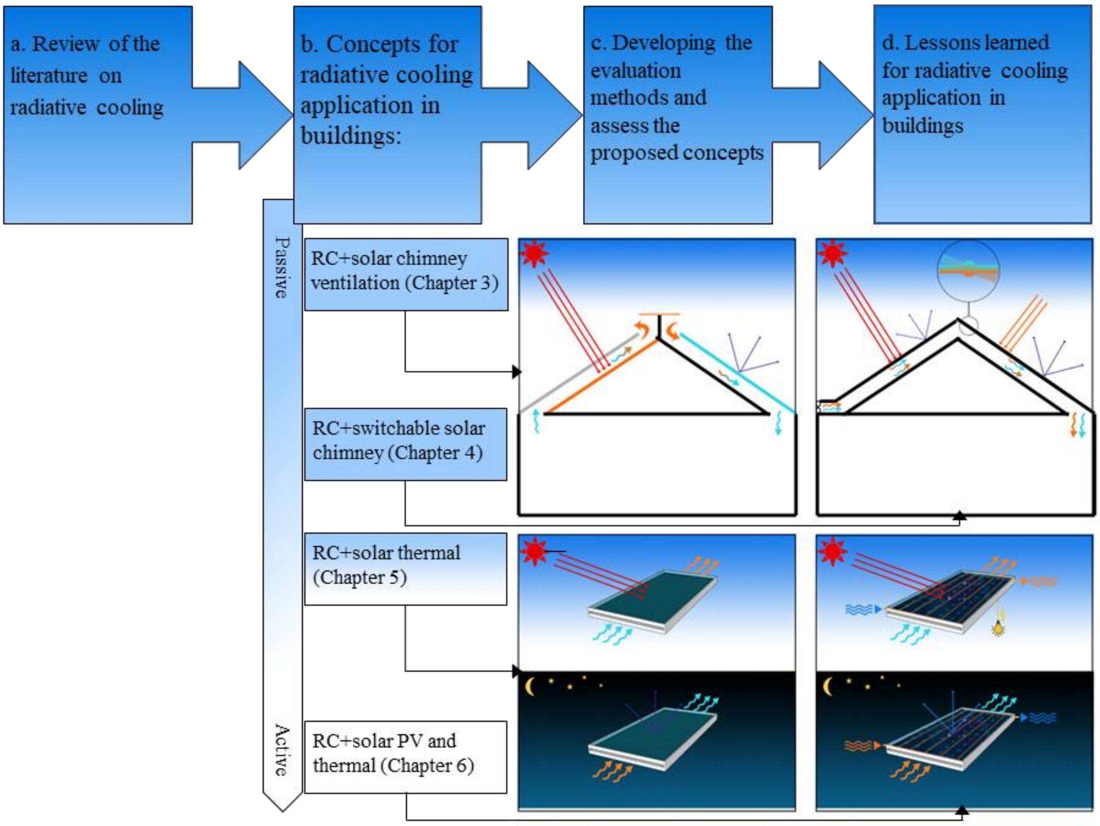

Figure 1-3 Flow chart of the thesis structure.

1.3 Thesis Outline

The thesis will be divided into 7 chapters. Chapter 1 has laid out the background in which radiative cooling emerges as a possible alternative to the solutions of the big issues surrounding the topic as well as the general direction of the research in the field. To find ways to utilise radiative cooling in buildings, we will first review the literature to find relevant research gaps in the topic. Chapter 2 will contain this review. It will elaborate on various applications of radiative cooling in buildings, whether as a stand-alone module or in combination with other technologies. At the end of this chapter, some proposed strategies will be offered.

Further, the proposed strategies in Chapter 2 will be investigated and be the subject of several chapters that follow it. These core chapters are arranged according to the level of passiveness of the strategy, *i.e.*, to what extent the strategy includes an active device to utilise radiative cooling. Chapter 3 will analyse a fully passive building-integrated radiative cooling system. The system employs the stack effect from a solar chimney to create a natural ventilation flow that is pre-cooled by a radiative cooling mechanism. If chapter three is a fully passive system involving natural ventilation, Chapter 4 will discuss an active system involving a fan in the form of RC-improved mechanical ventilation. Note that the only active device involved in the proposed strategy in Chapter 4 is a fan.

Further involvement of active devices in the utilisation of RC in buildings will be studied in Chapter 5. The chapter will investigate how radiative cooling can make the heating, ventilating, and air conditioning (HVAC) system more energy efficient. Thus, the proposed strategy in Chapter 5 will involve an HVAC system. Besides the fan and HVAC system, the radiative cooling mechanism can be also combined with a renewable energy generation system, and this will be the subject of Chapter 6. In Chapter 6, a photovoltaic (PV) panel will be modified to serve a solar air and water heating and radiative cooling function. Thus, the level of active devices involved is even more advanced than in Chapter 5.

Lastly, Chapter 7 will summarise all findings from the core chapters as well as discuss the further improvement that can be done, both in terms of the proposed concepts and research methods. This chapter will also offer an outlook on the research on this topic.

Chapter 2 Review of Applications of Radiative Cooling in Buildings[1]

As alternatives for space cooling in buildings are urgently needed nowadays, passive cooling mechanisms like radiative sky cooling are getting wide attention from building engineers and researchers alike. Various ways of integrating radiative cooling into building systems are continuously proposed. This chapter summarises some of the proposed concepts and discusses the outlook for the application of radiative cooling in buildings. To shorten the term and make reading more convenient, the term 'radiative cooling, is abbreviated to 'RC'.

2.1 Radiative Cooling Fundamentals

Before getting into the application of RC in buildings, it is compulsory to review how previous research utilised it. As previously mentioned, ancient people utilised the RC phenomenon itself for ice making. Yet, only in the 20th century, the mechanism of RC was started to be scientifically studied. By this time, it is known that all bodies radiate heat in the form of electromagnetic waves. For an ideal blackbody, the total power of this radiation is proportional to its temperature, and the distribution of this emissive power across the radiation wavelength is governed by Planck's law (Equation 2.1).

$$E_{\mathrm{B}\lambda}(T,\lambda) = \frac{2\pi h c_0^2}{n^2 \lambda^5 [e^{hc_0/n\lambda kT} - 1]} \quad (2.1$$

In Equation 2.1, $E_{\mathrm{B}\lambda}(T,\lambda)$ is the spectral emissive power of a blackbody at a certain temperature T for a particular wavelength λ, h is Planck's constant (6.626×10^{-34} J · s), c_0 is the light speed in vacuum (2.998×10^{8} m/s), n is the refractive index of the medium (1 for vacuum), and k is Boltzmann's constant (1.3807×10^{-23} J · K^{-1}). Figure 2-1 plots the distribution of blackbody emissive power for some temperatures against the wavelength. The figure shows that emissions from different blackbody temperatures peaked at different wavelengths. The wavelength in which this radiation peaked ($\lambda_{\max}$)

[1] Part of this chapter content is published in *Buildings* (Vol. 10, Issue 12) doi.org/10.3390/buildings10120215

can be estimated with Equation 2.2. When Equation 2.2 is applied to a 300 K blackbody, it gives $\lambda_{\max}$ of 9.6 µm (Modest, 2003).

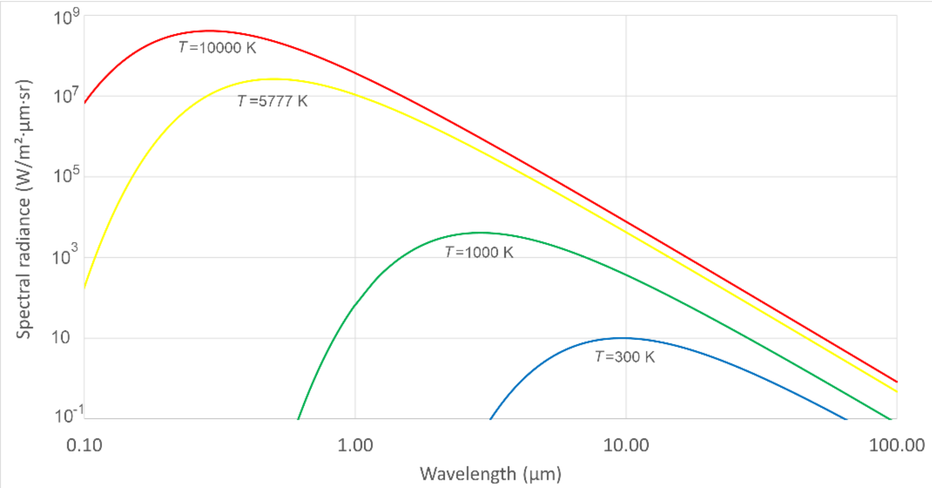

Figure 2-1 The spectral emissive power of a blackbody for various temperatures (SpectralCal.com, 2020).

$$\lambda_{\max} = \frac{2898}{T} \quad (2.2$$

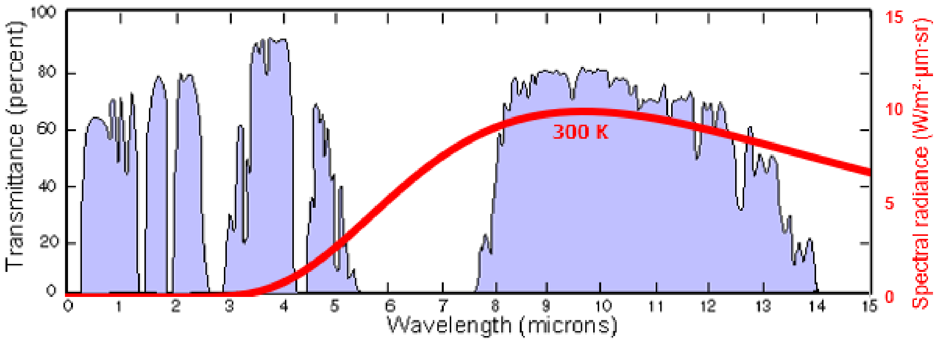

Figure 2-2 Spectral emissive power of a blackbody with a temperature of 300 K, overlayed on the transmissivity value of the atmosphere (Commons, 2020).

The earth's surface emits thermal radiation almost like a blackbody, and its spectral emissive power closely resembles Planck's law. Most of the radiation is absorbed by the atmosphere and some goes through to outer space. This is because the atmosphere is transparent in some wavelength bands. Figure 2-2 below plots the transmissivity of the atmosphere, superimposed with the spectral emissive power of a blackbody with 300 K temperature. It is seen in Figure 2-2 that the atmosphere is quite transparent in the radiation wavelength of 8-13µm. This wavelength band is called the atmospheric window band, and it nicely coincides with the peak of the spectral emission from a 300 K blackbody. Considering surfaces of a building are roughly in this temperature range, it is thus possible for any building surface to radiate heat to space if it has access to the sky. Additionally, if this emitted heat to space is higher than the heat gained by the surface (via radiation, conduction, and convection), the surface experiences cooling.

From the theoretical condition that makes possible cooling via radiation to the sky mentioned above, one can derive the optimal condition for radiative cooling. For instance, the best atmospheric condition for radiative sky cooling is when the total column water vapour is at its lowest because water vapour can block the atmospheric window (Ziming *et al.*, 2021). In other words, a clear sky and relatively dry ambient air are excellent conditions for radiative cooling to take place. In addition to the atmospheric condition, a radiative cooling emitter itself should have high (close to blackbody) emissivity in the 8-13 µm radiation wavelength. On top of that, the emitter should also reduce absorbed radiation from other wavelengths as well as prevent heat gain from conduction and convection. At night, this last requirement for radiative cooling is relatively easy to achieve, since there is no immense radiation from the sun,

Those derived radiative cooling prerequisites lead to a typical radiative cooling (RC) module design as illustrated by Figure 2-3. The RC module consists of an emitter, an insulated frame, and a transparent cover. The transparent cover protects the emitter from convection heat loss to the ambient air, and it *must* have high transmissivity in the atmospheric window band. Figure 2-3 also illustrates the energy balance for the RC module. The cooling power (q_{net}) of the RC module is defined as net heat transfer from the emitter. In the daytime, parts of radiation from the sun (q_{sol}) and the atmosphere (q_{atm}) are absorbed by the emitter. The emitter itself also emits radiation (q_{rad}) to the atmosphere. Besides those thermal radiation terms, the RC emitter also exchanges heat via conduction and convection ($q_{\mathrm{cond+conv}}$). Equation 2.3 summarises the energy balance of the RC emitter.

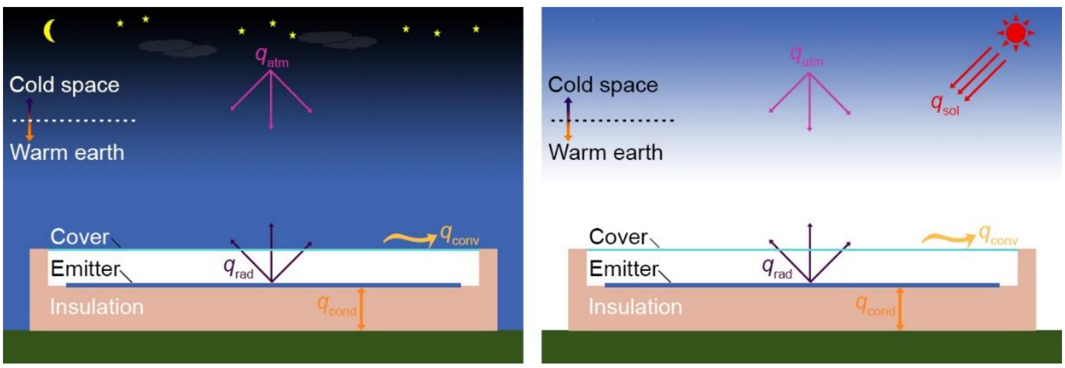

Figure 2-3 Illustration of typical radiative cooling (RC) panel design and heat transfer on the panel.

$$q_{\text{net}} = q_{\text{rad}}(T,\lambda) - q_{\text{atm}}(T_{\text{amb}}) - q_{\text{sol}}(\lambda) \pm q_{\text{conv+cond}}(T,T_{\text{amb}}) \quad 2.3$$

The heat balance equation above can be further detailed with a reference to the formula from Raman *et al.* (2014). The term q_{rad} is defined as the emissive power of the RC emitter surface with area *A*. As shown in Equation 2.4, the emissive power depends on the temperature of the emitter (*T*) and the wavelength of the electromagnetic radiation (λ).

$$q_{\text{rad}}(T,\lambda) = A \int d\Omega \, cos \ \theta \int_0^\infty d\lambda \, E_{\text{B}\lambda}(T,\lambda) \, \varepsilon(\lambda,\theta) \quad 2.4$$

The next term is the q_{atm} which represents the absorbed radiation from the atmosphere. It depends on the ambient temperature T_{amb} as shown in Equation 2.5.

$$q_{\text{atm}}(T_{\text{amb}}) = A \int d\Omega \, cos \ \theta \int_0^\infty d\lambda \, E_{\text{B}\lambda}(T_{\text{amb}},\lambda) \, \epsilon(\lambda,\theta) \, \varepsilon_{\text{atm}}(\lambda,\theta) \quad 2.5$$

The term $\int d\Omega$ in Equations 2.4 and 2.5 represent the angular integral over a hemisphere as shown in Equation 2.6.

$$\int d\Omega = 2\pi \int_0^{\frac{\pi}{2}} d\theta \, sin \ \theta \quad 2.6$$

Whereas the term $E_{\text{B}\lambda}(T,\lambda)$ in Equations 2.4 and 2.5 denote the spectral emissive power of the blackbody at temperature (*T*) for each radiation wavelength (λ) as shown in Equation 2.1. Moreover, there are also the $\varepsilon(\lambda,\theta)$ and $\varepsilon_{\text{atm}}(\lambda,\theta)$ terms, which are the wavelength- and angle-dependent emissivity of the RC emitter and the atmosphere respectively.

Furthermore, the absorbed solar radiation is detailed in Equation 2.7. Based on Kirchoff's radiation law, the absorptivity of the emitter in the solar radiation band equals its emissivity. Thus, in Equation 2.7 the term $\int_0^\infty d\lambda \, \varepsilon(\lambda,\theta_{\text{sol}})$ appears, which represents the absorptivity/emissivity of the emitter in the whole solar radiation band, with $\varepsilon(\lambda,\theta_{\text{sol}})$ as the emitter's emissivity in the direction of the sun (θ_{sol}). In Equation 2.7, $I_{\text{AM 1.5}}$ is solar intensity using AM 1.5 spectra.

$$q_{\text{sol}}(\lambda) = A \int_0^\infty d\lambda \, \varepsilon(\lambda,\theta_{\text{sol}}) \, I_{\text{AM1.5}}(\lambda) \quad 2.7$$

Additionally, the conduction and convection heat transfer $q_{\text{cond+conv}}(T,T_{\text{amb}})$ between the emitter and its surroundings are detailed as in Equation 2.8. In the equation,

h_c is the heat transfer coefficient, T_{amb} is the ambient temperature, and $T_{emitter}$ is the RC emitter's temperature.

$$q_{cond+conv}(T, T_{amb}) = A\, h_c(T_{amb} - T_{emitter}) \quad 2.8$$

At night, the RC module may easily achieve cooling and sub-ambient temperature since there is no solar irradiance. This is usually mentioned as nocturnal radiative cooling. For this nocturnal radiative cooling purpose, any natural materials with high emissivity would do. However, natural materials are usually diffuse materials, *i.e.*, materials that have a broadband emissivity or similar emissivity value over a broad wavelength band. This means they are also highly absorptive in the solar radiation band (0.2-3 um), and thus will absorb much of it during the daytime. Therefore, these naturally common materials are not suitable for daytime radiative cooling purposes. A daytime RC emitter must be reflective in the solar and other radiation bands and yet specifically absorptive/emissive in the atmospheric window band.

With the emergence of material science, this type of material is now feasible to be made. This was first demonstrated in 2014 when a group of researchers from the University of Colorado Boulder achieved a sub-ambient surface temperature of 4.9°C lower than the ambient (Raman *et al.*, 2014). Ever since, several materials have achieved a daytime radiative cooling effect (Gentle and Smith, 2015; Bao *et al.*, 2017; Huang and Ruan, 2017; Kou *et al.*, 2017; Huang *et al.*, 2018). These revolutions in material science for radiative cooling also revive a field of study for RC application in buildings. This chapter reviews the current state of this research field, elaborates on the pros and cons of the utilisation of RC in buildings, as well as offers some insights on further research on the topic.

2.2 Attempts to Use Radiative Cooling for Building Cooling

Historically, the RC phenomenon has been exploited for cooling in buildings since the 70s. Bartoli *et al.* (1977) experimented with an RC emitter used on the rooftop. Using a similar RC emitter, Harrison and Walton (1978) also developed a roof-integrated RC emitter with different materials. Following those experiments, Givoni (1977) proposed another design of an RC system. His design could provide heating and cooling depending on the season.

After a handful of studies in the 70s, the nocturnal RC for building use started to get more attention from the scholarly community in the 90s. The research in this period was focused more on the improvement of the cooling power of RC emitters (Argiriou *et al.*, 1992; Orel, Gunde and Krainer, 1993; Argiriou, Santamouris and Assimakopoulos, 1994; Diatezua *et al.*, 1996; Mihalakakou, Ferrante and Lewis, 1998). There is also research on the mechanism to extract the cooling power using working fluid (Ezekwe, 1990; Etzion and Erell, 1991; Al-Nimr, Kodah and Nassar, 1998) and desiccant (Lu and Yan, 1995). Since then, explorations on the application of RC in buildings have skyrocketed.

There are various ways to classify the precedents of RC applications in buildings. For instance, Erell (2012) categorises RC applications in buildings into two categories namely the movable insulation and the heat exchangers. His categorisation is based on the mechanism in which the emitter is utilised. In the RC emitter with movable insulation, the emitter is protected from solar radiation during the daytime and exposed to the sky at nighttime by moving the insulation off from the emitter (Hay and Yellott, 1969; Etzion and Erell, 1991). Further, in the RC emitter with a heat exchanger, the coldness of the emitter is harnessed with water or air, before being used to cool the building interior via the heat exchanger mechanism (Zhao *et al.*, 2019).

Another classification is proposed by Zeyghami *et al.* (2018). They classify RC applications in buildings based on the working time, which are the nocturnal (nighttime) and diurnal (daytime) RC emitter. The nocturnal RC emitter usually consists of two types of emitters. The first one is the grey emitter which emits in the broadband of the wavelength. The second type is the selective emitter which has higher or lower emissivity at a certain wavelength. The diurnal RC emitter, however, only works with the selective emitter material.

In discussing past RC research, this thesis uses different categorisations. The following three sections imply the categorisation used in this thesis. The sections divide the discussion into the RC emitter materials, systems, and architectural features that have been involved in the research. In addition to these three sections, Section 2.5 discusses the research gaps in the application of RC in buildings, and from that, proposes possible research directions.

2.3 Research on the Improvement of the Materials for Radiative Cooling

Improvement to the materials used for RC is done in three parts, *i.e.*, the emitter material itself, the convection cover material, and the insulation. A summary of the research on this topic and its classification is presented in Table 2-1.

Table 2-1 Summary of the strategies to improve the performance of the RC applications in buildings.

Improvement strategy		**Time**	**Output**	**Researcher**
Emitter material improvement	Film-based emitter	Nocturnal	energy saving for cooling up to 26-49%	(Muselli, 2010)
	Film-based emitter		43 W/m^2	(Cunha *et al.*, 2020)
	Photonic emitter		5 °C below ambient	(Han, Ng and Wan, 2020)
	Photonic emitter		5.2 °C below ambient	(Dong *et al.*, 2019)
	Film-based emitter	Diurnal	120 W/m^2	(Zhou *et al.*, 2019)
	Film-based emitter		not available (N/A)	(Gentle and Smith, 2015)
	Film-based emitter		2.5 °C below ambient	(Ao *et al.*, 2019)
	Film-based emitter		4.2 °C below ambient	(Li *et al.*, 2019)
	Film-based emitter		95.1 W/m^2	(Fan, Fu and Fu, 2020)
	Photonic emitter		110 W/m^2	(Torgerson and Hellhake, 2019)
	Nanoparticle-based emitter		25.5 °C below ambient	(Y. Liu *et al.*, 2019)
	Nanoparticle-based emitter		35 °C below ambient	(Kim and Lenert, 2018)
	Photonic emitter		N/A	(Huang *et al.*, 2018)
	Photonic emitter		14.3 W/m^2	(Shin Young Jeong *et al.*, 2020)
	Photonic emitter		7.7 ± 0.2 °C below ambient	(Gao *et al.*, 2019)
Cover material improvement	Film-based cover	Nocturnal	23 W/m^2	(Bathgate and Bosi, 2011)
	Film-based cover		175 W/m^2	(Naghshine and Saboonchi, 2018)
	Film-based cover		N/A	(Benlattar *et al.*, 2005)
	Film-based cover		N/A	(Benlattar *et al.*, 2006)
	Photonic cover	Diurnal	50 W/m^2	(Wong *et al.*, 2018)

Improvement strategy		Time	Output	Researcher
Insulation material and thermal contact improvement	Design aspect: water contact with the emitter, insulation	Nocturnal	97.8 W/m^2	(Dimoudi and Androutsopoulos, 2006)
	Design aspect: construction material		2.5 °C below ambient	(Okoronkwo *et al.*, 2014)
	Design aspect: water contact with the emitter		52 W/m^2	(Hosseinzadeh and Taherian, 2012)
	Design aspect: air duct		90 W/m^2	(Erell and Etzion, 1999)
	Design aspect: insulation, air duct		2.5-4 °C below ambient	(Bagiorgas and Mihalakakou, 2008)
	Design aspect: insulation		38 W/m^2	(Tso, Chan and Chao, 2017)
	Design aspect: insulation		N/A	(Fält, Pettersson and Zevenhoven, 2017)
	Design aspect: cover, air duct		1-6 °C below ambient	(Khedari *et al.*, 2000)
	Design aspect: insulation	Diurnal	37 °C below ambient through a 24-hour cycle	(Chen *et al.*, 2016)
	Design aspect: glazing and convection scheme		100 W/m^2	(Fält and Zevenhoven, 2011)
	Design aspect: orientation		7.4 °C below ambient	(B. Zhao, Ao, *et al.*, 2019)
	Design aspect: appearance		3.9 °C below ambient	(Lee *et al.*, 2018)
Combination with other technologies or passive strategies	Trombe wall	Nocturnal	energy saving for cooling up to 53%	(Benlattar *et al.*, 2006)
	Wall material		55.8 W/m^2	(Dong *et al.*, 2019)
	Wall material and insulation, cold water storage		87 W/m^2	(Fält and Zevenhoven, 2011)
	Solar collector, phase change material (PCM)		N/A	(B. Zhao, Ao, *et al.*, 2019)
	Photovoltaics (PV)		128.5 W/m^2	(Wong *et al.*, 2018)
	Solar collector		50.3 W/m^2	(Lee *et al.*, 2018)
	Cold storage		N/A	(Tevar *et al.*, 2015)
	Solar collector		27.3 W/m^2	(Granqvist and Hjortsberg, 1980)
	PV, HVAC system		123.9 W/m^2	(Muselli, 2010)
	PV		41.7 W/m^2	(Cunha *et al.*, 2020)
	HVAC		N/A	(Dobson, Hodes and Mastai, 2003)
	Solar collector and PV, cold-water storage		75 W/m^2	(Tso, Chan and Chao, 2017)

Improvement strategy		Time	Output	Researcher
	PCM		energy saving potential can reach 77% for low-rise buildings	(Han, Ng and Wan, 2020)
	Desiccant		5.5-7 °C below ambient	(Chen *et al.*, 2016)
	Solar collector, desiccant		energy saving up to 7400 kWh per year	(Zhou *et al.*, 2019)
	PV, solar collector, HVAC		N/A	(Laatioui *et al.*, 2018)
	HVAC		energy saving for cooling up to 46% for	(Yang, Chen and Zhang, 2018)
	Radiant cooling, air handling unit (AHU)		18.1 W/m^2	(Kou *et al.*, 2017)
	Fan or HVAC		5-10W/m^2	(B. Zhao, Hu, Ao and Pei, 2019a)
	Ground-coupled heat pump		energy saving 10.22% compared to conventional ground heat pump	(Gentle and Smith, 2015)
	PV, solar collector		72 W/m^2	(Ao *et al.*, 2019)
	HVAC		N/A	(Li *et al.*, 2019)
	Thermosyphon and cold-water storage		energy saving for cooling up to 8%	(Fan, Fu and Fu, 2020)
	Solar collector		36.61 W/m^2	(Y. Liu *et al.*, 2019)
	Heat pipe		14.5 W/m^2	(D. Liu *et al.*, 2019)
	Photovoltaic thermal (PV/T)		65 W/m^2	(Huang and Ruan, 2017)
	Thermosyphon and cold-water storage		N/A	(Yang *et al.*, 2019)
	Solar collector		4-5 °C below ambient	(Kim and Lenert, 2018)
	Solar collector		55.1 W/m^2	(Huang *et al.*, 2018)
	Solar collector		40 W/m2	(Wu *et al.*, 2018)
	Thermosyphon and cold-water storage		15 °C below ambient	(Wang *et al.*, 2019)
	Thermal mass		77.2 W/m^2	(Raman *et al.*, 2014)
	PV		72.94 W/m^2	(Shin Young Jeong *et al.*, 2020)
	Solar collector, HVAC		4.7 °C below ambient	(Li and Coimbra, 2019)
	Water tank		8.4 °C temperature reduction	(Zhai *et al.*, 2017)
	HVAC	Diurnal	16 W/m^2	(Jeong *et al.*, 2018)
	HVAC		more than 200 W/m^2	(Torgerson and Hellhake, 2019)

Improvement strategy		Time	Output	Researcher
	Thermoelectric, cold water storage tank		daytime and nighttime cooling of the radiative sky cooling subsystem contribute to 55.0% and 45.0% of annual cold generation, respectively	(Fu *et al.*, 2019)
	Attic insulation		energy saving for cooling up to 3.7-11.8 kWh/m^2	(Gao *et al.*, 2019)
	Cold water storage, radiant cooling in the room		12.5 W/m^2	(Benlattar *et al.*, 2005)
	PCM, thermosyphon		energy saving for cooling up to 25%	(Long, Yang and Wang, 2019)
	PCM, wall material		energy saving for cooling up to 47.9%	(Lee *et al.*, 2017)
	PCM, cold water storage		energy saving for cooling up to 10%	(Diatezua *et al.*, 1996)
	Wall material and insulation		50 W/m^2 on the wall, and 120 W/m^2 on the roof	(Sullivan, Krishna and Lee, 2018)
	Shading device		reduces solar gain by up to 40%	(Shahsafi *et al.*, 2019)
	Glazing		energy saving for cooling between 40.9-63.4%	(Sameti and Kasaeian, 2015)

2.3.1 Emitter material

The common objectives in research on the improvement of the emitter material include the refinement of the spectral properties of the emitter (Taylor *et al.*, 2020; Kishore, Booten and Wijesuriya, 2022; Yuan *et al.*, 2022), improve the durability of the material (Sullivan, Krishna and Lee, 2018), create more affordable materials (Li *et al.*, 2021), and provides alternatives for the appearance of the material (Son *et al.*, 2021). Meanwhile, the refinement of the cover material is targeted to make a durable cover (Bathgate and Bosi, 2011), refine the spectral emissivity (Benlattar *et al.*, 2006), as well as provide a better insulation effect Naghshine and Saboonchi (2018).

Regarding the emitter material, Zhao *et al.* (2019) classify the current RC material technologies into four categories, namely natural, film-based, nanoparticle-based, and photonic emitters (see Figure 2-4 for examples of the materials). With the recent development in material science, only the latter three methods that gained attention for the improvement of RC material, namely the film-based emitters (Gentle and Smith, 2015; Ao *et al.*, 2019; Li *et al.*, 2019; Zhou *et al.*, 2019; Fan, Fu and Fu, 2020), nanoparticle-based emitters (Kim and Lenert, 2018; Liu *et al.*, 2019), and photonic emitters (Huang *et al.*, 2018; Mengyu Gao *et al.*, 2019; Torgerson and Hellhake, 2019; Shin Young Jeong *et al.*, 2020).

As previously mentioned, there are at least three common objectives for the enhancement of the RC emitter material. The objectives are to refine the spectral properties of the emitter (Raman *et al.*, 2014; Fan, Fu and Fu, 2020), create materials that are more affordable material (Givoni, 1977; Erell and Etzion, 1999), and provide alternatives for the appearance of the material (Gonome *et al.*, 2014; Son *et al.*, 2020, 2021).

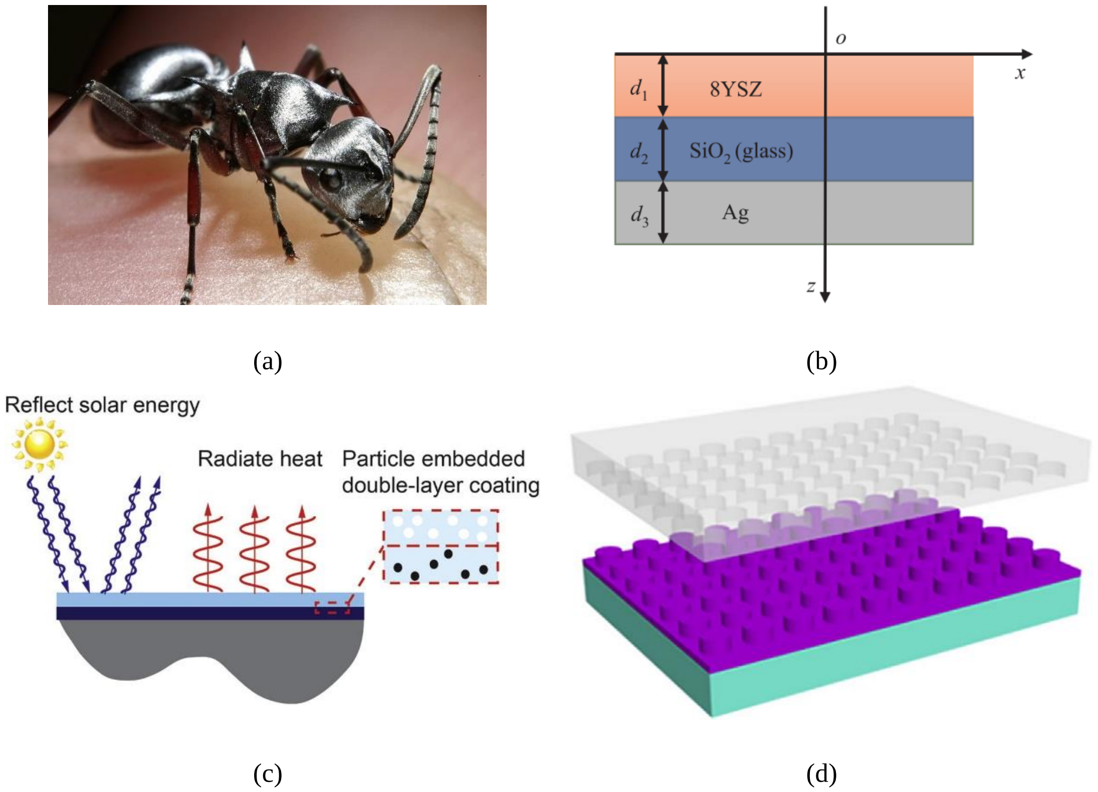

Figure 2-4 Different types of RC emitter materials: (a) natural emitter of a Saharan silver ant (S. Y. Jeong *et al.*, 2020); (b) film-based emitter design by Fan *et al.* (2020); (c) nanoparticle-based emitter design by Huang and Ruan (2017); (d) photonic emitter design by Gao *et al*. (2019).

The refinement of the spectral properties can enhance the daytime cooling effect of the RC emitter. The RC emitter material is engineered to be more reflective to the solar and atmospheric radiation (reflectivity value near unity) whilst also more emissive in the atmospheric window band (absorptivity/emissivity value near unity). Using the film-based emitter Zhou *et al.* (2019) can provide all-day cooling for buildings on a typical sunny day in northern US latitudes with the emitter temperature between 2-9 °C. Another approach, the photonic emitter, showed a cooling power of 110 W/m² under direct sunlight (Torgerson and Hellhake, 2019). Whereas nanoparticle-based Liu *et al.*

(2019) and Kim and Lenert (2018) were able to record sub-ambient temperatures during the daytime, with 25.5 °C and 35 °C below ambient, respectively. Those precedent studies show that the research on the refinement of RC emitter spectral properties is successful, at least for the climate where the experiments were done.

Nonetheless, other climate types still need attention for spectral improvement, which is the humid climate (C. Liu et al. 2020; Chen et al. 2021; Zhong et al. 2020). One study by Jeong *et al.* (2020) shows the discrepancy in the cooling performance of an RC emitter material between dry and humid climates. Their RC emitter could be at 7.2 C lower than ambient during the daytime in the subtropical dry climate, but in the humid climate, the RC hardly achieved cooling at all (Dong *et al.*, 2019; Fan, Fu and Fu, 2020; Han, Ng and Wan, 2020). The current best results for RC in humid climates are obtained by Don *et al.* (2019) and Han and Wan (2020). They experimented with an enhanced specular reflector (ESR) material by 3M (2018). They prove to be able to get sub-ambient emitter temperature on a very humid and cloudy night (Dong *et al.*, 2019; Han, Ng and Wan, 2020).

Despite many studies on the refinement of the spectral emissivity of the RC material, there is less attention given to the study on the affordability of the material (Li *et al.*, 2020). In the pursue of providing more affordable RC, Givoni,(1977) and Erell and Etzion (1999) proposed to use conventional solar absorber materials. But their cooling power is still considered low compared to the previous more sophisticated and expensive materials above. This indicates that the Current RC materials with high cooling power are still expensive to produce (Li *et al.*, 2019). A review by Li *et al.* (2020) suggested that the polymer-based porous emitter (Mandal *et al.*, 2018) might be a promising way to build an affordable RC emitter.

There is another other small consideration studied, namely the aesthetic look of the emitter. The look is especially important for architects because they are concerned about the aesthetic appearance of buildings. Lee *et al.* (2018) and Son *et al.* (2021) attempted to create coloured emitters by employing different techniques. For instance, Lee *et al.* (2018) create colourful RC emitters by adding photonic nanolayers below the emitter. The photonic nanolayer is structured in the order of metal-insulator-metal (MIM), consisting of Ag-SiO_2-Ag substances. The colour variations were achieved by varying the thickness of the SiO_2 layer. Further, Son *et al.* (2021) make the different appearance of RC emitters by coating them with silica-embedded perovskite material. Figure 2-5 displays the various colours of RC emitter by Son *et al.* (2021). Both coloured RC materials from those researchers could achieve sub-ambient temperatures during the daytime.

Figure 2-5 Samples of coloured daytime RC emitter researched by Son et al. (Son *et al.*, 2021).

2.3.2 Cover material

Regarding the enhancement of the convection cover material, the two key issues are spectral properties and durability. In early 2000, Benlattar *et al.* (2005, 2006) started to create a convection cover with better spectral properties. They created the cover from a cadmium sulphide (CdS) thin film which has high transmissivity for infrared radiation in the 8-13 µm band. The results showed a significant 65°C difference between the emitter surface with the cover compared to the emitter without cover (Benlattar *et al.*, 2006). The more recent study by Naghshine and Saboonchi (2018) compared 30 different multilayer combinations of 16 thin films for RC convection cover. See Figure 2-6 for an illustration of the multilayer structure of the thin film. The results indicate that multilayer structures that involve cubic zinc sulphide (ZnS) in their layers are the best options for protecting the RC emitter from parasitic heat loss (Naghshine and Saboonchi, 2018).

Nonetheless, the durability of the convection cover is also still an issue for the RC emitter. The widely used convection cover is polyethene (PE) film, which is not durable mechanically and environmentally. Selective cover structures may be the solution to this problem (Zhang *et al.*, 2021). In line with Naghshine and Saboonchi (2018), research from Bathgate and Bosi (2011) also revealed that ZnS thin film is the more durable alternative to convection cover for RC emitter was conducted by Bathgate and Bosi (2011).

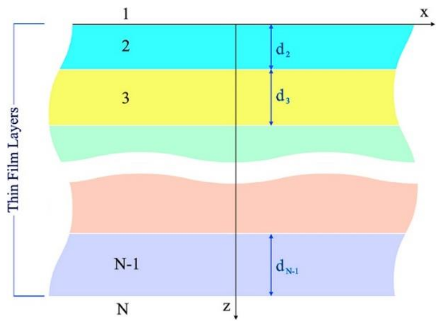

Figure 2-6 Multilayer structure thin film scheme of Naghshine and Saboonchi (Naghshine and Saboonchi, 2018).

2.3.3 Insulation material

When improved, the insulation material can contribute to the increase in cooling power of the RC emitter as well. This is shown by Craig *et al.* (2008) when they improved the insulation at the backside of a roof-integrated RC emitter by changing the configuration of the backside insulation. They found that if the backside insulation is good enough, even common roof materials could perform as an RC emitter. Similarly, Dimoudi and Androutsopoulos (2006) also designed a roof-integrated RC system that is protected from the parasitic thermal load by a configuration of roof insulation as shown in Figure 2-7.

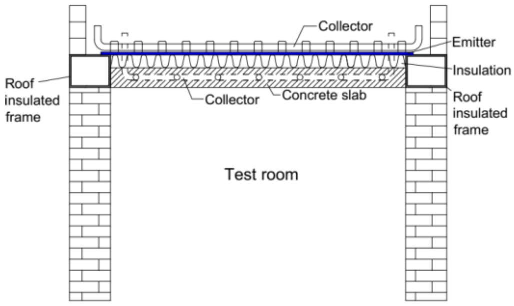

Figure 2-7 Proposed configurations of insulation for roof-integrated solar collector-RC emitters by Dimoudi and Androutsopoulos (2006).

Besides the backside insulation, several studies also propose to improve the insulation effect in the gap between the emitter and the convection cover. For instance, instead of being an air gap, the space between the emitter and the convection cover can be made a vacuum so the parasitic convection heat transfer is minimised (Chen *et al.*, 2016; Tso, Chan and Chao, 2017). Chen *et al.* (2016) demonstrate the increase in cooling power with this vacuum gap method in their design with a minimum temperature of 42 °C below the ambient in the daytime. Further, Tso *et al.* (2017) employ this vacuum gap method to obtain the RC effect in a humid climate in Hong

Kong. Their design, shown in Figure 2-8, could provide a cooling power of 38 W/m^2 at night.

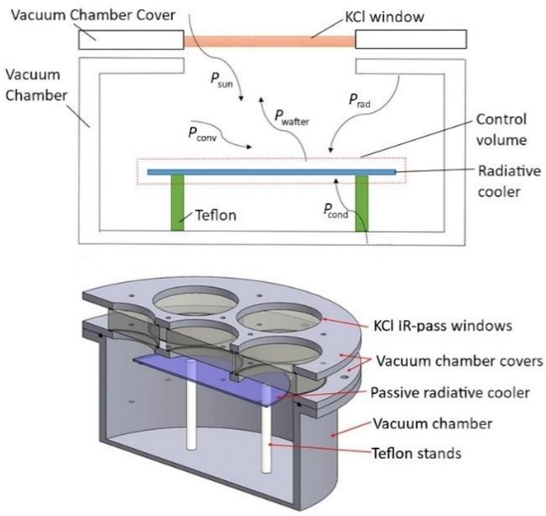

Figure 2-8 Design of vacuum chamber as insulation and part of the convective cover for the RC emitter (Tso, Chan and Chao, 2017).

2.4 Radiative Cooling System Design

2.4.1 Classification of the RC systems based on the working fluid

In addition to the abovementioned research on RC emitter materials, another important aspect of the RC application in buildings is the RC system design. To make use of cooling from an RC emitter, a building can integrate the RC emitter in various ways. In terms of the working fluid used in the utilisation, the system can be grouped into water-based and air-based systems. The water-based systems include open and closed systems. In water-based open systems, a body of water at rest (a pond or water storage) is directly in contact with the RC emitter. Whereas, in the closed system, the water is circulated in pipes to take the coldness from the RC emitter, and then stored in a water tank or delivered to a heat exchanger. The conceptual drawing of the typical water-based and air-based RC system is shown in Figure 2-9.

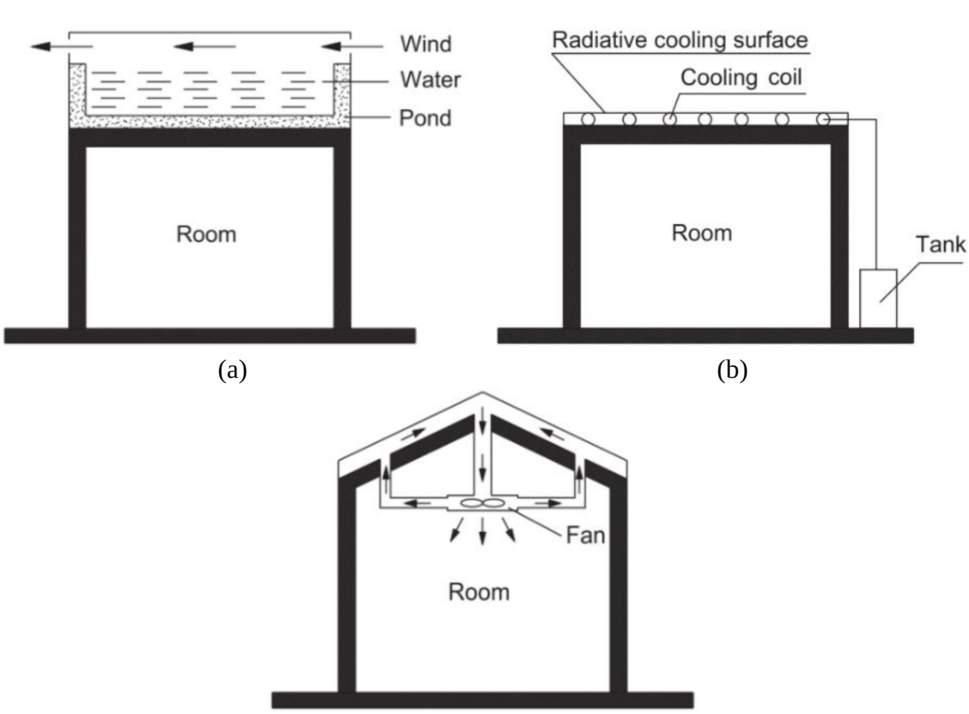

(a) (b)

(c)

Figure 2-9 Configuration of different ways to utilise cooling from the RC emitter: (a) water-based open system; (b) water-based closed system (c) air-based system (Zhang *et al.*, 2018).

In their review paper, Lu *et al.* (2016) and Zhang *et al.* (2018) summarise the advantages and disadvantages of water and air-based RC systems. Compared to the water-based RC systems, the air-based systems are simpler and cheaper. However, water-based RC systems usually have better cooling power due to the higher heat capacity or water. Nevertheless, the performance of both systems still can be further enhanced if the thermal contact between the fluid and the emitter is optimised (Erell and Etzion, 1999; Bagiorgas and Mihalakakou, 2008; Hosseinzadeh and Taherian, 2012; Okoronkwo *et al.*, 2014). The studies, such as research conducted by Hosseinzadeh and Taherian (Hosseinzadeh and Taherian, 2012), usually come up with the prescribed optimum mass flow rate of the fluid to obtain the maximum cooling effect.

2.4.2 Classification of the RC systems based on the level of involvement of mechanical devices

It is not uncommon to incorporate RC into other, already established, sustainable building technologies. Depending on the type of sustainable building technologies involved, one can categorise the RC systems into passive and active RC systems. Most water-based RC systems are active systems. Yet, a passive water-based RC system is still possible with a thermosyphon mechanism to drive the flow of the water or with an open-based system like the one shown in Figure 2-9a. On the other hand, air-based RC systems, are more often proposed as passive systems. A fan might be the only active mechanical device that is often used in air-based RC systems. A detailed comparison of the precedent of RC combinations is shown in Table 2-2.

Table 2-2 Comparison of different means of architectural implementation of RC.

Category		Combination	Researcher
Passive system	Air-based	Solar Collector	(Givoni, 1977)
	Air-based	Thermal mass	(Etzion and Erell, 1991)
	Air-based	Thermal mass	(Zhao *et al.*, 2019)
	Air-based	Attic Insulation	(Ali, 2007)
	Air-based	Wall material and insulation	(Oliveti *et al.*, 2012)
	Air-based	Trombe wall	(Sameti and Kasaeian, 2015)
	Air-based	Trombe wall	(Shen, Yu and Wang, 2020)
	Air-based	Glazing material	(Ziming *et al.*, 2020)
	Air-based	Glazing material	(Givoni, 1977)
	Water-based closed system	PCM wall	(He *et al.*, 2019)
	Water-based closed system	PCM wall	(Yong, Yiping and Li, 2015)
	Water-based open system	Water tank	(Hollick, 2012)
Active system	Air-based	Solar Collector, HVAC	(Parker and Sherwin, 2008)
	Air-based	Fan or HVAC	(Ali, 2013)
	Air-based	Desiccant	(Lu and Yan, 1995)
	Air-based	Solar Collector, Desiccant	(Fiorentini, Cooper and Ma, 2015a)
	Air-based	PV, Solar Collector, HVAC	(Imroz Sohel *et al.*, 2014)
	Air-based	PV, HVAC	(B. Zhao, Hu, Ao, Chen, Xuan, *et al.*, 2019a)
	Air-based	Solar Collector	(Hu, Zhao, Ao, Su, *et al.*, 2018a)
	Water-based closed system	HVAC	(Saitoh and Fujino, 2001)
	Water-based closed system	Solar Collector and PV	(Zhang and Niu, 2012)
	Water-based closed system	PCM	(Zhang *et al.*, 2018)
	Water-based closed system	HVAC	(Fernandez *et al.*, 2015)
	Water-based closed system	Radiant cooling, HVAC	(Man *et al.*, 2011)
	Water-based closed system	Ground-coupled heat pump	(Hu, Zhao, Ao, Zhao, *et al.*, 2018)
	Water-based closed system	PV, Solar collector	(Heidarinejad, Farmahini Farahani and Delfani, 2010)
	Water-based closed system	HVAC	(Chotivisarut and Kiatsiriroat, 2009)
	Water-based closed system	Heat pipe	(Eicker and Dalibard, 2011)
	Water-based closed system	PV, Solar collector	(Chotivisarut, Nuntaphan and Kiatsiriroat, 2012)
	Water-based closed system	Thermosyphon	(Hu *et al.*, 2019)
	Water-based closed system	Solar collector	(Al-Nimr, Kodah and Nassar, 1998)
	Water-based closed system	Thermosyphon	(Jeong *et al.*, 2018)
	Water-based closed system	HVAC	(Jeong *et al.*, 2018)
	Water-based closed system	HVAC	(Bergman, 2018)
	Water-based closed system	Cold water storage	(Wang *et al.*, 2018a)
	Water-based closed system	PCM	(Katramiz, Ghaddar and Ghali, 2020)
	Water-based closed system	Wall material and insulation	(Yi *et al.*, 2020)
	Air or water-based	Temperature-regulating module	(J. Liu *et al.*, 2020)

a. Passive systems

Passive RC systems offer various designs such as the roof-mounted RC (Ben Cheikh and Bouchair, 2004), the wall-mounted RC combined with phase change material (PCM) (He *et al.*, 2019; Shen, Yu and Wang, 2020), thermal mass (Etzion and Erell, 1991; Mihalakakou, Ferrante and Lewis, 1998), and Trombe wall (Sameti and Kasaeian, 2015; Hu *et al.*, 2016).

An example of the roof RC system was first proposed by Etzion (Etzion and Erell, 1991), where they attached an RC emitter to a concrete roof slab. By this design, the cooling effect of the RC emitter is absorbed by the thermal mass of the roof slab and in turn transmitted to the room. Furthermore, a water-based roof RC system resembling a roof pond design was proposed by Ali and Ben Cheick and Bouchair (Ben Cheikh and Bouchair, 2004; Ali, 2007). The system, however, has disadvantages such as the waterproofing issue, the significant addition to the structural load of the roof, and the additional work to maintain the cleanliness of the water. Also, this system can only be installed on flat roofs, and possibly affect the accessibility of the roof for other uses (Sharifi and Yamagata, 2015b). Another form of an RC roof system was developed similar to the cool roof concept (see the schematic diagram in Figure 2-10). Chen and Lu (2020) developed this concept and by using EnergyPlus simulation showed the improvement in the cooling effect to the building by the RC roof compared to the conventional cool roof.

Figure 2-10 Schematic diagram of roof RC in a building (Chen and Lu, 2020).

Moreover, an example of the passive wall-mounted RC system is the one proposed by He *et al.* (2019) and Shen *et al.* (2020). In principle, their designs are similar, *i.e.*, utilising the thermosyphon phenomenon to extract cooling from the wall and storing it in a PCM (see Figure 2-11). A similar design to He's *et al.* (2019) was also proposed by Yu *et al.* (2022). In terms of cooling performance, the wall-mounted dual-functional heating-cooling emitter was predicted to be able to reduce building energy consumption by 47.9% (Yong, Yiping and Li, 2015). The implementation of the RC-PCM wall in the testing room can be seen in Figure 2-12.

If in the previous RC application in a building, the PCM was used along with RC emitter material to regulate heat gains and losses in the wall or building enclosure, in another design researchers use insulation and thermal mass. In the RC-thermal mass design by Etzion and Erell (1991), The thermal mass is closely coupled with the radiative emitter. It aims to absorb the excessive heat received by the RC emitter during the daytime. This helps the RC emitter to maintain its temperature not too hot and thus easier for the emitter to achieve sub-ambient temperature at night. Etzion and Erell (1991) evaluate the best location for placing thermal mass and suggest that the thermal mass is best placed on the roof (Etzion and Erell, 1991).

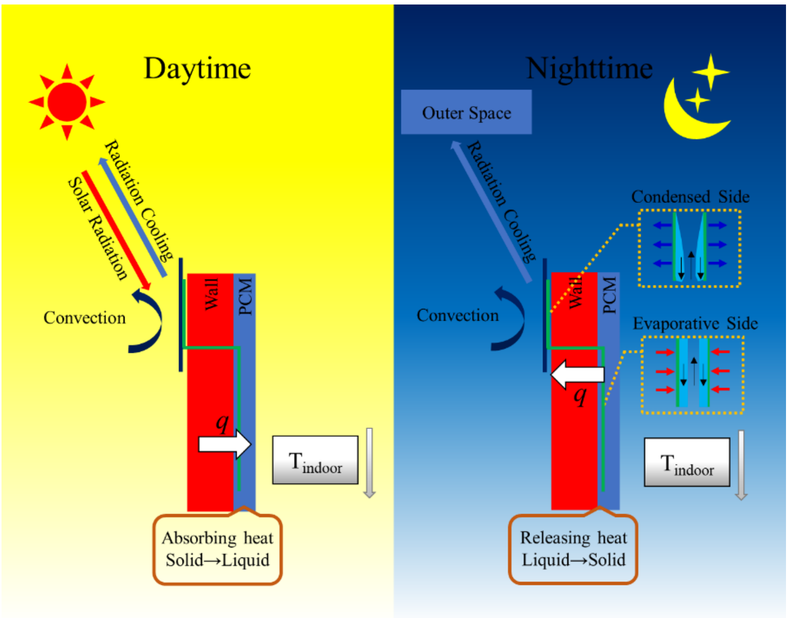

Figure 2-11 Dual-functional RC-PCM wall design by He et al. (He *et al.*, 2019).

Yet another way of fully utilising RC for buildings can be done using the thermoelectric effect. The temperature difference between the RC emitter surface with its surroundings can be turned into electric voltage. This combination of RC with a thermoelectric device to help generate electricity at night is a new direction in RC research (Lv *et al.*, 2021; Zhao *et al.*, 2021). The research conducted by Zhao et al. (2021) attempted to utilise the thermoelectric effect in a PV module. During the night, the PV module surface is allowed to have the RC effect, and thus the surface becomes sub-ambient. This temperature difference between the PV module and the ambient is then converted into electricity by a thermoelectric generator. Figure 2-13 illustrates the concept of thermoelectric utilisation of the RC phenomenon.

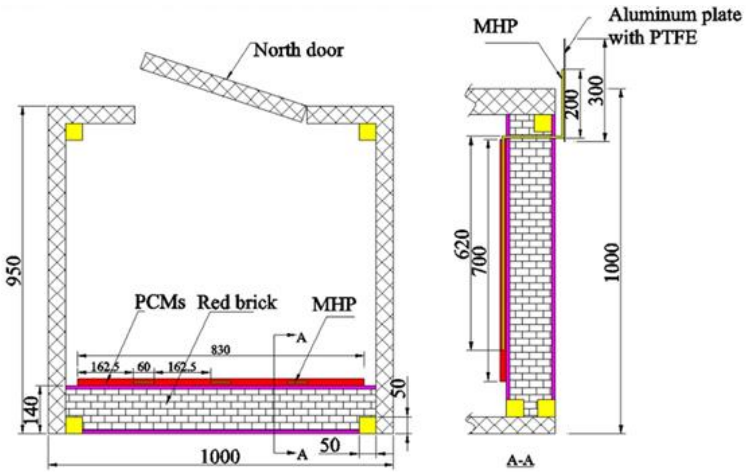

Figure 2-12 Drawing of the experimental room for an RC-PCM wall by Shen, Yu, and Wang (2020).

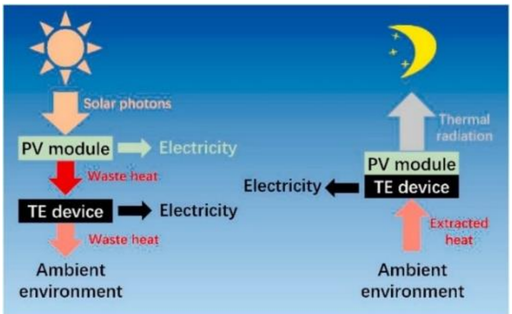

Figure 2-13 The conceptual diagram of using RC to generate electricity (Zhao *et al.*, 2021).

b. Active systems

Many proposals for RC applications in buildings involve some degree of mechanical devices, from fans to a full set of HVAC systems. There is more research on active RC systems than on passive ones. Among the technologies that have been combined with the RC are the solar collector (Givoni, 1977; Lu and Yan, 1995; Saitoh and Fujino, 2001; Hu *et al.*, 2019), photovoltaics (PV) (Saitoh and Fujino, 2001; Farmahini Farahani, Heidarinejad and Delfani, 2010; Eicker and Dalibard, 2011; Hu, Zhao, Ao, Zhao, *et al.*, 2018), air conditioning (AC) (Parker and Sherwin, 2008; Heidarinejad, Farmahini Farahani and Delfani, 2010; Bergman, 2018; Jeong *et al.*, 2018; Zhang *et al.*, 2018), and cold water storage (Al-Nimr, Kodah and Nassar, 1998; Chotivisarut, Nuntaphan and Kiatsiriroat, 2012; Wang *et al.*, 2018b; Katramiz, Ghaddar and Ghali, 2020).

As early as 1977, Givoni (1977) proposed to use a solar collector panel as an RC panel. The idea is to employ the absorber that collects heat from the sun during the day and emits heat to the sky at night. This dual-functional collector is further developed with more advanced techniques and materials (Eicker and Dalibard, 2011; Hu, Zhao, Ao, Su, *et al.*, 2018b; Hu *et al.*, 2019). For example, instead of the conventional solar absorber, researchers now use the spectral-selective coating. Also, instead of the conventional glass cover of the solar collector, the low-density polyethylene (LDPE) film is now commonly used as the cover in many studies. The latest dual-functional solar collector-RC emitter experiment by Hu *et al.* (2019) yields a 55.1 W/m^2 cooling power at night. Their design is illustrated in Figure 2-14.

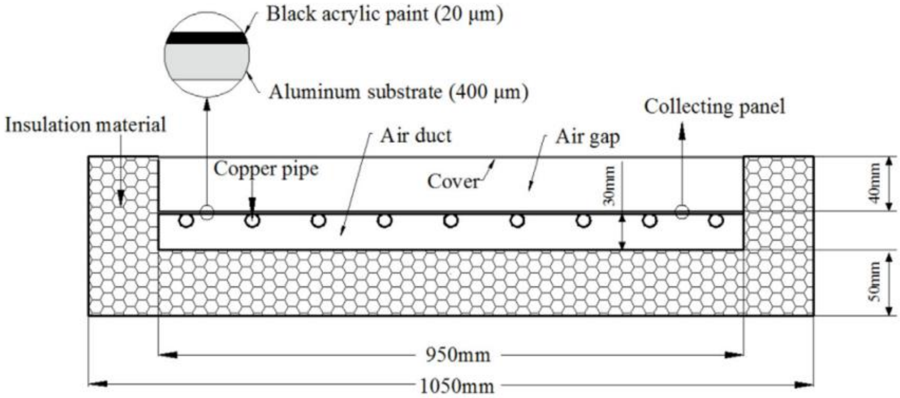

Figure 2-14 Cross-section schematic drawing of the PT-RC design by Hu *et al.* (2019).

A combination of PV with RC was initially proposed in the Harbeman House, designed by Saitoh and Fujino (2001). The house is aimed to be a sustainable house that integrates various sustainable technologies. Besides the one-off study in the Haberman House project, the PV-RC combination has also been studied more continuously by Zhao *et al.* (Zhao *et al.*, 2017, 2018; B. Zhao, Hu, Ao, Chen, Xuan, *et al.*, 2019a, 2019b). They propose several PV-RC combination strategies with the help of the photonic materials that they developed. Results from studies conclude that the PV-RC combination concludes that the combined electricity and cooling energy resulting from the system is more than the output energy from PV alone (Sohel *et al.*, 2014; B. Zhao, Hu, Ao, Chen, Xuan, *et al.*, 2019a).

Furthermore, another application of RC with active systems in buildings is the combination with HVAC systems. In combining RC with an HVAC system, the emitter is usually used to provide chilled water for the cooling coil of the AC, to make the HVAC works more efficiently (Bergman, 2018; Jeong *et al.*, 2018). For instance, Jeong *et al.* (2018) employ RC as the supplementary cooling supplier to the HVAC system. Their design was able to reduce cooling energy consumption by 35%. Another design by Zhang *et al.* (2018) added cold-water storage to stock the cooling energy from the RC emitter. Figure 2-15 schematically illustrate one design of an RC-assisted HVAC system.

Yet another active way of integrating RC into buildings is developed by Liu *et al.* (2020). It is a temperature-regulating module (TRM) for solar heating and RC which consists of a PE film as the convection cover, a porous material on top of an aluminium sheet as the RC emitter, and a solar absorber (Figure 2-16a). The layer order in Figure 2-16a is for the cooling function, whereas in the heating mode, the layer order was reversed as in Figure 2-16b. The TRM can maintain a maximum indoor temperature of 27.5 °C on the hottest days of summer and 25 °C for some hours on winter days. The heating and cooling provided by the TRM correspond to 42.4% energy saving.

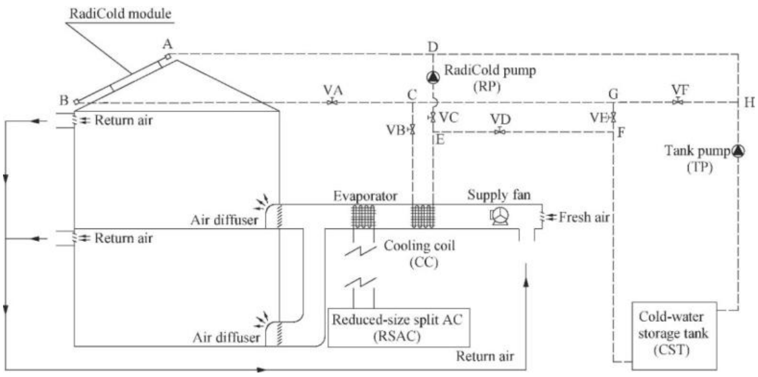

Figure 2-15 Schematic of a typical RC-assisted HVAC system (Zhang *et al.*, 2018).

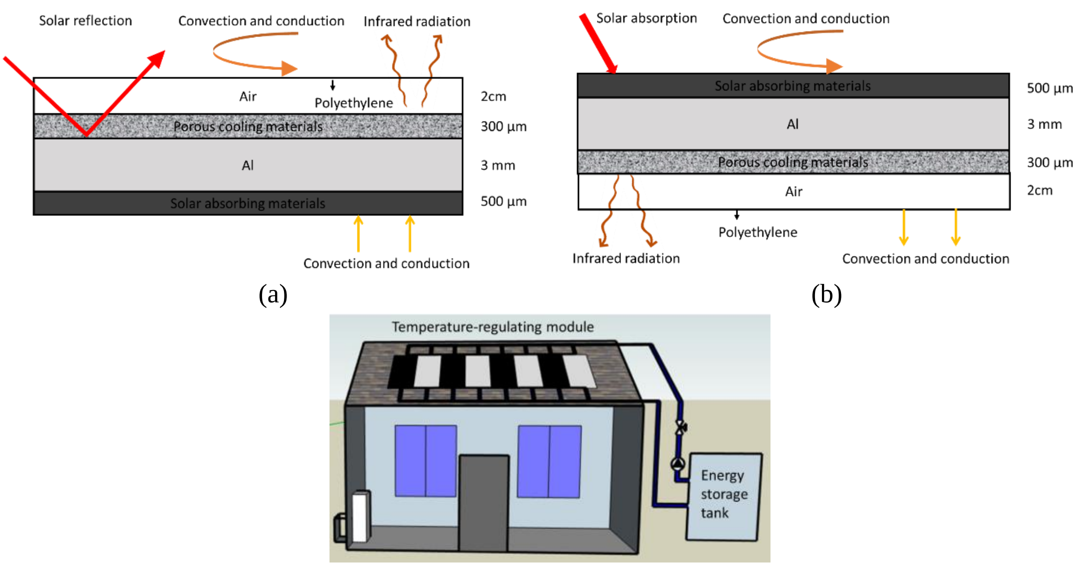

Figure 2-16 Temperature-regulating module by Liu *et al.* (2020); (a) cooling mode; (b) heating mode; (c) when applied on the roof.

2.5 Architectural Features of Current Radiative Cooling Systems

As Section 2.3 summarises, proposals for RC application in buildings are very diverse. Many of these proposals are combinations of RC with other technologies. Nevertheless, since buildings are the object in which RC is implemented in this thesis, the discussion on the previous RC research can also be done from an architectural point of view. The discussion can be guided by the architectural features involved in the current proposed concepts of RC application in buildings.

Besides summarising the passive and active RC systems, Table 2-2 also indicates some architectural features involved in the RC systems. Based on the sky view factor, the roof is theoretically the best location to place the RC emitter. However, for architects to offer some design flexibilities, researchers also proposed to use RC in the wall and façade. These other features, although very few, offer alternatives in RC applications in buildings.

2.5.1 Roof

As mentioned earlier, the roof has the highest sky view factor than other parts of the building envelope. On top of that, the space under the roof, or the attic, is also a common place for building service installations. Therefore, the roof is the most used building feature in terms of RC applications in buildings. The design of the roof-mounted RC systems includes both water and air-based systems. One simple design of roof water-based RC is an open system, rather like a roof pond design, as shown in Figure 2-17 (Ben Cheikh and Bouchair, 2004; Ali, 2007). This type of water-based RC system, although very simple, has disadvantages such as potential water-leaking, increasing the structural load on the roof, and difficulty in maintaining the cleanliness of the water (Sharifi and Yamagata, 2015b).

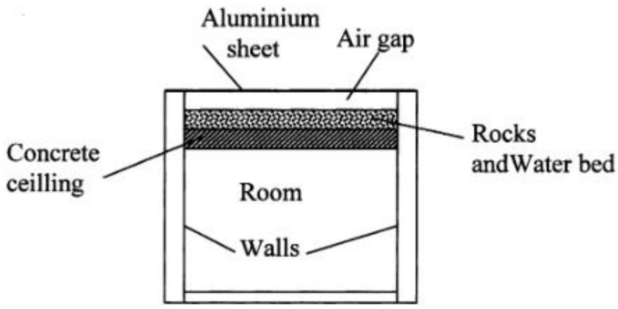

Figure 2-17 Water-based open system RC on the roof of a building (Ben Cheikh and Bouchair, 2004).

For the air-based RC systems, one simple example is proposed by Etzion (1991) as previously detailed in Section 2.3.2. The design resembles a cool roof, *i.e.*, a roof surface that is painted with high-reflectivity material. The difference with the cool roof is that in Etzion’s (1991) design the coating is a radiative cooling coating. Other air-based roof RC systems, employ a fan to extract the coldness of the RC emitter, guide the cooled air through an air channel, and deliver it to the building (Givoni, 1977; Zhao *et al.*, 2019). Figure 2-18 displays an example of how the air delivers cooling from the RC emitter (Zhao *et al.*, 2019). In the drawing shown in Figure 2-18, the cooling effect from the RC emitter was supplied to the attic to remove the heat in the attic. Nevertheless, the idea can be further extended for the heat removal in the room.

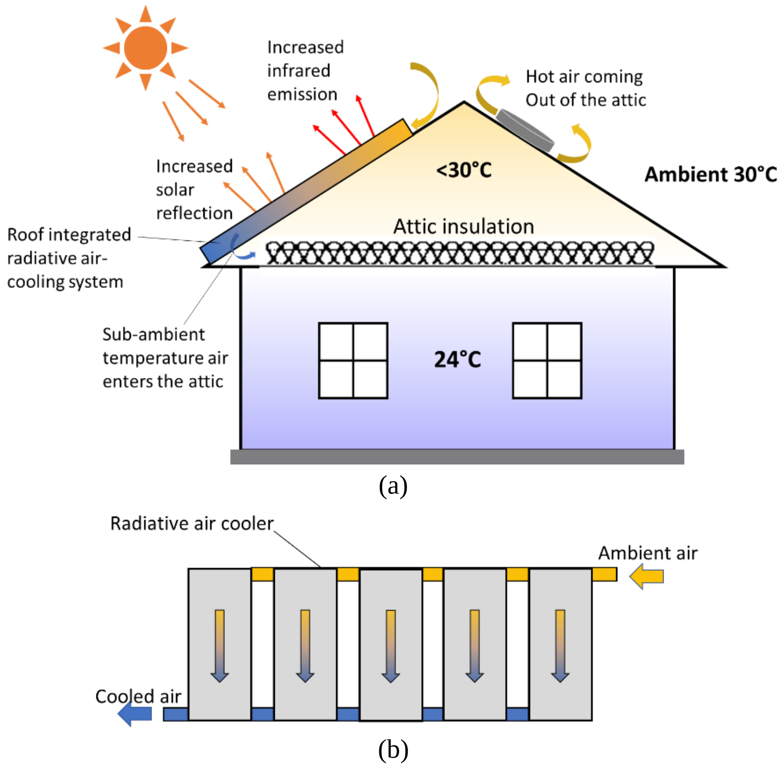

Figure 2-18 Air-based RC system on the roof using an air channel to utilise the cooling (Zhao *et al.*, 2019): (a) illustration of how the system works to remove heat from the attic; (b) schematic of the air channel and the RC panel.

Similar to the concepts from Zhao et al. above, many roof-mounted RC systems are used in the form of RC collectors, often combined with solar heaters or PV. This RC collector concept, either stand-alone or in combination with a solar collector or PV, offers flexibility in the utilisation. Firstly, the working fluid used in the system can be air, water, or others. Secondly, the cooling energy collected from the system can be directly used (on demand) or stored for later use. Yet, it is important to note that the roof-mounted RC collector employs active devices such as a fan, a pump, or even a set of HVAC systems.

2.5.2 Wall

The roof might have the best sky view factor compared to the wall. However, as the number of storeys of a building gets larger, the ratio between the roof's area to the total building envelope's area becomes smaller. This makes using the roof's surface only to collect cooling from the sky for such a building unprofitable. Thus, it is better to also exploit the wall, for instance, to mount the RC systems.

Like the roof-mounted RC system, the wall-mounted RC also consists of two systems, the air-based and the water-based systems. Many designs of passive wall-mounted RC systems serve heating and cooling in one device. For example, the air-based wall RC system design developed by Sameti and Kasaeian (2015) combined with the Trombe wall. The RC-Trombe wall design is built of a glass cover and a thermal mass wall behind the glass. During the day, the thermal mass absorbs heat from the solar radiation that enters the façade (heating mode). Among the key parameters for this RC-Trombe wall system are the glazing material, vents geometry and position, thermal storage, and Trombe wall area (Hu *et al.*, 2017; Bevilacqua *et al.*, 2019).

Furthermore, the example of an active system of wall-mounted RC is the one proposed by Oliveti et al. (2012) and Yong et al. (2015). Yong's et al. (2015) system, shown in Figure 2-19, works as a dual-functional solar collector in the daytime and RC in the nighttime. The system uses pumps to circulate water to be stored in the cold and hot water storage. The system itself can be constructed with or without an air gap. Figure 2-19a shows the design without an air gap so the RC emitter is directly insulated by the insulation board. In Figure 2-19b, an air gap is added at the backside of the emitter to help fasten the cooling effect with the convection with the ambient air at night.

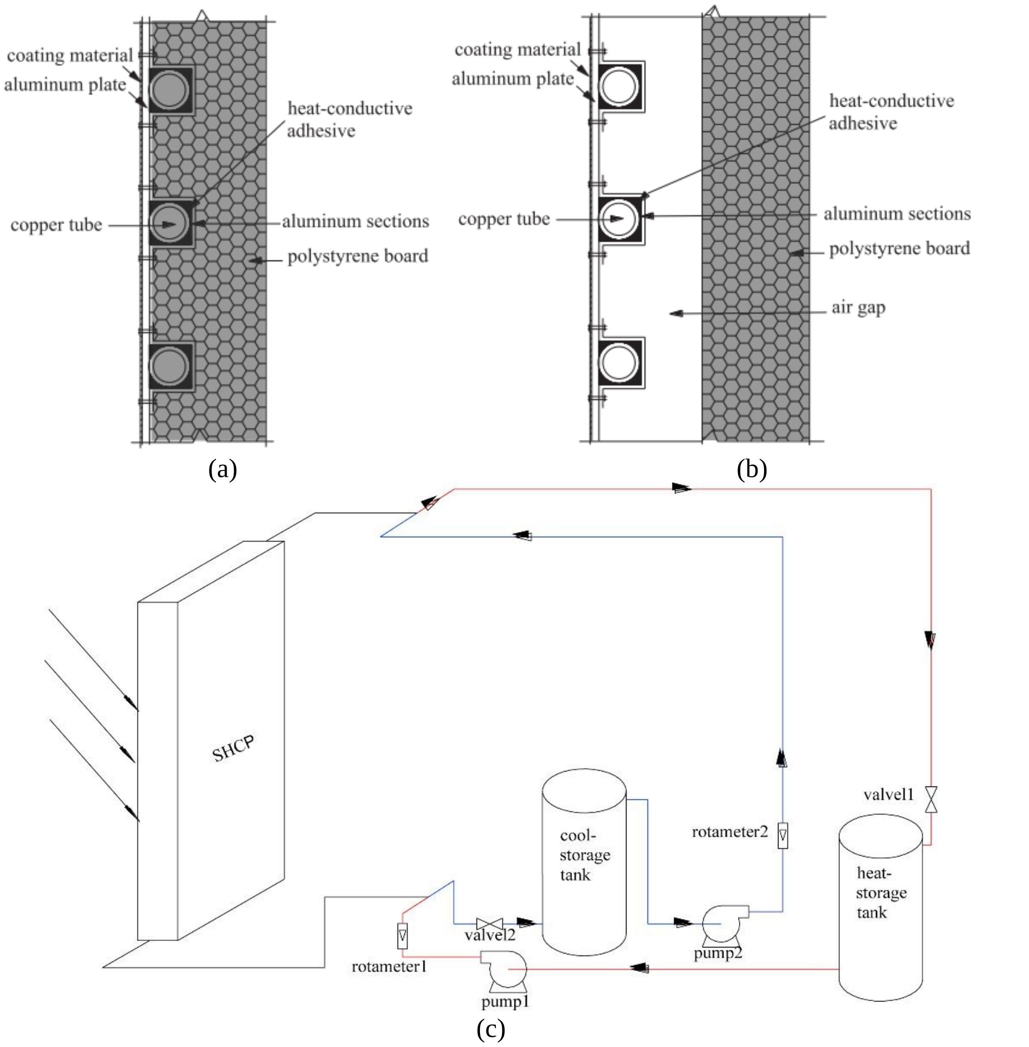

Figure 2-19 Illustration of the dual-functional solar heating-radiative cooling wall as designed by Yong *et al*. (2015): (a) design without an air gap; (b) design with an air; (c) schematic diagram showing the mechanism in which the dual-functional system works—a red line for heating, blue line for cooling.

2.5.3 Glazing Material

Still related to the building envelope, the next architectural feature that can be utilised as the place for RC emitter is the glazing material of the building openings. Openings are the main source of solar heat gain in a building. Currently, many glazing materials can reduce this solar gain by limiting the transmissivity of the material in the solar radiation band. Taking the same idea further, researchers also attempt to use the glazing material as the RC emitter by modifying its thermal emission in the atmospheric window band.

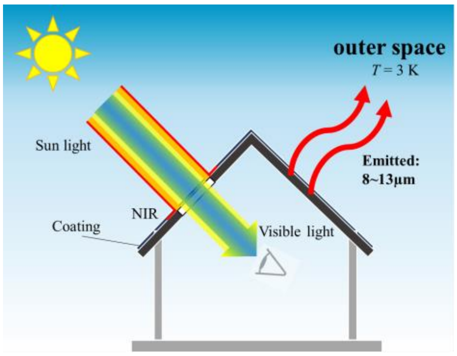

Figure 2-20 A transparent RC emitter used on a skylight to provide daylighting as well as passive cooling for buildings (Ziming *et al.*, 2020).

The idea is manifested into two prototypes of transparent RC emitter. One emitter is a transparent film and another one is a transparent coating (Cheng *et al.*, 2019; Yi *et al.*, 2020; Ziming *et al.*, 2020). They results show that the transparent RC glazing can reduce the cooling load of the building in summer. But, the cooling ability of the transparent RC glazing, also leads to the increase in heating load in winter. Nonetheless, the transparent RC materials are currently only proposed to be applied on the skylight as in Figure 2-20. However, the proposal to apply the T-RC as windows material might come into sight in the near future.

2.5.4 Paints/coatings

Although paints or coatings are a minimal architectural feature that one could think of, Mandal *et al.* (2020) argue that they might be the answer to the issue of scalability of the RC emitter material. This is considering paints or coatings technology as a mature technology. The RC paints or coatings could also promote the progress of aesthetic studies of RC surfaces because paints and coatings are almost certainly used in buildings as well. The success of cool roof coating is a precedent of the development in paint technology that can enhance paint performance. Recent development in the RC emitter material has allowed this to be realised. For instance, the study conducted by Lee *et al.* (2018) successfully created colourful RC emitters as shown in Figure 2-21.

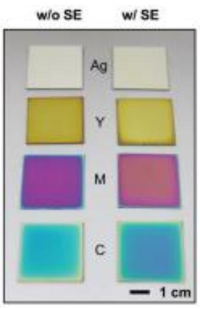

Figure 2-21 Coloured RC emitter materials from Lee *et al.* (2018).

2.6 Summary of the Research Gap in the Application of Radiative Cooling in Buildings

This chapter has laid out the basis for the ideas proposed in the next four chapters. Starting with the principles of the RC phenomenon, the chapter then suggests several research directions for the topic of RC application in buildings. As its name suggests, RC is passive cooling via radiation. Here the radiation specifically means the radiation heat exchange between the RC emitter and space. A space with a very cold temperature is an excellent heat sink for the RC emitter. However, the dumping of heat from the RC emitter to space via radiation can only occur effectively in the wavelength band of 8-13 μm. This band is called the atmospheric window band. Outside this band, the thermal radiation from the RC emitter is effectively blocked by the atmosphere.

With the understanding of this phenomenon, some researchers have begun to develop RC emitter materials that have high emissivity in the atmospheric window band while limit absorption in other bands. When this material is realised, the RC emitter can be at a sub-ambient temperature even under direct sunlight. There have been many high-performance RC emitters shown in experimentations. However, there are still challenges to utilising RC. In broad terms, the two challenges can be classified into technical and cost problems. Technical problems relate to low cooling power, geographical constraints, sophisticated material technology to produce the radiator, complicated system implementations, durability, and maintenance issues. Cost problems consist of high production costs and installation costs. It is worth noting that this thesis only addresses the technical challenges by means of RC combination with solar energy applications in buildings.

Despite those challenges, the success of passive daytime RC shown in some experiments has revived the research on RC application in buildings. Various strategies have been proposed, some are fully passive, and some are active strategies. It is not uncommon for the RC emitter to be combined with other more established technologies such as solar collectors, PV, HVAC, *etc.* In such a combination, the RC emitter can be used to either enhance the performance of the main technology or to extend its working time. Combining RC with a solar thermal collector or PV can also make the device dual-functional.

Furthermore, after that comprehensive outlook of various efforts to implement RC in buildings as well as the architectural features involved in the design has been discussed in the previous sections, this section will elaborate on the research gaps of the topic that relate to the thesis objective.

Meanwhile, the daytime RC material is developing, one can also research the utilisation of the nighttime RC effectively. As many proposed strategies discussed previously, studies on RC combination with the more established technologies are still open with opportunities. Among the established heating or cooling systems that have been combined with RC, the ones that involve solar energy are commonly used. One can see RC as the opposite of solar heating and thus combining the two can be done with one structure together.

Additionally, from the architectural point of view, there is still much room for improvement. The analysis of the architectural features of the current RC application in buildings in Section 2.4 implies that current designs are limited to only three or four architectural features. Architects with vast knowledge of passive design strategies could use that knowledge to be integrated with the RC phenomenon. For instance, it may be possible that RC enhances the performance of a natural ventilation strategy. Another important aspect from the architectural point of view is the limited study that concerns the aesthetic appearance of the RC emitter when applied to buildings.

Moreover, in terms of methodology used in the evaluation of radiative cooling systems, the experimental method is the main way to evaluate the RC materials. In the system scale, numerical simulations are conducted, and if the system is applied in a building, the building energy simulation software is also involved. Therefore, this thesis also includes all three methods to some degree. As this thesis focuses only on the RC system design, *i.e.*, the numerical simulations are mostly used in this thesis. The simulations employ the computational fluid dynamics (CFD) code from Ansys Fluent as well as EnergyPlus as the building energy simulation software. In addition to that, an experiment is also conducted to help validate one of the models.

Chapter 3 Procedure of Numerical Simulations for Radiative Cooling Applications in Buildings

This chapter describes the general procedure of the CFD (with Ansys Fluent) and building energy simulations (with EnergyPlus) employed in the Thesis. The flow chart in Figure 3-1 outlines the general steps involved in the simulations. Some evaluations of the proposed concepts in this study involve only Ansys Fluent simulation, and some others also include EnergyPlus simulation. In cases that involve EnergyPlus simulation, the Ansys Fluent was used to model the performance of the radiative cooling device. Whereas the EnergyPlus was then used to simulate the potential savings based on the performance data resulting from the CFD simulations. The energy-saving potential of the PT-RC system was analysed by comparing the results from the CFD simulation with the heating and cooling loads data from EnergyPlus. By combining these two simulation methods, the study provides a comprehensive evaluation of the performance and energy-saving potential of the PT-RC collector.

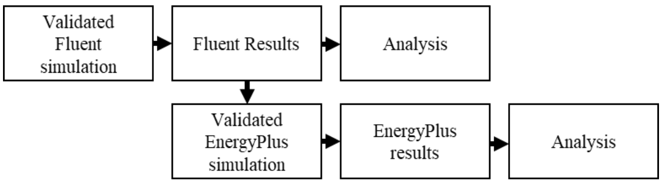

Figure 3-1. Flow diagram of the simulation procedure.

3.1 The Computational Fluid Dynamics (CFD) Simulations

As reviewed in Chapter 2, radiative cooling systems involve working fluid, usually air or water. Thus, CFD code with its conjugate heat transfer module is preferable to model the heat transfer between the radiative cooling emitter with the working fluid and its effect on the flow of the working fluid. However, there are some challenges in properly including the radiative heat transfer phenomena with the sky as the heat sinks. The first challenge is how to modify the code to allow for spectral-dependent radiation, not only diffuse radiation. The second challenge is how to include the sky as the heat sink without building it as the geometry. Also, when the radiative emitter is designed to focus its sky exposure to a specific region of the sky, there is a challenge in how to model the angle-dependent radiation to the sky. Therefore, before using Ansys Fluent to model the case study several sample cases from published papers that involve radiative cooling mechanisms are modelled with the software. It is found that the CFD code of Ansys Fluent can model radiative cooling very well (see Appendix A for a summary of the sample case simulations).

The CFD models start by creating the geometry of the radiative cooling device. The geometry was discretised with a structured hexahedral mesh. The mesh size used in the simulation was chosen after the mesh-independence study. For the radiation model, the discrete-ordinate (DO) radiation model was used due to its capability to include spectral-dependent radiation modelling (Ansys®, 2021). In addition to that, the Coupled algorithm for pressure-velocity coupling and the PRESTO! discretisation scheme for the pressure terms was used to run the solver. The residuals and simulation results of the key parameters were checked for convergence. Figure 3-2 below shows the flow chart of the CFD modelling. The details are available in the Appendix.

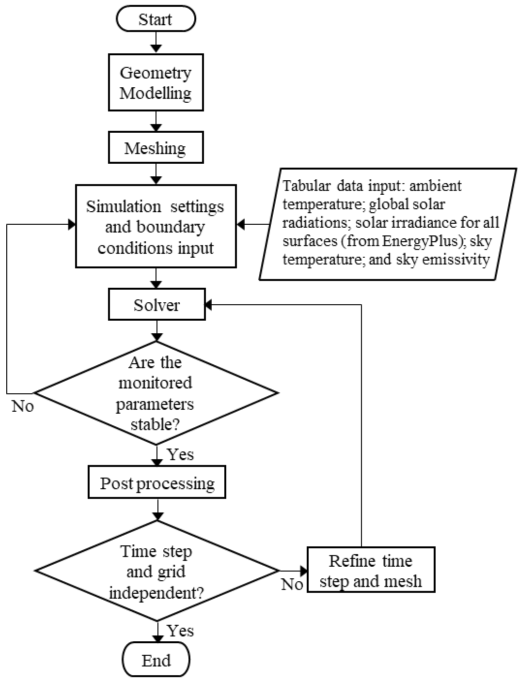

Figure 3-2 Flow diagram of the CFD simulation.

Furthermore, the boundary conditions of the radiative cooling device in this thesis were developed from the heat balance of the radiative cooling emitter. For convenience, the heat balance of the PT-RC collector from Chapter 5 is used here for the explanation, as shown in Figure 3-3. In the proposed design chapters, the geometry of the radiative cooling devices is different, yet the heat balance is similar to what is described in this chapter. Firstly, the heat balance of the PE cover is summarised by Equation 3.1. The cover receives radiation from the sun ($q_{\text{sol-cov}}$), as well as exchanged heat via radiation with the atmosphere and the PT-RC absorber/emitter below ($q_{\rm rad}$), and via convection with the ambient air ($q_{\rm wind}$) and the air gap ($q_{\rm ag-cov}$). On the right side of Equation 3.1, the transient term is introduced with $d_{\rm cov}$ as the PE cover's thickness. To be more detailed, each heat transfer component is defined in subsequent equations.

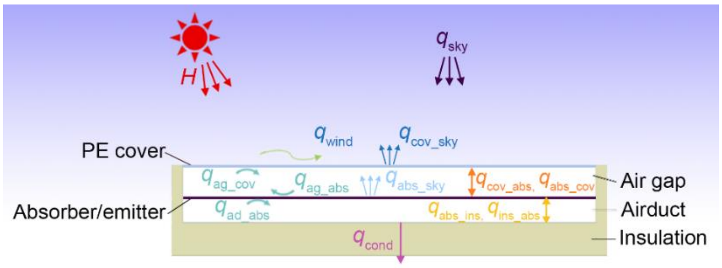

Figure 3-3 Heat balance of the PT-RC collector.

$$q_{\rm sol-cov} + q_{\rm rad} + q_{\rm wind} + q_{\rm ag-cov} = \begin{cases} 0, \text{steady state} \\ \rho c_{p_{\rm cov}} d_{\rm cov} \dfrac{\partial T_{\rm cov}}{\partial t}, \text{transient state} \end{cases} \tag{3.1}$$

In Equation 3.2, $q_{\rm sol-cov}$ is the amount of solar radiation that is absorbed by the cover, with $\alpha_{\rm cov}$ being the PE cover's absorptivity, and H is the total solar irradiance that falls onto the cover.

$$q_{\rm sol-cov} = \alpha_{\rm cov} H \tag{3.2}$$

Thermal radiation, $q_{\rm rad}$, describes the balance between incoming radiation from the sky ($q_{\rm sky}$) and the absorber/emitter ($q_{\rm a/e-cov}$), as well as the outgoing radiation from the cover upward ($q_{\rm cov-sky}$) and downward ($q_{\rm cov-a/e}$) (see Equation 3.3). The cover-atmosphere radiative heat exchange is represented in Equation 3.4 with F as the inclination angle effect of the thermal radiation power to the sky (Hu, Zhao, Suhendri, Cao, *et al.*, 2022b), $\varepsilon_{\rm cov}$ as the PE cover's emissivity in the atmospheric window band, σ as Stefan-Boltzmann constant, $T_{\rm sky}$ as the sky temperature, and $T_{\rm cov}$ is the PE cover's temperature. Note that for the energy saving analysis, the sky temperature was taken from the EnergyPlus weather data, while for the parametric studies, it was calculated from Equation 3.5. Moreover, the cover-absorber radiation exchange is internally calculated by Ansys.

$$q_{\rm rad} = (q_{\rm sky} - q_{\rm cov-sky}) + (q_{\rm a/e-cov} - q_{\rm cov-a/e}) \tag{3.3}$$

$$q_{\rm sky} - q_{\rm cov-sky} = F\,\varepsilon_{\rm cov}\,\sigma(T_{\rm sky}^4 - T_{\rm cov}^4) \tag{3.4}$$

$$T_{\rm sky} = 0.0552 T_{\rm amb}^{1.5} \tag{3.5}$$

Further, the q_{wind} represents convection heat transfer due to ambient wind (Equation 3.5), with the formula for heat transfer coefficient (h_{wind}) shown in Equation 3.6 (Watmuff, Charters and Proctor, 1977). In Equation 3.6, T_{amb} represents the ambient temperature, and in Equation 3.7, v denotes wind speed. Lastly, the convection heat transfer with the air gap ($q_{\mathrm{ag-cov}}$) in Equation 5.1, is internally calculated by Ansys Fluent.

$$q_{\mathrm{wind}} = h_{\mathrm{wind}}(T_{\mathrm{amb}} - T_{\mathrm{cov}}) \tag{3.6}$$

$$h_{\mathrm{wind}} = 2.8 + 3.0v \tag{3.7}$$

The second in the heat balance equation for the PT-RC collector is for the absorber/emitter (Equation 3.8). The absorber/emitter receives part of the solar radiation that is transmitted by the PE cover. Some of that solar radiation is reflected back and forth between the absorber/emitter and the PE cover. Equation 3.9 sums the solar radiation absorbed by the absorber/emitter ($q_{\mathrm{sol-a/e}}$) where τ_{cov} is the PE cover's solar transmissivity, $\alpha_{\mathrm{a/e}}$ is the solar absorptivity of the absorber/emitter, ρ_{cov} and $\rho_{\mathrm{a/e}}$ are the solar reflectivity of the cover and the absorber/emitter respectively.

$$q_{\mathrm{sol-a/e}} + q_{\mathrm{rad}} + q_{\mathrm{ag-a/e}} + q_{\mathrm{ad-a/e}} = \begin{cases} 0, \text{steady state} \\ \rho c_{p_{\mathrm{a/e}}} d_{\mathrm{a/e}} \dfrac{\partial T_{\mathrm{a/e}}}{\partial t}, \text{transient state} \end{cases} \tag{3.8}$$

$$q_{\mathrm{sol}} = \frac{\tau_{\mathrm{cov}}\alpha_{\mathrm{a/e}}}{(1 - \rho_{\mathrm{cov}}\rho_{\mathrm{a/e}})} H \tag{3.9}$$

Another heat transfer term in Equation 3.8, q_{rad}, is the radiation heat exchange between the absorber/emitter with the sky (represented by $q_{\mathrm{sky}} - q_{\mathrm{a/e-sky}}$ in Equation 3.10), the cover ($q_{\mathrm{cov-a/e}} - q_{\mathrm{a/e-cov}}$), and the back insulation ($q_{\mathrm{ins-a/e}} - q_{\mathrm{a/e-ins}}$). The latter two radiative heat exchanges are internally calculated by Ansys, whereas the absorber-sky radiation exchange is calculated using Equation 3.11, which is an adjusted version of Equation 3.4. to account for the infrared transmissivity of the PE cover (τ_{cov}). Lastly, convection heat transfer with the air gap ($q_{\mathrm{ag-a/e}}$) and the air duct ($q_{\mathrm{ad-a/e}}$) in Equation 3.8 are internally calculated by Ansys Fluent. The $q_{\mathrm{ad-a/e}}$ is dependent on the mass flow rate of air in the air duct.

$$q_{\mathrm{rad}} = (q_{\mathrm{sky}} - q_{\mathrm{a/e-sky}}) + (q_{\mathrm{cov-a/e}} - q_{\mathrm{a/e-cov}}) + (q_{\mathrm{ins-a/e}} - q_{\mathrm{a/e-ins}}) \tag{3.10}$$

$$q_{\mathrm{sky}} - q_{\mathrm{a/e-sky}} = F\,\tau_{\mathrm{cov}}\,\varepsilon_{\mathrm{a/e}}\,\sigma(T_{\mathrm{sky}}^4 - T_{a/e}^4) \tag{3.11}$$

Furthermore, the SIMPLE algorithm was used to solve the CFD model with the first-order discretisation scheme for the convection and viscous terms. Meanwhile, for the pressure terms use the PRESTO! discretisation method. The judgement on the convergence of the simulation results was based on the stability in the plotted value of the key parameters.

3.2 The EnergyPlus Simulations

Coupling between EnergyPlus with Ansys Fluent results was done manually. The results from the Ansys Fluent were inputted into the EnergyPlus weather data or other input to then used in the EnergyPlus simulation. The procedure of the EnergyPlus simulation itself is shown in Figure 3-4.

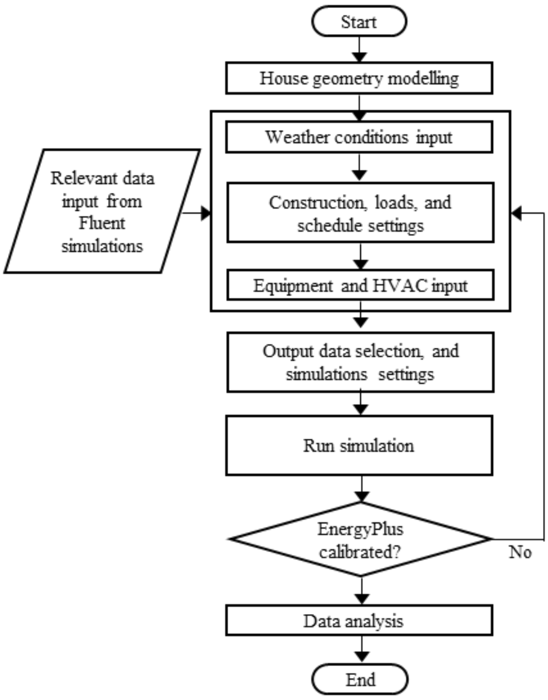

Figure 3-4 Flow diagram of the EnergyPlus simulation.

The geometry of the EnergyPlus model depends on the case study building used in each proposed strategy. The building geometry was then set with the default construction, load, and schedule sets for residential units. The weather data input was set according to the case study. It is worth noting that for the EnergyPlus simulation, the effects of the surrounding objects are neglected, thus the building is assumed as a single building in an open area. Furthermore, the set point temperatures for space heating and cooling were set at 21°C and 24°C respectively. The heating and cooling supply air temperatures were 40°C and 18°C respectively, provided by the selected

HVAC system with a gas heating coil with an efficiency of 0.9 and a direct expansion cooling coil (single speed) with a rated COP of 3.6 (ASHRAE, 2018). The ambient and sky temperature, solar irradiance, wind speed, and mass flow rate data were obtained from these EnergyPlus simulations (Lawrie and Crawley, 2022; LLC, 2022). Besides those parameters, the simulations also reported the heating and cooling loads for each case study location. These data were then used in the analysis of the energy-saving potential of the building-integrated radiative cooling system.

Chapter 4 Combination of Radiative Cooling with Roof Solar Chimney to Enhance Natural Ventilation[2]

As reviewed in Chapter 2, for building applications, radiative cooling has been used in both active technologies and passive design strategies. Examples of the integration of radiative cooling with active devices are numerous. For instance, radiative cooling can be used to improve the efficiency of a solar absorption chiller (Hu, Kwan and Pei, 2022) or combined with air-conditioning (AC) (Heidarinejad, Farmahini Farahani and Delfani, 2010; Bergman, 2018; Jeong *et al.*, 2018; Zhang *et al.*, 2018). Although the application of radiative cooling into active cooling devices is more common, a fully passive application of RC would be simpler for maintenance because it does not involve moving parts. Therefore, this thesis will first focus on the fully passive application of radiative cooling in this chapter and provide a more active application in the latter chapters.

4.1 Reasoning of the Strategy

Several proposals for fully passive building-integrated radiative cooling have been studied. Some studies apply radiative cooling solely as a coating on the roof of a building, a strategy similar to a cool roof (Feng *et al.*, 2022; Liu *et al.*, 2022; Mokhtari, Ulpiani and Ghasempour, 2022). Nonetheless, more studies combine radiative cooling with other more established passive design strategies. These combination strategies are preferred because limitations of the current RC emitter such as the low cooling power (Li and Lam, 2000) and highly-constraint cooling performance (Hossain, Jia and Gu, 2015; Bhamare, Rathod and Banerjee, 2019). Some precedents of such combinations are the combination of the radiative cooling emitter with phase change materials (PCM) (He *et al.*, 2019; Shen, Yu and Wang, 2020; Zhou, Zheng and Zhang, 2020), thermal mass (Etzion and Erell, 1991; Mihalakakou, Ferrante and Lewis, 1998), or Trombe wall (Sameti and Kasaeian, 2015). There are a couple of lessons that can be drawn from these combination strategies. First, the radiative cooling emitter is combined with other established cooling technologies. Second, the radiative cooling mechanism extends the

[2] Part of this chapter's content is published in *Building and Environment*, 209 and 225, doi.org/10.1016/j.buildenv.2022.109648 and doi.org/10.1016/j.buildenv.2021.108686

working time of a system or device that works only in the daytime, such as a solar chimney or Trombe wall. Therefore, what was initially the idle time for the device (*i.e.*, the night) can be used for radiative cooling.

Considering those two points, this chapter proposes and evaluates one possible fully passive combination of radiative cooling. The fully passive way is to integrate a radiative cooling mechanism in a natural ventilation strategy. In this thesis, solar chimney ventilation is chosen to be combined with the radiative cooling mechanism. As a widely adopted ventilation strategy, solar chimney ventilation still needs improvement, especially in terms of working time extension at night, ventilation rate increase, and cooling performance enhancement.

The conventional ways proposed by researchers to extend the working time extension of solar chimney ventilation is by incorporating PCM materials into the solar absorber (Frutos Dordelly *et al.*, 2019; Cao *et al.*, 2021; Omara *et al.*, 2021). Whereas, various ways have been studied to enhance the ventilation and cooling performances of solar chimneys, such as combination with wind catchers (Moosavi *et al.*, 2020), earth-to-air heat exchangers (EAHX) (Serageldin, Abdelrahman and Ookawara, 2018; Taurines, 2019; Long *et al.*, 2021), cooling cavity (Dai *et al.*, 2003; M Maerefat and Haghighi, 2010; Sayed *et al.*, 2013), *etc*. Differing from these precedents, radiative cooling can serve both aims, namely the extension of working time and improvement of ventilation and cooling performance of solar chimney ventilation.

In this study, the proposal of radiative cooling combination with solar chimney ventilation in the form of a novel roof solar chimney-radiative cooling (SC-RC) ventilation is examined. A detailed description of the proposed SC-RC ventilation is given in Section 4.1. Besides performance evaluations, a parametric study of the SC-RC ventilation for different working conditions is also. Because this chapter concerns natural ventilation flow, the computational fluid dynamics (CFD) model of SC-RC ventilation is developed using Ansys Fluent. This is especially challenging because the method of using Ansys Fluent in radiative cooling research is considered new. Thus, the CFD model developed here will be beneficial for further related research on radiative cooling involving force or natural convection.

4.2 Design of the Combined Solar Chimney and Radiative Cooling (SC-RC) Ventilation

Before getting into the SC-RC ventilation design, it is beneficial to describe the mechanism that drives the flow in the solar chimney and radiative cooling cavity. The buoyancy force that drives the SC-RC ventilation happens due to differences in air density, specifically between the density of indoor air and outdoor air. The static pressure exerted by the air depends on its density as described by Equation 4.1, with P as the static pressure, g as the gravitational acceleration, ρ as the air density, and z as the vertical distance.

$$P = -g \int_0^z \rho \, dz \tag{4.1}$$

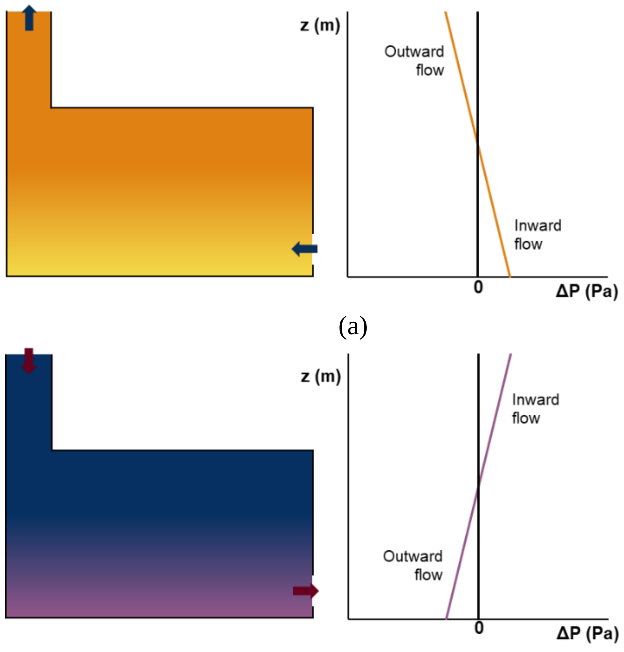

Figure 4-1 Flow direction and outdoor-indoor static pressure differences of (a) warm room and (b) cold room.

Usually, the density of the outdoor air (ρ_o) is considered constant, but the indoor air density (ρ) is dependent on height, $\rho(z)$. This creates a variation in the outdoor and indoor air pressure gradient ($\Delta P = P_o - P_i$) along the vertical axis. The example of pressure gradients of a warmer-than-ambient room is represented in Figure 4-1a (Chenvidyakarn, 2013). As seen in Figure 4-1a, there is a neutral level where the $\Delta P = 0$. Below this neutral level where $\Delta P > 0$, the ventilation flow direction is *in* the room. On the other hand, above this neutral level where $\Delta P < 0$, the ventilation flow direction is *out* of the room. For a room with an air temperature cooler than the ambient air, the situation is reversed. The $\Delta P < 0$ in such a room is below the neutral level, while the $\Delta P > 0$ level is above the neutral level, thus creating a ventilation flow from the top of the room to the bottom (see Figure 4-1b).

In conventional SC ventilation, the driving force for the upward ventilation flow is the absorbed heat from the sun. Using the same principle, one can use the RC emitter to create a downward flow channel for the air. Therefore, in the suggested SC-RC ventilation, the SC's effectiveness is anticipated to be improved by the RC cavity, which acts as both an assistant for buoyancy force and a potential channel for precooling air.

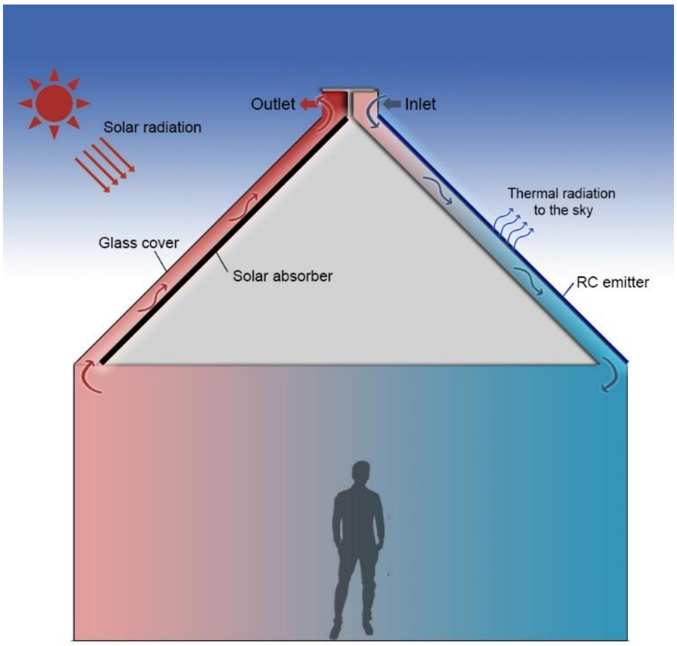

Figure 4-2 Schematic diagram of roof solar chimney combined with radiative cooling cavity applied in a building.

To further describe the mechanism of SC-RC ventilation when applied in a building, Figure 4-2 shows the schematic diagram of the ventilation strategy. The ventilation system design includes a solar chimney (SC) structure on the side of the roof that faces the sun, as well as a radiative cooling (RC) cavity on the opposite side. The SC is warmed by solar radiation during the day, creating a buoyancy effect that pulls air from the room and the RC cavity. As the air passes through the RC cavity, it is cooled by the RC surface and supplies cool air to the room. At night, the radiative sky cooling effect in the RC cavity creates a negative buoyancy that generates a downward airflow for ventilation.

A case study building was developed to test the SC-RC ventilation concept. The building has a cross-sectional width of 4 m and a ceiling height of 2.8 m with a planned depth of 6 m. Its roof is a pitched roof with a 45° inclination angle facing south and north. The SC on the south side and the RC cavity on the north side have an air channel gap of 20 cm. At the top, these air channels are 30 cm openings that act as the interface between the channel and the outside air. Another opening at the bottom of the RC-side wall (named as the wall opening), connects those abovementioned openings and serves as the initial inlet opening for SC ventilation. The geometry and dimensions of the case study building are depicted in Figure 4-3.

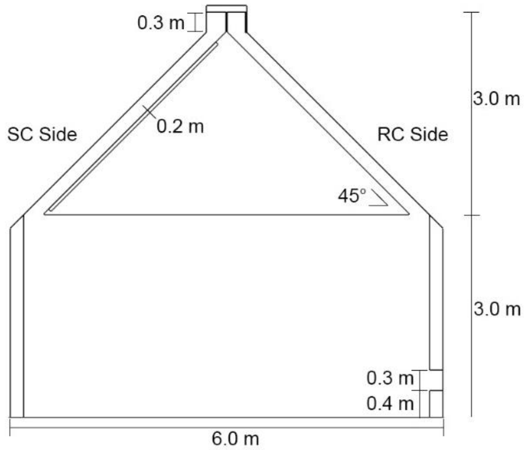

Figure 4-3 Geometry and dimension of the case study building.

Other details needed for the case study building are the construction materials' dimensions and properties. A 20 cm thick brick was used as the wall material. For the roof and ceiling, roof tile and timber are chosen. Meanwhile, the floor material is ceramic. The materials selection is based on the typical house-building material (Oikonomou and Bougiatioti, 2011). Furthermore, the base material for the absorber and emitter in the SC and RC cavity is aluminium with a thickness of 1 mm. They are coated with a heating/cooling coating suited for their purpose. Also, the convection cover of the RC emitter is a PE film with a thickness of 6 microns. The solar absorber was coated with a coating that has high absorptivity in the solar (0.2-3 µm) and thermal radiation (3-25 µm) bands. The RC emitter, on the other hand, was coated with a material with high emissivity in the 8-13 µm (atmospheric window) band only and low absorptivity in the solar and other thermal (3-8 µm and 13-25 µm) bands. The thermal properties of the construction materials as well as their spectral properties in those wavelengths are summarised in Table 4-1. Except for the absorber and emitter, the emissivity for all materials was taken from the ECOSTRESS spectral library (Meerdink *et al.*, 2019).

Table 4-1 Thermal and spectral properties of the construction materials.

Material	**Thermal properties**			**Absorptivity/emissivity**			
	Thermal conductivity ($W \cdot m^{-1} \cdot K^{-1}$)	Density ($kg \cdot m^{-3}$)	Specific heat capacity ($J \cdot kg^{-1} \cdot K^{-1}$)	0.2-3 μm	3-8 μm	8-13 μm	13-25 μm
Brick	0.72	1920	840	0.79	0.77	0.93	0.93
Ceramic tile	0.8	1700	850	0.34	0.94	0.93	0.93
Insulation board	0.033	38	1400	0.70	0.90	0.90	0.90
Roof tile	0.8	1890	880	0.87	0.93	0.95	0.95
Timber	0.16	720	1260	0.46	0.9	0.94	0.94
Absorber	202.4	2719	871	0.95	0.95	0.95	0.95
Glass	1.38	2203	703	0.05	0.88	0.88	0.88
Emitter	202.4	2719	871	0.05	0.95	0.95	0.95
PE film	0.45	910	1900	0.05	0.05	0.05	0.05

4.3 Validation of the CFD model for the SC-RC Ventilation

In this chapter, the 2-dimensional (2D) geometry representing the cross-sectional model of the case study building was used in the CFD simulations. This 2D geometry is considered acceptable for an unchanging room shape (Cook, 1998). Further, as the outdoor air pressure is important in the buoyancy-driven ventilation flow, its condition should be known (Cook, 1998). Thus, the geometry in this study also included the outdoor air as the computational domain (see Figure 4-4). As shown in Figure 4-4, the computational domain extension to represent the outdoor air was done by extending the boundary to 10 times the width (10W) and height (10H) of the case study building.

The external domain's top and side boundaries were set as pressure outlets, while the bottom boundary was designated as the ground. The building envelope's geometry was based on case studies depicted in Figure 4-3. A hexa-dominant mesh with a maximum size of 5 cm for the room (shown in Figure 4-5) was used for the simulation, and it was later refined for grid-independence study until the maximum size was reduced to 1 cm.

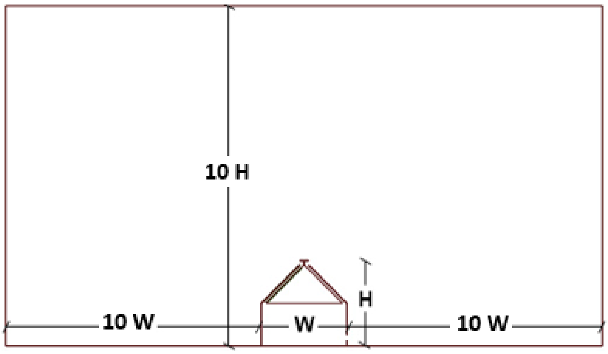

Figure 4-4 The computational domain.

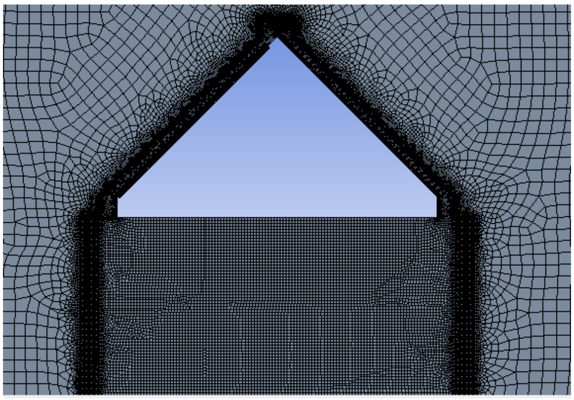

Figure 4-5 Initial computational grids with a 5 cm maximum size in the room.

To ensure the simulation results are independent of the grid and time-step sizes, results from five combinations of grid size and time-step size were compared. The simulation conditions and settings follow the steps as explained in Chapter 3. Figure 4-6 plots the comparison of simulation results for the room temperature, the indoor air velocity, and the ventilation flow rate through the SC opening. Starting from the 2.5 cm mesh and the 600 s time-step, the relative variations in the room temperature and velocity results between the grid and time-step sizes are small (roughly 0.2°C for temperature and 0.02 m/s for velocity on average). However, the hourly ventilation rate pattern only begins to be grid and time-step independent at the 1 cm mesh and the 450 s time step, with a relative variation of 0.01 m^3/s with the previous time-step size. Hence, the mesh and time step sizes of 1 cm and 450 s are used in this study.

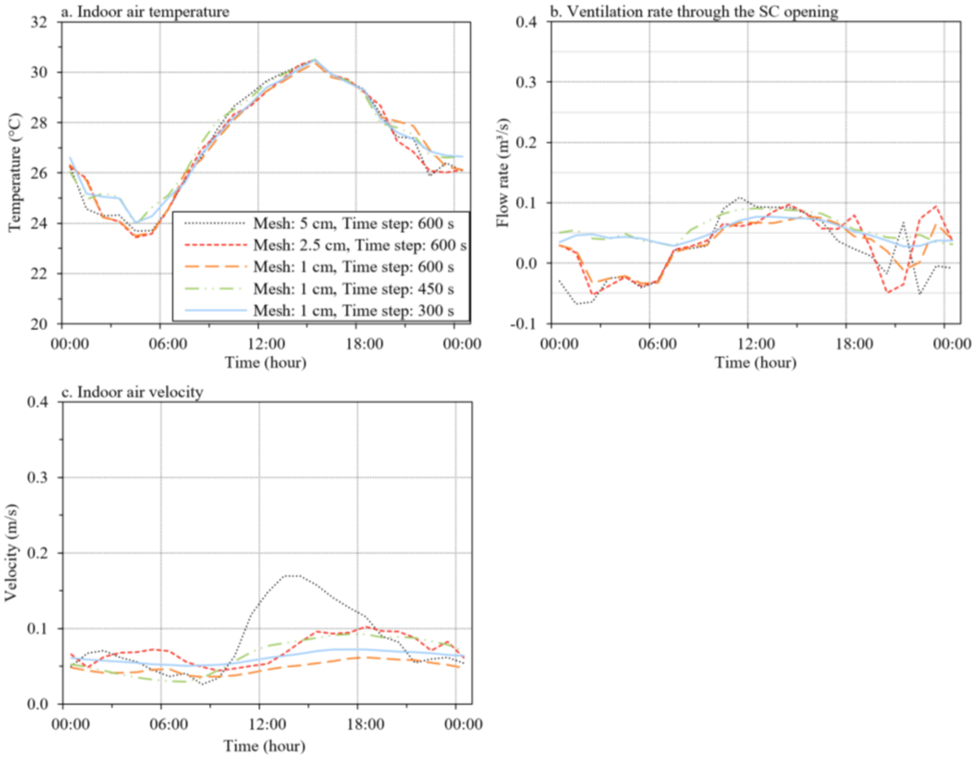

Figure 4-6 Comparison of the hourly (a) room temperature, (b) ventilation rate through the SC opening, and (c) indoor air velocity results from various grid and time step sizes.

The comparison to validate the heat transfer model and the ventilation flow model is done separately. The heat transfer model was validated against the experimental data from Hu *et al.* (2020) for their photothermal and radiative cooling (PT-RC) module. The PT-RC module was a modified solar air heater that can perform heating in the daytime and cooling at nighttime. Thus, the PT-RC module is considered appropriate to check the heat transfer models that also include both solar absorption and thermal radiation. Figure 4-7 shows the comparison between the simulation and the experiment. The figure shows good agreement between the glass and absorber/emitter temperatures from the simulation and the experiment. From the comparison, the root mean square deviation (RMSD) was then calculated using Equation 4.2, with $X_{\mathrm{sim},i}$ as the simulation data point and $X_{\mathrm{exp},i}$ as the experimental data point (Bahaidarah *et al.*, 2013; Hu *et al.*, 2020). The RMSD of the simulated glass temperature and absorber temperature are 0.8% and 1.7 %, respectively.

$$RMSD = \sqrt{\frac{1}{n}\sum_{i=1}^{n}\left[\frac{\left(X_{\mathrm{sim},i} - X_{\mathrm{exp},i}\right)}{X_{\mathrm{exp},i}}\right]^2} \qquad 4.2$$

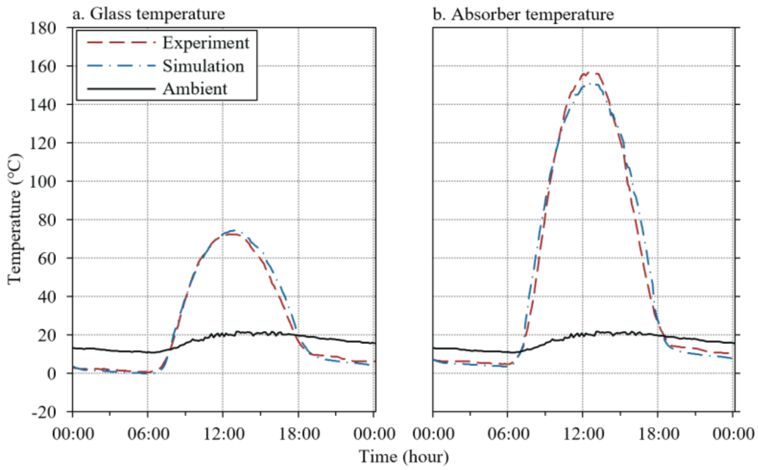

Figure 4-7 Comparison of experimental and simulation results of the PT-RC: (a) glass temperature and (b) absorber temperature.

Moreover, the ventilation flow resulting from the CFD simulations was validated against the data from a solar chimney experiment by Chen *et al.* (2003). The experiment conducted by Chen *et al.* (2003) used a 1.5 m solar chimney in which one of the sides was heated uniformly. The width of the chimney and its inclination angle could be changed accordingly to accommodate various solar chimney designs. One of the tests was for a 20 cm solar chimney with a 45° inclination angle, which is similar to the structure of the SC-RC ventilation. Thus, comparisons are made with this specific experimental setup. Results for the temperature and velocity profiles are summarised in Figure 4-8.

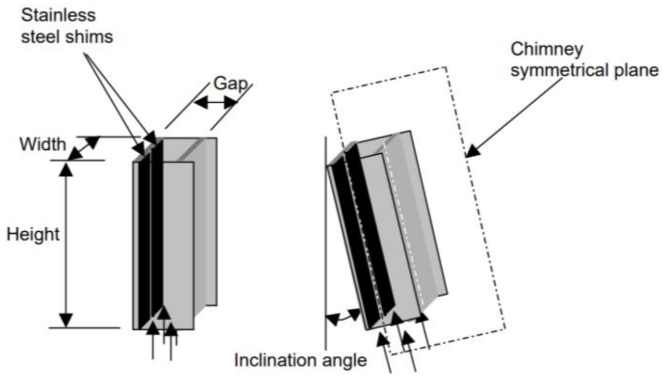

Figure 4-8 Illustration of the chimney from Chen *et al.* (2003).

In general, the simulation results closely match the experimental data, with RMSD values for temperature and velocity distributions inside the chimney of 3% and 14%, respectively. Differences between the simulation and experiment are observed in the velocity distribution near the walls (shown in Figure 4-9b), possibly due to discrepancies in the near-wall treatment model. Nonetheless, although the horizontal velocity profile between the simulation and experiment differed where it is closed to the walls, the airflow rate resulted from the simulations still shows a good agreement with the experiment, with RMSD values for temperature and velocity distributions inside the chimney of 0.16 and 0.14 respectively, which indicates a good agreement between our simulation with the experimental data. Also, the airflow rate obtained from the simulations is still in good agreement with the experiment, including the flow rate (0.037 m3/s compared to 0.035 m3/s from the experiment).

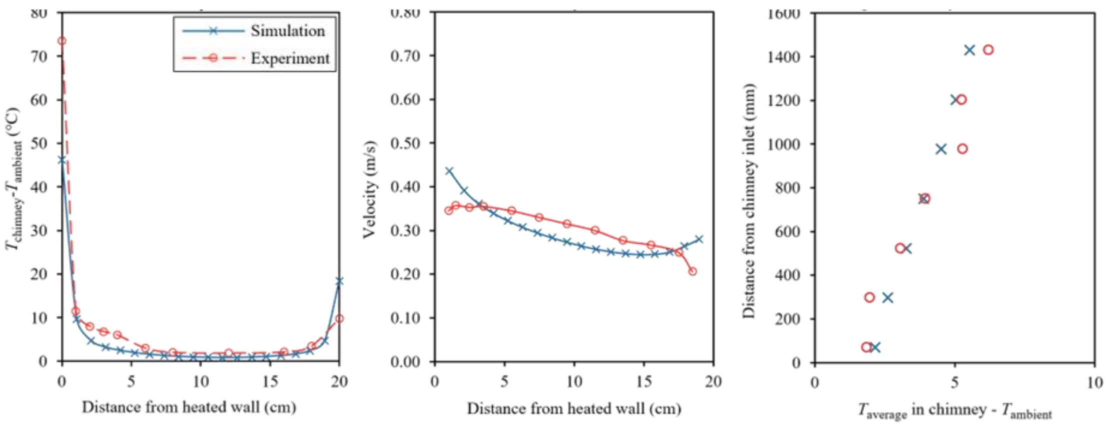

(a) (b) (c)

Figure 4-9 Comparison between the CFD simulation with the experimental data from Chen *et al.* (2003): (a) air temperature across the chimney, (b) velocity distribution across the solar chimney, and (c) air temperature along the chimney.

4.4 Performance Evaluation of Natural Ventilation in Combined Solar Chimney-Radiative Cooling

4.4.1 Evaluation scenarios

In examining the performance of the SC-RC ventilation, three opening configurations were set. These three configurations, later named scenarios, represent the conventional SC ventilation and two possible opening configurations for the SC-RC ventilation. The first scenario, which is the conventional SC ventilation, has only its wall and roof SC openings open (henceforth the SC+wall-opening), as shown in Figure 3-10a. The second scenario, which is the first configuration of the SC-RC ventilation, has its roof RC and SC openings open but wall opening closed (henceforth the SC-RC in Figure 4-103-10b). The third scenario is also the SC-RC ventilation configuration, but with the wall opening open (henceforth the SC-RC+wall-opening in Figure 3 10c).

In addition to the description above, a location with the appropriate climate conditions is needed for the simulation. In this study, Athens (38°N, 24°E), Greece, is selected as the location. Athens' climate is classified as Csa in the Köppen-Geiger classification, which is characterised by a dry and warm temperate climate with hot summer (Kottek *et al.*, 2006). These characteristics make Athens suitable for the ventilation and cooling purposes of the SC-RC ventilation.

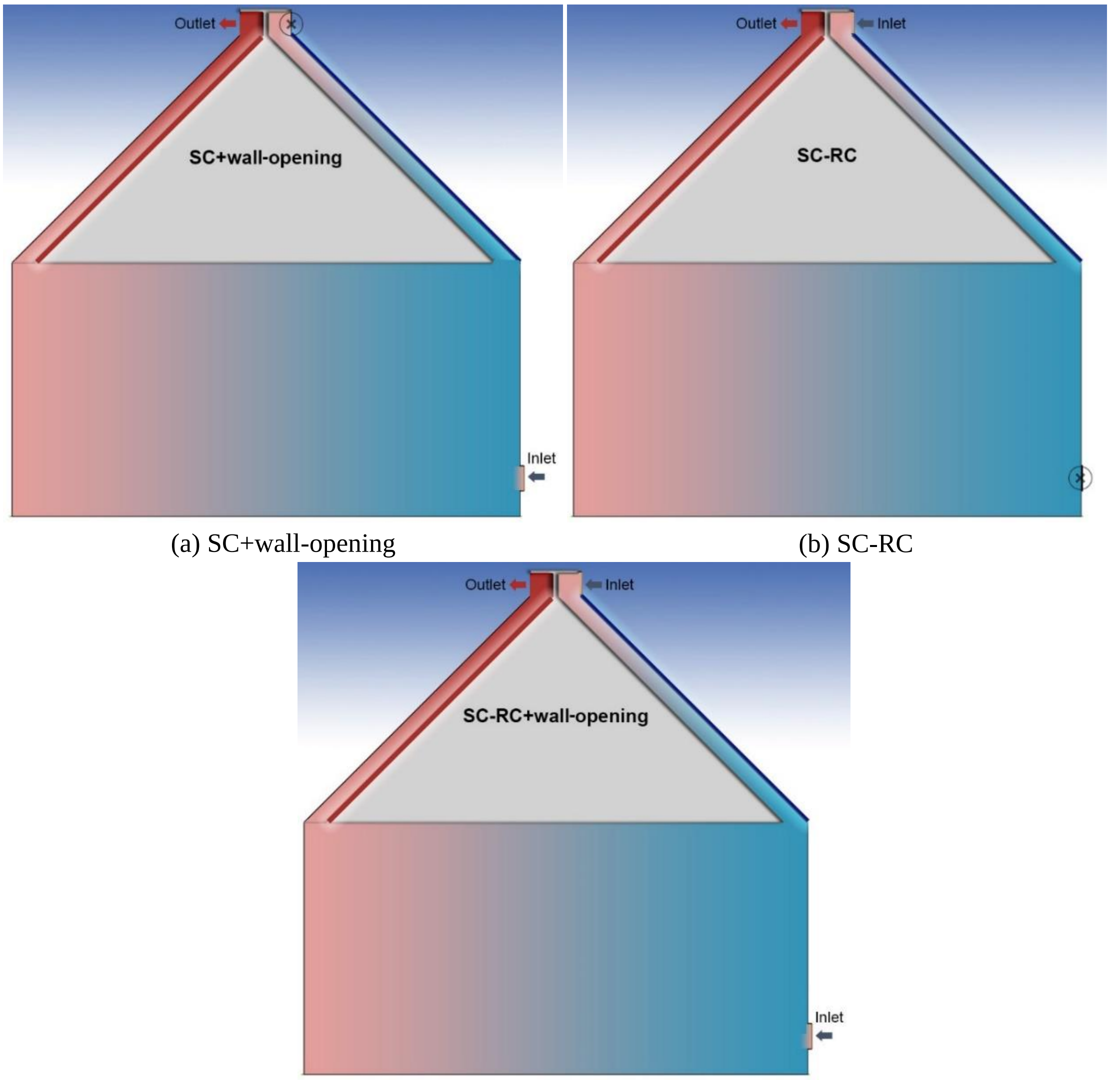

(a) SC+wall-opening (b) SC-RC

(c) SC-RC+wall-opening

Figure 4-10 Illustration of the ventilation scenarios: (a) SC+wall-opening, (b) SC-RC, and (c) SC-RC+wall-opening.

The weather data of Athens was obtained from the typical meteorological year (TMY) data of Athens (EnergyPlus, 2021). Specifically, the average monthly data in the summer month of July was selected for the performance evaluation of the SC-RC ventilation, as it is the hottest period of the year in Athens. Figure 4-11 displays the summary of weather conditions on the selected day. Note that, this study only accounts for the buoyancy-driven ventilation flow generated by the SC and RC cavity, and thus the wind effect on ventilation is neglected for simplicity.

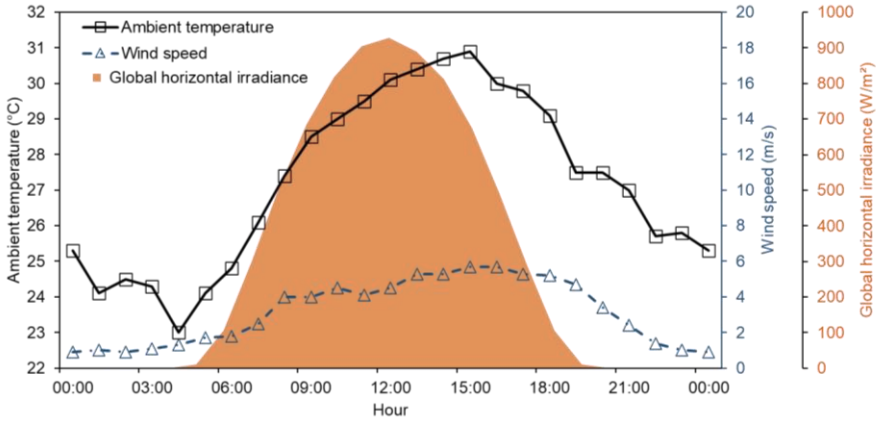

Figure 4-11 The average temperature, wind speed, and solar radiation during the summer month of July in Athens (EnergyPlus, 2021).

The evaluation is done for the ventilation and cooling performance. For the ventilation performance, besides the volumetric flow rate, the air change rate per hour (ACH) resulting from the three scenarios is compared. In addition to that comparison, the ACHs of the scenarios are also compared with the required ventilation rate for residential buildings, which is 0.7 ACH (air change per hour) (ANSI/ASHRAE, 2019). Whereas for the cooling performance, the inlet and room temperatures provided by the three scenarios are analysed. In analysing the room temperature, the requirement from the ASHRAE's adaptive thermal comfort model was used (ASHRAE, 2020). This is because the adaptive thermal comfort model is suitable for a naturally ventilated building with occupants' activity mostly near-sedentary. As the proxy to the operative temperature, this thesis uses the room air temperature (ASHRAE, 2020).

4.4.2 Ventilation performance

The first evaluation concerns the ventilation performance of the SC-RC ventilation. The evaluation begins with the analysis of the flow rate through each opening, namely the SC, RC, and wall openings for all the scenarios. Examination of flow rates at the openings separately is useful for understanding the effect of the RC cavity on ventilation performance.

Figure 4-12a shows the hourly flow rate from the SC opening for the three scenarios in the 24-hour simulation day. With the negative value indicating an outward flow, the figure shows how the SC opening works as the outlet most of the time, except in the few hours at night. This SC opening's behaviour occurs similarly in all scenarios. The outward flow in the SC opening peaks around 3 p.m. or when the ambient air is at its hottest temperature. It then gradually decreases until it becomes zero at late night. However, in the scenarios with wall opening, this decrease in outward flow rate continues until a reversed inward flow occurs late night to early morning. Magnitude-wise, this night's reversed flow through the SC opening is lower than the outward flow during the daytime.

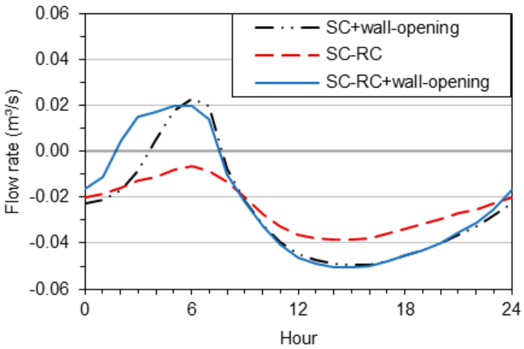

(a) Flow rate from the roof SC opening

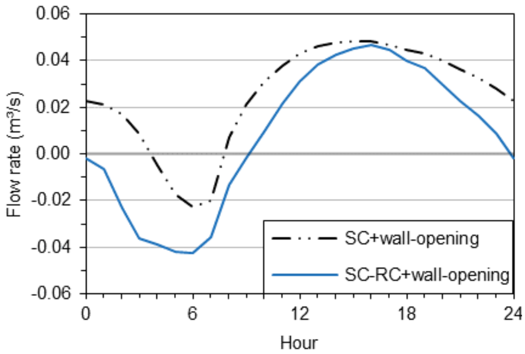

(b) Flow rate from the wall opening

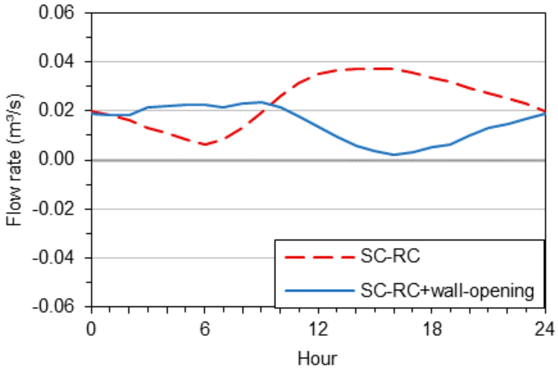

(c) Flow rate from the RC opening

Figure 4-12 Flow rate through the openings in each scenario: (a) through the roof SC opening, (b) through the wall opening, (c) through the RC opening.

Correspondingly, the flow pattern of the wall opening is like the reversed direction of the SC opening flow, but the two are different in terms of the magnitude of the flow rate (Figure 4-12b). On average, the highest inward flow rate through the wall opening is found in the SC+wall-opening scenario. This is because all the ventilation flow enters the building through this opening only for this scenario. In the SC-RC+wall-opening scenario, however, the inlet function is shared between two openings, *i.e.*, the wall and RC openings. For the SC-RC+wall-opening the higher flow rate through the wall opening happens at late-night until early morning (outward flow period). Additionally, Figure 4-12c indicates that the flow rate in the RC cavity for the SC-RC+wall-opening scenario is also better than the SC-RC scenario during the period between late night to early morning. This period of flow rate improvement from the SC-RC+wall-opening coincides with the time of the optimal night sky cooling. This indicates that the flow rate improvement is due to the cooling effect from the RC emitter.

Further, the ACH resulting from all the openings in each scenario is shown in Figure 4-13. As a comparison, the standard minimum ACH (0.7 ACH) is plotted as a straight line in the graph. It should be noted that the ACH value does not represent the flow direction, and thus its value is always positive. This differs from the flow rate data where the negative value represents the outward flow, and the positive value is the inward flow. Therefore, a kind of 'turning point' pattern in the ACH graph is observed in Figure 4-13, representing the time when the reversed flow occurs in the flow rate data.

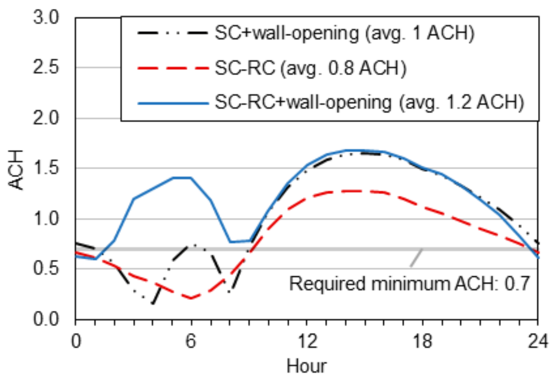

Figure 4-13 The hourly ACH of all scenarios.

Nevertheless, it is seen in Figure 4-13 that there are similar patterns found in all scenarios. The ventilation performance of the three scenarios begins to fall under the line of standard ACH minimum around midnight. However, unlike the other two scenarios, this drop in ventilation for the SC-RC+wall-opening scenario does not extend until the morning. Also, different from the other scenarios that find their ACH plunge far below the standard line, the ACH value provided by the SC-RC+wall-opening scenario only falls slightly below. This better performance in the late night to early morning is the distinctive feature of the SC-RC+wall-opening scenario (see Figure 4-13). Supported by the previous flow rate analysis, this distinctive feature can be regarded as the RC cavity's capability to provide more incoming air during that period. In terms of the daily average ACH, the SC-RC+wall-opening scenario has the highest value with 1.2 ACH compared to 1.0 ACH by SC+wall-opening and 0.8 ACH by SC-RC.

4.4.3 Cooling performance

In addition to the enhancement in ventilation performance, the proposed SC-RC ventilation should also prove to be able to provide cooling to the room. To analyse this cooling effect, Figure 4-14 compares the hourly room temperature and air velocity provided by the three ventilation scenarios. Figure 4-14 reveals that the temperature of the room is slightly warmer than the ambient air during the daytime. It happens in all scenarios. However, the figure also shows a spell of sub-ambient room temperature occurs in the SC-RC and SC-RC+wall-opening scenarios. These sub-ambient periods occur at late night and early morning. These periods make the daily average room temperature of the SC-RC (27.22°C) and the SC-RC+wall-opening (27.17 °C) cooler than in the SC+wall-opening (27.45°C). Nevertheless, the daily average room air temperatures of the three case studies are still within the thermal comfort limits (23-28°C) (Tartarini *et al.*, 2020).

The cooling performance of the SC-RC ventilation can be analysed by separating the average indoor air temperature between daytime (6 a.m. to 6 p.m.) and nighttime (6 p.m. to 6 a.m.). Table 4-2 shows that the SC-RC scenario has the lowest room temperature (28.79°C), followed by the SC-RC+wall-opening (28.88°C) and the SC+wall-opening scenario (28.91°C). Despite the cooler daytime average temperature provided by the ventilation scenarios with the RC cavity, the data suggests that the cooling from the RC cavity is not enough to create a sub-ambient indoor air temperature. Similar to the daytime average indoor temperature, Table 4-2 also reveals that the scenarios with RC cavity are cooler at night, with the SC-RC+wall-opening scenario providing the coolest room (25.51°C) than the other scenarios. The nighttime average temperatures from SC-RC and SC-RC+wall-opening are sub-ambient, demonstrating the ability of the RC cavity to provide a better cooling effect during the night.

A deeper analysis of the RC cavity's role in reducing the room temperature can also be done by comparing the inlet air temperature of the wall opening in the SC+wall-opening scenario with the inlet air temperature of the RC cavity in the SC-RC scenario. The comparison is made relative to the corresponding indoor air temperature, *i.e.*, how much higher or lower the inlet temperature is compared to the indoor air temperature ($\Delta T_{\mathrm{inlet}} = T_{\mathrm{inlet}} - T_{\mathrm{indoor}}$). Note that the RC cavity air temperature is measured at the ceiling opening after the incoming air passes through the whole length of the RC cavity.

ΔT_{inlet} helps to assess whether the inlet air potentially makes the room warmer or cooler.

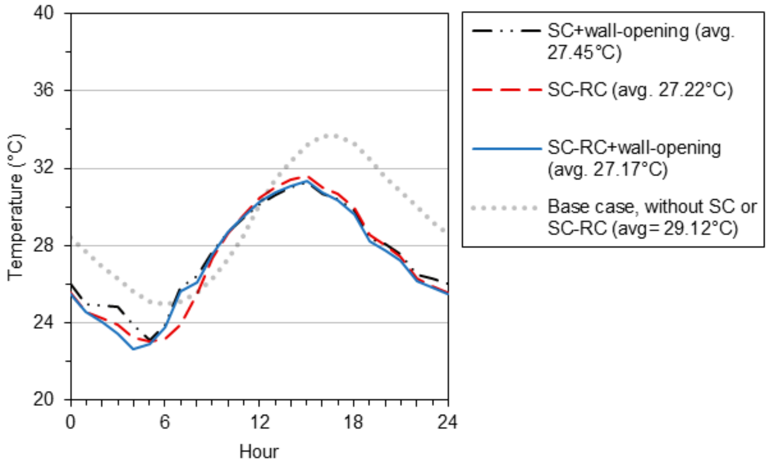

Figure 4-14 The hourly indoor air temperature and of all scenarios.

Table 4-2 Daily, daytime, and nighttime average room temperature.

	Base case (°C)	**SC+wall-opening (°C)**	**SC-RC (°C)**	**SC-RC+wall-opening (°C)**
Daily	29.12	27.45	27.22	27.17
Daytime (6 a.m. - 6 p.m.)	29.64	28.91	28.79	28.88
Nighttime (6 p.m. - 6 a.m.)	28.63	26.02	25.68	25.51

Figure 4-15 reveals a remarkable cooling effect that the RC cavity provides as an inlet. The ΔT_{inlet} of the SC+wall-opening scenario barely reaches -1°C even with the reversed flow from the SC opening at late night. On the other hand, the ΔT_{inlet} of the SC-RC scenario surpasses -3°C during the night. In the daytime, moreover, the SC+wall-opening scenario only adds warmer air to the room, while the SC-RC scenario delivers slightly cooler air to the room. If the cooling effect in the RC cavity could be enhanced, either through cavity design or a better emitter the inlet air would in the daytime would be cooler.

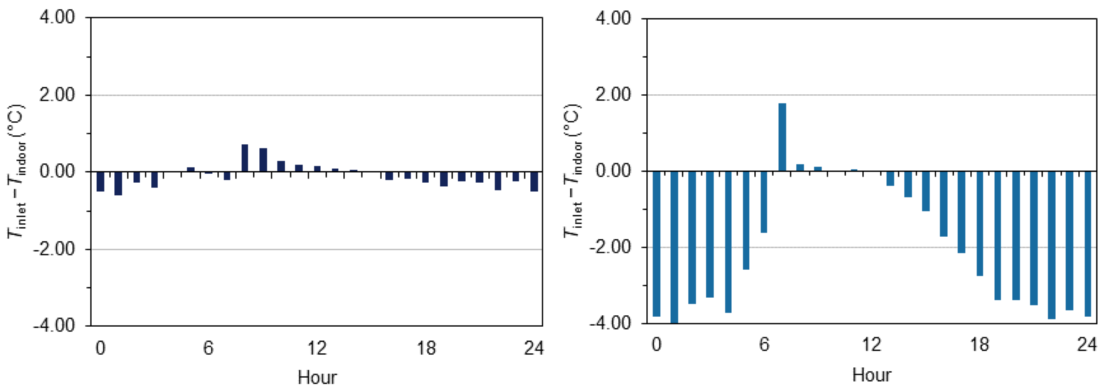

Figure 4-15 Comparison between: (a) ΔT_{inlet} of the wall opening, and (b) ΔT_{inlet} of the RC cavity.

On top of the above analysis of the air temperatures, another analysis can be added in terms of the air velocity provided by the ventilation scenarios. The hourly average velocity magnitude and the velocity field in the room are depicted in Figures 4-16 and 4-17. As seen in Figure 4-16, the indoor air velocities are below 0.1 m/s in all case studies, with the fastest breeze provided by the SC-RC scenario (average of 0.09 m/s). However, this value is considered too small to give a cooling sensation to the occupants because the breeze should be at least 0.3 m/s to create a sensation of cooling in a naturally ventilated building (ASHRAE, 2020).

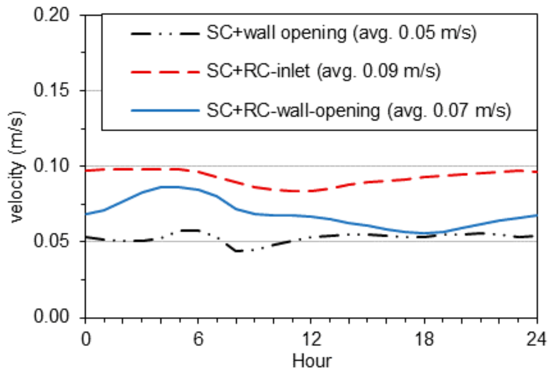

Figure 4-16 The hourly indoor air velocity of all scenarios.

Moreover, using Figure 4-17 one can assess the relation between the velocity field and the corresponding temperature distribution of each scenario. Two moments representing the hot and cool (room air temperatures are chosen, namely at 3 p.m. and 6 a.m. respectively. Figure 4-17 reveals how the SC-RC ventilation generates more breeze in the room due to its inlet position. Unlike the wall opening, the RC opening can push the incoming air deeper into the room and thus induce air movement in the room. However, because the inlet function in the SC-RC+wall-opening scenario is shared between the roof RC and wall openings, the flow rate from the RC cavity is reduced. Therefore, the breeze delivered into the room by this scenario is slower than the SC-RC. Nonetheless, both ventilation scenarios with the RC cavity create more breeze in the room than the conventional SC+wall-opening scenario.

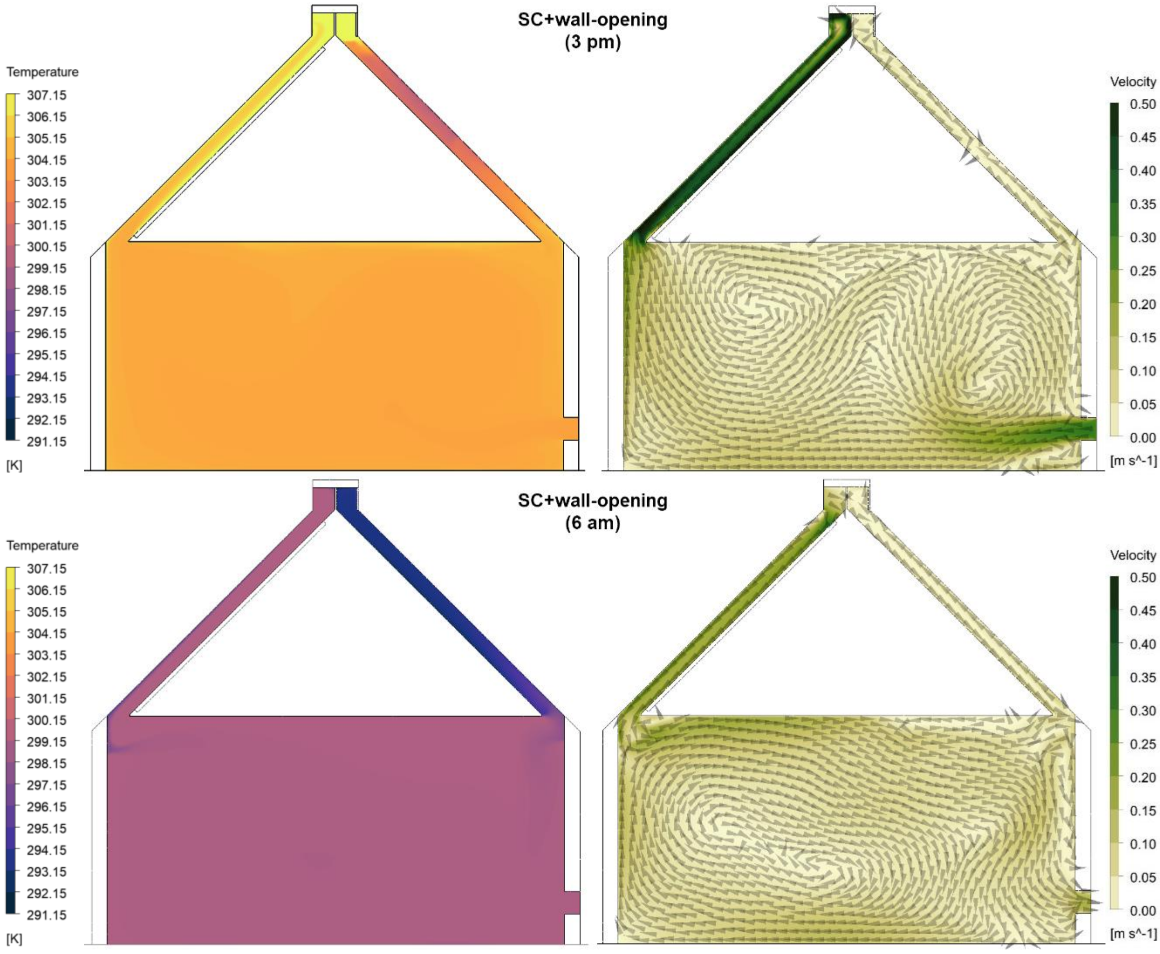
SC+wall-opening
(3 pm)
Temperature
307.15
306.15
305.15
304.15
303.15
302.15
301.15
300.15
299.15
298.15
297.15
296.15
295.15
294.15
293.15
292.15
291.15
[K]
Velocity
0.50
0.45
0.40
0.35
0.30
0.25
0.20
0.15
0.10
0.05
0.00
[m s^-1]
SC+wall-opening
(6 am)
Temperature
307.15
306.15
305.15
304.15
303.15
302.15
301.15
300.15
299.15
298.15
297.15
296.15
295.15
294.15
293.15
292.15
291.15
[K]
Velocity
0.50
0.45
0.40
0.35
0.30
0.25
0.20
0.15
0.10
0.05
0.00
[m s^-1]

(a)

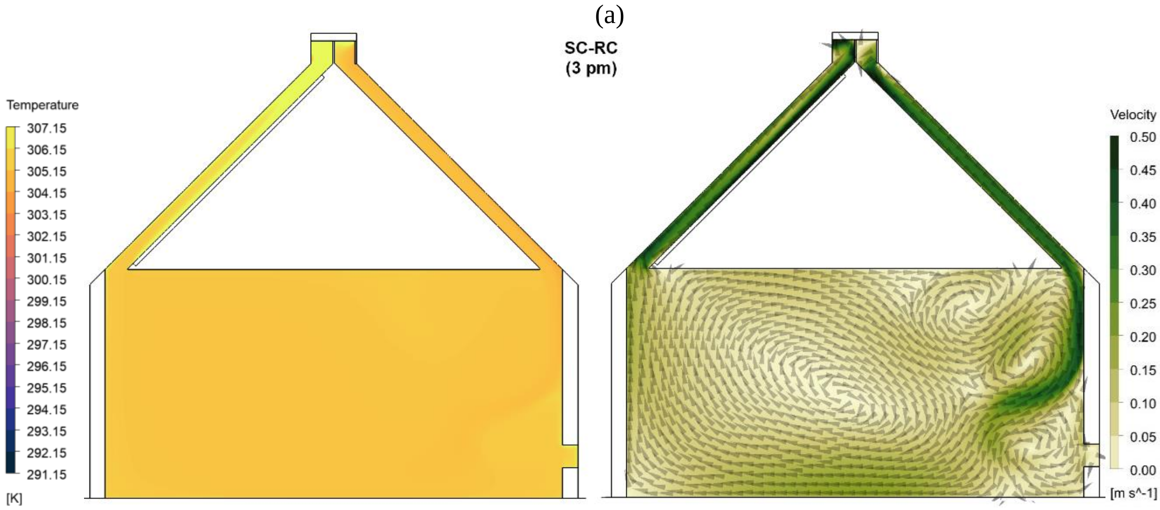
SC-RC
(3 pm)
Temperature
307.15
306.15
305.15
304.15
303.15
302.15
301.15
300.15
299.15
298.15
297.15
296.15
295.15
294.15
293.15
292.15
291.15
[K]
Velocity
0.50
0.45
0.40
0.35
0.30
0.25
0.20
0.15
0.10
0.05
0.00
[m s^-1]

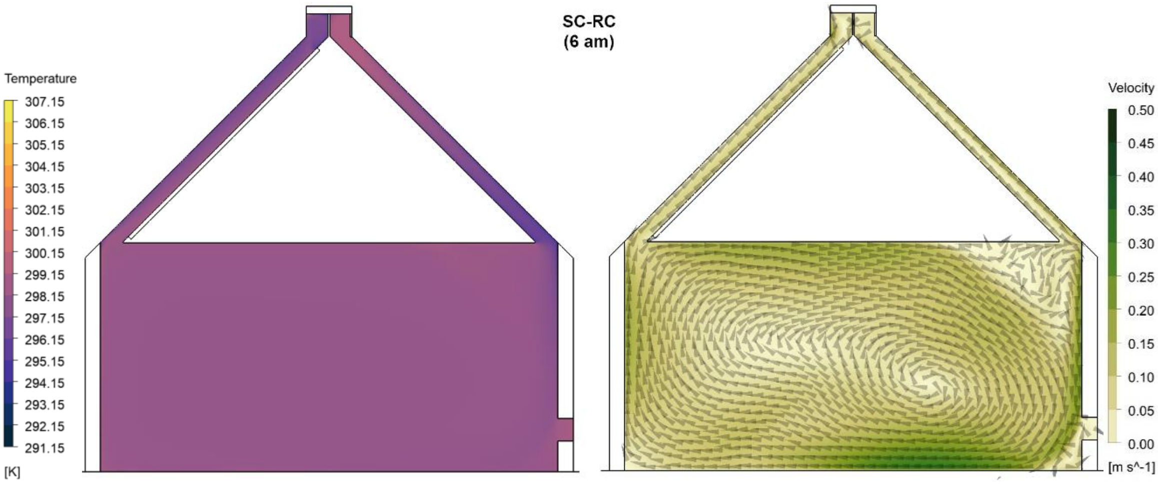

(b)

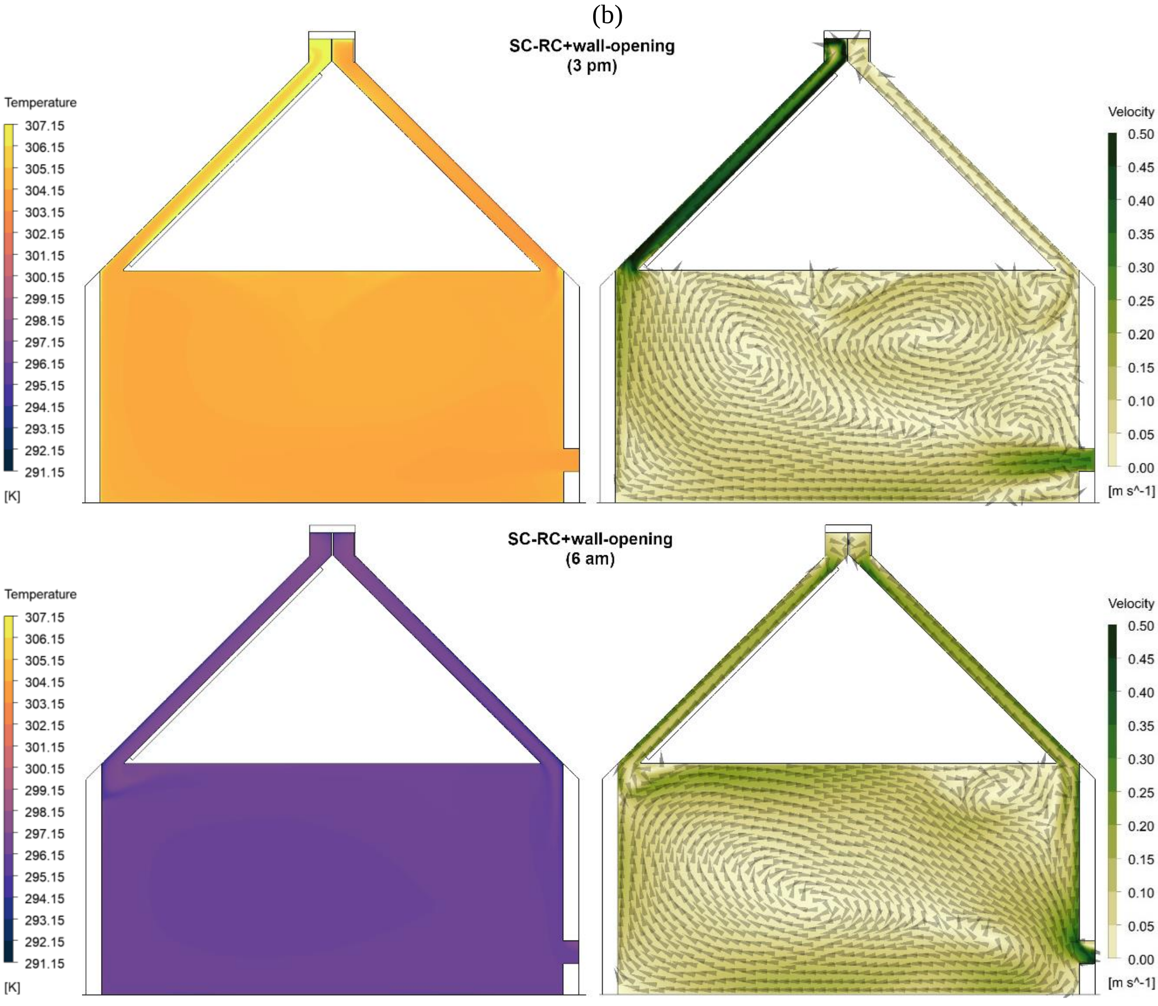

(c)

Figure 4-17 The temperature and velocity contour of the case studies at 3 p.m. and 6 a.m.: (a) SC+wall-opening, (b) SC-RC, and (c) SC-RC+wall-opening.

4.5 Effect of Various Parameters on the Performance of the SC-RC Ventilation

To understand the effect of various design and environmental parameters and obtain the optimal design, this chapter provides parametric studies for SC-RC ventilation. The parametric studies used Valencia (40°N, 1°W) as the default location due to its similarity with Athens in terms of climate type (Kottek *et al.*, 2006). The selected day for simulation is the hottest in the TMY data of Valencia, with the important weather parameters plotted in Figure 4-18 (Lawrie and Crawley, 2022).

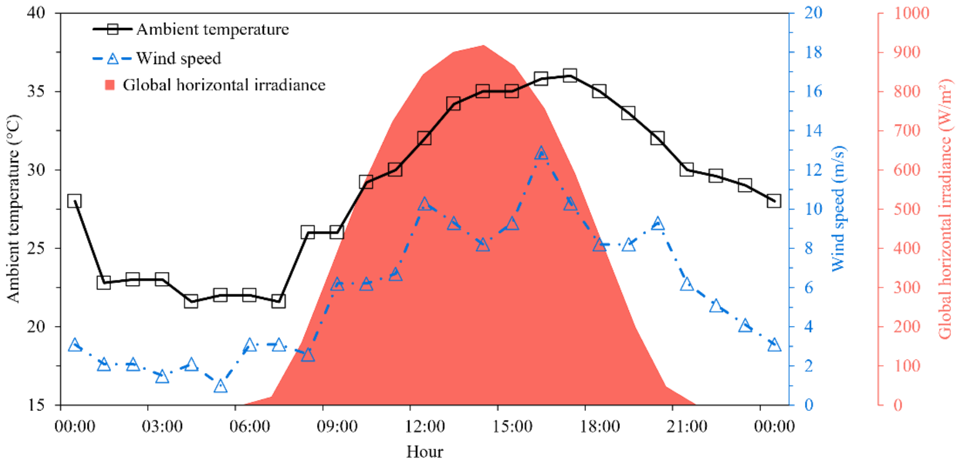

Figure 4-18 The ambient temperature, wind speed, and global solar irradiance on the hottest day in Valencia (EnergyPlus, 2021).

In this section, six parameters that have a significant effect on the SC and/or RC performance are discussed. Firstly, this section discusses the effect of the RC emitter's convection cover on the performance of the SC-RC ventilation. The RC emitter's connection cover aims to reduce the convective heat gain and improve the RC power. It usually uses polyethene (PE) film because the material is transparent in the atmospheric window band (Hu, Suhendri, *et al.*, 2021a).

The second discussion in the parametric studies is about the effect of the building's wall material, *i.e.*, whether the wall uses thermal mass or lightweight materials. Thermal mass materials are commonly used as wall materials, and they cover a substantial part of a building. The thermal storage capacity of the thermal mass regulates the external heat gain of the building. Hence, it may directly or indirectly affect the ventilation rate of a buoyancy-driven ventilation strategy (Kuczyński *et al.*, 2021). Therefore, an analysis of the effect of thermal mass walls on the performance of SC-RC ventilation should be conducted.

Further, the length and width of the air channel for the SC and RC cavity are also influential parameters (Z D Chen *et al.*, 2003; Lal, 2014; Villar-Ramos *et al.*, 2020). It is reported that the preferred SC length is 1.5 m, although it is not uncommon for SC to have the same length as the wall or roof in which it is placed. The reported optimal width of the SC is more varied, ranging from 5 cm to 30 cm or more. Yet a 20 cm chimney gap is usually considered the best width (Z D Chen *et al.*, 2003). Analysis of the optimal SC and RC cavity gap in the SC-RC ventilation design is discussed in the third section of this parametric study.

The fourth parameter is the internal heat gain. Besides the external heat gains that, as mentioned earlier, relate to the wall material, the building's internal heat gains also matter when using buoyancy-driven ventilation. It is due to the effect of internal heat gains on the room temperature (Dharmasastha *et al.*, 2022).

Fifth in the discussion list of the parametric studies is the climate condition which governs parameters such as solar irradiance, clear sky index, ambient temperature, humidity level, and wind speed (Hu, Zhao, Ao, Su, *et al.*, 2018a; B. Zhao, Hu, Ao and Pei, 2019; B. Zhao, Hu, Ao, Huang, *et al.*, 2019). In comparing the performance of the SC-RC ventilation in different climates, the locations were changed accordingly, but the selected day was still the hottest in the respective climate. There are five warmest climates based on the Köppen-Geiger climate classification chosen in the parametric study. The climate types and its location are the tropical humid (Af) of Singapore, the steppe climate (BSh) of Lahore, the desert climate (BWh) or Riyadh, the warm temperate and humid climate (Cfa) of Shanghai, as well as the warm temperate and dry climate (Csa) of Valencia (Kottek *et al.*, 2006).

Table 4-3 Summary of the studied parameters and their related base and reference cases.

<table>
<tr><th>Parameter</th><th>Variable to compare</th><th>Reference case SC ventilation</th></tr>
<tr><td>Convection cover</td><td>PE-covered SC-RC vs. uncovered SC-RC with light wall material (insulation board)</td><td rowspan="6">SC-only ventilation, with a 20 cm thick brick wall, and other conditions follow the respective variable and base cases of SC-RC.</td></tr>
<tr><td>Thermal mass</td><td>SC-RC with light wall material (insulation board) vs. SC-RC with thermal mass material</td></tr>
<tr><td>Gap</td><td>SC-RC with various RC cavity gaps:
10 cm, 15 cm, 20 cm, 25 cm, 30 cm</td></tr>
<tr><td>Internal heat gain*</td><td>SC-RC with various internal heat gains:
0 W/m^2, 1 W/m^2, 2 W/m^2, 3 W/m^2, 4 W/m^2</td></tr>
<tr><td>Climate</td><td>SC-RC with various climate conditions:
Tropical humid, Af (Singapore), Steppe, BSh (Lahore), desert, BWh (Riyadh), Temperate humid, Cfa (Shanghai), Temperate dry, Csa (Valencia)</td></tr>
<tr><td>Fan-assisted</td><td>SC-RC with various fan flow rates:
Naturally ventilated (NV), fan 0.05 m^3/s, fan 0.1 m^3/s, and fan 0.5 m^3/s</td></tr>
</table>

*The standard value for internal heat gain for a large building area is 2.1 W/m^2 (Passipedia, 2021)

Using the SC-RC ventilation naturally or fan-assisted is also a factor to be considered. In some SC research, a fan is used to assist the performance of the natural ventilation when the condition is not desirable (Bansal, Mathur and Bhandari, 1993; M. Maerefat and Haghighi, 2010; Calautit *et al.*, 2020). Hence, in the context of SC-RC ventilation, the condition in which a fan could be beneficial for ventilation is also worth studying. Therefore, the effect of using a fan in the RC cavity on the overall performance of the SC-RC ventilation is included as the sixth parametric study. Table 4-3 summarises all the parameters and their related simulation scenarios.

Recall that the formula for the sky temperature, the empirical formula in Equation 3.5 is used for the Athens climate. In this parametric study, the sky temperature is calculated based on the appropriate empirical formula for the climate. This study estimates the sky temperature using the sky emissivity value because that is the most employed model used in empirical sky temperature research (Evangelisti, Guattari and Asdrubali, 2019). Table 4-4 summarises the empirical formula and the relation between the sky emissivity and the sky temperature. The term T_{dp} in the equations is the dew point temperature, available from the TMY data.

Table 4-4 Empirical formula used for $\varepsilon_{\mathrm{sky}}$ and T_{sky}.

Climate condition (Location)	$\boldsymbol{\varepsilon_{\mathrm{sky}}}$	$\boldsymbol{T_{\mathrm{sky}}}$
Tropical humid, Af (Singapore)	$\varepsilon_{\mathrm{sky}} = 0.711 + 0.56\left(T_{\mathrm{dp}}/_{100}\right) + 0.73\left(T_{\mathrm{dp}}/_{100}\right)^2$ (Berdahl and Martin, 1984)	$T_{\mathrm{sky}}^4 = \varepsilon_{\mathrm{sky}} T_{\mathrm{amb}}^4$, (Li and Coimbra, 2019)
Steppe, BSh (Lahore)	$\varepsilon_{\mathrm{sky}} = 0.56 + 0.08 P_v^{0.5}$ (Melchor V, 1982)	
Desert, BWh (Riyadh)		
Temperate humid, Cfa (Shanghai)	$\varepsilon_{\mathrm{sky}} = 0.754 + 0.0044 T_{\mathrm{dp}}$ (Watmuff, Charters and Proctor, 1977)	
Temperate dry, Csa (Valencia)		

Moreover, an analysis of the effect of different parameters on the performance of SC-RC is conducted by comparing two primary variables, *i.e.*, the cooling performance and ventilation performance. The cooling performance is indicated by the difference between indoor air temperature with ambient temperature ($\Delta T_{\mathrm{room}} = T_{\mathrm{room}} - T_{\mathrm{amb}}$). Whereas the ventilation performance is analysed using the flow rate through the RC cavity (m3/s) and the total ventilation rate in both m3/s and ACH.

4.5.1 Effect of the RC emitter's convection cover

The PE cover is undoubtedly beneficial for the RC emitter in terms of reducing the convection heat gain from the ambient air. But PE is not a long-lasting material, and amid the lack of options for a durable cover for the RC emitter, one could suggest using the emitter without the convection cover. Therefore, an assessment of how much the presence of the convection cover affects the performance of the SC-RC ventilation is needed. Figure 4-19a reveals that the PE-covered RC emitter's temperature is around 2°C lower than the uncovered RC emitter. The temperature of the PE-covered RC emitter is consistently sub-ambient throughout the day, whereas the uncovered RC loses its cooling power in the high solar radiation period between 10 a.m. to 5 p.m.

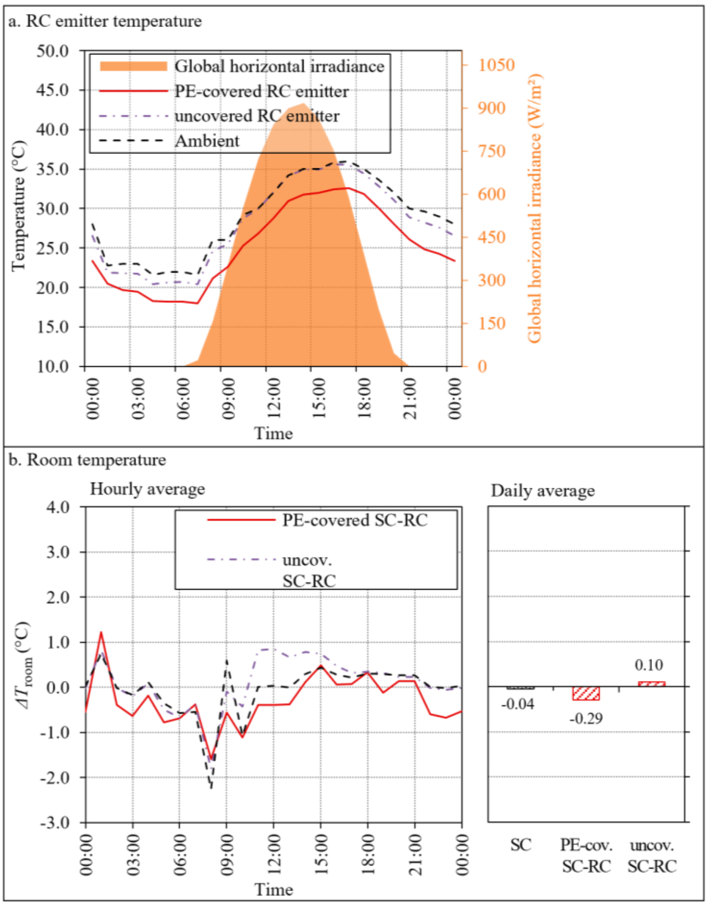

Figure 4-19 (a) RC emitter's temperature and (b) Hourly and daily average ΔT_{room} of SC-RC with and without PE cover.

The emitter temperature influences the PE-covered SC-RC ventilation performance. With the RC emitter covered under the PE film, the SC-RC ventilation provides around 0.39°C lower daily average room temperature than the uncovered SC-RC ventilation, as shown in Figure 4-19b. A distinguishable pattern of hourly ΔT_{room} between the PE-covered SC-RC ventilation, the uncovered SC-RC ventilation, and the reference case SC ventilation is also apparent from Figure 4-19b. The PE-covered SC-RC ventilation creates a sub-ambient room for a longer period than the uncovered SC-RC ventilation or the reference case SC ventilation.

In terms of ventilation performance analysis, Figure 4-20 reveals a reverse flow in the RC cavity of the uncovered SC-RC ventilation, indicated by negative values of flow rate between 11 a.m. to 6 p.m. The cooling effect of the uncovered RC emitter in this period is not sufficient to generate a downward natural convection flow. Instead, the warmer room air due to solar heat gain forces an upward flow in the RC cavity. This upward flow then makes the average room temperature of the uncovered SC-RC ventilation room warmer than the PE-covered SC-RC ventilation.

Despite this difference in the RC cavity flow, the PE-covered and uncovered SC-RC share a comparable ACH, namely 2.0 and 2.1 ACH respectively. These ACHs are higher than the conventional SC ventilation which has 1.8 ACH. But Figure 4-20 also reveals that the hourly total flow rate pattern of the uncovered SC-RC ventilation is closer to the SC ventilation than the PE-covered SC-RC ventilation. This is especially true in the daytime when the upward RC cavity flow occurs in the uncovered SC-RC ventilation. Considering all the above discussion, it is preferable to use the PE-covered SC-RC because it can provide more ACH with a cooling effect on the room.

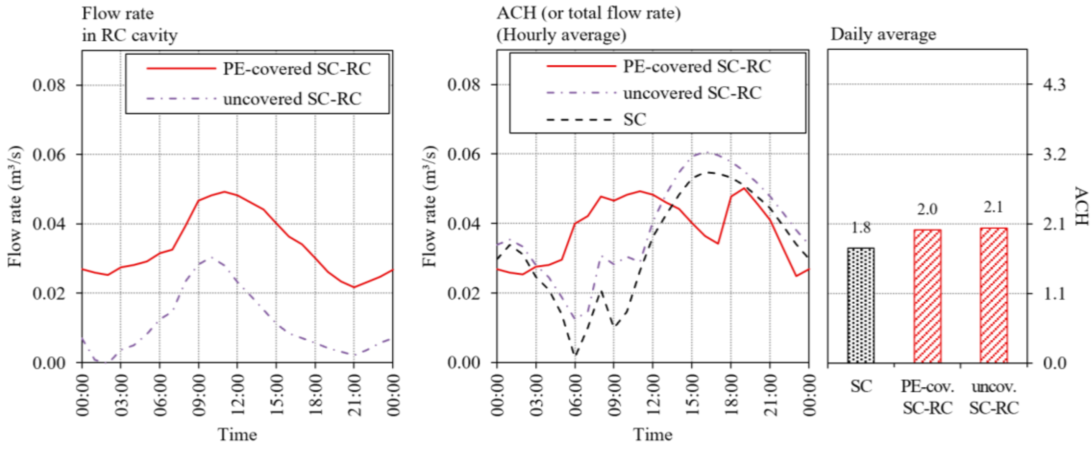

Figure 4-20 The RC cavity flow and the total flow rates of the SC-RC with and without PE cover.

4.5.2 Effect of the building's thermal mass

In real conditions, buildings use heavyweight and long-lasting materials like brick, stone, or concrete for the wall material. These materials are thermal mass materials that can absorb heat slowly and store it for some time before releasing it in a later period. To see the effect of this thermal mass property of the wall material, Figures 4-21 and 4-22 compare the cooling and ventilation performance of the SC-RC ventilation with a brick wall (the base case) and a lightweight insulation board wall. As the reference case, the conventional SC ventilation with a brick wall is also included in the comparison.

Figure 4-21 implies that the thermal mass shifts the starting point of warmer ΔT_{room} from 3 p.m. in the lightweight wall case to 9 p.m. in the thermal mass case. This could be one benefit offered by the SC-RC ventilation with thermal mass. It is better to have a warm indoor air temperature in the evening rather than in the afternoon because the latter has a higher ambient temperature than the former. Besides this shifting in the warm ΔT_{room} period, there is no noticeable difference in the daily average ΔT_{room} of the base case SC-RC ventilation with thermal mass and the SC-RC with light wall material. Only, the base case has a slightly better cooling performance (-0.30°C) compared to -0.29°C the case without thermal mass.

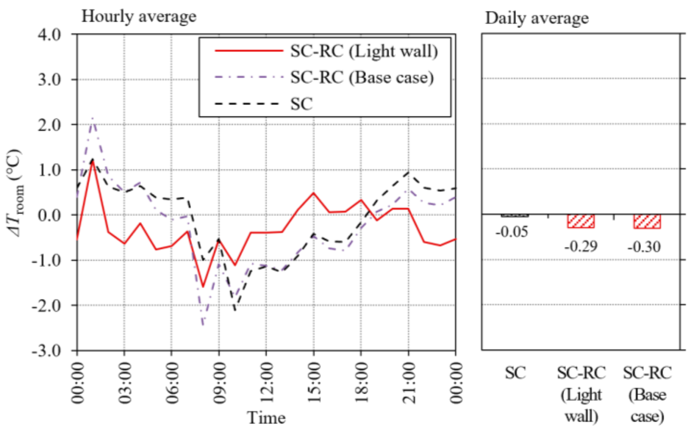

Figure 4-21 ΔT_{room} of SC-RC with different wall materials.

Moreover, regarding the ventilation performance, the SC-RC ventilation with thermal mass has a similar total ACH with the SC-RC with light wall material. Figure 4-22 shows that the discrepancy in the total ACH between the two cases is less than 0.1 ACH. Despite this similarity in total ACH, the flow pattern from the two cases is different. In the light wall SC-RC ventilation, the RC cavity flow rate peaks before noon and drops in the early evening. In the SC-RC ventilation with thermal mass, these maximum and minimum RC cavity low rates are shifted. The RC cavity maximum flow rate in the thermal mass case moves to 3 hours later (at 2 p.m.), and the minimum shifts to 6 hours later (at 3 a.m.).

Furthermore, due to its heat storage capacity, the thermal mass wall releases the daytime heat gain to the night. This heat release then makes the room warmer, and in turn, changes the flow tendency to be an upward flow. This upward flow tendency conflicts with the downward flow from the cool RC cavity air. Thus, the RC flow rate of the SC-RC ventilation with thermal mass becomes lower than the light wall case and consequently has a slightly lower daily ACH. Nonetheless, with only a minuscule difference in ACH and a better cooling effect, the long-lasting heavyweight wall might be more favoured over the lightweight wall in practice.

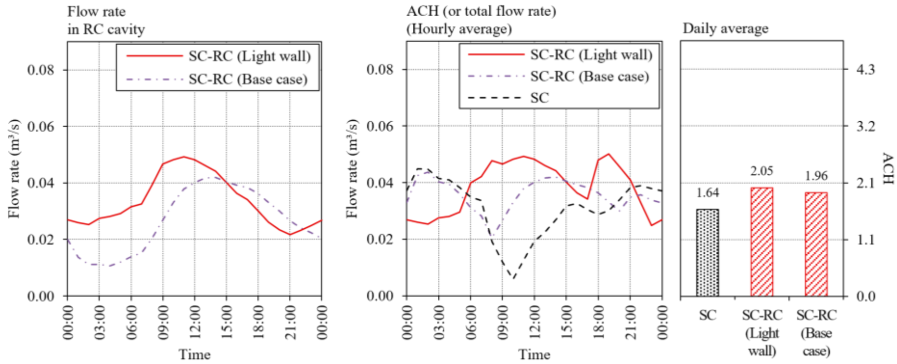

Figure 4-22 The RC cavity flow and the total flow rates of the SC-RC with different wall materials.

4.5.3 Effect of the RC cavity gap

A narrower RC cavity gap would provide a better condition for heat exchange between the RC emitter and the cavity air and would supply a cooler air temperature from the RC cavity. This is apparent in the ΔT_{room} data of different RC cavity gaps are shown in Figure 4-23. The RC cavity with a 10 cm width results in the coolest room with a daily average indoor air temperature at least 0.41°C lower than ambient. The cooling effect from the RC cavity diminishes as the RC cavity gap gets wider. However, the cooling performance of the SC-RC ventilation is still better (0.23°C lower) than the conventional SC ventilation even with a cavity gap of 30 cm.

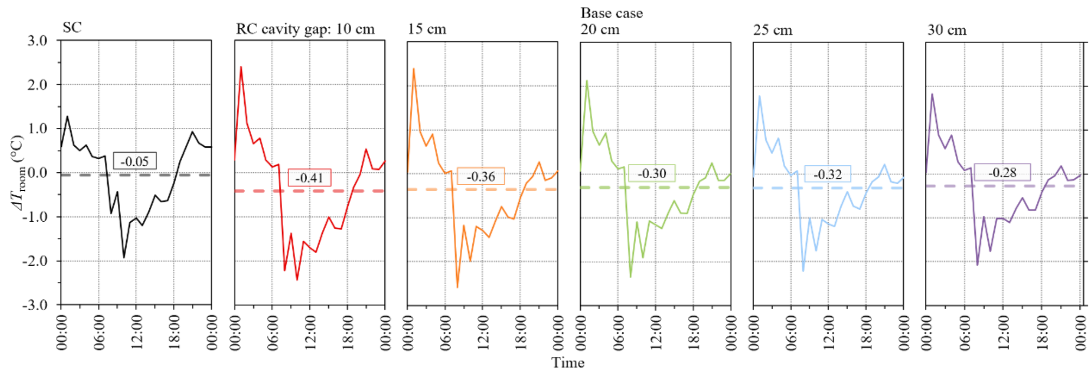

Figure 4-23 ΔT_{room} of SC-RC with different RC cavity gaps.

Although the cooling performance from the narrower cavity gap is appealing, the ventilation performance shows the opposite result. Figure 4-24 indicates that the flow rate through the RC cavity gradually increases with the wider cavity gap, and it is seen both in the hourly and daily average terms. The total ventilation rate also shows a similar trend with the RC cavity flow, with an average 0.14 ACH improvement per 5 cm gap enlargement. The widest gap studied, which is a 30 cm RC cavity, provides a 2.19 ACH. However, the narrowest cavity gap (10 cm) of the SC-RC ventilation only provides 1.65 ACH, or only 0.01 ACH better than the conventional SC ventilation.

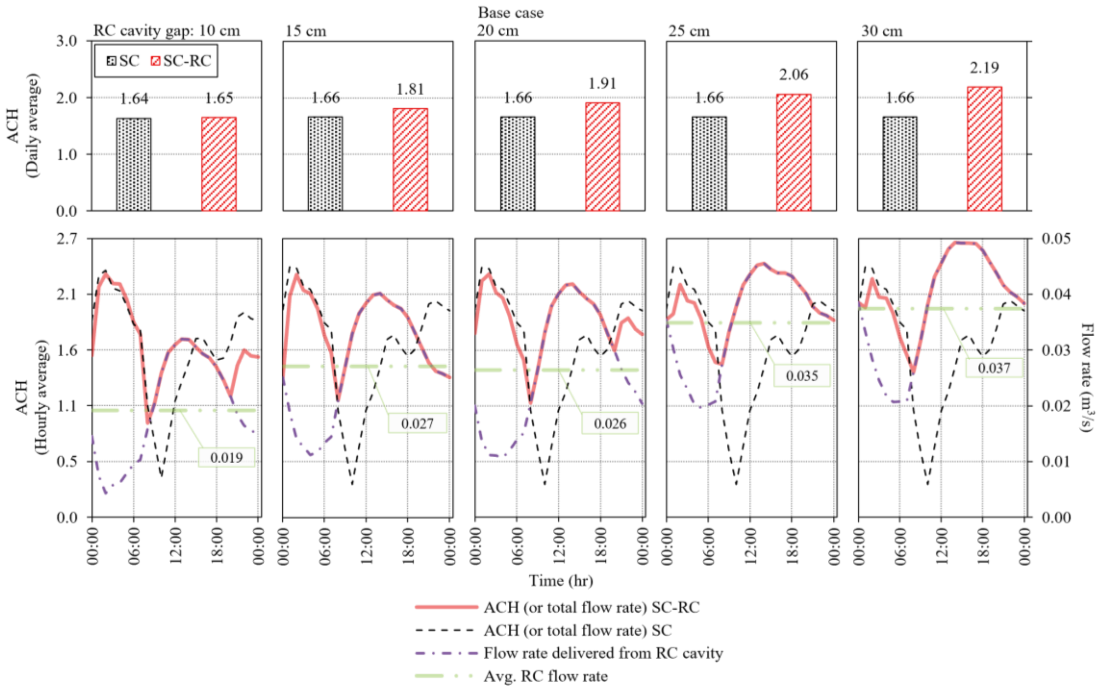

Figure 4-24 The RC cavity flow and the total flow rates of the SC-RC with different RC cavity gaps.

4.5.4 Effect of internal heat gains

Internal heat gains cause the indoor air temperature to increase. Figure 4-25 reveals the expected increase in ΔT_{room} as the internal heat gain increases. Nonetheless, analysis of the effect of various internal heat gains to ΔT_{room} to the performance of the SC-RC ventilation hints at the maximum condition in which the SC-RC still gives a sub-ambient ΔT_{room}. It is clear from the figure that conventional SC ventilation can only deliver sub-ambient daily average ΔT_{room} when there is no internal heat gain. On the other hand, SC-RC ventilation can achieve sub-ambient ΔT_{room} even at an internal heat gain of 4 W/m^2. The discrepancies of ΔT_{room} between the SC and SC-RC ventilations becomes larger in the higher internal heat gain condition, with -0.24°C ΔT_{room} gap in 0 W/m^2 to -0.29°C in 4 W/m^2.

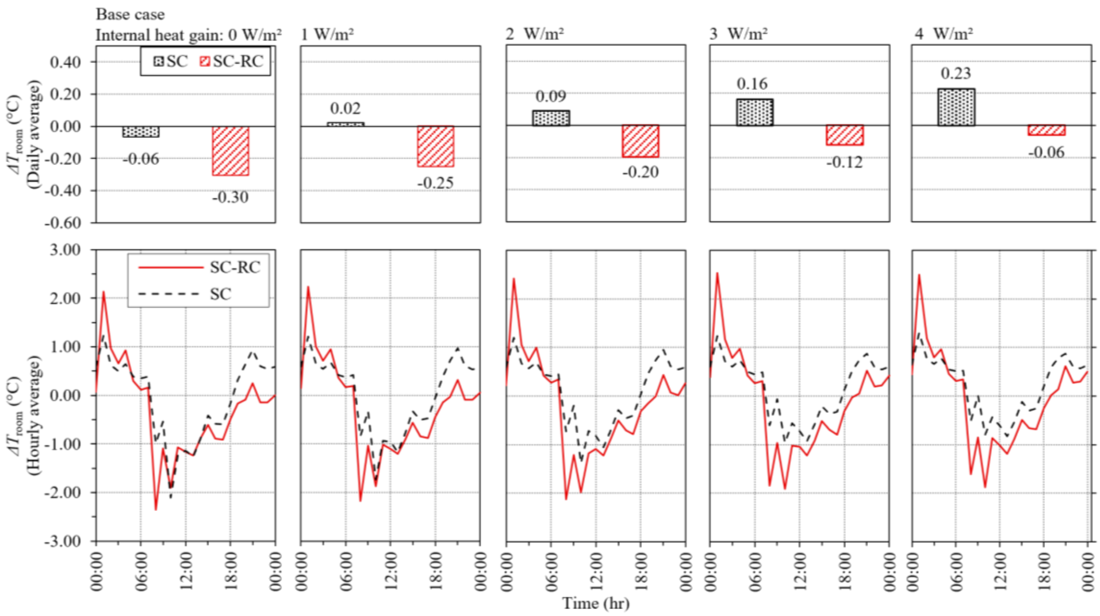

Figure 4-25 ΔT_{room} of SC-RC with different room's internal heat gains.

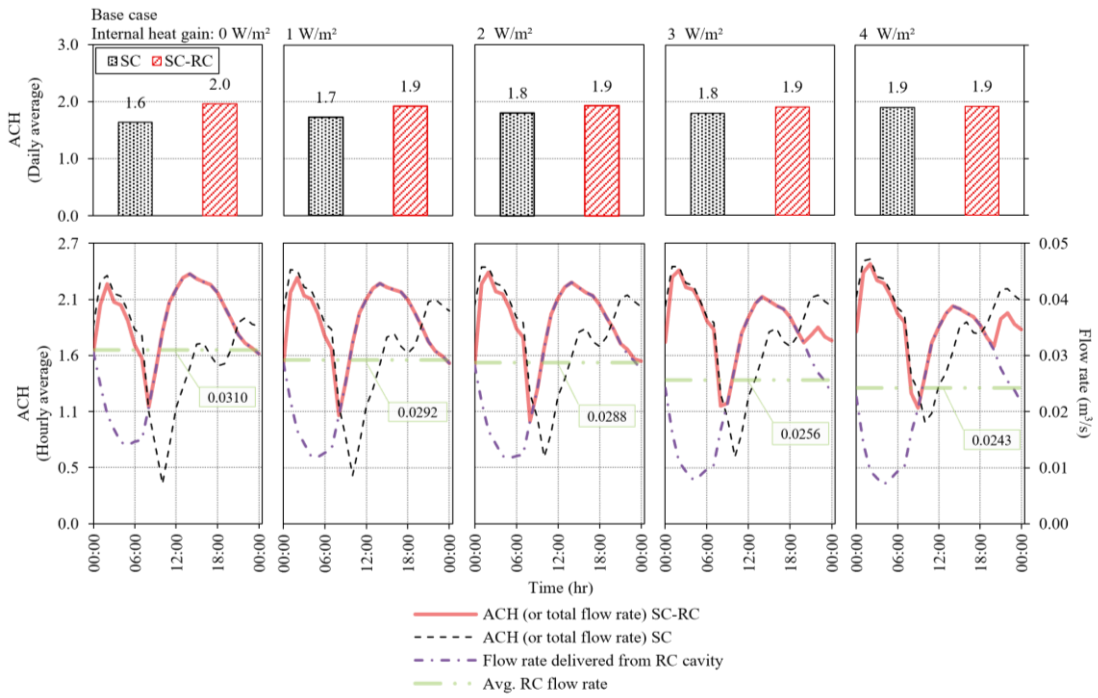

Figure 4-26 The RC cavity flow and the total flow rates of the SC-RC with different internal heat gains.

Moreover, Figure 4-26 implies when the internal heat gain increases, the RC cavity flow decreases. The figure shows a reduction of 0.008 m^3/s (8 L/s) in the daily average RC cavity flow rate between the 0 W/m^2 and the 4 W/m^2 internal heat gains. However, this reduction is too small to affect the total ACH. The total ACH is stable around the 1.9 ACH mark as the heat gain gets higher. This stable figure of ACH means that only the RC cavity's contribution to the overall ventilation rate is reduced, whilst the contribution of the SC increases with the raise of internal heat gains. It can be seen as the widening gap between the ACH line and the RC cavity flow line in the early evening in Figure 4-26. It thus follows that, at a certain value of internal heat gain (>4 W/m^2), the RC cavity will no longer be able to produce a downward flow, and instead become a channel for an upward flow.

4.5.5 Effect of climate conditions or geographical location

Among the five selected climates in this parametric analysis, three climates have dry conditions with high clear sky index such as the steppe climate (Lahore), the desert climate (Riyadh), and the temperate dry climate (Valencia). They are the place where the SC-RC ventilation works best as confirmed by Figures 4-27 and 4-28. In Figure 4-27, all climates seem to have a sub-ambient daily average ΔT_{room}, but with different hourly patterns. However, the ΔT_{room} is limited to be only around 0.7°C lower than ambient in both humid climates such as the tropical humid (Af) and the temperate humid (Cfa) climates. On the other hand, the ΔT_{room} can reach >2°C lower than ambient, with the lowest possible ΔT_{room} found in temperate dry (Valencia) climate. Although the temperate dry climate has the lowest ΔT_{room}, the desert and the steppe climates are more stable to give hourly sub-ambient room temperature (18 hours of sub-ambient ΔT_{room}). This makes the two climates obtain the coolest room with the daily average ΔT_{room} of -0.46°C for Lahore and -0.56°C for Riyadh, respectively.

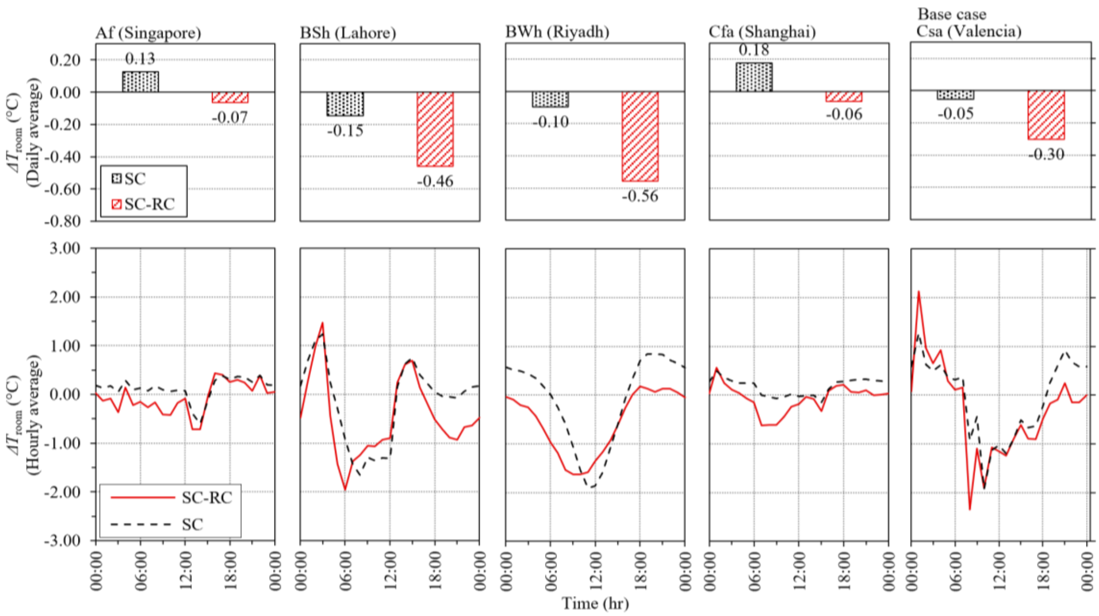

Figure 4-27 ΔT_{room} of SC-RC in different climates.

Like the cooling performance, the ventilation performance of the SC-RC ventilation is better in the three dry climates than in the humid regions (Figure 4-28). In tropical and temperate humid climates, the daily average ACH of the SC-RC ventilation is even lower than the SC ventilation. This inferior performance from the SC-RC ventilation in the humid regions can be explained using the data in Figure 4-27. It is seen in the figure that the ΔT_{room} for the SC ventilation in both tropical humid and temperate humid are positive, while their respective ΔT_{room} for the SC-RC ventilation are effectively zero. This is a supportive condition for an upward flow through the SC rather than a downward flow through the RC cavity.

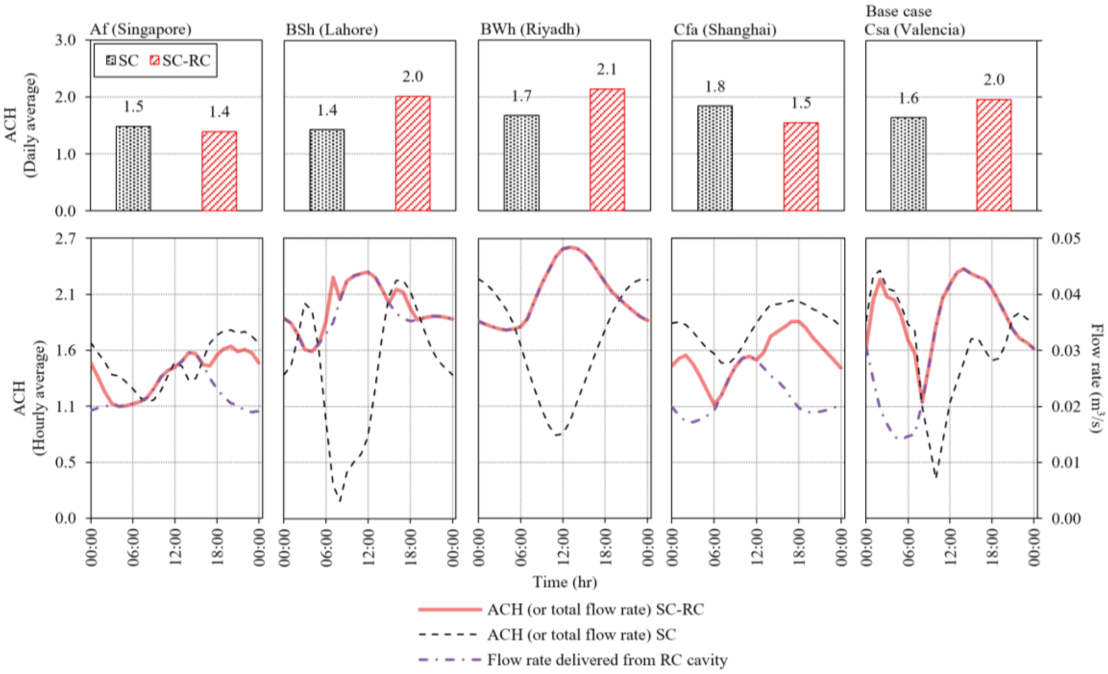

Figure 4-28 The RC cavity flow and the total flow rates of the SC-RC in different climates.

The previous analysis of the ventilation performance of the SC-RC ventilation indicates that this ventilation strategy may not be suitable for humid climates. In the three dryer climates the total flow rate of the SC-RC ventilation can exceed the conventional SC ventilation. The total ACH of the SC-RC ventilation in the steppe (Lahore), desert (Riyadh), and temperate dry (Valencia) climates are better than the conventional SC ventilation with improvements of 0.6, 0.4, and 0.4 ACH, respectively.

4.5.6 Effect of using a fan-assisted flow in the RC cavity

As previously mentioned, a fan can be used in the RC cavity when the cooling effect on the emitter is not sufficient for the downward flow. In the condition when the fan is used, one would expect to know the optimal volumetric flow rate from the fan to optimise the cooling effect from the RC emitter. Figure 4-29 reveals that the optimal RC flow rate to get the lowest ΔT_{room} varies between climate types. It is found that in climates in which SC-RC ventilation performs better than SC ventilation, adding a fan does not increase their cooling performance. It means that the naturally ventilated (NV) scenario of the SC-RC ventilation is the better option in the three dry climates (steppe, desert, and temperate dry). However, for the humid regions where the SC-RC ventilation performs worse than conventional SC ventilation, fan-assisted SC-RC ventilation can improve the cooling power of the RC cavity with 0.1°C ΔT_{room} reduction at the optimal fan flow rate of 0.05 m^3/s. In these two humid regions, the cooling performance is still slightly better than the NV scenario when the fan flow rate increased to 0.1 m^3/s. But a fan flow rate higher than 0.1 m^3/s will not be effective in providing sub-ambient ΔT_{room}.

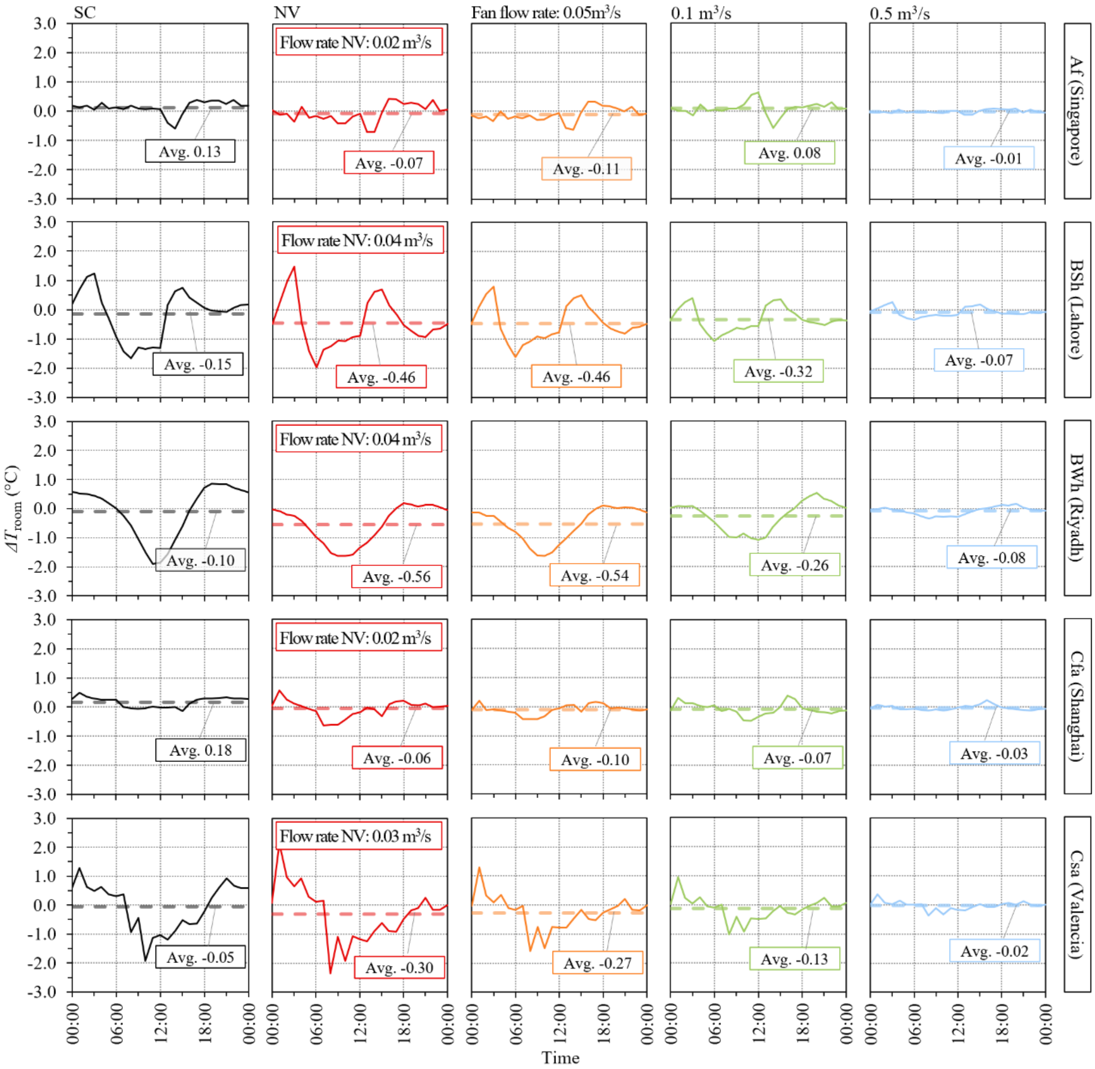

Figure 4-29 ΔT_{room} of SC-RC in different locations with different fan power.

4.6 Summary of Findings

In this chapter, a fully passive application of radiative cooling in buildings is proposed and analysed. The proposed concept is a combination of solar chimney (SC) ventilation with radiative cooling (RC) cavity and is thus named SC-RC ventilation. The SC-RC ventilation consists of a solar chimney on the south (sun-facing) side of the roof, and an RC cavity on the north side. Using CFD simulations in Ansys Fluent, the performances of the SC-RC ventilation applied in a case study building are evaluated. The evaluation is done with three scenarios that represent the conventional SC ventilation and two possible opening configurations for the SC-RC ventilation.

The simulation results show that the SC-RC ventilation has indeed better ventilation and cooling performance than the conventional SC. In terms of ventilation performance, the SC-RC+wall-opening scenario has a ventilation rate of 1.2 ACH, compared to the SC+wall-opening with 1 ACH. Also, the SC-RC+wall-opening configuration can maintain the ventilation performance at nighttime, when the conventional SC cannot even achieve the required minimum ACH. Regarding the cooling performance, the RC cavity can provide an average daily room temperature of 27.17 °C compared to the 27.45 °C room temperature from the conventional SC. Analysis of the hourly differences between the inlet and room temperature (ΔT_{inlet}) indicate that the SC-RC ventilation supplies chilled air into the room throughout the 24-hour period. The chilled air provided by the RC cavity is become apparent at night with inlet air temperature up to 4 °C lower than the room air temperature.

Moreover, this chapter also presents a parametric study on SC-RC ventilation. The influence of six factors or parameters on SC-RC ventilation is analysed. The first and second factors, namely the PE cover above the RC emitter and the thermal mass wall of the case study building have a positive effect on the ventilation and cooling performance of the SC-RC ventilation. The third factor or parameter is the width of the RC cavity. It is found from the investigation on this third parameter that the narrower width cools the ventilated air better but reduces the ventilation rate. This chapter suggested using a 20 cm RC cavity (similar to the width of the solar chimney) for optimal cooling and ventilation performance.

The fourth parameter is the building's internal heat gain. It is found that the internal heat gain decreases the cooling effect from the RC cavity. At a high internal heat gain the ability of the SC-RC ventilation to create a sub-ambient room temperature diminishes. Additionally, with the rise of internal heat gain, the flow from the RC cavity also weakens. Hence, at a very high internal heat gain, the RC cavity starts to produce an upward flow rather than a downward flow of chilled air.

Moreover, regarding the climate type, the parametric study finds that the dry climates of Lahore (steppe climate), Riyadh (desert climate), and Valencia (dry temperate climate) are the most suitable locations for the SC-RC ventilation. Especially in Lahore's and Riyadh's climates, the SC-RC ventilation provides better ventilation and cooling performance compared to other locations. The daily average room temperatures of the case study building in those two locations are 0.46 °C and 0.56 °C lower than ambient. Additionally, the ventilation rates in the two climates achieved 2.0 ACH in Lahore and 2.1 ACH in Riyadh. On top of that, in the climates where the SC-RC ventilation performs best, adding a fan may only increase the flow rate but also diminish the cooling capability of the RC cavity.

Nevertheless, there are some limitations to this study of the SCRC ventilation. First, the exclusion of internal heat gain and window, together with the use of 2D CFD simulation and exclusion of the wind effect on the ventilation flow, are made to simplify the ventilation flow and focus the study only on the buoyancy-driven flow induced by the SC and RC cavity. Also, it is important to note that in a real situation, when there is considerable wind speed, some internal heat gains, and solar fenestration through windows, the indoor temperature and flow pattern might be significantly different than those considered in our study.

Chapter 5 Incorporation of Switchable Solar Thermal and Radiative Cooling in Roof Solar Chimney for Adjustable Heating/Cooling in Ventilation

Architects prefer passive strategies for space cooling or heating because they can explore its implementation early in the design phase and the strategies are usually simpler than involving active mechanical devices. However, fully passive systems have drawbacks such as the unsteadiness of the natural resource used in the system, lower efficiency than the active system, as well as the mismatching between availability and demand (Etheridge, 2011; Pacheco, Ordóñez and Martínez, 2012). For instance, a Trombe wall as a passive heating strategy relies on the condition of high solar irradiance, so much so that when the sky is overcast, its effectiveness drops substantially. Its reliance on the sun also means it cannot supply heat during the cold night. Thus, relying on a building on fully passive design strategies might not be reliable in extreme or multi-seasonal climates. Combinations of passive design strategies and active devices offer more potential energy savings for buildings (Pacheco, Ordóñez and Martínez, 2012).

In this chapter, the first involvement of an active part in the implementation of radiative cooling in buildings is proposed and evaluated. If the fully passive radiative cooling system in Chapter 3 only works for cooling purposes, the system in Chapter 4 offers multi-seasonal heating and cooling functions. The proposed design still includes a solar chimney, not to generate ventilation flow, but rather for heating. The cooling effect is still provided by the radiative cooling cavity. The season-dependant heating and cooling functions are provided by a novel idea in the *switchable* feature of the absorber/emitter surface. The involvement of an *active* part is limited only to the use of a fan to draw into an air channel.

5.1 Reasoning of the Strategy

A multi-seasonal space heating-cooling device proposed in this chapter would be beneficial for a wider region since most of the world lives in climate conditions that need both heating and cooling (Klinger and Ryan, 2022). Using separate devices for space heating-cooling could double the installation and maintenance costs. Since the surge of energy-efficient buildings, attempts to design dual-functional space heating-cooling systems that are sustainable have been rising. The latest examples of combined heating and cooling systems are mostly developed from active systems such as air-conditioning or heat pump systems (Chen *et al.*, 2022; J. Wang *et al.*, 2023; Q. Wang *et al.*, 2023). Other common features are they also utilise solar energy as the sole renewable energy source for heating and cooling. The proposed systems thus can only directly utilise the sun for heating and electricity generation, whilst the cooling is provided by further mechanism. In the Wang et al. (2023) and Chen et al. (2022) systems, the cooling is provided by a heat pump that is made more efficient by circulating the heated air from the solar collector to the heat pump condenser (Chen *et al.*, 2022; J. Wang *et al.*, 2023). Yet, another mechanism to provide cooling is using a thermochemical process of a LiBr adsorption chiller (Q. Wang *et al.*, 2023).

All the systems above, however, heavily rely on active devices. More passive-dominant heating-cooling systems are also being developed by researchers. The following systems use either a fan or circulating pump only or both simultaneously. One of the simplest strategies that is currently studied is a kind of solar wall or Trombe wall (Solovyev, Ruipu and Phuong, 2021; Li and Cui, 2022). Utilising the heating from a solar wall can be done using air (Solovyev, Ruipu and Phuong, 2021) in which the air is circulated through the solar wall and directly blown to the room. It can also be a water system where the water is circulated through the solar façade and passed to a heat exchanger or stored in a water tank to be used when needed (Li and Cui, 2022). In terms of cooling, the solar wall works by becoming a buffer zone where excessive solar heat gain is removed by the circulating air or water (Solovyev, Ruipu and Phuong, 2021; Li and Cui, 2022). A more advance version of the solar wall, and yet still mostly passive system, involves PV to generate electricity and phase change material (PCM) to store the excess heating or cooling energy (Ke *et al.*, 2021). A different strategy of mostly passive heating-cooling systems is the earth-air heat exchanger (EAHE) (Ahmad and Prakash, 2022; Michalak, 2022; W. Yu *et al.*, 2022). The EAHE system benefits from the roughly constant temperature of the ground at a certain depth throughout the year. Hence when the outdoor air passes through the EAHE before it enters the room, its temperature changes to the thermal comfort range.

Nonetheless, none of the abovementioned strategies exploits radiative cooling as the mechanism to provide cooling. This is due to a stringent requirement for a radiative cooling emitter to have a very low solar absorptance to be able to provide cooling in the daytime. However, the fact that heating and cooling demands occur at different seasons means a single-purpose solar absorber surface would be useless during the cooling season. Similarly, a surface that is dedicated solely to a radiative cooling emitter would be a disadvantage for buildings in the heating season. This issue could be overcome by a surface that can switch between solar heating or radiative sky cooling functions.

The ideas for this switchable solar heating and radiative cooling surface have been investigated by many researchers (Pech-May and Retsch, 2020; Taylor et al., 2020; X. Liu et al., 2020; Hu, Zhao, et al., 2021; Jia et al., 2021; Kim et al., 2021; Butler and Argyropoulos, 2022; B. Zhao et al., 2022; Fei et al., 2022; Luo et al., 2022; X. Zhao et al., 2022). Based on the mechanism in which the spectral properties of the solar heating-radiative cooling are switched, the proposed materials and coatings can be classified into mechanically switched (Pech-May and Retsch, 2020; X. Liu *et al.*, 2020; Hu, Zhao, *et al.*, 2021; Butler and Argyropoulos, 2022; B. Zhao *et al.*, 2022), thermally switched (Taylor *et al.*, 2020; Jia *et al.*, 2021; Kim *et al.*, 2021; Designed Research; X, 2022; Fei *et al.*, 2022; Luo *et al.*, 2022), or electrically switched (X. Zhao *et al.*, 2022). However, because the research field of this switchable solar heating-radiative cooling surface is a newly emerging field, many investigations are conducted in the material stage only. One research by Hu et al. (2021b) aims for the application of such a switchable surface for solar and radiative cooling collectors. Another application of the switchable solar heating-radiative cooling surface study is done by Zhao *et al*. (2022), in which they apply the switchable mechanism for glazing materials, especially those used for skylight windows.

This chapter will discuss a novel utilisation of the switchable solar heating-radiative cooling surface. Regarding the switching mechanism, this thesis employs the mechanically switched surface, similar to what was previously used by Hu *et al*. (2021). This mechanical method of switching surfaces is considered simpler than the thermally and electrically switched surfaces.

Moreover, the switchable solar heating-radiative cooling surface in this study is coated as a solar absorber on one side and a radiative cooling emitter on the other side, and the sides could be switchable (rotatable) according to the season. The switchable surface is installed on a pitched roof in an air channel design similar to solar chimney ventilation, henceforth the name switchable solar chimney-radiative cooling ventilation (Switchable SC-RC ventilation) is used. Section 5.1 details the proposed concept and the mechanism by which it provides heating and cooling in different seasons. The Switchable SC-RC ventilation is hypothesised to be able to improve indoor thermal comfort, indicated by the reduction in unmet hours of a building. The rest of the chapter is dedicated to explaining the research methodology and discussing the results as well as summarising the insight from the proposed concepts.

5.2 Description of the Switchable SC-RC Ventilation

The Switchable SC-RC ventilation is a further development of the combination of the solar chimney with the radiative cooling cavity discussed in Chapter 3. The main modification is the switchable feature of the absorber/emitter surface. In this Switchable SC-RC ventilation, the two sides of the absorber/emitter surface have different absorptivity/emissivity characteristics. The absorber side has high solar absorptivity and low infrared emissivity, while the emissive side has high emissivity in the atmospheric window band (8-13 um) and low absorptivity in other bands. Another change is also made for the absorber location in the air channel. If in Chapter 2's SC-RC ventilation, the absorber is on the bottom side of the channel, the Switchable SC-RC puts the absorber on the top side of the channel. This is done to make an air gap between the absorber/emitter to a polyethylene cover, so the radiative cooling effect can be maximised.

Figure 5-1 below illustrates the schematic design of the Switchable SC-RC ventilation. A 20 cm air channel that covers the south to north sides of a gabled roof is devised to be the channel for the Switchable SC-RC ventilation. On top of this air channel is the switchable absorber/emitter surface, equipped with a 3 cm air gap above the surface. Covering the air gap is the polyethylene (PE) cover. The whole roof is 3 metres high with an inclination angle of 45°. The roof air channel has an intake fan on the south-facing side, and ceiling diffusers as the outlet to a room. The room is a 6 m by 6 m room with a ventilation outlet placed on the lower side of the north-facing wall. This is then set as the case study building. The 3-dimensional visualisation of the case study building is also shown in Figure 5-1.

Based on the description of the Switchable SC-RC ventilation above, compared to the conventional SC or RC ventilation, the proposed ventilation design has additional components that add up to the installation cost. The first additional cost is the coating for the radiative cooling emitter that makes the switchable surface bifacial. This could mean the coating expense for the Switchable SC-RC ventilation could be more than double that of the conventional SC or RC only. The second additional feature that increases the installation cost is the rotatable device that allows the switching between the surfaces.

Besides those additional installation costs, the Switchable SC-RC ventilation has also additional operational costs compared to the single-purpose SC or RC ventilation. This operational cost is for the control of the rotatable mechanism of the surface. Together, the installation and operational cost of the Switchable SC-RC are the trade-off for the potential savings from the Switchable SC-RC ventilation.

Moreover, Brick was used for wall material with 20 cm of thickness, along with ceramic, timber, and roof tile for floor, ceiling, and roof materials, respectively (Oikonomou and Bougiatioti, 2011). In the study of the effect of thermal mass on the ventilation flow, a comparison between a heavyweight brick wall and a 5-cm thick lightweight insulation board was made. Further, the absorber and emitter in the SC and RC cavity used aluminium with a thickness of 1 mm as its base, coated with a heating/cooling coating suited for its purpose. The solar absorber was coated with a high absorptivity in the solar radiation band (0.2-3 µm) and thermal radiation band (3-25 µm) coating, whereas the RC emitter was coated with a coating that has high emissivity only in the atmospheric window band (8-13 µm) and low absorptivity in solar (0.2-3 µm) and other thermal bands (3-8 µm and 13-25 µm). A PE film was used as the convection cover for the RC emitter and will be compared with a case study without a convection cover to see the effect of the PE cover on the ventilation flow. The spectral properties of the construction materials in those wavelengths and their respective thermal properties are summarised in Table 5-1. Except for the absorber and emitter, the emissivity for all materials was taken from the ECOSTRESS spectral library (Meerdink *et al.*, 2019).

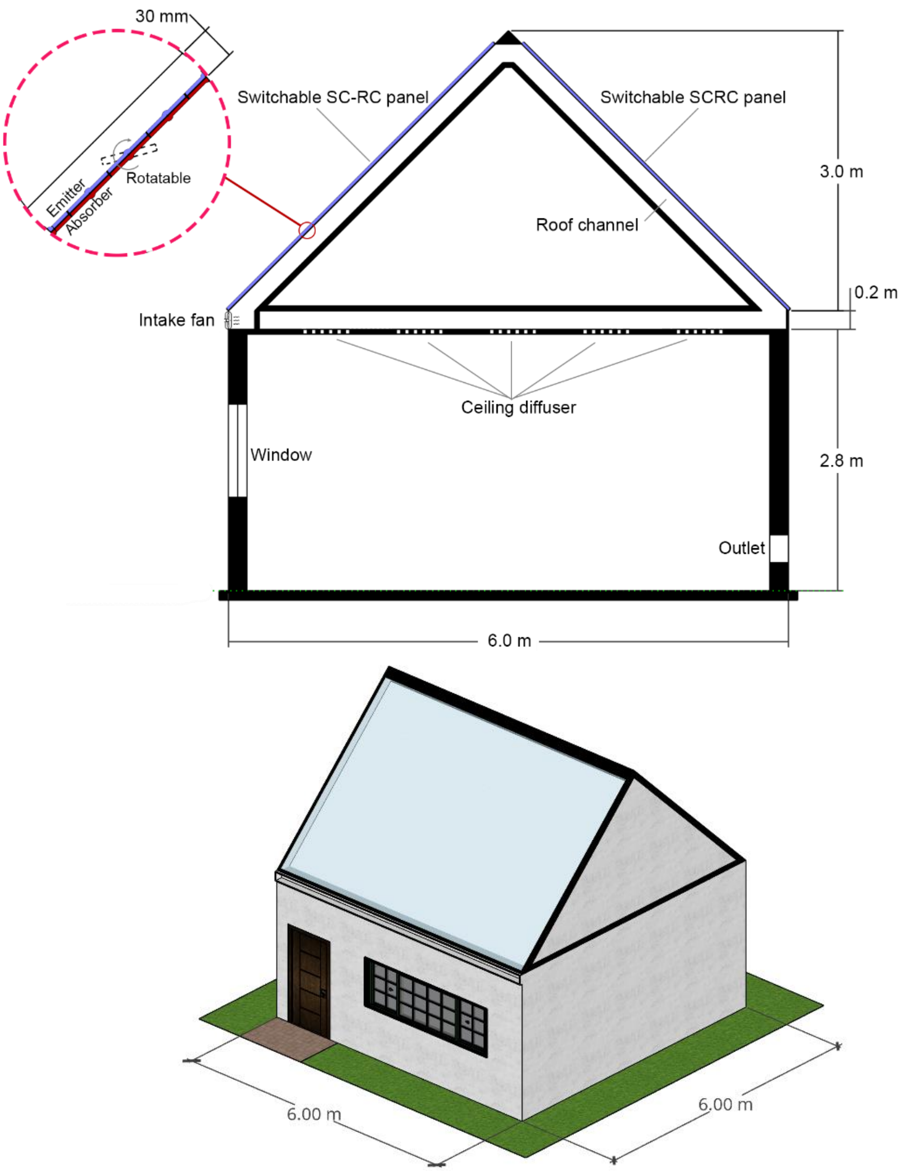

Figure 5-1 Geometry, dimensions, and the 3D visualisation of the case study building.

Table 5-1 Thermal and spectral properties of the construction materials.

Material	**Thermal properties**			**Absorptivity/emissivity**			
	Thermal conductivity ($W{\cdot}m^{-1}{\cdot}K^{-1}$)	Density ($kg{\cdot}m^{-3}$)	Specific heat capacity ($J{\cdot}kg^{-1}{\cdot}K^{-1}$)	0.2-3 μm	3-8 μm	8-13 μm	13-25 μm
Brick	0.72	1920	840	0.79	0.77	0.93	0.93
Ceramic tile	0.8	1700	850	0.34	0.94	0.93	0.93
Insulation board	0.033	38	1400	0.70	0.90	0.90	0.90
Roof tile	0.8	1890	880	0.87	0.93	0.95	0.95
Timber	0.16	720	1260	0.46	0.9	0.94	0.94
Absorber	202.4	2719	871	0.95	0.05	0.05	0.05
Glass	1.38	2203	703	0.05	0.88	0.88	0.88
Emitter	202.4	2719	871	0.05	0.05	0.95	0.05
PE film	0.45	910	1900	0.05	0.05	0.05	0.05

In the Switchable SC-RC design above, the outdoor air is drawn by an intake fan to the air channel. In the heating season, the absorptive part of the absorber/emitter surface faces upward to get the solar heating. The heated surface due to solar absorption then provides the heating to the air in the channel and further warms the room. In the cooling season, the emissive part of the absorber/emitter surface is turned upward to reflect as much solar radiation as possible and emit thermal radiation to the sky. With the radiatively cooled surface, the ventilation air will then be cooled and thus the room air temperature decreases. Figure 5-2 below shows the working schemes of the Switchable SC-RC ventilation.

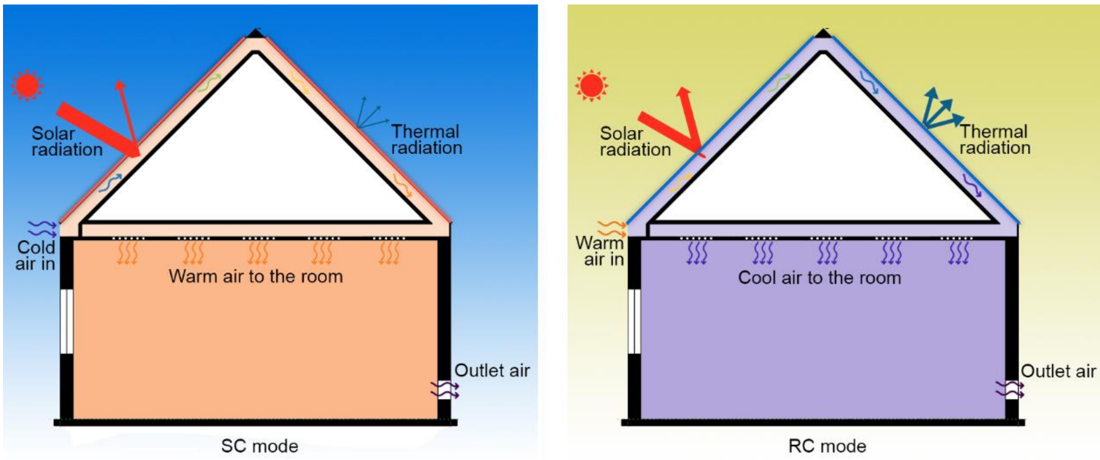

(a) (b)

Figure 5-2 Illustration of the working principles of the Switchable SC-RC ventilation in (a) heating and (b) cooling seasons.

5.3 Validation of the CFD and EnergyPlus models of the Switchable SC-RC Ventilation

The heating and cooling effects of the switchable panel were modelled in Ansys Fluent. These CFD simulations from Ansys Fluent provide the outlet temperature data from the Switchable SC-RC ventilation. These data were then fed to the EnergyPlus model of the case study building to be used in the calculation of the indoor operative temperature. The flow chart in Figure 5-3 summarises the general step in modelling the Switchable SC-RC ventilation. It is worth reiterating that the CFD only models the Switchable SC-RC ventilation part, that is the roof part of the case study building, as shown in Figure 5-4.

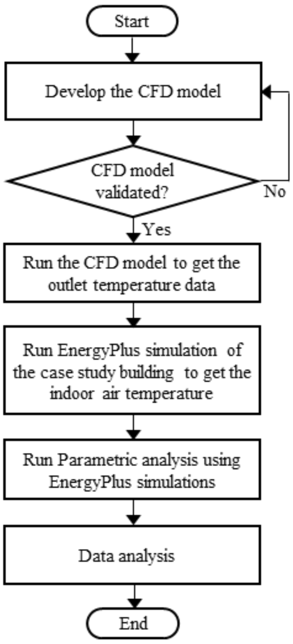

Figure 5-3 Simulation flow diagram.

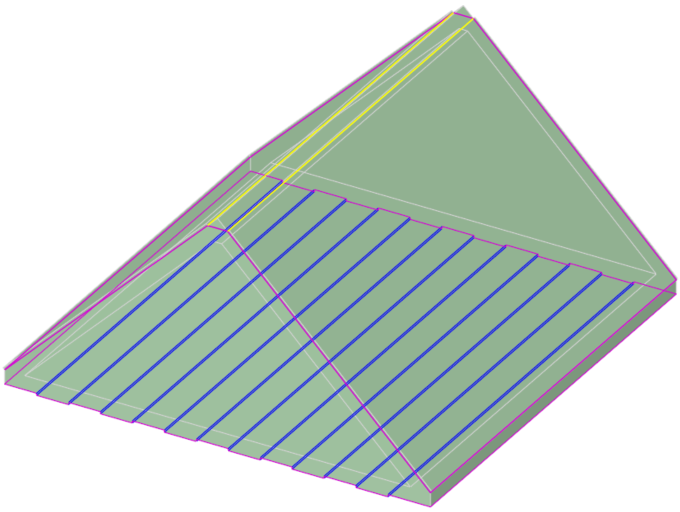

Figure 5-4 The computational domain of the CFD model of the Switchable SC-RC ventilation.

The coupling between the CFD model and the EnergyPlus model can be represented by the following mathematical model. For the case study building (with one thermal zone only) EnergyPlus employs the heat balance formula shown in Equation 5.1 to model the indoor temperature (LLC, 2022).

$$C_z \frac{dT_z}{dt} = \sum_{i=1}^{N_{sl}} \dot{Q}_i + \sum_{i=1}^{N_{surfaces}} h_i A_i (T_{si} - T_z) + \dot{m}_{\text{inf}} C_p (T_\infty - T_z) + \dot{Q}_{sys} \qquad 5.1$$

where:

$C_z \frac{dT_z}{dt}$ = energy stored in zone air = 0 for steady state condition

$$\sum_{i=1}^{N_{sl}} \dot{Q}_i = \text{the sum of the convective internal loads}$$

$$\sum_{i=1}^{N_{surfaces}} h_i A_i (T_{si} - T_z) = \text{convective heat transfer from the zone surfaces}$$

$\dot{m}_{\text{inf}} C_p (T_\infty - T_z)$ = heat transfer due to infiltration of outside air

$\dot{Q}_{sys}$= air system output

For this study, the air system output is the output of the Switchable SC-RC ventilation. The adjusted version of the $\dot{Q}_{sys}$ formula used in the EnergyPlus simulation is shown in Equation 5.2, where $\dot{m}$ and T_{outlet} are the mass flow rate and outlet temperature of the Switchable SC-RC ventilation, C_p is the specific heat capacity of the air, T_{indoor} is the indoor air temperature.

$$\dot{Q}_{sys} = \dot{m} C_p (T_{\text{outlet}} - T_{\text{indoor}}) \quad 5.2$$

The T_{outlet} above is where the results from CFD simulations are inputted into the EnergyPlus model. The outlet air temperature results from the Switchable SC-RC ventilation calculated by the CFD model as explained in Chapter 3Before validating the CFD model of the Switchable SC-RC ventilation, a grid independence study was conducted. Results from several grid sizes were compared as shown in Figure 5-5. As shown in the figure, the result starts to be stable at a mesh size of 2 cm (mesh number 21800). The differences between ΔT results from 2 cm to 1.5 cm and 1.5 cm to 1 cm are 1% and 2% respectively, indicating mesh-independent results between them. Hence, this study uses a 1 cm mesh size in the simulation.

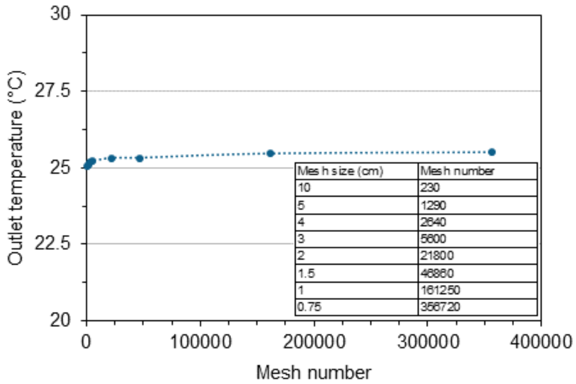

Figure 5-5 Comparison of hourly pattern of (a) indoor air temperature, (b) volume flow rate through the SC opening, and (c) indoor air velocity resulting from the different grid and time step sizes.

5.3.1 Validation of the CFD model

The remodelling of an experimental study by Wu *et al.* (2023) provides the validation of the CFD model of the Switchable SC-RC ventilation. The experiment investigates the effect of aspect ratio and wind velocity on a Trombe wall performance. The Trombe wall used in the experiment is 1.46 m high, and 0.5 m wide, with an air channel of 20 cm (Wu, Wu and Xiao, 2023). Figure 5-6 below depicts the experimental settings from Wu *et al*. (2023). Although the experimental rig is supposed to represent a Trombe wall, the structure of the air channel and the inclusion of the heated plate and fan that blows the air in the inlet at the bottom of the channel resemble the air channel of the Switchable SC-RC ventilation. The differences between the Wu *et al*. (2023) experiment with the Switchable SC-RC ventilation are only in the inclination angle and the length of the air channel.

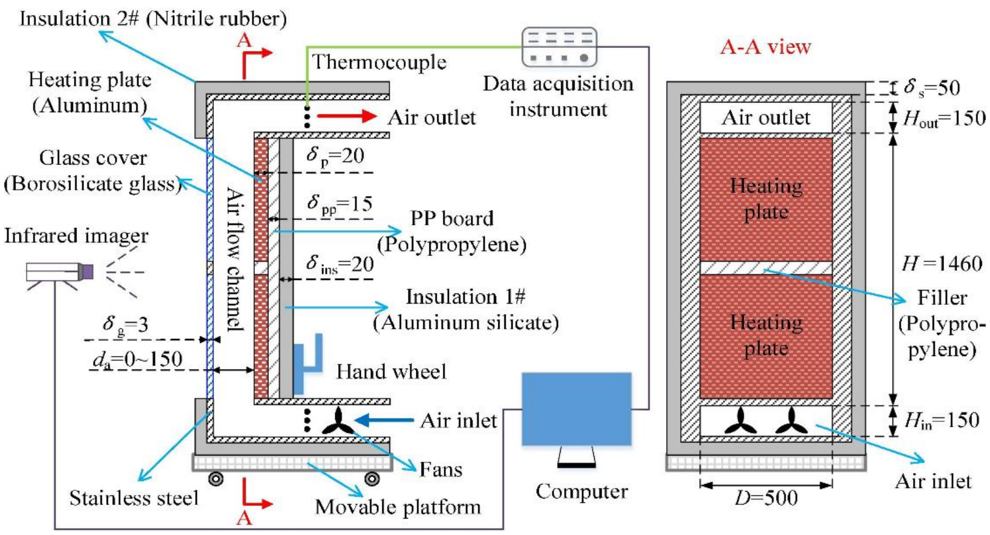

Figure 5-6 Experimental rigs from Wu *et al*. (2023).

To represent the solar absorption, the experiment employs a heated wall in which the heat flux level can be varied accordingly. The comparison between the experimental data from Wu *et al.* (2023) and the CFD model of this study is shown in Figure 5-7. The differences between outlet temperature from the Trombe wall with the ambient temperature (ΔT) from various inlet wind speeds are plotted. To further verify the CFD model, experimental data for three wall heat flux levels are also included. Overall, the ΔT profiles resulting from the simulation show a close agreement with the experimental data for all wall heat flux levels. The RMSD value for all three heat flux levels is 2.5%.

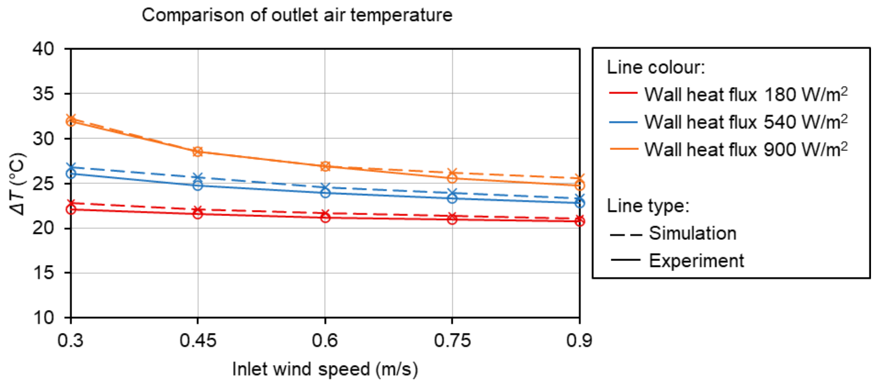

Figure 5-7 Comparison of experimental and simulation results.

The validation above was conducted with a 3D geometry. Undoubtedly, simulating the Switchable SC-RC ventilation with 3D geometry is a better representation of the real transport phenomena than a 2D geometry. However, using the 3D model for whole-year simulations with sub-hourly time step size is time- and resource-consuming. Thus, a comparison of 3D and 2D simulation results for the Switchable SC-RC ventilation to check whether a 2D model is sufficient for the whole year simulation. The comparison is done using transient simulation for a typical summer day in Rome. The outlet temperature data in Figure 5-7a shows no substantial differences between the 3D and 2D models of the Switchable SC-RC ventilation. Yet, a further comparison of the ΔT implies that attention should be made when ΔT is sub-ambient because the 2D model seems to overestimate the cooling performance of the Switchable SC-RC ventilation. Nevertheless, the average discrepancy of ΔT between the 3D and 2D models is only 0.07°C, indicating a comparable result between the two models.

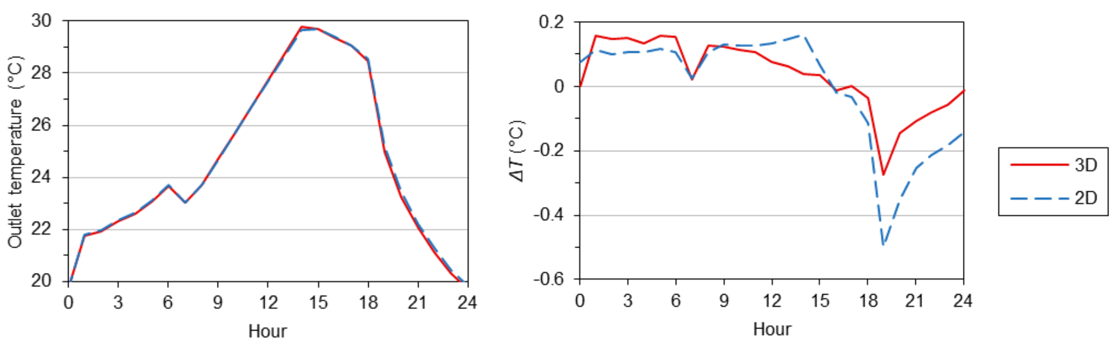

(a) (b)

Figure 5-8 Comparison between the (a) outlet temperature and (b) ΔT from the 3D and 2D simulations of the Switchable SC-RC ventilation.

5.3.2 Validation of the EnergyPlus model

To validate the EnergyPlus model of the case study building used in the Switchable SC-RC ventilation evaluation, the building from the EnergyPlus comparative testing report (BESTEST) was used (Henninger, Witte and Crawley, 2004). The building is a single-room building with geometry dimensions as shown in Figure 5-9. The building resembles the case study building of the Switchable SC-RC ventilation but differs only in the dimension. Furthermore, the comparison of the EnergyPlus results with the data from various energy simulation models is shown in Figure 5-10. As seen in the figure, the EnergyPlus model is capable of providing comparable results with the provided data from the report.

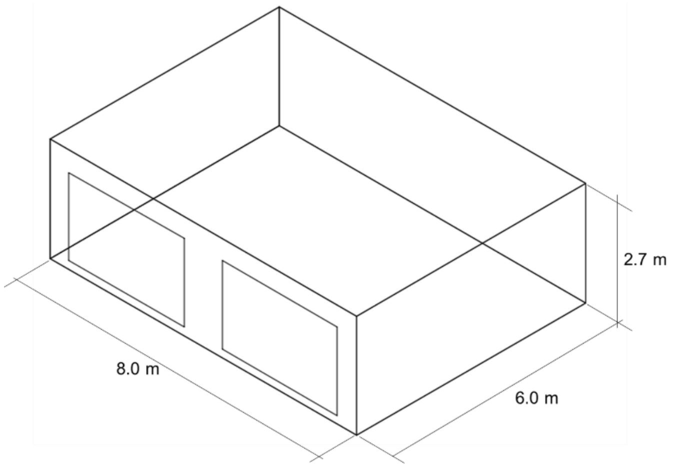

Figure 5-9 The geometry and dimensions of the BESTEST building.

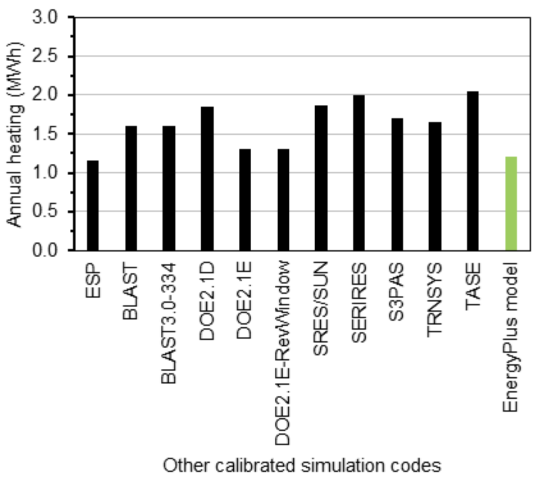

(a)

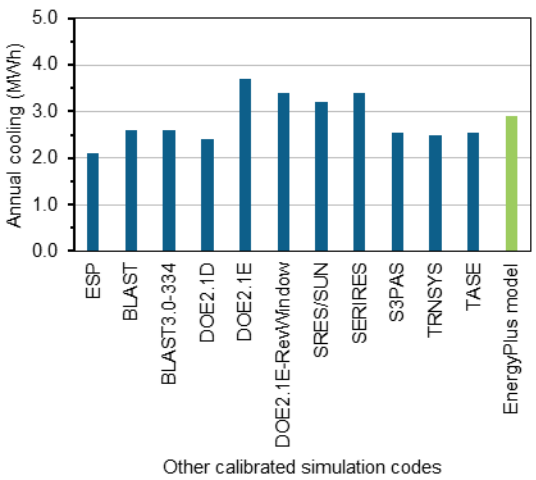

(b)

Figure 5-10 Comparison between the EnergyPlus results with other simulation codes for (a) Annual heating load, and (b) annual cooling load.

5.4 Heating and Cooling Performance of the Switchable SC-RC Ventilation

5.4.1 Performance Comparison Between the Conventional SC, RC, and Switchable SC-RC Ventilations

Multi-seasonal capabilities of the Switchable SC-RC ventilation should be tested in comparison with the one-functional SC and RC ventilation. To do that, a case study location with heating/cooling seasons and relatively dry air with many clear-sky days was selected. With its Mediterranean climate, characterised by warm temperate, dry, and hot summer (Kottek *et al.*, 2006), Rome is selected as the case study location. Figure 5-11 illustrates the climate condition of Rome by summarising several weather parameters from the Typical Meteorological Year (TMY) data of the city (Lawrie and Crawley, 2022). Figure 5-11 shows that Rome has a high solar irradiance level and also a wide gap between the sky and ambient temperature, two prerequisites for Switchable SC-RC ventilation.

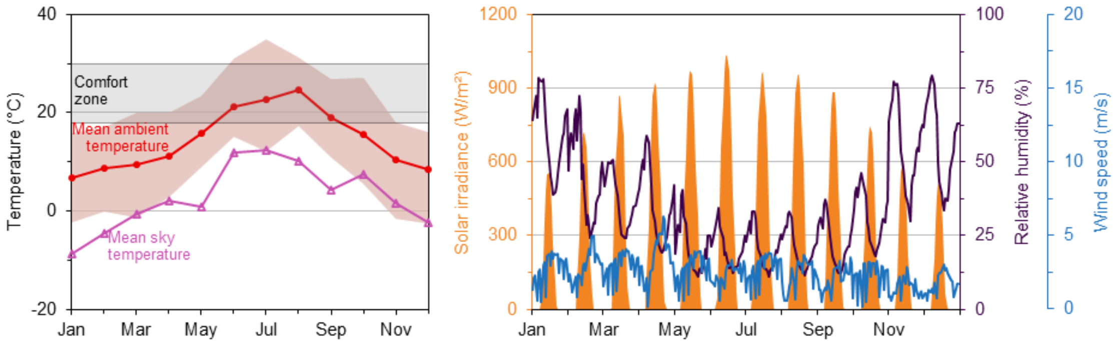

Figure 5-11 The ambient temperature, wind speed, and global solar irradiance on the hottest day in Rome (EnergyPlus, 2021).

The TMY data of Rome provides the environmental parameters of the typical winter and summer days, such as the ambient and sky temperatures, solar irradiance, and wind speed data. The typical winter and summer days represent the heating and cooling seasons and are thus appropriate for evaluation of the performance comparison between the conventional SC, RC, and Switchable SC-RC ventilations. From the ambient temperature (T_{amb}) data, one can derive the comfortable temperature (T_{c}) in Rome with Equation 5.3 (Humphreys and Nicol, 2000; Nicol and Humphreys, 2002).

$$T_{\mathrm{c}} = 13.5 + 0.54T_{\mathrm{amb}} \quad 5.3$$

Maximum and minimum of the comfortable temperature range are calculated using Equation 5.1 from the average ambient temperature of the typical summer and winter days respectively. A comparison of the outlet temperature from the SC, RC, and Switchable SC-RC ventilations is shown in Figure 5-12. The comfortable temperature range is overlaid on each graph in Figure 5-12. On a typical winter day in Rome (Figure 5-12a), the SC and SC-RC ventilation can provide warmer-than-ambient outlet temperatures. However, the outlet temperatures from both ventilations only reach the comfortable limit in around 3 hours in the afternoon. Yet, these SC and Switchable SC-RC performances in the typical winter days are superior to the RC ventilations. The outlet temperature of RC ventilation is far below the acceptable temperature range for the whole day.

On the other hand, on a typical summer day, it is the RC ventilation that prevails with outlet temperature mostly in the range of comfortable limit. Only 2-3 hours in the daytime the outlet temperature from the RC ventilation lies outside the comfort range (Figure 5-12b). The Switchable SC-RC ventilations also perform similarly to the RC ventilation, leaving the SC ventilation as the least preferable ventilation strategy during the summer. Figures 5-12a and 5-12b demonstrate the multi-seasonal advantage of the Switchable SC-RC ventilation compared to the other two conventional strategies.

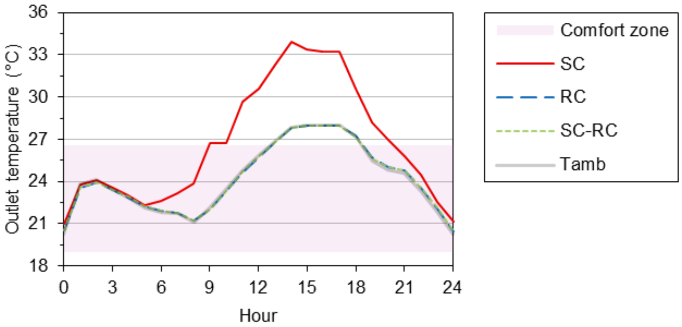

(a)

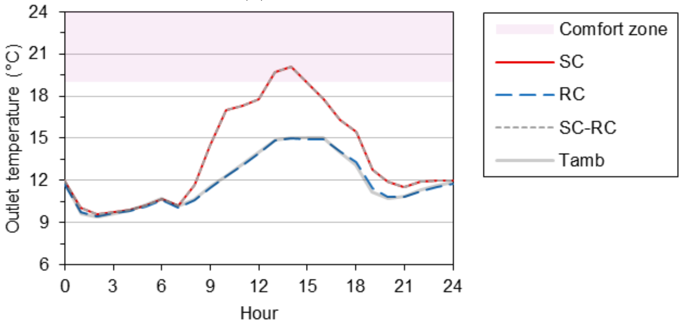

(b)

Figure 5-12 Comparison of the outlet temperature from the SC, RC, and Switchable SC-RC at: (a) typical winter day, and (b) typical summer day.

5.4.2 Unmet Hours of the Switchable SC-RC Compared to the Base Case Study Building

Moreover, the indoor air temperature (T_{ind}) resulted from the EnergyPlus simulations are assessed based on the comfortable temperature range. There are two other key indicators used in this assessment, namely the unmet hours due (hot) and unmet hours (cold), which are represented in Equation 5.4 below. The case study building without the Switchable SC-RC ventilation (base case) is compared with the building with Switchable SC-RC ventilation.

$$Unmet\ hours \begin{cases} hot\ hours = number\ of\ hours\ when\ T_{\mathrm{ind}} > T_{\mathrm{c}} \\ cold\ hours = number\ of\ hours\ when\ T_{\mathrm{ind}} < T_{\mathrm{c}} \end{cases} \quad (5.4)$$

Figure 5-13 summarises the hourly room temperature data as well as the number of unmet hours for both too-hot and too-cold conditions. From Figure 5-13 below, it is clear that during the winter the case with Switchable SC-RC ventilation shows higher room temperatures, shown by the warmer position of the dashed blue line compared to the red line (Figure 4-10a). The coldest room of the base occurs at 7 a.m. on the 24th of January with a temperature of 16.8°C. Meanwhile, the Switchable SC-RC ventilation can provide 17.2°C at the same time. On the contrary, the Switchable SC-RC ventilation creates lower room temperature during the summer. The hottest room temperature in the summer is 28.3°C in the afternoon on the 18th of August. At the same time, the case with Switchable SC-RC ventilation has a room temperature of 27.8°C.

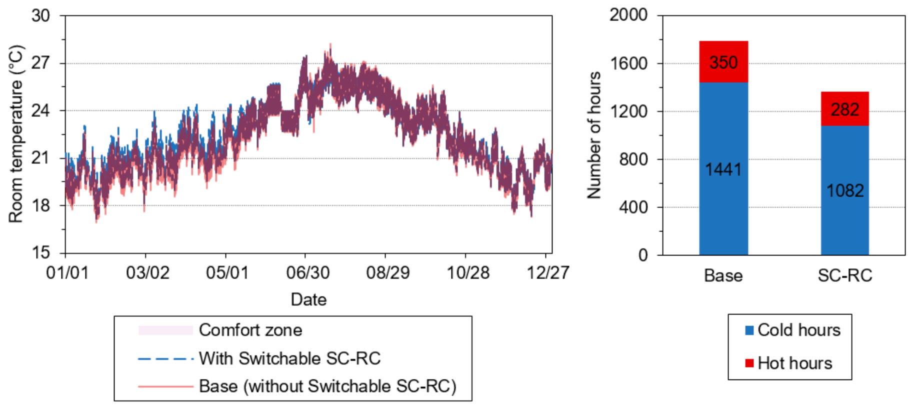

Figure 5-13 The hourly room temperature and the unmet hours data.

These two expected conditions from the Switchable SC-RC ventilation also prove to be able to enhance the room temperature to be in the thermal comfort range. As Figure 5-13 indicates, the hourly room temperature of the base case lies outside the comfort zone for a much longer period compared to the case with Switchable SC-RC ventilation. Consequently, the unmet hour (hot) and the unmet hour (cold) of the Switchable SC-RC ventilation case are a few hundred times less than the base case. In a year, the total unmet hour (hot) and unmet hour (cold) or the base case are around 1441 hours and 350 hours respectively. Whereas, the unmet hour (hot) and unmet hour (cold) or the Switchable SC-RC ventilation case are around 1082 hours and 282 hours respectively, an additional 429 comfortable hours without using the HVAC system.

5.5 Effect of Various Passive Design Strategies on the Switchable SC-RC Ventilation Performance

Several passive design strategies can enhance the performance of the Switchable SC-RC ventilation, with some strategies being more effective for heating and others for cooling. To evaluate the impact of these strategies on creating a comfortable indoor environment, this chapter analyses four passive design techniques. Additionally, the base case (that is, the case without Switchable SC-RC ventilation) from each passive strategy is also plotted for comparison.

5.5.1 Effect of the wall's U-value

The first commonly applied passive design strategy to be investigated in combination with the Switchable SC-RC ventilation is the U-value of the wall. By reducing the wall's U-value, heat transfer between the indoor and outdoor environment can be minimized, resulting in a consistent room temperature in both hot and cold conditions. Thus, using a small U-value is the recommendation for buildings in various climate conditions, especially cold climates. As depicted in Figure 5-14, the differences in the numbers of hot and cold hours annually are lesser with the smaller wall's U-value.

Furthermore, Figure 5-14 also illustrates the impact of various wall U-values on Switchable SC-RC ventilation. The figure compares different U-values with and without the Switchable SC-RC ventilation and shows that the Switchable SC-RC ventilation improved the building's thermal comfort by reducing the number of unmet hours even at a very high wall's U-value (50W/m^{2}K). Although larger U-values still offer some benefit to room thermal comfort when combined with the Switchable SC-RC ventilation, the reduction in unmet hours is not as significant as with a smaller U-value. This is because for the high wall's U-value, the outdoor conditions' effect on the room temperature is more significant, and thus heating or cooling provided by the SC-RC ventilation contributes less. Therefore, combining a smaller U-value with the Switchable SC-RC ventilation is recommended to achieve the best results with fewer unmet hours, as annotated in the data table under the graph in Figure 5-14.

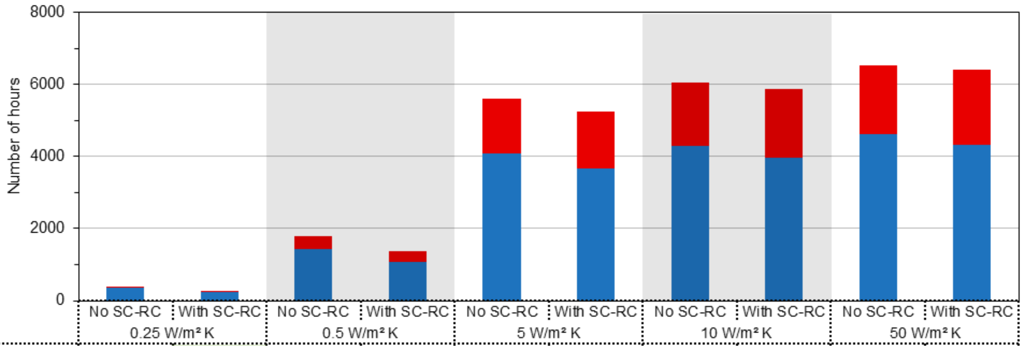

	0.25 W/m² K		0.5 W/m² K		5 W/m² K		10 W/m² K		50 W/m² K	
	No SC-RC	With SC-RC	No SC-RC	With SC-RC	No SC-RC	With SC-RC	No SC-RC	With SC-RC	No SC-RC	With SC-RC
Total unmet hours	379	264	1791	1364	5604	5236	6068	5864	6541	6404
■ Hot hours	17	10	350	282	1508	1554	1768	1884	1915	2085
■ Cold hours	362	254	1441	1082	4096	3682	4300	3980	4626	4319

Figure 5-14 Effect of various wall's U-values on Switchable SC-RC ventilation performance.

Furthermore, a detailed analysis of the reduction in unmet hours for both too-cold and too-hot conditions provides insight into the optimal effect of the Switchable SC-RC ventilation. For the smallest U-value, the wall's contribution is greater than that of the Switchable SC-RC ventilation, as indicated by 115 hours of total reduction compared to 368 for a U-value of 5 (Figure 4-12). However, as previously mentioned, the large U-values may be too thermally transparent to the outdoor condition thus reducing the effectiveness of the Switchable SC-RC ventilation. Starting from the wall's U-value of 5 W/m²K, the number of unmet hours (hot) is worse in the case study with the Switchable SC-RC ventilation. This again emphasises the combination of the Switchable SC-RC with the lower U-value, as well as implies the resilience of the SC-RC ventilation for heating rather than for cooling.

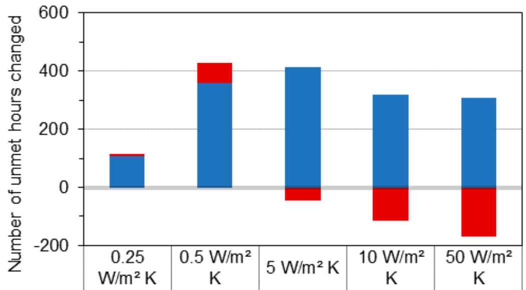

	0.25 W/m² K	0.5 W/m² K	5 W/m² K	10 W/m² K	50 W/m² K
Total reduction	115	427	368	204	137
■ Reduction in hot hours	7	68	-46	-116	-170
■ Reduction in cold hours	108	359	414	320	307

Figure 5-15 Reduction in unmet hours due to the Switchable SC-RC ventilation for various wall's U-values.

5.5.2 Effect of window's orientation

Another design consideration that can affect a building's heat gain is the window's orientation. With the 0.2 window-to-wall ratio of the case study building, the influence of the window's orientation on the effectiveness of the Switchable SC-RC ventilation is studied. Generally, for Rome's latitude, the south-facing window is preferable, because it harnesses the power of the sun more than the other window's orientation. This is especially needed for the heating season, but for the cooling season, the opposite north-facing window might be more beneficial. Figure 5-16 confirms this by showing the unmet hours of the case studies without the Switchable SC-RC ventilation. Indeed, the unmet hours (too hot) for the north window are fewer than that of the south window, with the indoor temperature lying above the comfortable limit of 251 hours for the north window compared to 350 hours for the south window. Yet, consistent with the common notion, the south window has the fewest unmet hours annually.

Considering the finding above, it is expected that the Switchable SC-RC ventilation performs best when combined with the south-facing window. As Figure 5-16 also summarises, using the Switchable SC-RC ventilation with south south-facing window improves the thermal comfort condition of the base case by reducing the total unmet hours to 1,364, followed by the east direction with 1,474 hours. But, when the contribution of the unmet hour (too hot) and unmet hour (too cold) are separated, one can again see that the north window is preferable for cooling, whilst the south window is better for heating. Moreover, the west is the least beneficial direction for the window's orientation since it produces more unmet hours than the other directions.

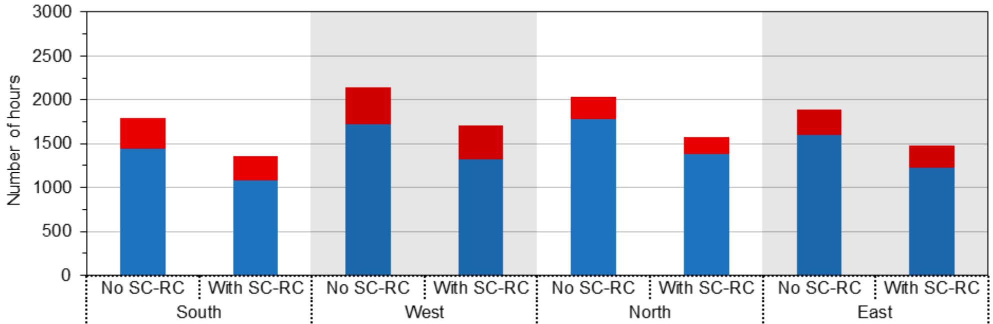

	South No SC-RC	South With SC-RC	West No SC-RC	West With SC-RC	North No SC-RC	North With SC-RC	East No SC-RC	East With SC-RC
Total unmet hours	1791	1364	2144	1711	2030	1580	1891	1474
Hot hours	350	282	420	391	251	200	297	247
Cold hours	1441	1082	1724	1320	1779	1380	1594	1227

Figure 5-16 Effect of different window orientations on Switchable SC-RC ventilation performance.

Furthermore, limiting the analysis to see the effect of the Switchable SC-RC gives an interesting insight into the heating and cooling performance of the novel ventilation strategy. It is clear from Figure 5-16 that the west window has the most unmet hour (hot) with 420 hours, and the north window has the most unmet hour (too cold) with 1,779 hours. When the Switchable SC-RC ventilation is involved, one would expect the biggest reduction in unmet hour (too hot) and unmet hour (too cold) from these two orientations. the window's orientation with the most unmet hour (too hot) and unmet hour (too cold). However, Figure 5-17 shows that the heating and cooling power of the Switchable SC-RC ventilation can only optimally reduce each unmet hour (too hot) and unmet hour (too cold) not for the worst, but rather for the second worst window orientation. The south window which has an annual 350 uncomfortably hot hours, can reduce its too hot hours by 68 hours using the Switchable SC-RC ventilation. Similarly, the west window with 1724 uncomfortably cold hours annually, can have a 440 too-cold hours reduction with the Switchable SC-RC ventilation. Nonetheless, summing up the reduction in unmet hour (too hot) and unmet hour (too cold) hints that the Switchable SC-RC ventilation contributes more when used for a building with north north-facing window.

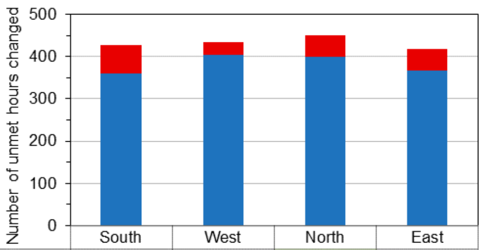

	South	West	North	East
Total reduction	427	433	450	417
Reduction in hot hours	68	29	51	50
Reduction in cold hours	359	404	399	367

Figure 5-17 Reduction in unmet hours due to the Switchable SC-RC ventilation for different window orientations.

5.5.3 Effect of the window-to-wall ratio (WWR)

The third design aspect, which is widely recognised as an effective way to passively control the thermal environment of a building is the window-to-wall ratio (WWR). Selecting the optimal WWR is a balancing act between increasing the daylight intensity and limiting the solar heat gain or building heat loss. Small WWR means smaller daylight intensity, solar heat gain, and building heat loss, and vice versa. In the heating season with long nights, it is preferable to prevent heat loss from the building, hence a small WWR. Likewise, in the cooling season, a smaller window has lower solar heat gain than a larger one. With a south-facing window, Figure 5-18 shows that smaller windows indeed have fewer unmet hours annually. As seen in the figure, the 0.1 WWR is shown to be the most comfortable among the base without Switchable SC-RC ventilation with a total of 1,613 hours. When combined with the Switchable SC-RC ventilation, the thermal comfort performance of the 0.1 WWR is even better with 1,181 hours, a 432 reduction in the annual unmet hours.

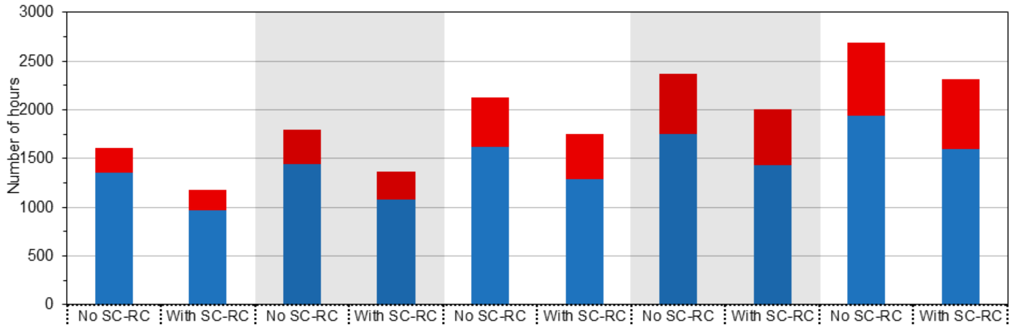

	No SC-RC WWR 0.1	With SC-RC WWR 0.1	No SC-RC WWR 0.2	With SC-RC WWR 0.2	No SC-RC WWR 0.3	With SC-RC WWR 0.3	No SC-RC WWR 0.4	With SC-RC WWR 0.4	No SC-RC WWR 0.5	With SC-RC WWR 0.5
Total unmet hours	1613	1181	1791	1364	2131	1753	2366	2009	2687	2319
Hot hours	262	212	350	282	515	469	610	572	744	722
Cold hours	1351	969	1441	1082	1616	1284	1756	1437	1943	1597

Figure 5-18 Effect of various WWR SC-RC ventilation performance.

To be more specific on the unmet hour reduction due to the Switchable SC-RC ventilation, a separate plot is given in Figure 5-19. From Figure 5-19, the total unmet hour reduction by the Switchable SC-RC ventilation is found when combined with the lowest 0.1 WWR. The heating power of the Switchable SC-RC ventilation in the cold seasons contributes the most to this total unmet hour reduction with 382 cold hours improved to be more comfortable. This is because the minimal heat loss provided by the small WWR value helps the Switchable SC-RC ventilation to deliver heating more efficiently. When looking at the cooling effect only, this small window with 0.1 WWR is also preventing more solar heat gain, and thus the lowest hot hours by the 0.1 WWR seen in Figure 5-18 is mostly the contribution of the WWR rather than the Switchable SC-RC ventilation. The contribution of the Switchable SC-RC ventilation for cooling optimally occurred when combined with the 0.2 WWR, as shown in Figure 5-19. WWR larger than 0.2 limits the cooling power of the Switchable SC-RC ventilation as they have a higher amount of solar fenestration into the building.

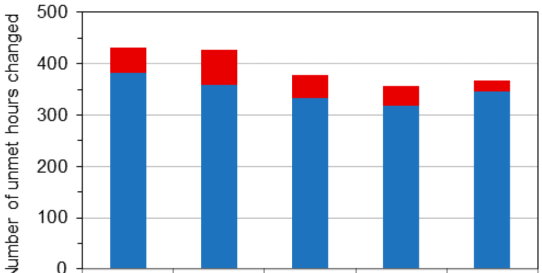

	WWR 0.1	WWR 0.2	WWR 0.3	WWR 0.4	WWR 0.5
Total reduction	432	427	378	357	368
Reduction in hot hours	50	68	46	38	22
Reduction in cold hours	382	359	332	319	346

Figure 5-19 Reduction in unmet hours due to the Switchable SC-RC ventilation for various WWRs.

5.5.4 Effect of shading device

The shading device is a common feature used by architects to protect buildings from excessive solar fenestration and is among the simplest passive cooling techniques. If the overhang projection factor (OPF), that is the ratio of the shading device's length to the window's length, is too large, its solar prevention feature, might be a disadvantage for heating in winter. Therefore, there is usually an optimal OPF, so the shading device still blocks direct sunlight during the summer when the sun's altitude is high, and lets it enter during the winter when the sun's altitude is low. This optimal OPF is undoubtedly related to the altitude of the building's site or location.

In the case of this case study location, Rome, latitude 41°N, the optimal OPF for a south-facing window of the case study building is between 0.3 and 0.5. As seen in Figure 5-20, with an OPF of 0.3, the total unmet hour is 1,742 hours, while with an OPF of 0.5, it is 1,752 hours. Detailed looks at separate hot and cold hours show that lower OPF means worse cooling (more hot hours), while higher OPF means worse heating (more cold hours). The Switchable SC-RC ventilation is able to reduce the unmet hours in all the base cases. The lowest total annual unmet hours were found in the combination of Switchable SC-RC ventilation with 0.3 OPF shading device, with 1,294 unmet hours, very close to the OPF 0.5 shading device with 1,295 unmet hours.

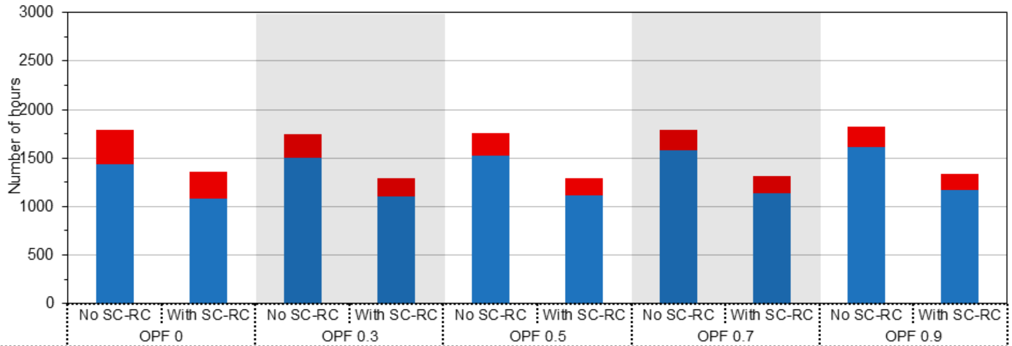

	No SC-RC (OPF 0)	With SC-RC (OPF 0)	No SC-RC (OPF 0.3)	With SC-RC (OPF 0.3)	No SC-RC (OPF 0.5)	With SC-RC (OPF 0.5)	No SC-RC (OPF 0.7)	With SC-RC (OPF 0.7)	No SC-RC (OPF 0.9)	With SC-RC (OPF 0.9)
Total unmet hours	1791	1364	1742	1294	1752	1295	1793	1311	1821	1341
Hot hours	350	282	245	194	222	179	215	175	209	172
Cold hours	1441	1082	1497	1100	1530	1116	1578	1136	1612	1169

Figure 5-20 Effect of the shading device on Switchable SC-RC ventilation performance.

Figure 5-21 displays a closer look at the contribution of the Switchable SC-RC ventilation on the unmet hour reductions. As previously discussed, the lower OPF creates more hot hours and higher OPC creates more cold hours. The base conditions provide the chance for the Switchable SC-RC ventilation to contribute more if the heating and cooling effectiveness stays the same for all OPF values. This may be the case as observed in Figure 5-21. The reduction in hot hours due to the Switchable SC-RC ventilation contribution is at best for the 0 OPF. Whereas the reduction in cold hours due to the Switchable SC-RC ventilation contribution is at best for the 0.9 OPF. Also, because the total of unmet hours is the worst in the 0 OPF, the number of unmet hour reductions due to the contribution of Switchable SC-RC ventilation alone was found for this shading device. Nevertheless, despite this contribution from the Switchable SC-RC ventilation, the 0 OPF shading device cannot help to provide the most thermally comfortable room, especially compared to the optimal options between 0.3 and 0.5 OPF.

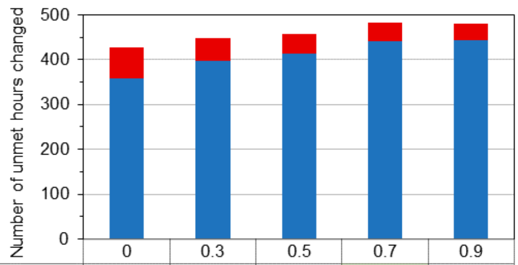

	0	0.3	0.5	0.7	0.9
Total reduction	427	448	457	482	480
Reduction in hot hours	68	51	43	40	37
Reduction in cold hours	359	397	414	442	443

Figure 5-21 Reduction in unmet hours due to the Switchable SC-RC ventilation for various OPFs.

5.6 Summary of Findings

The first proposal to combine radiative cooling with solar technology in buildings in this thesis is a fully passive system. Nonetheless, fully passive systems may not always be reliable, especially when faced with high heating and cooling loads as well as the multi-seasonal nature of the loads. This thesis offers to introduce little by little active devices into the integration of radiative cooling with solar technologies in buildings. In this chapter, the involvement of a fan as the only active device in a combination of solar chimneys and radiative cooling has been discussed.

The proposed design includes a solar chimney-like channel, but now the traditional absorber is changed with a switchable absorber/emitter surface, and a PE cover is added on top of the switchable surface. This switchable feature of the surface offers a novel idea of a season-dependent heating and cooling air channel. It is called Switchable solar chimney-radiative cooling (SC-RC) ventilation. A multi-seasonal space heating-cooling strategy such as this Switchable SC-RC ventilation would be beneficial for a wider region since most of the world lives in climate conditions that need both heating-cooling.

A comparison of the Switchable SC-RC with one-functional SC and RC ventilations demonstrates the superiority of the former. On typical winter and summer days in Rome, the outlet temperature results from the Switchable SC-RC ventilation simulations show the multi-seasonal flexibility of the ventilation. On a typical winter day in Rome, the SC and Switchable SC-RC ventilation can provide warmer-than-ambient outlet temperature while the outlet temperature of RC ventilation is far below the acceptable temperature range during the whole day. On the contrary, on a typical summer day, the SC and Switchable SC-RC ventilations prevail with outlet temperature mostly in the range of comfortable limit, while the SC ventilation supplies too hot air for the room.

Besides the clear advantage when compared to single-functional SC or RC ventilation above, the thermal comfort assessment between the base case with the Switchable SC-RC ventilation case also shows a promising result. This is indicated by the reduction in unmet hours, namely the number of hours in which the indoor temperature is not comfortable. Annually, the unmet hours of the Switchable SC-RC ventilation case are 429 hours fewer than the base case. Additionally, a parametric study of the potential combination of the Switchable SC-RC ventilation with other passive heating and cooling techniques was also conducted. It is found that the Switchable SC-RC works optimally with the lower wall’s U-values, a south-facing window, the smaller window-to-wall-ratios, and the shading device with a 0.3-0.5 projection factor.

Chapter 6 Combination of a Diurnal Solar Thermal and Nocturnal Radiative Cooling Collector with HVAC for Building Energy Saving[3]

The previous two chapters have explored the integration of radiative cooling with solar chimney ventilation. This chapter discusses another integration of radiative cooling with another type of solar energy application in buildings. Recall that, in Chapter 2 as well as in the previous chapter, the introduction of radiative cooling into a solar heating device can extend the working time of the device throughout the night, or even throughout the cooling season. In this chapter, that benefit is also exploited to improve the performance of a solar collector.

6.1 Reasoning of the Strategy

The background behind this integration is the unanticipated need for cooling in the temperate and cool climate regions. Extreme heat waves accompanied by record-breaking hot temperatures occur every other year (Nasa Earth Observatory, 2022; USA Today, 2022). With more frequent and hotter heatwaves predicted in the future (Brown, 2020), the need for cooling in buildings in temperate climate regions surges (Farahani *et al.*, 2021). Thus, adjustments to the current heating system to also support the unaccustomed cooling demand are required.

Buildings in the aforementioned regions could easily rely on conventional heating, ventilating, and air conditioning (HVAC) to provide heating and cooling in one device. However, the HVAC system is a big contributor to the building's energy consumption and is harmful to the environment (Pérez-Lombard, Ortiz and Pout, 2008; Chua *et al.*, 2013). It is responsible for 63% of annual energy consumption in a typical EU house (Eurostat, 2022) and 77% of the world's fluorinated greenhouse gas emissions (Climate Change Committee, 2020). In this context, renewable space heating and cooling technologies are therefore the preferred solutions to fulfil the recent thermal comfort requirements.

[3] Part of this chapter's content is submitted as a research article, and is under review, in *Energy and Buildings*

The most common technique used in renewable space heating devices is the utilisation of heat from the sun. Among the solar-based space heating devices are the solar collector (Zhang and Zhu, 2022), solar walls (SolarWall, 2022), and solar windows (Hoffman *et al.*, 1983; Dawood, Jalil and Ahmed, 2022). The working principles of these solar heating devices are substantially the same, that is to use a material with high solar absorptivity to absorb as much heat during the day. To prevent heat losses from the absorber to the ambient air, it is usually protected using a glass cover.

Mechanisms used to provide space cooling more sustainably include cooling via wind convection, water evaporation, and radiative sky cooling. The wind-driven cooling is manifested in the form of a wind catcher that can direct the ambient wind to the indoor environment to promote air movement inside (Santamouris, 2012). Meanwhile, the cooling mechanism via evaporation of water is realised by passing the ambient air through a water system (a pond, a water spray, a heat-exchanger, *etc*.) before it enters a building (Basit *et al.*, 2021; Rasheed *et al.*, 2022). Yet another mechanism to cool a building is radiative sky cooling that, as reviewed in Chapter 2, can be used to cool the building envelope directly or through thermal carriers (Fan and Li, 2022; Hu, Zhao, Suhendri, Ao, *et al.*, 2022).

Nevertheless, all the previously mentioned renewable heating and cooling systems are separate systems. If a building needs both heating and cooling, two devices would be required for each function, and this could be costly. For instance, a solar collector only delivers heat and only works during the day. Yet, a building's heating and cooling demands vary throughout the year depending on the season. This means that the solar collector is useful roughly only for half of the year in the heating season. Likewise, a separate renewable space cooling system would be needed for the cooling season, and hence work only half of the year as well. Therefore, a device that offers both renewable space heating and cooling would be more seasonally adaptive and more cost-effective in terms of installation and maintenance.

From the example above, the solar collector is indeed a potential candidate to be such a device if the absorber and glass cover of the collector are modified accordingly. The absorber of a solar collector has very high absorptivity in the solar band (0.2-3 μm) but low emissivity in other radiation bands. If the absorber is made to be emissive in the atmospheric window band (8-13 µm), it also can be employed as a nocturnal radiative cooling emitter. Figure 6-1 illustrates the characteristics of the spectral properties of an ideal solar thermal-radiative cooling absorber/emitter. It should be noted that, to make a continuation of the abbreviation in the next chapter and to avoid a similar abbreviation with the SC-RC in the previous chapters, here the solar thermal-radiative cooling collector is abbreviated as PT-RC (from photothermal-radiative cooling).

Moreover, the glass cover that prevents the solar absorber surface from convective heat loss is transparent for solar radiation but opaque for infrared radiation and thus blocks the surface's radiation to the sky. For this reason, the cover must also be changed with a material that has high transmissivity in both solar and atmospheric window bands, usually a polyethene (PE) film (Bathgate and Bosi, 2011; Hu, Suhendri, *et al.*, 2021b).

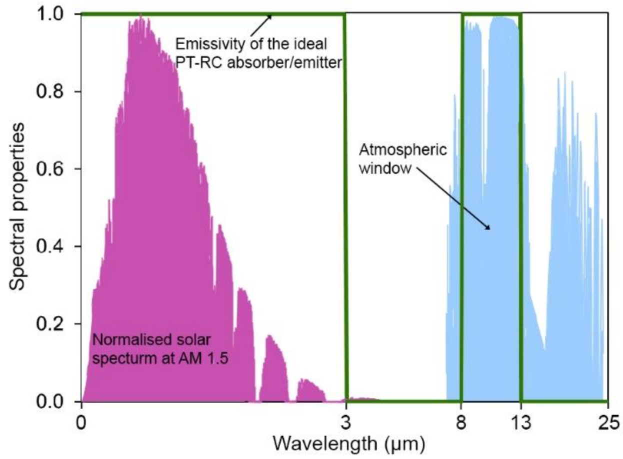

Figure 6-1 The ideal spectral properties of the PT-RC absorber/emitter.

In this chapter, the evaluation of the proposed dual-functional PT-RC collector idea in terms of its heating and cooling performance is discussed. This chapter also explains the adaptability of the PT-RC collector in different seasons compared to the mono-functional solar heating (SH) and RC collectors. In addition to that, a parametric study involving various environmental, structural, and operational conditions of the PT-RC collector is also presented in the incoming sections.

To better understand its impact when applied to buildings, a case study where an array of PT-RC collectors is integrated into a house building was also devised. The case study building is chosen from the test house of the International Energy Agency's (IEA) Energy in Buildings and Communities (EBC) programme (IEA-EBC Annex 58)

(Strachan, Svehla, Kersken, *et al.*, 2016). Thus, the case study provides a way to estimate the energy-saving potential of the PT-RC collector when installed onto a building roof. Three cities, each with different climate types, are selected to be the case study locations. All the abovementioned analyses are conducted using computational fluid dynamics (CFD) and EnergyPlus simulations.

6.2 Description of the PT-RC collector and the Case Study Building

6.2.1 The PT-RC collector

As briefly mentioned before, the PT-RC collector is a modified version of a solar collector, and it consists of an absorber/emitter, a convection cover, and insulation. The absorber/emitter has a length of 1960 mm in length, a width of 964 mm, and a thickness of 0.4 mm. Above it, there is a 40 mm air gap and the PE film is the convection cover with a thickness of 6 μm. Below the absorber is a 30 mm air duct where the collected air passes through. Under this air duct is a 40 mm insulation board. The insulation board also covers the side of the air gap and the air duct, with a thickness of 25 mm (see Figure 6-2). The air inlet and outlet are located at the ends of the air duct.

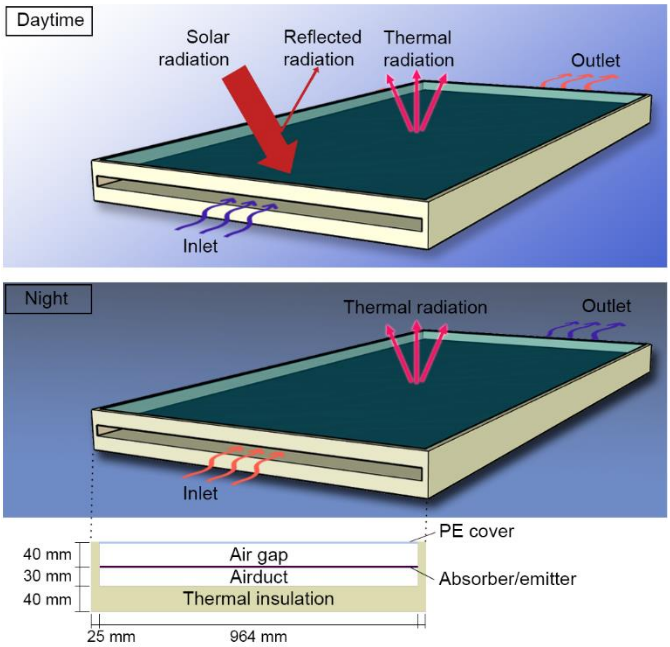

Figure 6-2 Illustration of the air-based PT-RC collector.

The material developed by Zhao *et al.* (2020) is used as the PT-RC absorber/emitter material. It has a 0.92 absorptivity in the solar radiation band and a 0.84 emissivity in the atmospheric window band. Other thermal and spectral properties of the materials of the collector are detailed in Table 6-1. For comparison, the conventional solar absorber material (Hu, Zhao, Suhendri, Cao, *et al.*, 2022a) and RC emitter material (Li *et al.*, 2021) are also included in Table 6-1.

Table 6-1 Thermal and spectral properties of the materials.

Material	Thermal properties			Absorptivity/emissivity			
	Thermal conductivity (W·m^{-1}·K^{-1})	Density (kg·m^{-3})	Specific heat capacity (J·kg^{-1}·K^{-1})	0.2-3 μm	3-8 μm	8-13 μm	13-25 μm
SH absorber	202.4	2719	871	0.92	0.17	0.09	0.06
RC emitter				0.04	0.27	0.78	0.59
PT-RC absorber/emitter				0.92	0.51	0.84	0.54
PT-RC ideal				0.92	0.05	0.84	0.05
PE film	0.45	910	1900	0.05	0.05	0.05	0.05
Insulation board	0.042	38	1400	0.70	0.90	0.90	0.90

6.2.2 The building-integrated PT-RC collector

The building-integrated system of the PT-RC collector consists of an array of 5 collectors mounted on the pitched roof of the building and integrated with the HVAC system. When integrated with the HVAC system, the PT-RC collectors offer possible working modes as shown in Figure 6-3. The first mode is when the outdoor air is in the comfortable temperature range, in which the ambient air is directly drawn into the room and the room air is directly exhausted outside (Figure 5-3a). The second working mode is the HVAC-only mode, *i.e.*, when the outdoor air is too cold or too hot and needs heating or cooling, but the PT-RC collector works in opposition to the outdoor condition (Figure 5-3b). This condition occurs, for instance, in the winter nights (the PT-RC collector works as a cooling source) or summer noon (the PT-RC collector acts as a heating source). The third mode is when the PT-RC collector assists the HVAC system by being a precooling or preheating device to the outdoor air (Figure 5-3c). It is in the third mode that the PT-RC collector contributes to the energy saving of buildings.

To assess the energy-saving potential of the building integrated PT-RC, a case study building needs to be devised. However, the heating and energy consumption of single-room buildings like those in Chapters 4 and 5 do not sufficiently represent the energy consumption of a normal 4-occupant house building. Fortunately, there is a benchmark building developed by IEA-EBC Annex 58 that can be used as the case study building (Strachan, Svehla, Kersken, *et al.*, 2016). The house building has a south-facing facade, a 10 m by 10 m floor plan, and 1 living room, 2 bedrooms, 1 kitchen, and 1 bathroom.

All rooms have window access to the outdoor environment. Figure 6-4 visualises the case study building with the integrated PT-RC collector on the roof. Five PT-RC collectors are connected in parallel with a total area of 9.43 m^2 to supply the pre-heated or pre-cooled air accordingly.

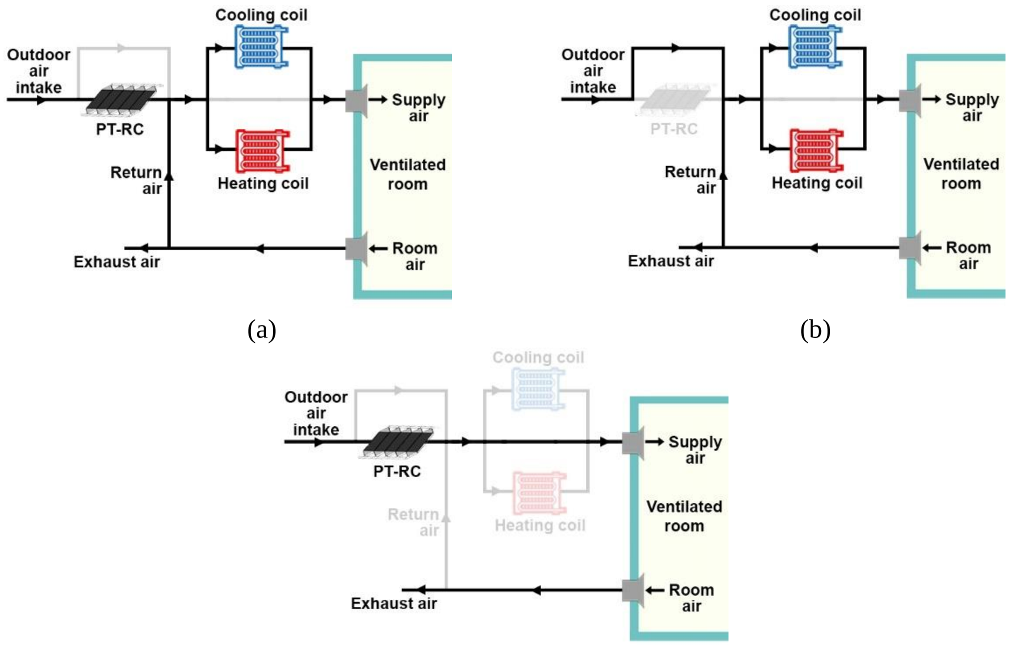

(a) (b)

(c)

Figure 6-3. Schematic diagram of the PT-RC-assisted HVAC system: (a) fan ventilation mode, (b) HVAC mode, and (c) PT-RC-HVAC mode.

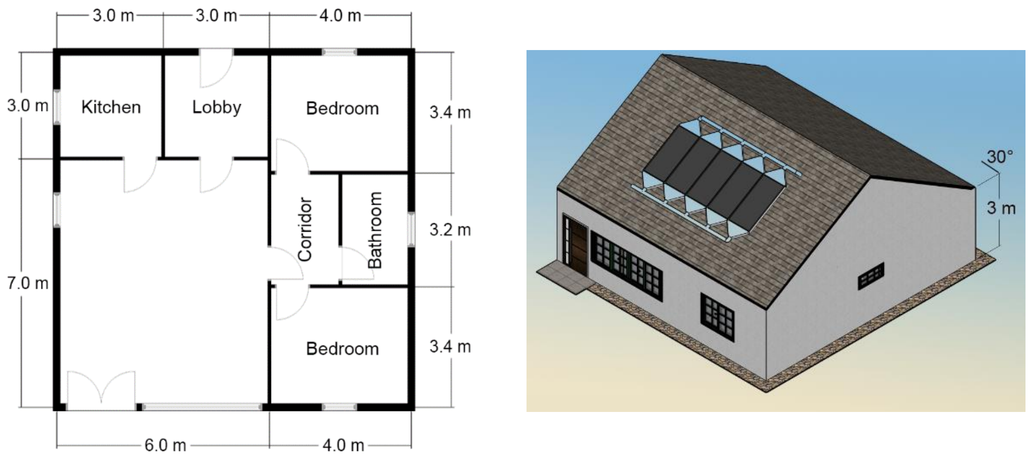

Figure 6-4. Illustration of the building-integrated PT-RC collector applied in the case study building.

6.3 Validation of the CFD and EnergyPlus model of the PT-RC collector

As previously mentioned, CFD (with Ansys Fluent software) and EnergyPlus simulations were used to evaluate the performance of the PT-RC collector and assess its energy-saving potential when applied to the building. The mathematical model and the procedure for the simulations are explained in Chapter 3. For this study, the CFD simulations were used to model the performance of the PT-RC collector, while EnergyPlus was used to simulate the annual heating and cooling loads of the case study building. The energy-saving potential of the PT-RC system was analysed by comparing the results from the CFD simulation with the heating and cooling loads data from EnergyPlus. By combining these two simulation methods, the study provides a comprehensive evaluation of the performance and energy-saving potential of the PT-RC collector.

6.3.1 CFD model of the PT-RC collector

To accurately model the performance of the PT-RC collector, a geometry model was created based on its dimensions, as shown in Figure 6-3. The geometry was then discretised using a structured hexahedral mesh, with a maximum mesh size of 5 mm swept along the computational domain with a 5 cm distance. The meshing result is shown in Figure 6-5. This mesh size is selected after the mesh-independence study indicating its reliability in giving a grid-independent simulation result, as summarised in Figure 6-6. As seen in Figure 6-6, the simulation starts to give a stable result from the 5 mm mesh size (mesh number 76214).

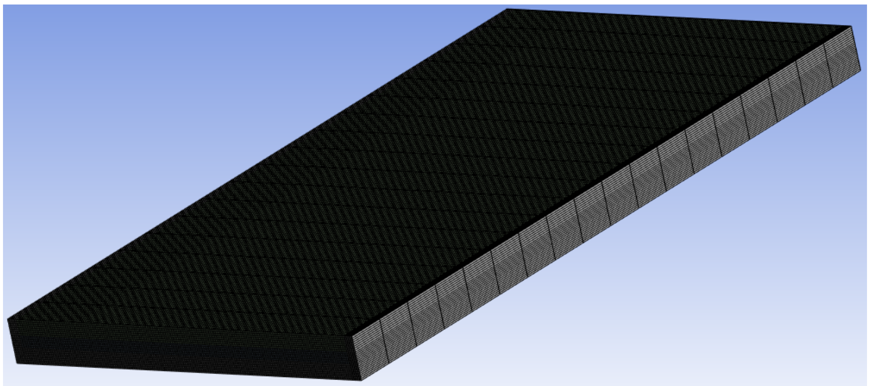

Figure 6-5 The geometry and mesh of the PT-RC collector.

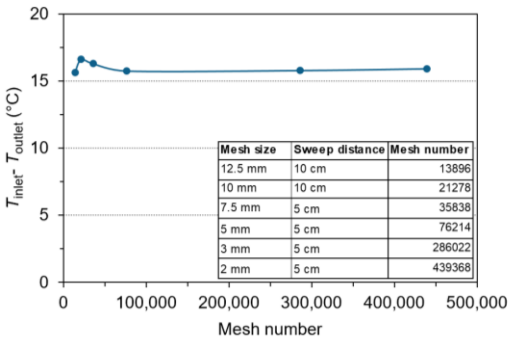

Mesh size	Sweep distance	Mesh number
12.5 mm	10 cm	13896
10 mm	10 cm	21278
7.5 mm	5 cm	35838
5 mm	5 cm	76214
3 mm	5 cm	286022
2 mm	5 cm	439368

Figure 6-6 Results from the mesh independence study.

To validate the CFD model, results from the simulations were compared to the experimental data from Hu *et al*. (2022a). The solar collector measured by Hu *et al.* (2022a) has the same dimension and structure as the PT-RC collector in this study, but the measured data available were for the conventional solar collector only as shown in Figure 6-7. Thus, for validation, the CFD simulation modelled the solar collector in the experiment using transient simulation with a time step size of 60 s (1 minute). As seen in Figure 6-8 below, there is a good agreement between the CFD model and the experiment. The root mean square deviation (RMSD) assessment shows good conformity between the two. The RMSD of the simulated outlet temperature is 4.2%.

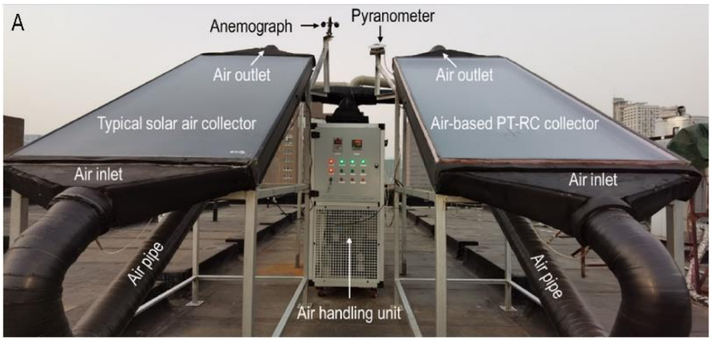

Figure 6-7 Experimental rigs from Hu *et al*. (2022a).

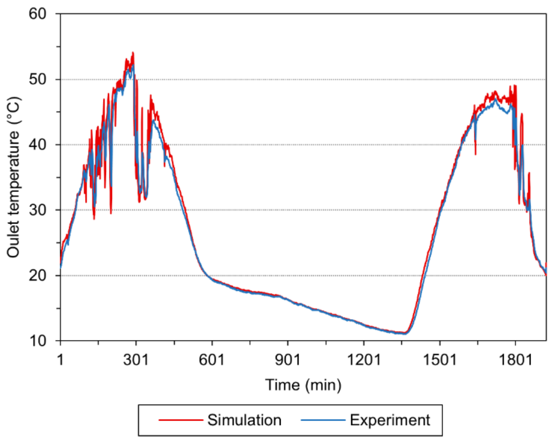

Figure 6-8 Comparison between simulation results from the CFD model and experimental data from Hu *et al*. (2022a).

6.3.2 EnergyPlus simulation setup

Before the case study building was simulated in EnergyPlus for energy-saving analysis, the EnergyPlus model of the building was first validated against the experimental data of the IEA-EBC Annex 58 building (Strachan, Svehla, Heusler, *et al.*, 2016). The experiment on the building (see Figure 6-4) was done in Munich, Germany (48.1° N, 11.6 ° E), measuring the indoor temperatures of all rooms when the heat load from two heaters were applied. The construction materials of the EnergyPlus model were set according to the detail given by Strachan et al. (Strachan, Svehla, Heusler, *et al.*, 2016). Figure 6-9 below compares the indoor temperature of the living room from the simulation and the experimental data. The figure shows a good agreement between the simulation and the experiment with an average difference of 0.5°C and RMSD of 3.7%.

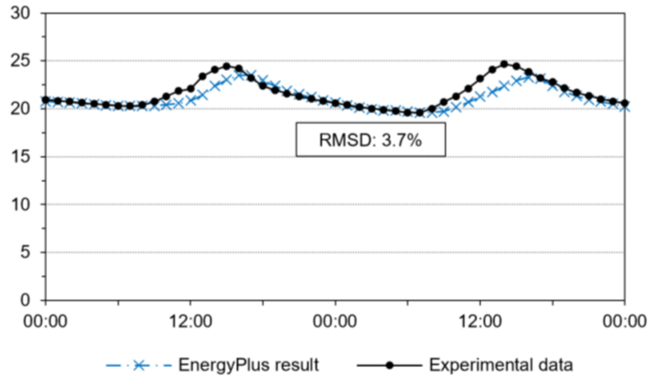

Figure 6-9 EnergyPlus model validation.

Further, the calibrated EnergyPlus model was used in the energy-saving analysis of the building-integrated PT-RC system in three case study locations. The locations were chosen to assess the most appropriate climate condition for the PT-RC collector among the climate types that have heating and cooling seasons. Based on the Koppen-Geiger climate classification (Kottek *et al.*, 2006), the three climate types are the cold desert climate (BWk), represented by Isfahan, Iran; the hot summer Mediterranean climate (Csa) represented by Madrid, Spain; and the humid subtropical climate (Cfa) represented by Tokyo, Japan. Figure 6-10 illustrates the ambient temperature variations in these locations, which indicate a need for space heating and cooling, as the outdoor temperature variations lie outside the adaptive thermal comfort zone (ASHRAE, 2020). In addition, Figure 6-10 shows that Isfahan and Madrid with dry climates and low relative humidity levels, have a higher potential for radiative sky cooling due to the larger gap between the ambient and sky temperature, and thus a high potentiality for radiative sky cooling (Kottek *et al.*, 2006)

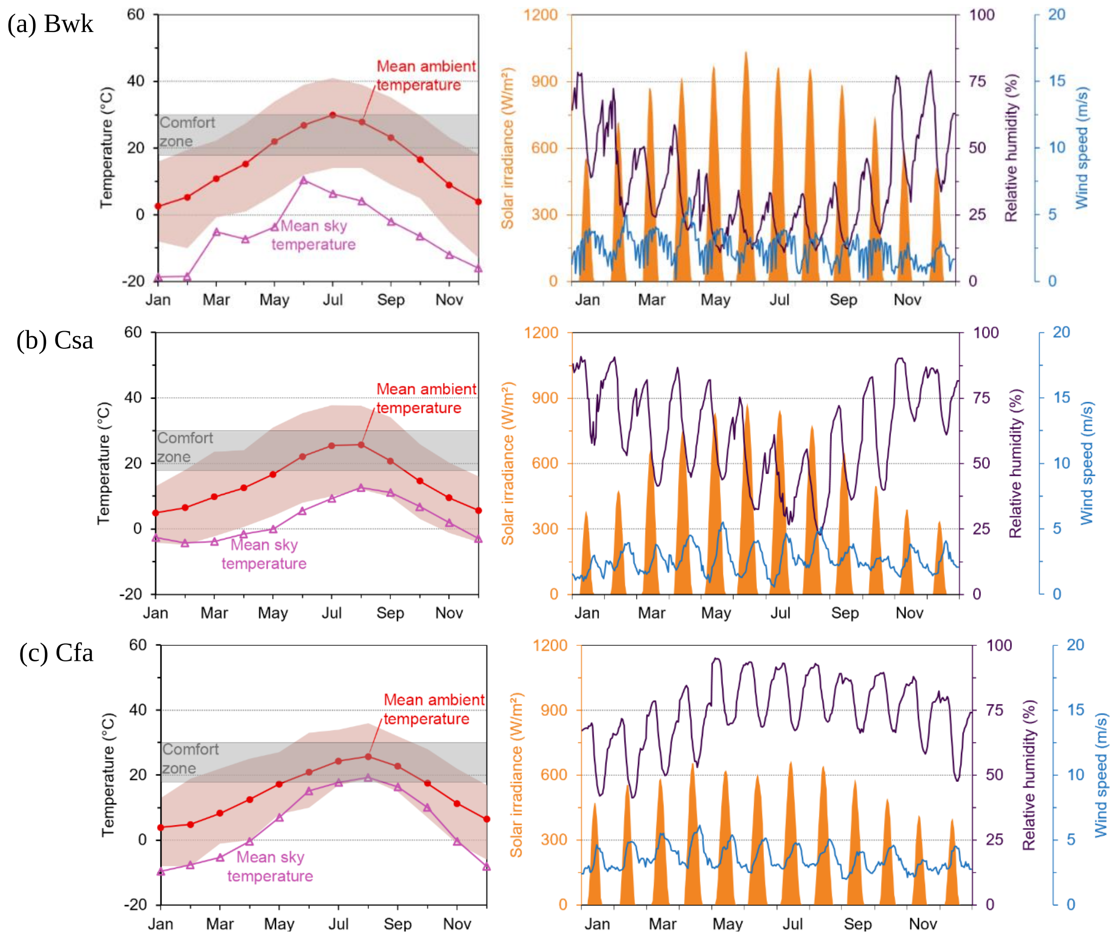

Figure 6-10 Dry bulb temperature data for (a) Isfahan, Iran; (b) Madrid, Spain; and (c) Tokyo, Japan (Liggett and Milne, 2021; Lawrie and Crawley, 2022).

Furthermore, the set point temperatures for space heating and cooling were set at 21°C and 24°C respectively. The heating and cooling supply air temperatures were 40°C and 18°C respectively, provided by the selected HVAC system with a gas heating coil with an efficiency of 0.9 and a direct expansion cooling coil (single speed) with a rated COP of 3.6 (ASHRAE, 2018). The ambient and sky temperature, solar irradiance, wind speed, and mass flow rate data were obtained from these EnergyPlus simulations (Lawrie and Crawley, 2022; LLC, 2022). Besides those parameters, the simulations also reported the heating and cooling loads for each case study location. These data were then used in the analysis of the energy-saving potential of the PT-RC collector, by comparing it with the heating and cooling energy yield data from CFD simulations.

6.3.3 Performance evaluation of the PT-RC collector

The PT-RC collector performance is measured using three indicators, namely the outlet temperature, the heating/cooling power, as well as the thermal efficiency. The outlet temperature data are obtained through the CFD simulations, while the heating/cooling power ($q_{\text{heating/cooling}}$) is calculated using Equation 6.1 below.

$$q_{\text{heating/cooling}} = \left(\dot{m}c_p(T_{\text{outlet}} - T_{\text{in}}) - P\right)/A \quad 6.1$$

Furthermore, the thermal efficiency (η_{th}) is calculated using Equation 6.2, where A in Equations 6.1 and 6.2 is the collector's area. Considering the energy used by the fan, Equation 6.2 includes the ideal fan power consumption in the form of $P = \Delta p \cdot \dot{Q}$, with Δp as the pressure drop across the air duct (Pa) and $\dot{Q}$ as the volumetric flow rate of the air (m^3/s).

$$\eta_{\text{th}} = q_{\text{heating}}/H \quad 6.2$$

Sensitivity analyses were conducted using a one-day CFD simulation of the typical summer day of Isfahan, to assess the effect of various key parameters on the collector's performance. Moreover, for the energy-saving analysis of the building-integrated PT-RC collector, one-year transient CFD simulations in ANSYS were conducted to get the hourly outlet air temperature for the whole simulation year. From the one-year simulations, the heating and cooling energy yields, $E_{\text{heating/cooling}}$ (Wh), were calculated using the formula in Equation 6.3 below, with A_{total} is the total area of the PT-RC collector's array, and t as the simulation's time step size.

$$E_{\text{heating/cooling}} = q_{\text{heating/cooling}}\, A_{\text{total}}\, t \quad 6.3$$

It is anticipated that the time in which the heating/cooling load arises does not match the time in which the heating/cooling energy yielded. Therefore, the analysis of the energy-saving potential of the PT-RC collector also accounts for the time matching between the yield energy and the load conditions (supply-demand matching). For a given period, one can calculate the percentage of matched time using Equation 6.4 below. Then, it follows that the energy saved by implementing the PT-RC collector is the product of energy yield multiplied by the percentage of the matched time.

$$\%\ of\ matched\ time = \frac{Matched\ hours\ between\ yield\ \&\ load}{Total\ hours\ of\ energy\ yield} \times 100\% \quad 6.4$$

6.3.4 Sensitivity analysis

a. Differences between steady and transient simulation results

The differences between the results from steady and transient simulations are also worth analysing. The steady simulation will not be used for the annual energy-saving analysis, yet it is useful in the study of the effect of various environmental conditions on the PT-RC performance. Comparing the results from the two simulation models can give an overview of the differences between them and whether they can be used interchangeably. Figure 6-11 compares the steady simulation results with the transient simulation with 300 s time step size using the typical summer day data of Isfahan. It can be seen from the figure that the results from the steady simulation are close to the transient one, with an RMSD of 1.9%. Thus, principally the two can be used interchangeably. However, for practical reasons, the steady simulation will be used for the analysis of the effect of various environmental conditions on the PT-RC performance, while the transient simulation will be used for the annual simulation.

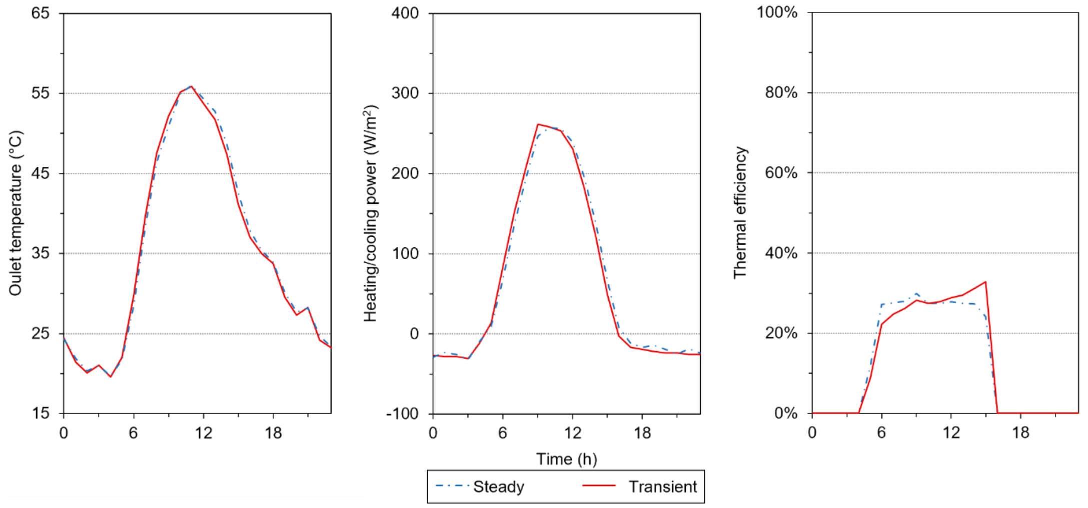

Figure 6-11 Comparison between the results from the steady and transient CFD simulations for the PT-RC collector ($\dot{m} = 0.023$ kg/s).

b. Effect of time step size

A large time step size may not be reliable for a transient simulation, but a very fine time step size is time-consuming and resource-intensive. Figure 5-10 summarises the results from one-day transient simulations, using the typical summer day data of Isfahan, with several time step sizes. It is seen in Figure 5-10 that the time step of 900 s (15 minutes) or larger results in not reliable outlet temperature, and thus gives unreliable power and thermal efficiency as well. RMSDs of the 3600 s, 1800 s, and 900 s to the 60 s time step sizes are 12.2%, 7.9%, and 4.4% respectively. The large time step sizes, especially the 3600 s and the 1800 s, underestimate the heating effect during daytime and the cooling effect at nighttime (see Figure 6-12). The intended RC effect is not observed when using the ≥1800 s time step size. This is because the simulation with a large time step size does not fully develop into a stable condition in the hourly weather data. This is apparent in the thermal efficiency plotting in Figure 6-12, the larger time step sizes show sudden changes in the afternoon (around 3 p.m.), displaying results that are more like minutely rather than hourly conditions.

Furthermore, the simulation results of the small time-step sizes (≤600 s) are converging. RMSD of the simulations results from the 600 s and 300 s, compared to the 60 s, are 3.1% and 1.5% respectively. However, using the 60 s (1 minute) time step size for the annual simulations used in the energy-saving analysis is impractical. Hence, the 300 s and 600s time step sizes are the best options, since they can resemble the simulation results with the 60 s time step size. However, when looking at the thermal efficiency data, the 600 s time step size still has the characteristic of the large time step, *i.e.*, that it has a sudden change in the afternoon. Thus, in this regard, the 300 s one is the more feasible time step size to use for reliability and speed of calculation.

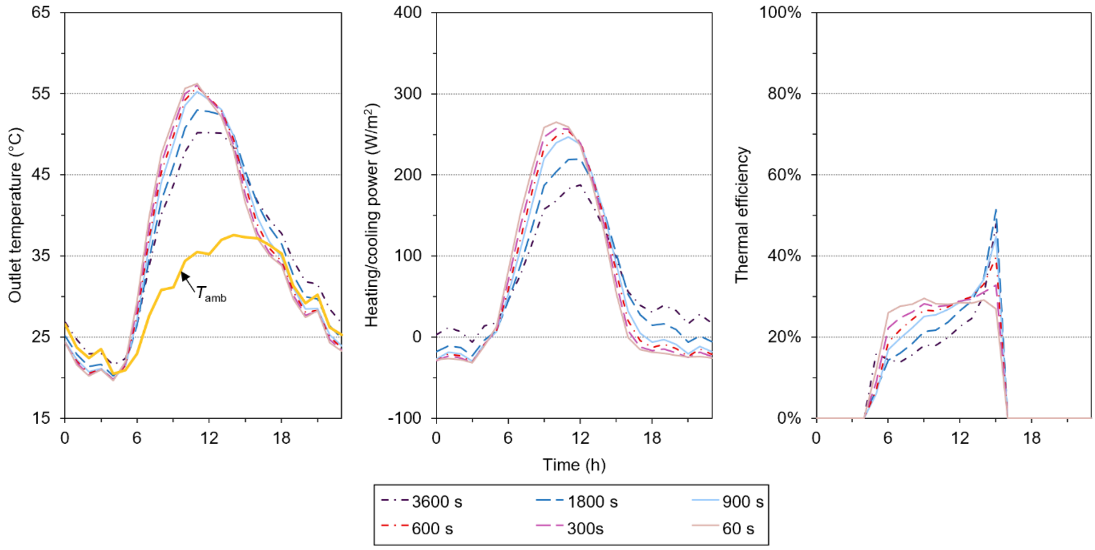

Figure 6-12 Effect of time step sizes on the PT-RC collector's performance ($\dot{m}$ = 0.023 kg/s).

c. Differences between 3-dimensional and 2-dimensional simulation results

From the time step size analysis, the preferred time step size for the PT-RC transient simulation is chosen. However, a 3-dimensional (3D) CFD model may still be time-consuming for simulations involving an annual simulation. To shorten the simulation time of the annual energy-saving analysis, the geometry used in the model can be simplified into a 3D with a symmetry wall (3D-half) or a 2D geometry. The comparison of simulation results from the 3D-full, 3D-half, and 2D models are compared in Figure 6-13. The figure shows the very close agreement in all parameters between the 3D full and 3D half, with 0.4% RMSD between the two. As for the 2D model, it is seen that the model tends to overestimate the heating performance. This is because the 2D model assumes the heating condition in the middle of the PT-RC collector to be uniform across its width. There will always be a gradation of temperature distribution farther from the middle. Outlet temperature differences can be up to 4°C higher in the 2D than in the 3D models, leading to a heating power gap of around 45 W/m^2. Nevertheless, the RMSD of the 2D model compared to the 3D-full model is 4.3% and the plotting of all parameters in Figure 6-13 shows no considerable differences in the hourly pattern. Thus, for this reason, 2D is considered reliable to be used in the annual energy-saving analysis.

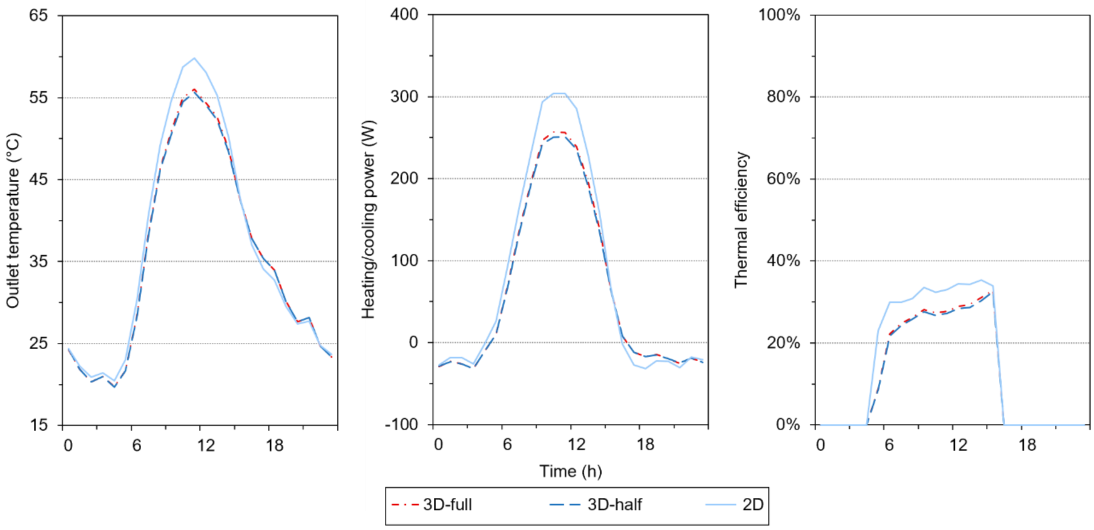

Figure 6-13 Effect of the CFD geometry model on the PT-RC collector's performance ($\dot{m} = 0.023$ kg/s).

6.4 Performance evaluation of PT-RC collector in different parameters

6.4.1 Parametric studies

a. The effect of solar irradiance, ambient temperature, and mass flow rate

The performance of the PT-RC collector is strongly influenced by ambient conditions, particularly ambient temperature and solar irradiance. Figure 6-14 illustrates the impact of various ambient temperatures and solar irradiance levels on the heating and cooling power of the PT-RC collector at five different air mass flow rates ($\dot{m}$). The figure shows that the heating power of the PT-RC increases with solar irradiance and that the rate of increase is consistent across different ambient temperatures. However, a closer examination of the data reveals that the collector's heating power performs better at low ambient temperatures when solar irradiance is high (>800 W/m^2). For example, at an ambient temperature of 5°C, a heating power of 200 W/m^2 can be achieved with 900 W/m^2 solar irradiance, while at 35°C ambient temperature, the same power can only be achieved with ~1000 W/m^2 solar irradiance.

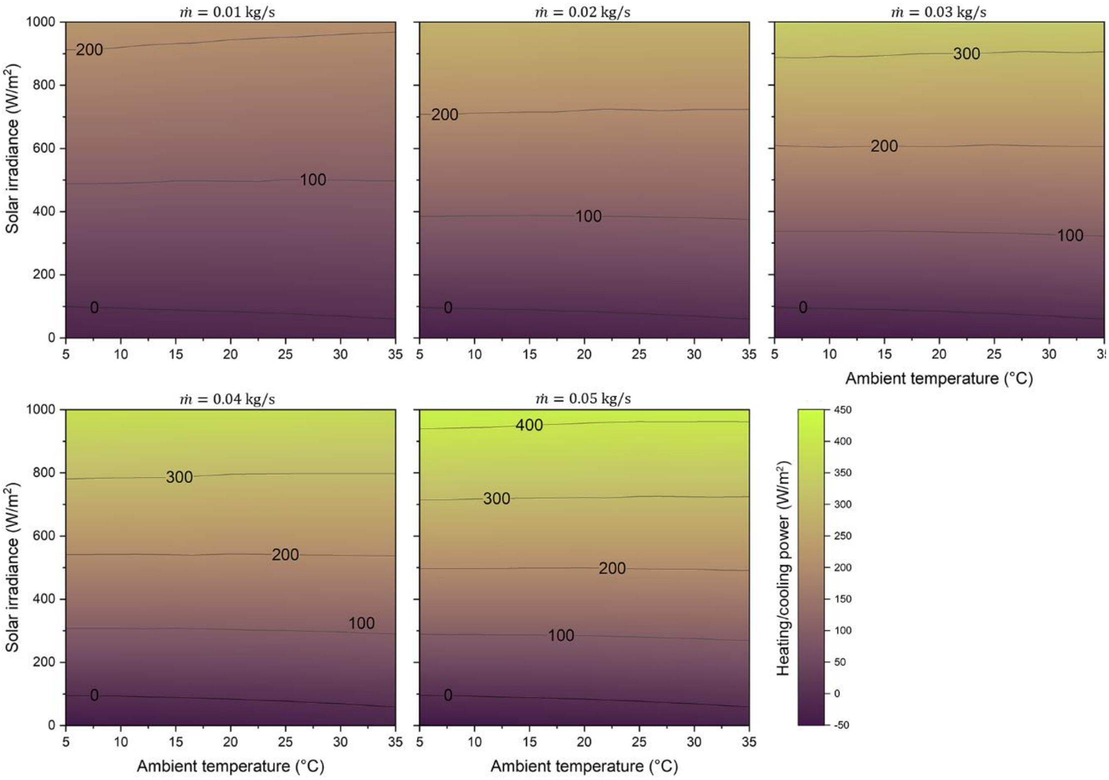

Figure 6-14 Effect of ambient temperature and solar irradiance on the PT-RC collector's performance with five different air mass flow rates.

Additionally, one notable point from the effect of solar irradiance on cooling power is that cooling occurs not only when the solar irradiance is 0 (*i.e.*, during the night). It is deduced from Figure 6-14 that the PT-RC collector starts to give cooling power at solar irradiance below 100 W/m^2. The solar irradiance level in which the cooling effect starts is higher at the low ambient temperature, and this is quite consistent in all mass flow rates. This means that it is easier for the PT-RC collector to start to cool the air at the low ambient temperature, mainly because the sky temperature formula in Equation 3.5 gives a larger gap between the ambient and sky temperature at the lower ambient temperature.

In terms of the mass flow rate's effect, it is expected that the higher mass flow rate generates a better heating and cooling performance. But they also result in higher pressure differences and thus greater fan power consumption. Therefore, the heating and cooling power provided by the PT-RC collector in Figure 6-14 is the adjusted value considering the fan power for each mass flow rate. At a mass flow rate of 0.01 kg/s, the

PT-RC collector can only achieve around 200 W/m^2 of heating and 28 W/m^2 of cooling power at best. Whereas, with the mass flow rate of 0.05 kg/s, the collector can provide more than 400 W/m^2 of heating and 50 W/m^2 cooling power. Also, the influence of ambient temperature on the collector's heating/cooling power is more pronounced at lower mass flow rates, as shown by the steeper contour line gradients in Figure 6-14 for a mass flow rate of 0.01 kg/s compared to 0.02 kg/s. As the mass flow rate increases, the contour lines become more horizontal, indicating that ambient temperature has a lesser effect on the collector's heating/cooling power.

b. The effect of the air duct and air gap heights

Besides the environmental conditions, the collector’s design is also an influential factor for the heating/cooling power. Using the typical summer day in Isfahan, the effect of various air duct and air gap heights were simulated, and the results are summarised in Figure 6-15. It is noteworthy that a smaller air duct means higher pressure is needed by the fan, and hence the fan will need more power to deliver the same mass flow rate in the smaller air duct. Therefore, Figure 6-15 is the adjusted heating and cooling power after the fan power effect due to the increase in pressure is subtracted. The effect of air duct height is more apparent around noon time when the solar irradiance level is high. Thus, the optimal air duct design can be deduced by comparing mainly the heating performance during the daytime. As expected, the smaller air duct transfer heats more efficiently from the collector to the air, as Figure 6-15a shows the superiority of the 1 cm air duct over the other larger heights. With a 1 cm air gap, the PT-RC collector has 422.7 W/m^2 maximum heating power (at least 65.3 W/m^2 higher than the other air ducts) during the day and 43.6 W/m^2 maximum cooling power (or at least 4.3 W/m^2 higher than the other air ducts) at night.

Similarly, the effect of air gap height is also more obvious during the sunlit period. But, unlike the air duct, the heating/cooling power is not neatly correlated with the air gap height. Although small air gaps are presumably worse insulations than large air gaps, increasing the air gaps to be larger does not necessarily mean a better heating/cooling performance. Hence, there is an optimal air gap height that should be used, as shown in Figure 6-15b. The figure shows that 1 cm and 2 cm air gaps have lesser heating power at noon, the 3 cm air gap has slightly better performance, and the 4 cm and 5 cm air gaps show the best results. But Figure 6-15b also shows that there is hardly any difference in heating/cooling power between the 4 cm and 5 cm air gaps. The difference in maximum heating power between the two air gaps is 1.39 W/m^2 larger for the 4 cm air gap. Therefore, the optimal air duct and air gap heights that can be used for the energy-saving analysis are 1 cm and 4 cm respectively.

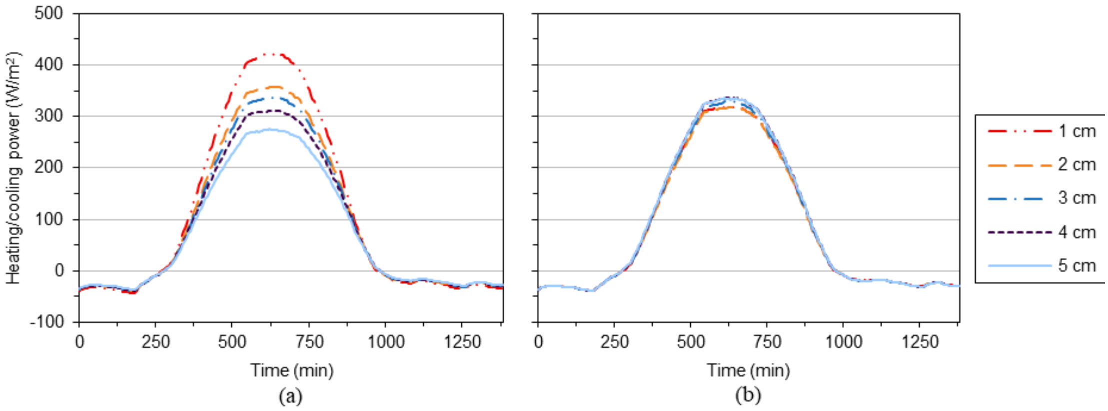

Figure 6-15 (a) The effect of air duct heights (simulated with an air gap of 4 cm), and (b) the effect of air gap heights (simulated with an air duct of 3 cm) on the heating and cooling power of the PT-RC collector (typical summer day of Isfahan (28-Jun,) $\dot{m} = 0.04$ kg/s).

6.4.2 Energy saving potential of the building-integrated PT-RC collector

a. Comparison with the mono-functional solar and RC collectors

The PT-RC collector is designed to offer an additional function for nighttime cooling to the conventional solar collector. This additional function requires a different structure for the PT-RC collector, which may impact its heating performance. Figure 6-14 displays the comparison between the solar, RC, and PT-RC collectors' energy yield for the typical winter and summer days (Figure 5-14a) of Isfahan. The simulations for the energy yield were done for the building-integrated system which consists of 5 collectors (9.43 m^2 collector area). To illustrate the benefit of the PT-RC collector results from a collector with near ideal PT-RC spectral properties (*i.e.*, by reducing the emissivity in other infrared bands to 0.05 and increasing the emissivity in the atmospheric window band to 0.9) were added in the analysis.

As expected, the heating energy yield of the PT-RC collector is lower than the solar collector, and similarly, the cooling energy yield is also lower than the RC collector. The hourly differences in heating energy yield between the solar and PT-RC collectors are wider as the solar irradiance peaks, as shown in Figure 5-14a. Likewise, the discrepancy in cooling energy yield between the RC and PT-RC collectors is widened during the day. These discrepancies in heating and cooling energy yield from the PT-

RC collector compared to the solar and RC collectors are due to differences in the spectral properties of the three collectors. The high emissivity in the atmospheric window band of the PT-RC collector is responsible for the inferior heating performance of the solar collector, and the high solar absorptivity is responsible for the absence of a cooling effect during the day. Results from the near-ideal PT-RC collectors confirm this by showing the reduction in heating energy yield even more because it has a higher emissivity in the atmospheric window band compared to the current PT-RC collector (Figure 5-14a, green bar). This very high emissivity value is also responsible for the higher cooling effect of the near-ideal PT-RC collector even compared to the RC collector late at night.

Nevertheless, Figure 6-16a also reveals the advantage of the PT-RC collector. On a typical winter day, the solar and PT-RC collectors can deliver heating, while the RC collector barely provides any heating at all. On the other hand, on the typical summer days when cooling is needed, only the RC and PT-RC collectors can supply cooling energy, while the solar collector does not perform (Figure 6-16a). In this regard, the PT-RC collector has the advantage of multi-seasonal performance over the solar and RC collectors. The daily heating and cooling energy yields by the PT-RC collector in the typical winter and summer days are around 37.3% lower than the solar collector and 31.9% lower than the RC collector respectively. Compared to the non-existent heating energy provided by the RC collector in the winter, or cooling energy by the solar collector in the summer, the previous energy yield reduction is preferable. This advantage is also shown in Figure 6-16b where the combined heating and cooling energy savings by the PT-RC collector is at least 1.5 kWh higher than the conventional solar or RC collectors. Compared to the near-ideal PT-RC collector, the current PT-RC collector gives similar combined heating and cooling energy savings with only 10 Wh gaps between them.

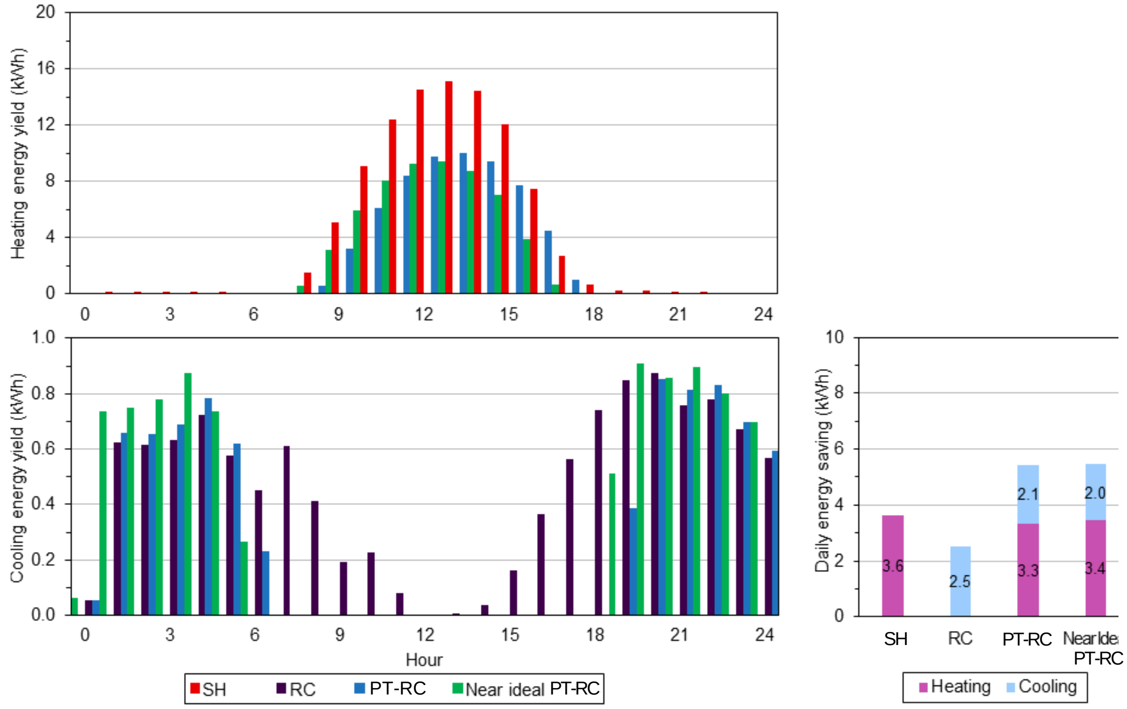

(a) (b)

Figure 6-16 Comparison between the (a) heating and cooling energy yield, based on typical winter (6-Jan) and summer (28 Jun) days in Isfahan (A = 9.43 m^2, $\dot{m}$ = 0.04 kg/s), and (b) energy saving potential of SH, RC, PT-RC, and near ideal PT-RC collectors.

b. Energy saving potential in different climates

Since the PT-RC collector performance is highly dependent on solar irradiance (for heating) and clear sky and humidity level (for cooling), its energy-saving potential in different climates must be different. To assess which climate condition is appropriate for the PT-RC collector, Figure 6-17 compares the heating load, energy yield, as well as potential savings from the PT-RC collector in three different climates. The figures reveal the mismatching and the discrepancy in magnitude between the heating and cooling loads with the available energy. In Figure 6-17a, the heating energy is available throughout the year roughly with a magnitude >1,000 kWh per month in all three climates. This heating energy yield is used 100% in the winter months, but because there is no heating load in the summer, the energy is wasted in the summer with 0% of match time between the supply and demand (Figure 5-15b).

In addition to that, Figure 6-17c summarises the annual heating load, yield, and useful heating energy in the three climates. The PT-RC collector provides a huge amount of heating energy yield in the three climates, which are 21,585 kWh in Isfahan, 17,929 kWh in Madrid, and 16,373 kWh in Tokyo. These results indicate the superiority of the PT-RC collector performance in the two dryer climates, namely Isfahan and

Madrid, compared to the humid climate in Tokyo. However, considering the differences in heating load between the climates, the percentage of yield and useful energy compared to the load can be seen as higher in Madrid (temperate dry climate) compared to Isfahan (cold desert climate), and Tokyo (temperate humid climate). Five PT-RC collectors in Madrid climate can reduce energy consumption for heating up to 36.9%, while Isfahan and Tokyo can save up to 14.7% and 27.2% respectively (Figure 5-15d).

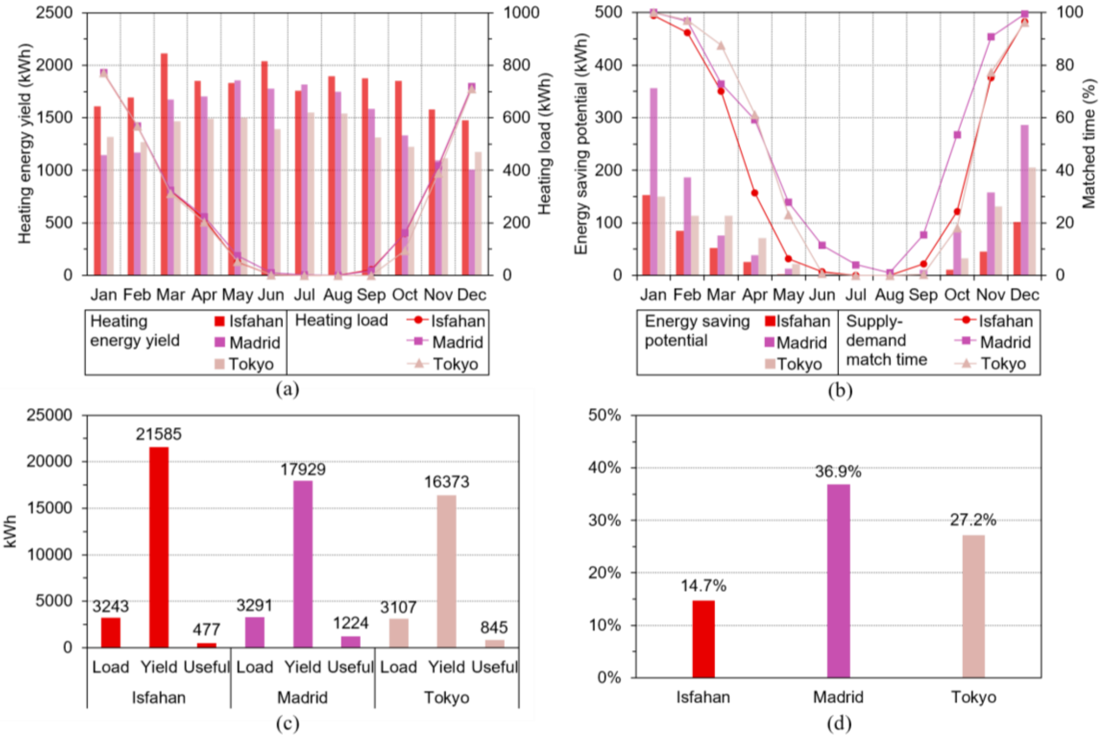

Figure 6-17 (a) The monthly heating load and energy yield; (b) the monthly supply-demand time matching and energy saving potential; (c) the total annual heating load, yield, and useful/saved energy; and (d) the percentage of useful heating energy to the heating load ($A = 9.43$ m^2, $\dot{m} = 0.04$ kg/s).

Furthermore, Figure 6-18 summarises the cooling load, as well as the available and useful cooling energy from the PT-RC collector in the three climates. Like the heating, the cooling energy available also mismatches the cooling demand, as seen in Figure 6-18a where the available cooling coincides with zero cooling load in the winter. But, unlike the heating energy that is 100% useful during the heating season, the cooling energy from the PT-RC collector cannot even achieve a 30% match time during the cooling season (see Figure 6-18b). This is because the PT-RC collector provides cooling mostly at night, but the demand mostly occurs during the daytime. In other words, the mismatch between the cooling load and energy yield is not only seasonal but also diurnal. This condition is also responsible for the lower percentage of energy-saving potential from cooling compared to heating, as summarised by the annual cooling energy numbers shown in Figure 6-18c. In the figure, the energy yields exceed the cooling loads in three climates. But this available cooling energy is again reduced by the mismatch time between the cooling load and energy yield. The percentage of useful cooling energy compared to the load is 12.5% in Isfahan, 10.3% in Madrid, and 3% in Tokyo (Figure 6-18d). This shows that the Isfahan climate is the most appropriate condition to optimally use the PT-RC collector for cooling, in line with the weather data in Figure 6-10 that shows the lower sky temperature in Isfahan compared to the other case study locations.

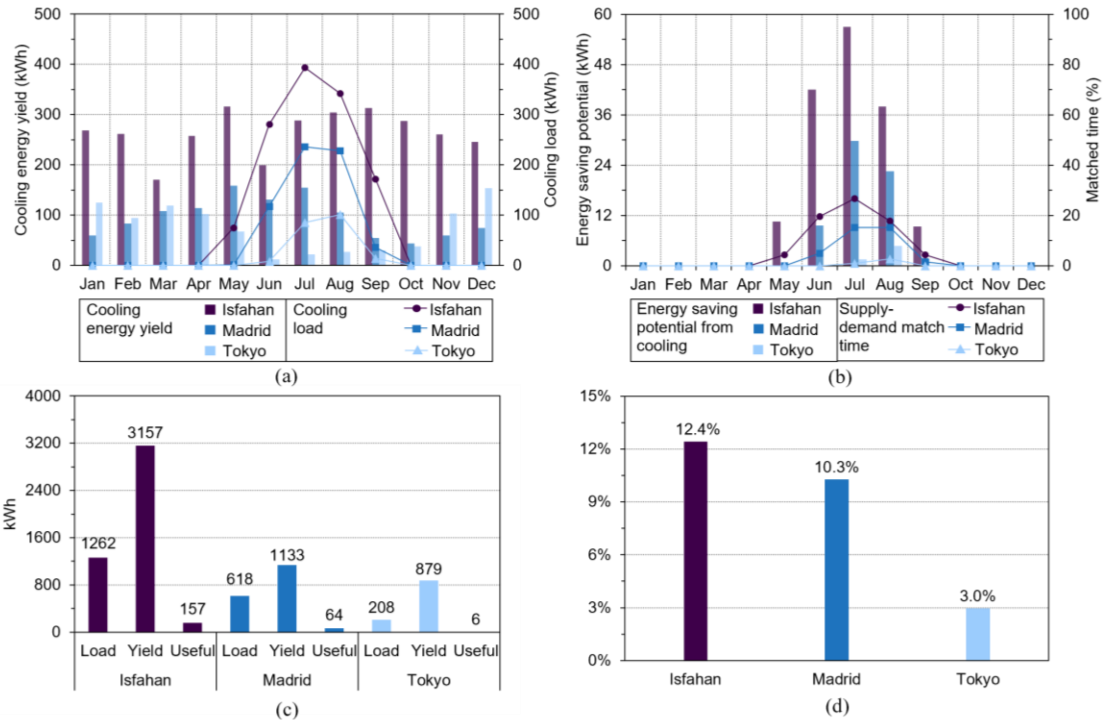

Figure 6-18 (a) The monthly cooling load and energy yield; (b) the monthly supply-demand time matching and energy saving potential; (c) the total annual cooling load, yield, and useful/saved energy; and (d) the percentage of useful cooling energy to the cooling load (A = 9.43 m^2, $\dot{m}$ = 0.04 kg/s).

6.5 Summary of Findings

This chapter has presented the evaluation of the idea of combining radiative cooling with solar energy technologies in an active system. The solar energy technology involved in this chapter is the air-based solar photothermal (PT) collector. The proposed PT-RC collector offers the benefit of a dual-functional device which can work in different seasons. Unlike the conventional solar collector which has high absorptivity in the solar band (0.2-3 µm), the PT-RC collector has high absorptivity in the solar band and infrared band (especially the atmospheric window band). Also, the glass cover that originally protects the solar collector from convective heat loss is changed to a PE cover that is transparent for infrared radiation. These adjustments in the spectral properties of the collector and the cover make the daytime-only solar collector a whole-day PT-RC collector.

For regions with heating and cooling seasons (arguably most of the world), a dual-functional device catering for heating and cooling would be more beneficial than two single-purpose devices. Examination of the proposed PT-RC collector in this chapter supports this hypothesis. Using CFD simulations, the performance comparison between the PT-RC collector and the PT or RC collectors alone is conducted. In the typical winter and summer days of Isfahan, the total energy yield of the PT-RC collectors is at least 1.5 kWh higher than the conventional solar or RC collectors. This superior figure is due to the multi-seasonal advantage of the PT-RC collector. When the heating and cooling performance in the winter and summer days are analysed separately, the PT-RC is inferior to the respective performance of the single-functional collectors. For instance, the daily heating energy yield by the PT-RC collector on a typical winter day is around 37.3% lower than the solar collector. Whereas the daily cooling energy yield by the PT-RC collector on a typical summer day is around 31.9% lower than the RC collector. However, that reduction in energy yield for the PT-RC collector is preferable to the non-existent heating energy provided by the RC collector in the winter, or the absence of cooling energy provided by the solar collector in the summer.

In addition to the CFD simulations, EnergyPlus simulations were also conducted to provide the building energy-saving potential of a building-integrated PT-RC collector. A case study building is developed from the IEA EBC Annex 58. It is a 100 m^2 building with a 9.43 m^2 collector area attached to the roof. The simulation results for three different locations estimate the potential annual energy saving by the PT-RC collector. In Madrid climate the building-integrated PT-RC collector potentially saves 36.9% heating energy. In a humid subtropical climate like Tokyo, the heating energy saving can be up to 27.2% annually, while in a cold-dessert climate like Isfahan, the figure is about 14.7%. In terms of cooling energy, the building-integrated PT-RC collector is found capable of reducing the cooling energy demand by 12.5% in Isfahan, 10.3% in Madrid, and only 3.0 % in Tokyo. The combined heating and cooling energy savings by the PT-RC collector annually are 32.7% in Madrid, 25.5% in Tokyo, and 14.0% in Isfahan. Those combined energy-saving potential figures reveal that Madrid climate is the most suitable condition for the building-integrated PT-RC collector.

Nevertheless, the building-integrated PT-RC system may have a potential conflict in its combination with the HVAC system. As described in Section 7.2 the building-integrated system of the PT-RC collector has three working modes namely natural ventilation mode, HVAC only mode, and the PT-RC assisted HVAC mode (Figure 6-3). With these connections between the three working modes, there is a need for a responsive and reliable actuator for opening and closing the inlet that follows the ambient temperature and solar irradiance conditions. The failure of the actuator would mean that the air inlet for the HVAC might come from an unintended source. For instance, at noon on a summer day, the PT-RC is supposed to be closed and the HVAC is on, drawing air from the ambient to be cooled before it enters the building. If the intended scenario did not work, the inlet for the HVAC would also be the heated air from the PT-RC collector, and thus will deteriorate the cooling efficiency of the HVAC system. Therefore, the building-integrated PT-RC system must include a reliable ambient conditions sensor and the inlet opening actuators.

Chapter 7 Investigation of a Trifunctional Bi-fluid Solar Photovoltaics-Thermal Collector Incorporated with Radiative Cooling (PVT-RC)

Previous chapters have discussed proposals to combine radiative cooling with solar technologies in buildings from a fully passive system to a fully active system. Yet, the inquiry for a combination of radiative cooling with solar energy application in buildings can still be advanced further, for instance, into a system that not only actively uses energy, but also generates energy. In this chapter, the possibility of making solar photovoltaics work in combination with radiative cooling is discussed.

7.1 Reasoning of the Strategy

Solar energy applications can provide electricity generation using photovoltaic (PV) cells, and space heating using photothermal (PT) collectors. In the PV cell, photon energy is transferred into electrons in a P-N semiconductor material so the electron can move (Boyle, 1997). In this scheme, the semiconductor material needs to be engineered to allow the electron to move while the photon energy must be above the energy activation of the electron. For typical monocrystalline PV, the useful solar radiation is roughly in the wavelength of 0.3-3 µm only (Bundgaard and Krebs, 2007). Unlike PV, the PT does need a high energy photon, since it can be heated by photons in a wide range of radiation wavelengths, namely 0-25 um (Minmin Gao *et al.*, 2019).

Usually, PV and PT are different devices. But, considering PV suffers from energy loss in the form of heat (only around 15% of solar radiation is converted into electrical energy, and most becomes heat energy), people come up with the idea to utilise PV also for heating, hence PVT (Teo, Lee and Hawlader, 2012; Joshi and Dhoble, 2018). A typical PVT collector is illustrated in Figure 7-1 below. It consists of a PV module that is attached with a fluid channel under it and covered with a glass sheet over it. Between the glass and the PV module, there is a few centimetres gap, which can be an air gap or a vacuum gap. To prevent heat loss from under the PV module and the pipe to the ambient, a thermal insulation layer is attached as the lowest layer in the PVT structure.

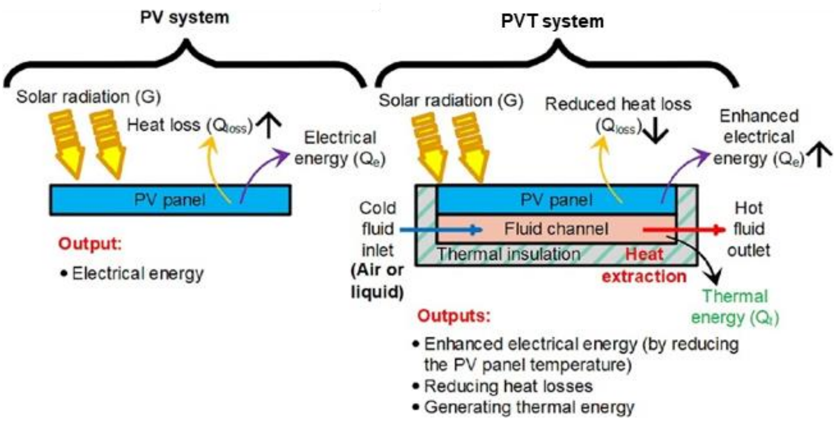

Figure 7-1 Conceptual diagram of a typical PVT (Şirin, Goggins and Hajdukiewicz, 2023).

The most common fluid used in the PVT collector is water, although there are also some utilisations of air-based or bi-fluid PVT collectors (Baggenstos *et al.*, 2020). Nevertheless, the thermal efficiency of the air-based PVT collector is larger than the air-based one. Some water-based PVT collectors can achieve more than 56% thermal efficiency (or around 69% total efficiency) (Mojumder *et al.*, 2016). Meanwhile, the current best thermal efficiency of an air-based PVT collector is roughly 42% (or 55% total efficiency) (Sardarabadi *et al.*, 2017). Recently, there have also been attempts to combine water and air-based PVT collectors. The so-called bi-fluid PVT collector can achieve a total efficiency of around 85% (Lebbi *et al.*, 2021).

However, the conventional PVT collector, either water or air-based, is idle at night. Considering the PVT's high absorptivity/emissivity in the whole solar and infrared spectrum, it is possible to use it as a radiative cooling (RC) emitter as well during the night. But the conventional PVT collector uses a glass cover (see Figure 7-1) that can block infrared radiation from the PV module to the sky, and thus prevent the radiative sky cooling. To get the benefit from radiative cooling at night, the glass cover of the PVT collector should be changed to a polyethylene (PE) cover. Hence, the collector can work as a PVT collector and daytime and RC collector at night to be a PVT-RC collector.

The idea of a PVT-RC collector has been around since 2011 when Eicker and Dalibard (2011) proposed a water-based PVT-RC collector. Ever since research on the improvement of this technology has been steadily growing. Most of the researched PVT-RC collectors are water-based collectors (Hu, Zhao, Suhendri, Ao, *et al.*, 2022). This is mainly due to its efficiency and flexibility in the utilisation, *i.e.*, the coldness collected can be stored and used later when needed (Hu, Zhao, Suhendri, Ao, *et al.*, 2022). The current best cooling power obtained from the water-based PVT-RC under a clear night sky is 72 W/m^2 (Hu, Zhao, Ao, Zhao, *et al.*, 2018). Although not as flexible, the air-based PVT-RC is arguably simpler than the water-based, and more direct in the way of utilisation. However, this type of PVT-RC is still understudied, with only a few published articles on the topic (Lin *et al.*, 2014; Fiorentini, Cooper and Ma, 2015b; Fiorentini *et al.*, 2015).

Nonetheless, until recently, the developed PVT-RC collector works with one fluid only. Thus, to fill in the research gap, the PVT-RC developed in this chapter is bi-fluidal and works with water and air simultaneously. There are at least a couple of benefits of using bi-fluid for the PVT-RC collector. The first benefit is by using bi-fluid, the total efficiency of the PVT-RC will be increased since the heat is collected both by water and air. Secondly, the bi-fluid PVT-RC collector offers wider possible utilisation for buildings such as for water heating/cooling and space heating/cooling with the same device.

Similar to the studies discussed in the previous chapters, these chapters examine the performance of the PVT-RC collector using CFD simulations in Ansys Fluent. To support the simulations, this study also involves experimental work. Analysis of the performance consists of the thermal and electrical performances of the PVT-RC collector. Thermal performances include the thermal (heating) efficiency during the sunlit period and net cooling power in the nighttime. Additionally, the potential contribution of the bi-fluid PVT-RC collector when applied to the building is also discussed.

7.2 Description of the trifunctional PVT-RC collector

The PVT-RC collector is made from a PV module with a dimension of 1475 mm by 670 mm. This dimension is based on the 150 W peak PV panel available on the market and purchased for the experimental study in this study. Further, on the top side of the module, a PE film is placed with a 30 mm gap. The selection of the PR film as the cover is to accommodate radiative heat exchange between the PV and the sky at night.

On the bottom side of the module copper pipes for the water channel are attached. There are eight 15 mm diameter pipes on the bottom of the PV module joined into a 22 mm manifold at each end. To enhance the thermal contact between the pipe and the PV panel, aluminium plates are attached to the pipe to the back of the PV panel. These aluminium plates also help to strengthen the attachment of the pipe to the PV panel. For the air channel, an air duct measuring 30 mm from the bottom side of the module is devised. To distribute the airflow from the fan uniformly in the air channel, a triangle-like structure is built at the inlet side. This triangle-like structure is also built at the outlet side for convenience in opening or closing the outlet. The closing of the inlet and outlet is needed when the water mode experiment is conducted.

Moreover, surrounding the whole structure is the insulation material to prevent heat loss to the ambient. The thickness of the insulation is based on the available insulation board on the market. See Figures 7-2 and 7-3 for the illustration of the PVT-RC collector design. In addition to that Table 7-1 details the materials used in the PVT-RC collector.

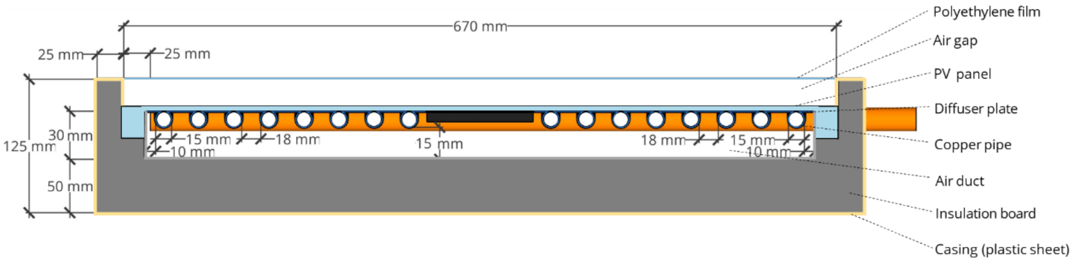

Figure 7-2 Schematic of the cross-section of the PVT-RC module.

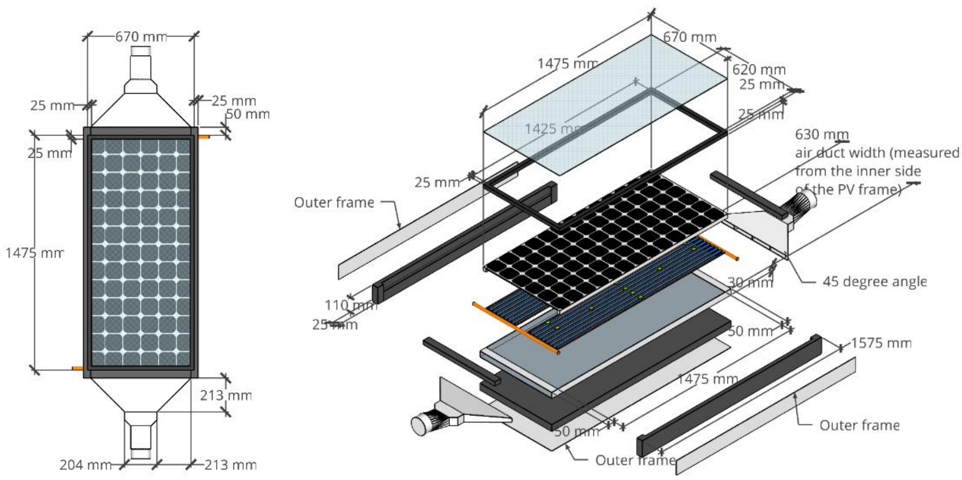

Figure 7-3 Detailed dimensions of the PVT-RC module.

Table 7-1 Material list, dimensions, characteristics, and brands.

Component	Material	Dimension and characteristics	Brand
PV	Monocrystalline PV	1475 mm × 670 mm 150W - 12V Off Grid Solar Kit & 300W Power Inverter	Sunshine Solar
Water pipe	Copper	15 mm	Wickes
Manifold	Copper	22 mm	Wickes

Air inlet-outlet channel	PVC pipe	100 mm	Manrose PVC
Insulation board	Polyisocyanurate	Kingspan TP10 Insulation Board - 2400 × 1200 × 25mm	Kingspan
Outer frame	Polystyrene Sheet	2000 ×1000 × 1.5mm	Eagle Plastics

As briefly mentioned in the introduction, the PV module converts solar energy to electricity and heat during the sunlit period, but only the electricity is collector, while the heat is wasted. With the PVT-RC collector, the heat is collected by water in the pipe and air in the air duct. The PE film is installed as the convective protection against the ambient wind to minimise heat loss. During the night, the PE film allows thermal radiation from the PVT-RC collector surface to the sky and thus makes it possible for nighttime cooling collection. This convection cover is the differentiating feature of the PVT-RC collector from the conventional PVT collector, which uses a glass cover instead of a PE cover.

Moreover, the use of bi-fluid, water, and air, for this PVT-RC collector serves two functions. Firstly, it aims to increase the thermal efficiency of the collector, as there is more energy collected from the absorbed heat by two working fluids than one working fluid. Secondly, using air and water as the working fluid offers more functions for buildings, such as for space heating and cooling as well as domestic water heating. The chilled water collected from the PVT-RC collector can also be used for space cooling, and thus this operational flexibility is the third benefit of using a bi-fluid PVT-RC collector. Figures 7-4 and 7-5 below illustrate how the bi-fluid PVT-RC collector is implemented in a building and the schematic diagram of its operation.

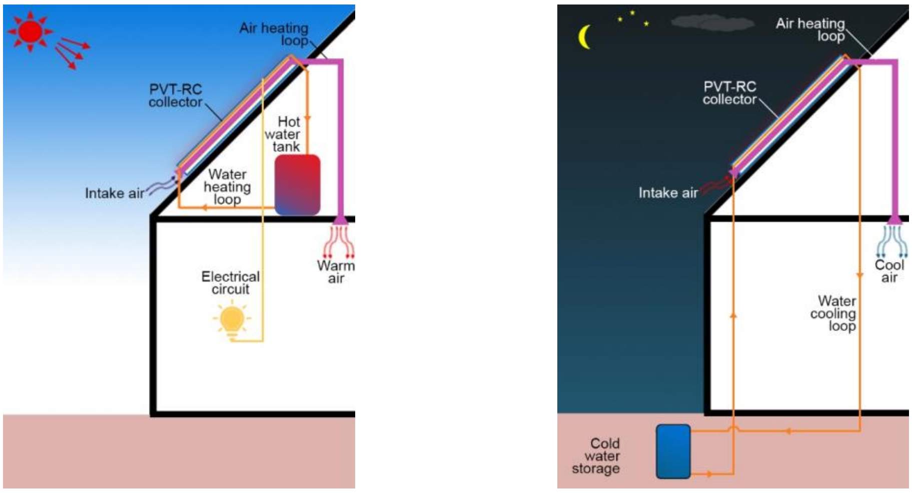

(a) (b)

Figure 7-4. Schematic diagram of the building-integrated PVT-RC collector: (a) heating mode, (b) cooling mode.

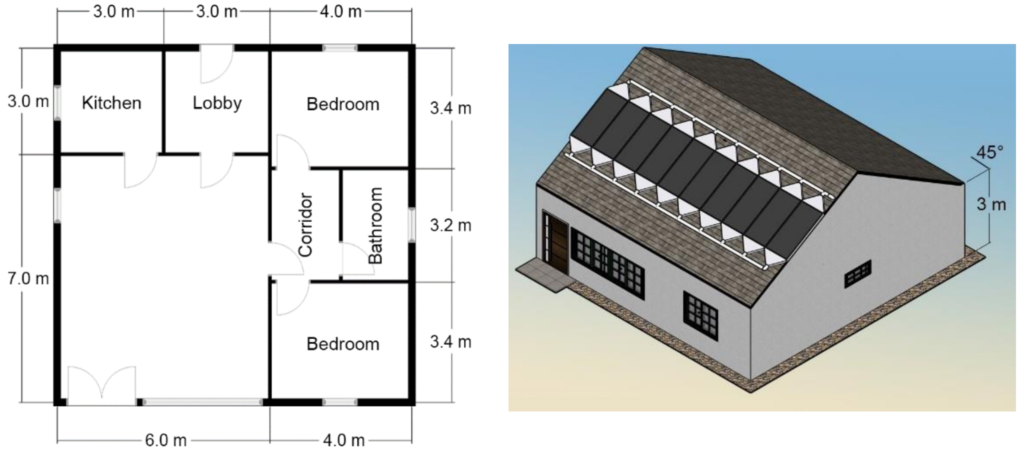

Figure 7-5. Illustration of the building-integrated PVT-RC collector applied in the case study building.

7.3 Experimental Study of the Trifunctional PVT-RC module

7.3.1 Experiment settings

This study conducted the proof of concept to the PVT-RC collector using experiments as well as CFD and EnergyPlus simulations. The CFD simulations will be covered in Section 7.4 onwards. Regarding the experiment, it serves as the means to investigate the performance of the PVT-RC collector as well as to provide some data for the validation of the CFD simulations. Whereas the EnergyPlus simulations will provide an energy-saving analysis of the building-integrated PVT-RC system.

The PVT-RC collector described in Section 7.3.1 was constructed, with the specification of the module components detailed in Table 7-2. It was a modification of the standard PV module, adjusted to be the PVT-RC collector as described in the previous Section. To measure the three functions of the PVT-RC collector, an experimental rig illustrated in Figure 7-6 was devised. were measured in the experiment. The electricity generated from the PVT-RC collector flows through an MPPT controller. From the MPPT controller, the electrical current is directed to the battery and loads. Measurements of the current and voltage of the PVT-RC collector were done by voltage and current sensors. The current and voltage data were then recorded by the data logger.

For the water heating/cooling part, eight copper pipes were attached to the back surface of the PV module, while a PE film was set on top of the module with a 30 mm gap. Two main pipes act as the manifold to collect the water from the eight water pipes. One end of the lower manifold pipe was the water inlet of the panel, while another end of the upper main was the water outlet (See Figure 7-6). The water inlet of the panel was connected to the water outlet of a water tank, while the water outlet of the panel was connected to the water inlet of another water tank. These tanks are not connected to make sure the outlet water does not disturb the inlet water temperature. A water flowmeter and a water pump were installed on the water pipe between the water inlet of the panel and the water outlet of the water tank. Two platinum resistors (±0.1 °C) were set at the water inlet and outlet of the panel, respectively.

Moreover, the air duct for the air channel was built with 50 mm thick and 30 mm wide thermal insulation under the PVT-RC module. The structure is illustrated in Figures 7-2 and 7-3. To create a stable and uniformly distributed air flow inside the air duct, the air intake from the fan flows through a 1.5 m insulation pipe before it gets into a flow separator near the inlet of the air duct (See Figure 7-8 for the flow separator structure). A hot wire anemometer was placed at the end of the insulation pipe just before the flow separator to measure the air velocity (mass flow rate). Whereas the inlet and outlet air temperatures were measured at their respective points with platinum resistors. In addition to the water and air temperature measurements, ten thermocouples were attached to the back surface of the PVT-RC module to measure the surface temperature of the module. The placement of the thermocouples is shown in Figure 7-7. The construction process of the experimental rig is shown in Figure 7-8.

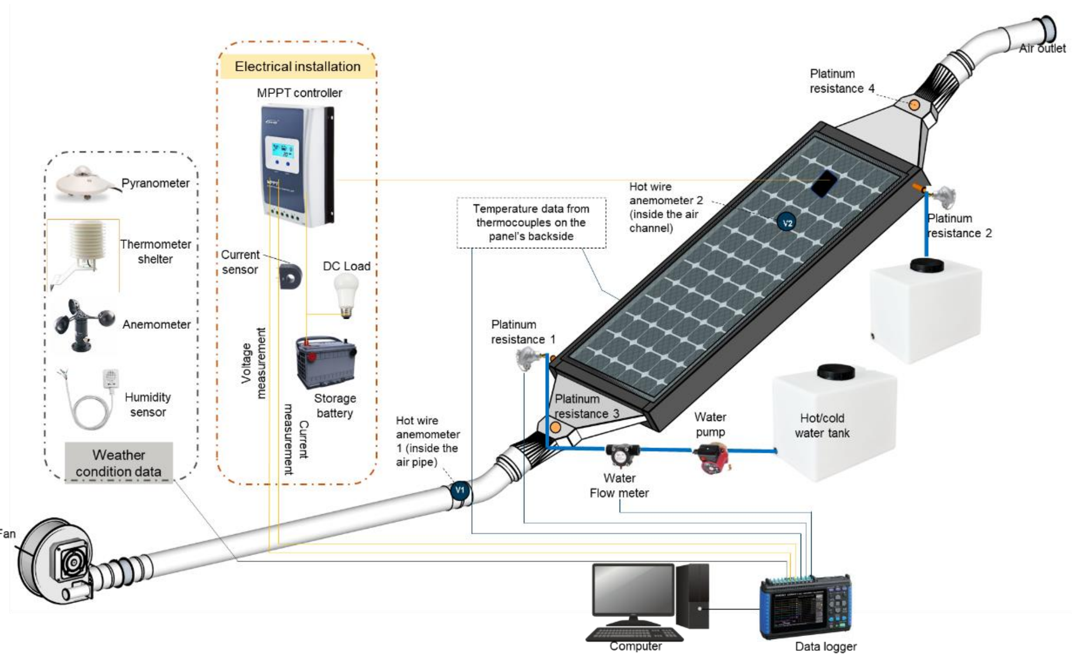

Figure 7-6 Schematic diagram of the PVT-RC experimental system.

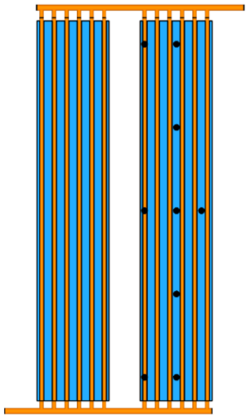

Figure 7-7 Locations of the thermocouples for measurement of the module temperature.

Additionally, data on environmental parameters such as ambient temperature, solar irradiance, wind speed, and relative humidity were also collected. The ambient temperature data was collected by a thermocouple placed inside a radiation shield to protect it from solar radiation. The solar irradiance level was measured by Skye Instruments' HOPL pyranometer sensor, while the wind speed and relative humidity were recorded by a PCE Instruments' Weather Station PCE-FWS 20N. Table 7-2 below summarises all the measurement devices in the experiment. The platinum resistors and thermocouples were calibrated beforehand, to improve measurement accuracy.

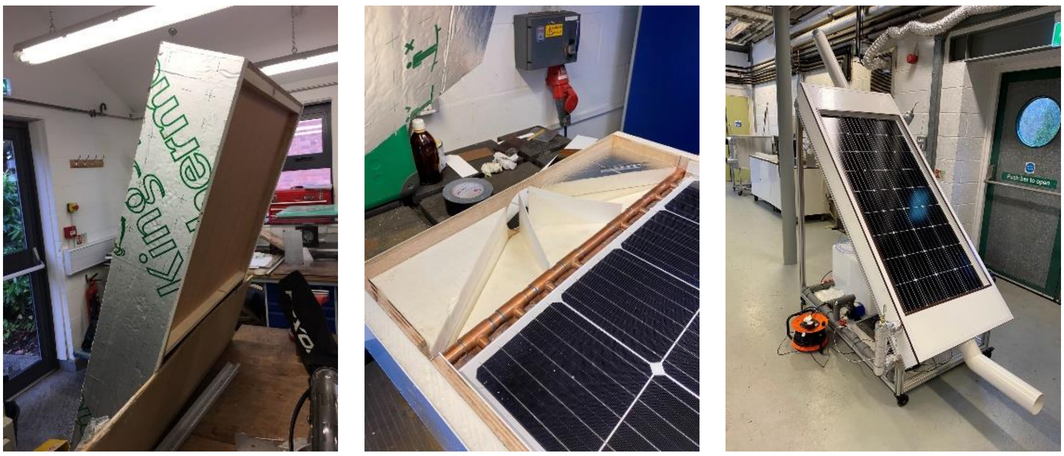

Figure 7-8 Construction and preparation of the PVT-RC module to be connected to the experimental system. See the flow separator structure marked in the image above.

Table 7-2 Detail of the measurement devices.

Measurement device	**Brand/Type**	**Measurement range**	**Uncertainty**
Thermocouple	RS PRO Type K Thermocouple	-40 to 1000°C	±0.004 or ±1.5°C
Hot wire anemometer	PCE Instruments: Hot Wire Anemometer PCE-423	0 to 30 m/s	• ±0.10 m/s or ± 5% of full scale at 0-5 m/s • ±0.30 m/s or ±5 % of full scale at 5-30 m/s

Flow meter	Gems Sensors FT-110 Series Turbine Flow Sensor	0.5 to 5 L/min	±3%
Pyranometer	Skye Instruments: HOPL pyranometer sensor, 0-2 V output	0 to 2000 W/m^2	±5%
Weather station	PCE Instruments: Weather Station PCE-FWS 20N	• Temperature: -40 to 60°C • Relative humidity:1 to 99% • Air pressure: 300 to 1100 hPa • Wind speed: 0 to 50 m/s	• ±1°C • ±4 % • ± 3 hPa • ±1 m/s
Voltage sensor	Akozon 25V	0 to 25 V	±5%
Current sensor	AZDelivery ACS712	-20 to 20A	±5%
Data logger	Datataker DT85M	-	-

7.3.2 Measurement process and parameters

All the testing and experiments were performed in the Department of Architecture and Built Environment, University of Nottingham (52.9° N, 1.1° W) in the period between May 2022 to June 2023. This long period of experiment is due to the rarity of the clear sky day in the UK. Also, the expected outcome could only be obtained after several attempts of experiment.

The step-by-step processes of the measurement are summarised as follows.

- Before a start
  - No shades on the RC-PVT panel
  - No blockage in the air duct
  - Open both vent grilles/damper
  - Fill 35-40 L of water into the inlet tank (adjust the water temperature using some hot water (for a warmer than ambient water temperature) or ice (for a cooler than ambient water temperature))
  - Make sure the water temperature is uniformly distributed (using thermometers or thermocouples at multiple points in the water)
- To start
  - Turn the battery to the solar controller switch on
  - Turn the PV to solar controller switch on
  - Open the water valve from the tank and switch on the water pump
  - Switch on the fan, measure the air speed in the air duct, and adjust the fan speed/vent grille/damper to get the required air flow rate.

- Connect all the meteorological station sensors (pyranometer, thermocouple, and anemometer) to the data logger
- Setup the laptop and data logger and start to collect the data

- To finish
  - Switch off the fan.
  - Switch off the water pump and close the water valve.
  - Turn off the PV controller and solar controller-battery switches.
  - Close the outlet grill/damper.
  - Cover the experimental rig with tarpaulin.

Figure 7-9 shows the photograph taken at the time of the experiment. For both daytime and nighttime experiments, there are three modes of experiment conducted to test the PVT-RC collector's performance. The modes are water mode, air mode, and bi-fluid mode PVT-RC collector.

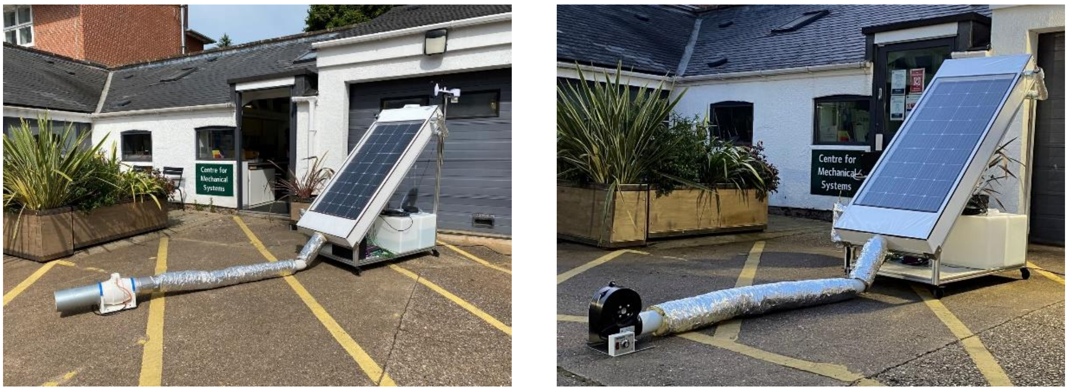

(a) (b)

Figure 7-9 Photo of the experimental rig during the (a) daytime, (b) evening

Parameters measured in the daytime experiments were the electrical current and voltage from the PV; the water flow rate, as well as inlet and outlet temperature; and the air velocity, as well as inlet and outlet temperature. Data recording for all the parameters was done every second. Besides the electrical current and voltage which are recorded by an Arduino system (El Hammoumi *et al.*, 2018), all other data were recorded by Datataker DT85M.

From the abovementioned data, the analysis of the PVT-RC collector performance was done by evaluating the thermal efficiency and electrical efficiency. For thermal efficiency (η_{th}), the formula used was shown in Equation 7.1, where $\dot{m}_{\text{f}}$, $C_{p_{\text{fluid}}}$,

$T_{\mathrm{f,inlet}}$, and $T_{\mathrm{f,outlet}}$ as the mass flow rate, specific heat capacity, inlet temperature, and outlet temperature of the working fluid respectively.

$$\eta_{\mathrm{th}} = \dot{m}_{\mathrm{f}} C_{p_{\mathrm{fluid}}} \left(T_{\mathrm{f,outlet}} - T_{\mathrm{f,inlet}}\right)/(AH) \quad 7.1$$

Meanwhile, electrical efficiency (η_{el}) is calculated by Equation 7.2, with V and I as the voltage and current from the PVT-RC collector, A as the collector area, and H as the solar irradiance.

$$\eta_{\mathrm{el}} = VI/(AH) \quad 7.2$$

The night experiment only focuses on cooling power measurements and thus with Equation 7.3 as the method to calculate the power (P_{cooling}).

$$P_{\mathrm{cooling}} = \dot{m}_{\mathrm{f}} C_{p_{\mathrm{fluid}}} \left(T_{\mathrm{f,inlet}} - T_{\mathrm{f,outlet}}\right)/A \quad 7.3$$

7.3.3 Experimental results

a. Daytime experiment

Results from the daytime experiments are presented in three different working modes, namely the water mode, air mode, and bi-fluid mode. Figure 7-10 shows the results of the water mode PVT-RC collector from the experiment. These results are obtained from an experiment conducted on the 14th of September 2022. The figure shows that under solar irradiance of almost 1000 and the ambient temperature of around 21°C, the water mode PVT-RC module achieved a total efficiency of 42.2% on average with a water mass flow rate of 0.04 kg/s. Out of this total efficiency, 30.8% of it comes from the water by the water heating efficiency, and 11.4% is the portion of the electrical efficiency.

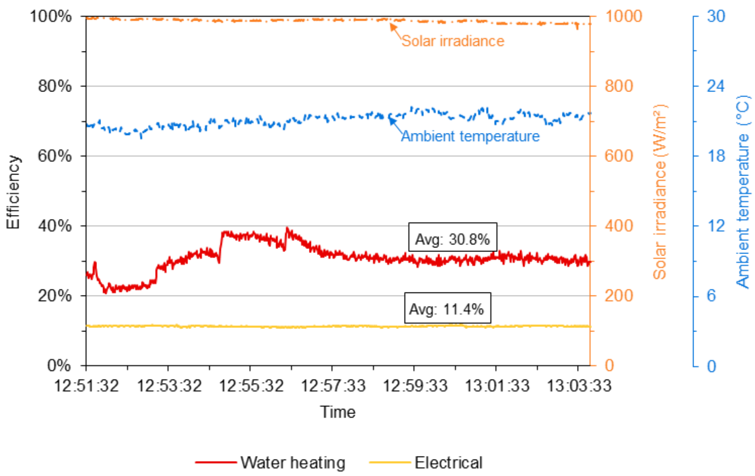

Figure 7-10 Experimental results on the thermal and electrical efficiency of the water mode PVT-RC collector.

Figure 7-11 shows the results of the air mode PVT-RC collector from the experiment. Compared to the water mode, the air mode PVT-RC collector yields more energy than the water mode PVT-RC. The figure shows that the air mode PVT-RC collector can achieve thermal and electrical efficiencies of 45.5% and 11.7% respectively, or a total efficiency of 57.2%. This total efficiency is 15% better than the water mode PVT-RC collector. This discrepancy is because the air channel has a larger area of thermal contact with the PV module than the water pipe, thus it has higher thermal efficiency.

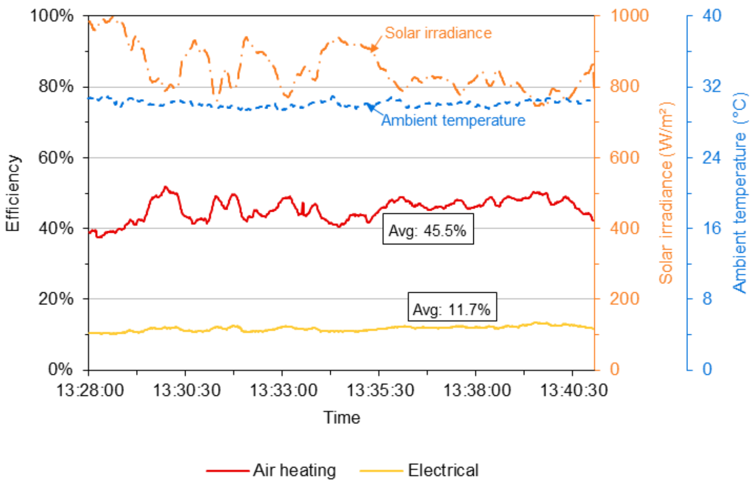

Figure 7-11 Experimental results on the thermal and electrical efficiency of the air mode PVT-RC collector with mass flow rate of 0.035 kg/s.

When the air and water modes are combined into the bi-fluid mode PVT-RC collector, the total efficiency increases even further. Experimental data plotted in Figure 7-12 show that a maximum thermal efficiency of 80% is possible to achieve, although as time progresses, it reduced with an average efficiency of 64.6%. This value is about 22% and 8% higher than the water and air only respectively. The contribution of air heating remains the highest, while the electrical efficiency is still at 11%.

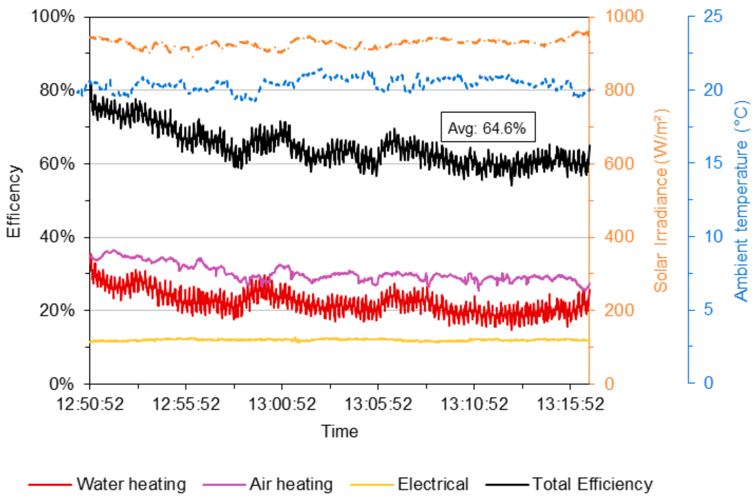

Figure 7-12 Experimental results on the thermal and electrical efficiency of the bi-fluid mode PVT-RC.

b. Nighttime experiment

To show the occurrence of the cooling effect in the PVT-RC collector, nighttime experiments were conducted for the air-mode PVT-RC collector. Data from the night experiment 9th of August 2022 are plotted in Figures 7-13 below. With the ambient temperature of 23.5°C, the sub-ambient outlet air temperature could be achieved during the test period. While the PVT-RC module temperature was recorded to be 1.6°C lower than ambient, the maximum temperature reduction in the air outlet was 1.1°C. The respective cooling power obtained from the experiment was 44.7 W/m^2 on average.

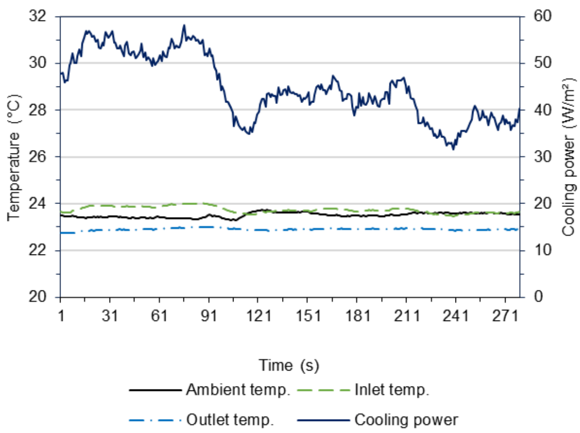

Figure 7-13 Cooling power air mode (m=0.05 kg/s)

7.4 Modelling of the PVT-RC Collector

Figure 7-14 shows the general steps in modelling the PVT-RC collector in Ansys Fluent. The PVT-RC collector structure in Figure 7-3 was translated into Fluent's geometry as in Figure 7-15. The geometry was simplified by removing the manifold pipes at both ends of the water channel to reduce the complication in the meshing process. This simplification then means the model assumes that the flowing water is uniformly distributed into the eight copper pipes. Furthermore, the geometry was discretised with structured hexahedral meshes with a maximum size of 5 mm similar to the previous mesh used in Chapter 6. Similarly, the setups of the CFD models for this chapter also follow the description in the chapter.

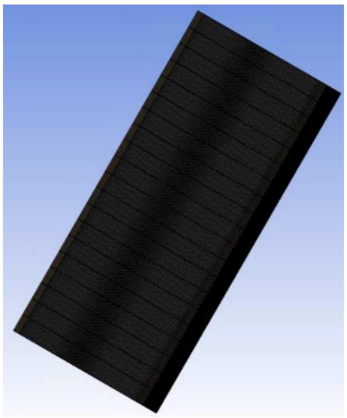

Figure 7-14 Ansys Fluent's geometry of the PVT-RC collector and its meshing.

7.4.1 Electrical efficiency

The performance of the PVT-RC collector in generating electrical energy is characterised by its electrical efficiency. To calculate the electrical efficiency (η_{el}) of the PVT-RC collector, the formula developed by Duffie and Beckman (2013) shown in Equation 7.4 is introduced. In Equation 7.4, η_{STC} is the efficiency of the PV used in the PVT-RC collector at the STC (1000 W/m^2 solar irradiance, 25°C ambient temperature), β_c id temperature coefficient of efficiency (given as 0.0045 K^{-1} by Duffie and Beckman (2013)), and T_{PV} is the surface temperature of the PV.

$$\eta_{\mathrm{el}} = \eta_{\mathrm{STC}}(1 - \beta_c(T_{\mathrm{PV}} - 25)) \qquad 7.4$$

From the equation, the electrical power delivered per square meter of the PVT-RC collector can be derived as in Equation 7.6 with H as the solar irradiance, and τ_{cov} as the transmissivity of the PE cover.

$$q_{\mathrm{el}} = \eta_{\mathrm{el}}\tau_{\mathrm{cov}}H \qquad 7.5$$

7.4.2 Heating/cooling power and thermal efficiency

From the heat balance equations described in Chapter 3 and applied to the boundary conditions of the CFD model, the simulation then can result in the thermal efficiency and heating/cooling power. The outlet temperature data obtained from the CFD simulations are used in the heating/cooling power ($q_{\text{heating/cooling}}$) calculation with Equation 7.6.

$$q_{\text{heating/cooling}} = \dot{m}c_p(T_{\text{outlet}} - T_{\text{in}}) \quad 7.6$$

From Equation 6.18, one can then derive the thermal efficiency (η_{th}) equation for daytime operation as in Equation 7.7, with A as the PV area.

$$\eta_{\text{th}} = q_{\text{heating}}/AH \quad 7.7$$

7.4.3 Validation of the CFD model

To validate the CFD model, results from the simulations were compared to the experimental. The model needs to show agreement for both the daytime and nighttime performance of the PVT-RC collector from the experiment. For the daytime performance, the outlet temperature and electrical efficiency data from the bi-fluid PVT-RC collector experiment were used to validate the model. The results are summarised in Figures 7-15 and 6-18. As seen in Figure 7-15a, the outlet temperature from the simulation both for air and water matches closely with the experiment. The RMSD values for the air and water heating are 3.3% and 1.6% respectively. For the electrical efficiency of the PVT-RC collector, Figure 7-15b also shows a good agreement between the model and experiment. Although there is a difference in the variability of the data (experimental data is more fluctuated than the simulation), the RMSD is still very low at 2.0%.

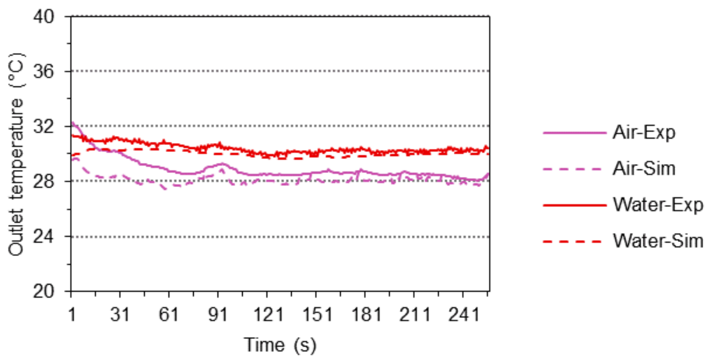

(a)

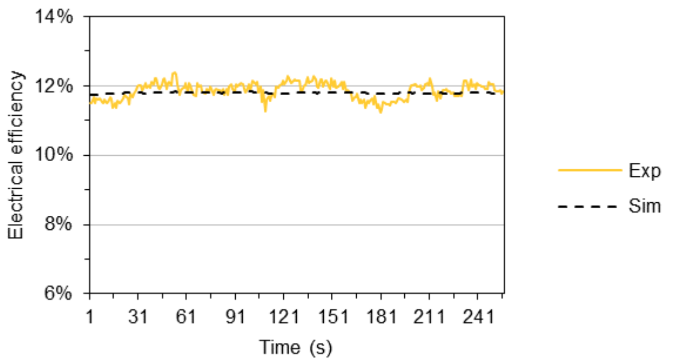

(b)

Figure 7-15 Validation of the mathematical model for the daytime (a) heating and (b) electricity generation.

Further, in terms of the nighttime performance, the model also shows good agreement with the experimental data. Figure 7-16 shows the alignment of the simulation results with the experimental data. Here, the air outlet temperature of the PVT-RC collector is used to calibrate the model. The results give an RMSD value of 2.4%.

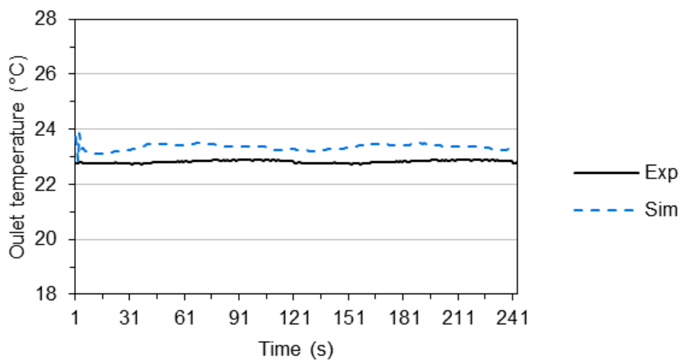

Figure 7-16 Validation of the mathematical model for the nighttime cooling.

7.5 Effects of various parameters on the performance

Analysis of the effect of various parameters on the PVT-RC collector's performance is conducted separately for water- and air-only modes, as well as for the bi-fluid mode. In the water mode, two influential parameters need to be analysed, *i.e.*, mass flow rate and water inlet temperature. The latter parameter is analysed because the water inlet temperature can be different from the ambient temperature, and its effect can be influential. On the other hand, the air inlet draws from the ambient temperature and thus, analysis of the air-mode PVT-RC is concerned only with the effect of the mass flow rate. Meanwhile, the parametric analysis of the bi-fluid PVT-RC collector is conducted using fixed water and air mass flow rates, and thus the analysis only discusses the effect of ambient temperature.

7.5.1 Water mode

The effect of mass flow rate on the thermal and electrical efficiency of the water-mode PVT-RC is depicted in Figure 7-17. Higher mass flow rates create better heat transfers between the pipe wall and the water. Thus, the thermal efficiency of the PVT-RC increases with the rise in water mass flow rate with logarithmical relation. However, since the contact between the water pipe and the PVT-RC module is limited only in several places, the increase in thermal efficiency is not as dramatic as the air-mode PVT-RC that is shown later in Section 7.5.2. There is about a 2% increase in thermal efficiency between the 0.01 kg/s and 0.05 kg/s water mass flow rate.

Moreover, because the absorbed heat by the PVT-RC module is carried more by the higher water mass flow rates, it is also observed that the electrical efficiency also increases. Yet, the rate of electrical efficiency is even less than the thermal efficiency of the water-mode PVT-RC. As seen in Figure 7-17, the electrical efficiency line seems flat in the range of 10.3% to 10.4% range, with an increase of only 0.1% between the 0.01 kg/s and 0.05 kg/s water mass flow rate.

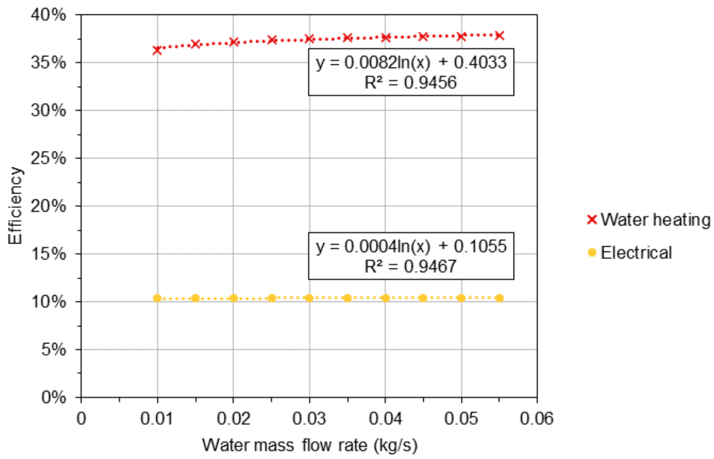

Figure 7-17 Effect of water mass flow rate on the thermal and electrical efficiency of the water-mode PVT-RC collector (H=1000 W/m^2, T_{amb}=25°C).

Similarly, the water mass flow rate also has a positive impact on the cooling power of the water-mode PVT-RC at night. There is an increase of around 2 W/m^2 between the 0.01 kg/s and 0.05 kg/s water mass flow rate. As previously mentioned, the limited contact between the PVT-RC module with the pipe is responsible for this relatively small increase in cooling power for the water-mode PVT-RC collector. Figure 7-18 summarises the cooling power of the water-mode PVT-RC collector with different mass flow rates.

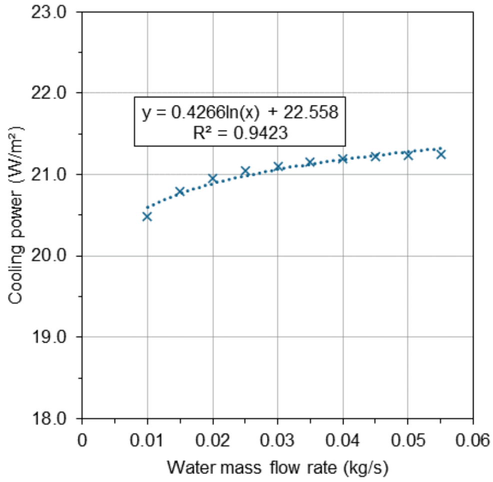

Figure 7-18 Effect of water mass flow rate on the cooling power of the water-mode PVT-RC collector (H=1000 W/m^2, T_{amb}=25°C).

For the effect of water inlet temperature on the thermal efficiency in the daytime, the term reduced temperature ($(T_{wi} - T_{amb})/H$) is introduced, which is a relationship between the water inlet temperature, ambient temperature, and solar irradiance. As shown in Figure 7-19, both thermal and electrical efficiency decreases when the reduced temperature becomes larger. This means the effectiveness of the heat transfer from the PVT-RC module to the water is lower for the warmer-than-ambient water inlet temperature. In a 1000 W/m^2 solar irradiance, there is around a 4% reduction in thermal efficiency for every 10°C warmer inlet temperature. The effect is less noticeable in the electrical efficiency, with only <1% reduction for every 10°C warmer inlet temperature.

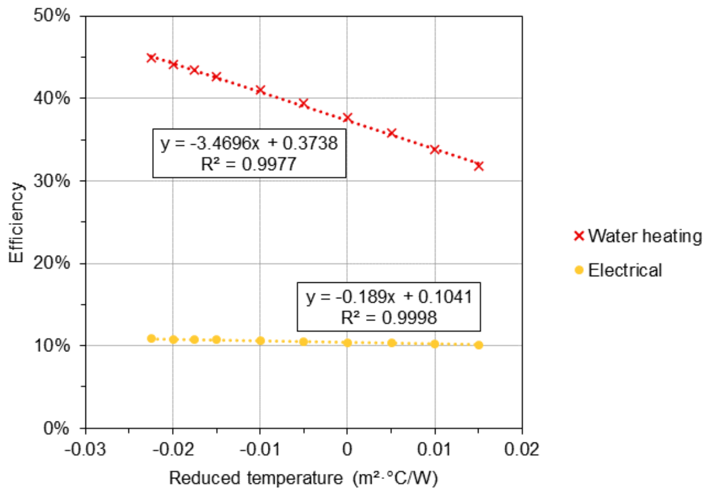

Figure 7-19 The relation between the reduced temperature with the thermal and electrical efficiency of the water-mode PVT-RC collector (H=1000 W/m^2, T_{amb}=25°C).

Contrary to the effect of water inlet temperature on the heating and electrical performance, the cooling performance of the water-mode PVT-RC collector shows a positive correlation with the water inlet temperature. This is because in a certain ambient temperature and assuming the sky condition is perfect for radiative cooling, there is a minimum sub-ambient surface temperature for the PVT-RC module. With this minimum sub-ambient temperature being related to the ambient, one can expect that the warmer the water inlet temperature than the ambient, the larger the cooling effect obtained from the PVT-RC collector. Likewise, if the water inlet temperature is below this minimum surface temperature, cooling cannot be extracted from the PVT-RC collector.

The abovementioned analysis is properly summed up in Figure 7-20. In the figure, it is seen that the cooling effect of the PVT-RC collector escalates along with the water inlet temperature. It is also found that with an ambient temperature of 25°C the PVT-RC collector cannot deliver cooling when the water inlet temperature is around 6°C lower than ambient. This limit temperature might vary with different ambient temperatures.

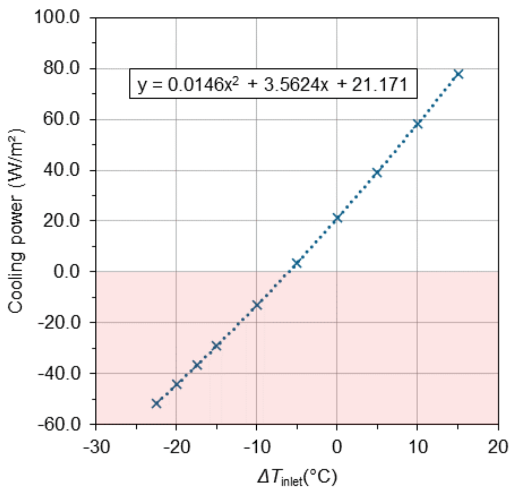

Figure 7-20 Effect of inlet temperature on the cooling power of the water-mode PVT-RC collector (H=1000 W/m^2, T_{amb}=25°C).

7.5.2 Air mode

The effect of air mass flow rate on the thermal and electrical efficiency of the air-mode PVT-RC collector is similar to the water-mode. The higher the air mass flow rate the greater the efficiency of the air-mode PVT-RC collector. The apparent difference is in the rate of increase of the thermal efficiency of the air-mode PVT-RC collector. As shown in Figure 7-21, the thermal efficiency of the air-mode PVT-RC collector increases at a higher rate than the water-mode. There is almost a 20% gap in thermal efficiency between 0.01kg/s and 0.05kg/s air mass flow rates, compared to 2% in the water mode. The better thermal contact between the air in the air duct with the PVT-

RC module and the water in the pipe is one of the reasons for this discrepancy. For electrical efficiency, however, there is not much difference with the water-mode PVT-RC collector.

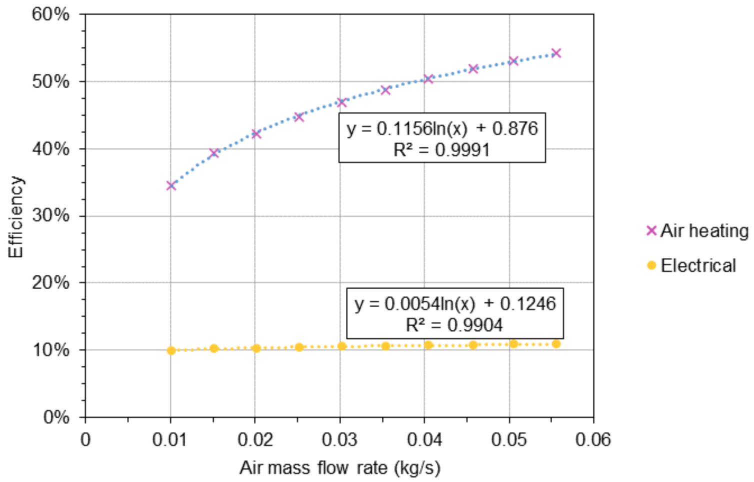

Figure 7-21 Effect of air mass flow rate on the thermal and electrical efficiency of the air-mode PVT-RC collector (H=1000 W/m^2, T_{amb}=25°C).

Similarly, the rate of increase in cooling power with the rise of air mass flow rate of the air-mode PVT-RC collector is also greater than in the water-mode (Figure 7-22). There is around 10 W/m^2 cooling power increase between 0.01 kg/s and 0.05 kg/s air mass flow rate. This value outpaces the 2 W/m^2 in cooling power for the same increase in the mass flow rate. Also, the cooling power of the air-mode PVT-RC collector is always higher than the water-mode even with the lowest mass flow rate. The air-mode PVT-RC collector's cooling power can be up to 1.5 times higher than the water mode. This discrepancy can again be attributed to the differences in the contact area between the air duct with the PVT-RC module and the water pipe with the PVT-RC module.

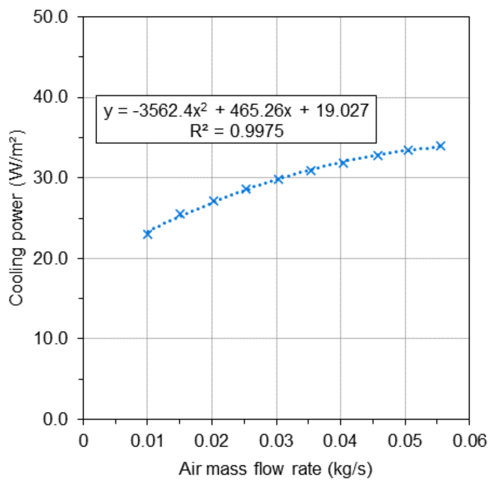

Figure 7-22 Effect of various air mass flow rate on the cooling power of the air-mode PVT-RC collector (H=1000 W/m^2, T_{amb}=25°C).

7.5.3 Bi-fluid mode

Compared to the previous single-fluid mode of the PVT-RC collector, the bi-fluid mode undoubtedly has better total efficiency and cooling power. Because there is no significant difference between the bi-fluid and single-fluid modes of the PVT-RC collector except for the number of working fluids involved, it can be deduced that the effects of mass flow rates and water inlet temperature on the collector's performance are the same as in the Sections 7.5.1 and 7.5.2. Thus, for the bi-fluid mode PVT-RC collector, this section only discusses the effect of ambient temperature on the PVT-RC collector's performance.

Figure 7-23 reveals that as the ambient temperature rises during the daytime, the total efficiency (and total power) of the PVT-RC collector follows linearly. However, the rate of this efficiency increase is minuscule. In a 1000 W/m^2 solar irradiance, the total efficiency rises just about 1% (or 10 W/m^2 total power) for every 15°C ambient temperature raised. Nonetheless, the bi-fluid PVT-RC collector can achieve a total efficiency of more than 70% during the daytime.

Further, a detailed analysis of the efficiency of each component of the bi-fluid PVT-RC collector reveals the reason for the slight increase in the total efficiency. As shown in Figure 7-23, the electrical efficiency reduces as the temperature becomes warmer, while the water heating efficiency stays relatively constant. This condition leaves only the air heating efficiency as the main contributor to the raised in total efficiency of the PVT-RC collector in the warmer ambient temperature. Considering the reduction from the electricity side, the contribution of the air heating efficiency to the total efficiency becomes even less, thus the total efficiency only escalates slightly with the warmer ambient temperature.

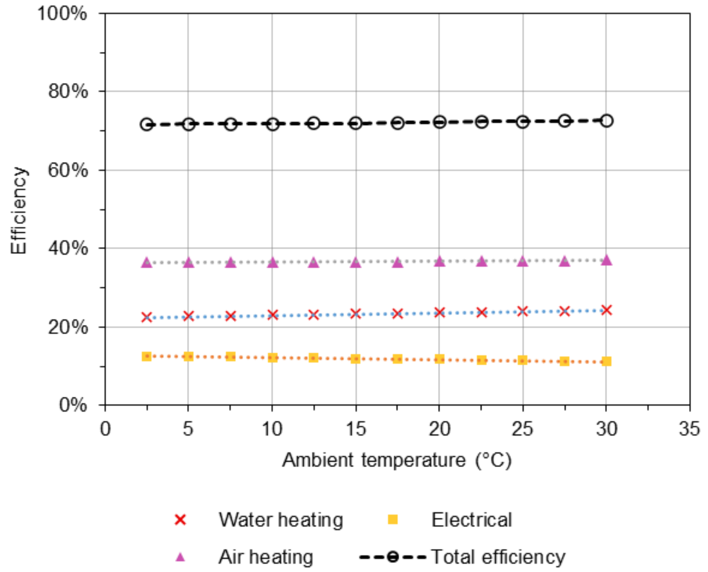

Figure 7-23 Effect of air mass flow rate on the thermal, electrical, and total efficiency of the air-mode PVT-RC collector (H=1000 W/m^2, $T_{\text{in}} = T_{\text{amb}}$).

In terms of the effect of ambient temperature on the cooling power at night, Figure 7-24 shows a contrasting pattern to the daytime performance. If the warmer ambient results in a better total power during the daytime, it is unfavourable during the night. As shown in Figure 7-24, there is a significant reduction in cooling power in the higher ambient temperature. This polynomial pattern between the cooling power and the ambient temperature might be caused by the sky temperature formula in Equation 3-5, which gives a higher gap between the sky and ambient temperatures as the latter becomes smaller. Nevertheless, Figure 7-24 also indicates that the PVT-RC collector potentially achieves more than 40 W/m^2 of cooling power during the night.

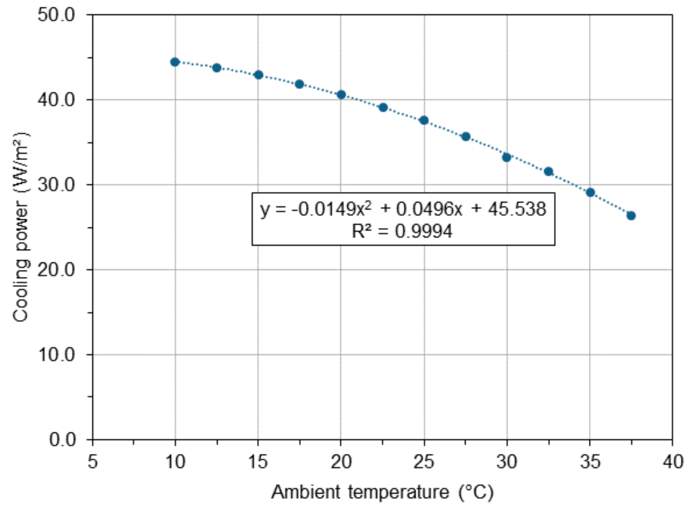

Figure 7-24 Effect of ambient temperature on cooling power of the bi-fluid PVT-RC.

7.6 Performance Evaluation of the Trifunctional Bi-fluid PVT-RC Collector

7.6.1 Comparison between PV, PVT, and PVT-RC

The main advantage of the bi-fluid PVT and PVT-RC collectors for daytime performance is their ability to exploit more thermal energy compared to conventional PV modules. Figure 7-25a summarises this superiority of the PVT and the PVT-RC collectors by depicting the efficiency of each component and the respective total efficiency of the PV module, PVT, and PVT-RC collectors. The data are obtained from steady-state simulations in the STC (1000 W/m^2 solar irradiance, 25°C ambient temperature). Due to the multifunctionality of the PVT and PVT-RC collectors, it is at least 65% more efficient in energy production than the PV module. The electrical efficiencies of the PVT and PVT-RC collectors are also better than the PV module only because the two working fluids cool down the PV surface.

Further, a comparison between the PVT collector and PVT-RC collector for daytime performance hints at the better thermal efficiency of the former. As shown in Figure 7-25a, the thermal efficiency of the PVT collector (for water and air heating) is 77.5%. Meanwhile, the thermal efficiency of the PVT-RC collector is 63.8% or 13.7% less than the bi-fluid PVT collector. This is due to the difference in the convection cover, which is a glass cover for the PVT collector and the PE cover for the PVT-RC collector. The glass cover is better at blocking thermal radiation from the PV panel to the sky. Thus, the surface temperature of the PV is higher when using the glass cover rather than when employing the PE cover.

Nonetheless, this cover modification that causes the slightly lower daytime thermal efficiency is a trade-off for the PVT-RC collector to get a much better nocturnal cooling performance than the PVT collector. Figure 7-25b compares the water- and air-cooling power of the PV module, PVT collector, and PVT-RC collector. The conventional PV module is not intended to benefit from nighttime radiative cooling, and thus no cooling energy is collected from it. Whereas a comparison of the cooling performance of the PVT and PVT-RC collectors hints at the superiority of the latter in providing cooling. The PVT-RC collector can provide up to 38.7 W/m^2 of cooling power, divided into 27.4 W/m^2 from air cooling and 11.3 W/m^2 from water cooling. The total cooling power from the PVT-RC collector is more than 7 times higher than the PVT collector with only 5 W/m^2 total cooling power. Therefore, the bi-fluid PVT-RC collector can work as a tri-functional collector rather than only serve two functions like the bi-fluid PVT collector. This advantage also makes the PVT-RC collector possible for multi-seasonal use.

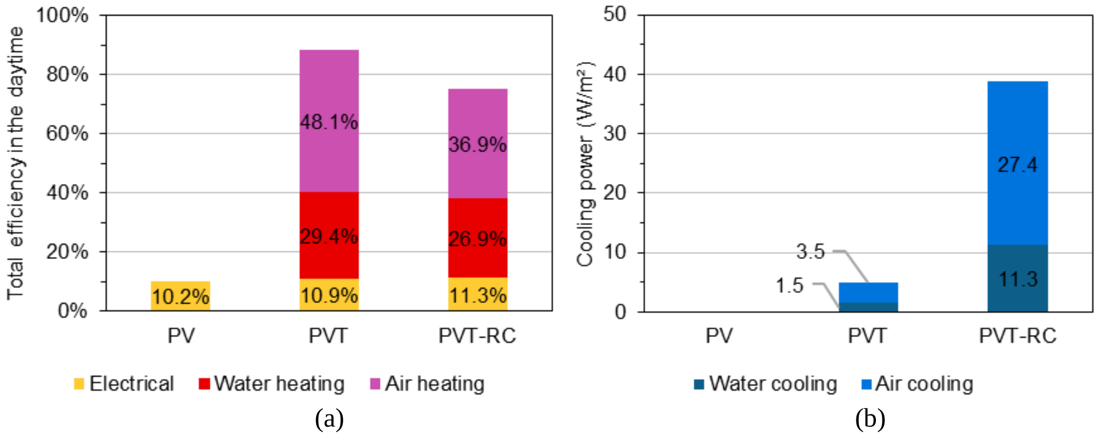

Figure 7-25 Comparison between daytime thermal and electrical efficiency and nighttime cooling power of PV, PVT, and PVT-RC (water and air mass flow rates: 0.035 kg/s each).

Regarding the cost, it is clear that the PVT and PVT-RC collectors would have higher initial costs compared to the PV only. However, the total efficiency of the PVT and PVT-RC collectors is several times of that PV only. Although the operational cost of the PVT and PVT-RC collectors (which are also higher than the PV-only) should be deducted from the total efficiency, the total energy generated by the two collectors is higher than the PV-only system. Moreover, between the PVT and PVT-RC collectors, the initial cost would be roughly similar, or the PVT-RC could be even cheaper in initial cost than the PVT collector because of the use of a cheaper cover (PE film compared to glass). But, in terms of the maintenance cost for the PVT-RC collector would be more than the PVT collector due to the same reason since the PE film cover is much less durable than the glass cover.

7.6.2 Annual energy generated by the building-integrated PVT-RC collector.

After the advantages of the PVT-RC collector over the PV or PVT collector are quantitatively evaluated, it is appropriate to then appraise its annual energy generation. Two cities are selected in this chapter to assess the building-integrated PVT-RC collector performance in different climates. The cities are Madrid (representing warm-temperate and dry climate), and Seoul (representing cold-temperate and more humid climate). A summary of some important climatic parameters of each city is shown in Figure 7-26 below. The differences between the two climates are apparent from the solar irradiance and humidity data. Madrid has more solar irradiance and a dryer climate than Seoul. This dryer condition leads to a larger gap between the sky temperature and ambient temperature in Madrid compared to Seoul, indicating the higher radiative sky cooling potential in Madrid.

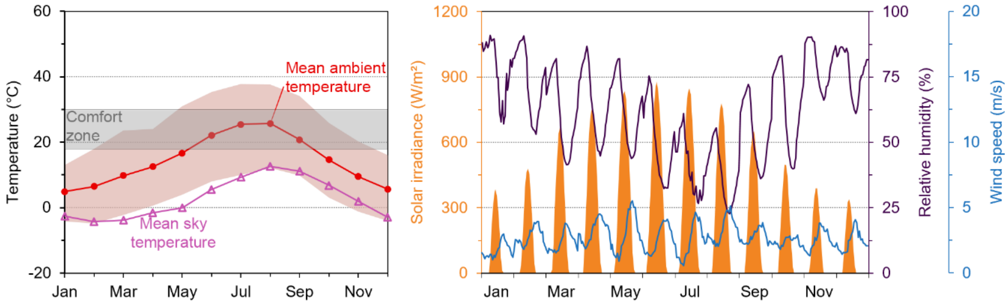

(a) Csa

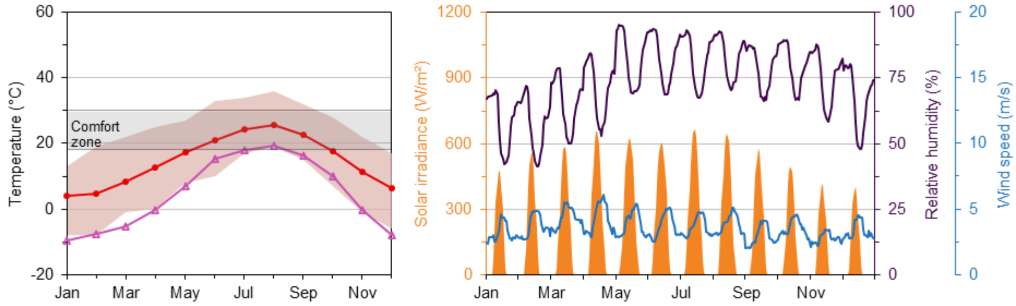

(b) Cfa

Figure 7-26. Dry bulb temperature data for (a) Madrid, Spain; and (c) Seoul, Korea (Liggett and Milne, 2021; Lawrie and Crawley, 2022).

In terms of heating energy yield, one could expect the total daytime energy yield to peak in summer months, since the solar radiation level and duration are higher in this period. This is rightly shown in the heating and electrical energy yield data for the PVT-RC collector in Madrid (Figure 7-27a). In the summer months in Madrid, the PVT-RC collector can reach almost 80 kWh/m^2 of total heating and electrical energy monthly. Nonetheless, one should also expect variations in the total amount of daytime energy generated between climates. Figure 7-27a shows that the total daytime energy in Seoul does not peak in the summer. Rather, the PVT-RC collector performs best around March in Seoul. This different pattern is due to the dryer conditions in Seoul during the spring season compared to the summer (Figure 7-27a). With only little variations in the solar irradiance level between spring and summer in Seoul, these dryer months with clear sky days are more advantageous for the PVT-RC collector.

Moreover, in both climates, the air heating function has more portion to the total energy yield in the daytime, as apparent from the graph in Figure 7-27a. The percentages of contribution from the air heating function in the total daytime energy yield are 39.8% and 40.3% in Madrid and Seoul respectively. The second most energy yield in the daytime by the PVT-RC collector is for water heating, which accounts for about 20.3% and 19.4% of the total daytime energy yield in Madrid and Seoul respectively. These percentages leave the electrical energy yield with only around 13% contribution to the total daytime energy yield.

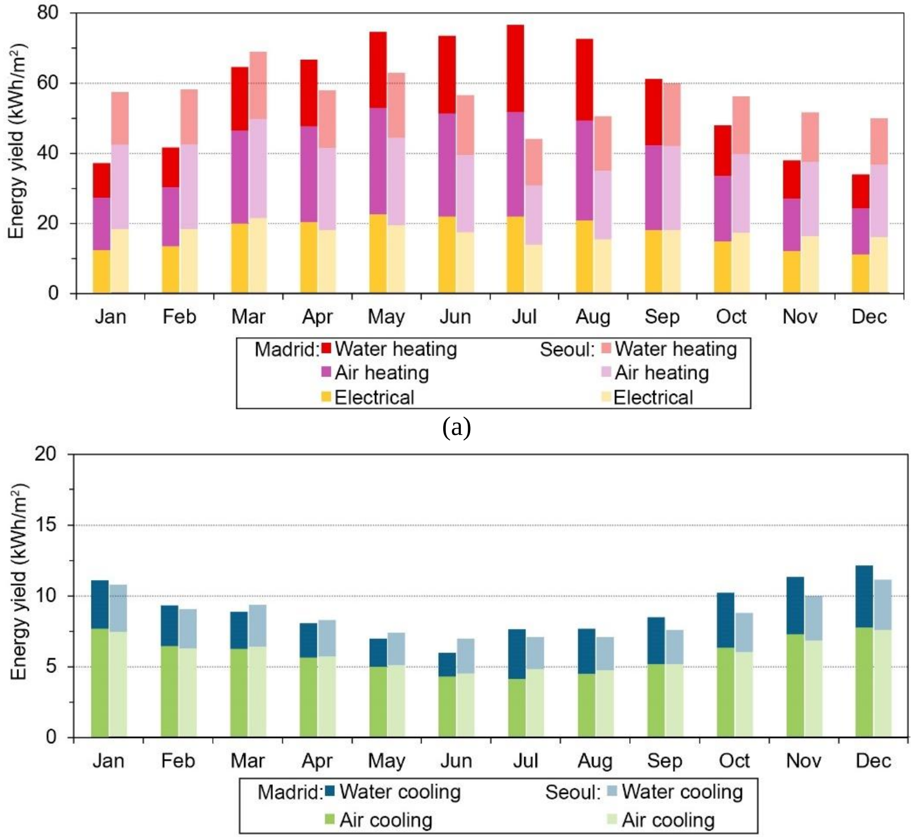

(b)

Figure 7-27 Monthly energy yield from the PVT-RC collector in Madrid and Seoul for (a) daytime heating and electrical energy, and (b) nighttime cooling energy.

If the daytime total energy for two climates has different monthly patterns, in terms of the nighttime cooling energy yield, their patterns are similar. Months of long nights during the winter provide the condition for the PVT-RC collector to collect more cooling energy. Thus, in Figure 7-27b, the total nighttime cooling energy by the PVT-RC collector peaks in December both in Madrid and Seoul. It is also found that the air-cooling function yields more energy than the water cooling with almost 70% contribution to the total cooling energy yield in both cities. Nevertheless, one would expect variations in the amount of cooling energy yield between the cities. As seen in Figure 7-27b, the PVT-RC collector in Madrid yields more cooling energy than in Seoul most of the months. In the total annual cooling energy figure, the PVT-RC collector yields almost 5 kWh/m^2 more cooling energy than Seoul.

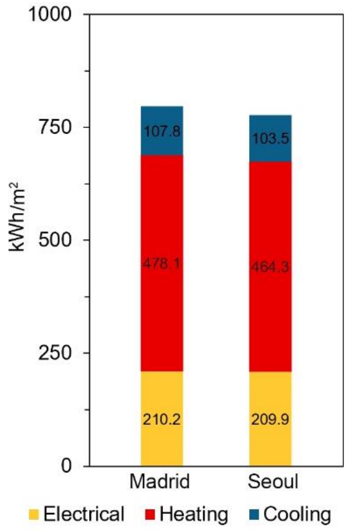

Figure 7-28 Annual heating, cooling, and electrical energy yield by the PVT-RC in Madrid and Seoul.

Further, in terms of the total annual energy generated, combining the heating, electrical and cooling energy, the PVT-RC collector has better performance in Madrid than in Seoul. As shown in Figure 7-28, the collector can yield a total energy of 623.6 kWh/m^2 annually in Madrid. This value is almost 20 kWh/m^2 higher than the total annual energy generated by the PVT-RC collector in Seoul. In both climate types, most of the total annual energy (around 77%) is contributed by heating energy, followed by cooling energy with 17%, and electrical energy with 6%.

7.6.3 Energy saving potential of the building-integrated PVT-RC collector

The previous section has examined the energy yield of the PVT-RC collector when applied in the case study building. In this section, the potential saving from that energy yield is estimated. To recall Section 7.1, the case study building is a 100 m^2 residential building with two bedrooms (see Figure 7-5 for the building plan and 3D representation). The PVT-RC collectors are arranged in an array of 10 collectors mounted on the pitched roof of the building. As in Figure 7-4, the PVT-RC is connected to electrical, hot- and cold-water tanks, as well as a hot or cold air supply system.

As the PVT-RC collector is connected to those functions, the discussion on the energy-saving potential is divided into three parts namely the electrical, water heating, as well as space heating and cooling energy savings. All energy loads, whether it is electrical, water heating, space heating, or space cooling loads, are obtained from the EnergyPlus simulation of the case study building in the two locations. Assumptions made on the load calculations are detailed in each part of the discussion below. The EnergyPlus settings follow similar settings as in Section 6.3.

a. Electricity

Firstly, the reduction in the electrical energy is directly estimated from the electricity load data from the EnergyPlus simulation with the electrical energy yield data from Section 7.6.2. In the EnergyPlus model, the electricity load is calculated from the people, lighting, and equipment load input, which are all set in terms of power per space floor area. For the case study building in Madrid and Seoul, this study used a people load input of 0.028 W/m^2, lighting load input of 10.66 W/m^2, and equipment load input of 3.87 W/m^2. The usage of these loads is then dependent on the scheduling and climate conditions of Madrid and Seoul.

The comparison of electricity load and the potential saving from the PVT-RC collector for the two case study locations is shown in Figure 7-29. The monthly electrical load patterns in the two locations are similar. The only difference is in the total amount of energy consumption annually. Nevertheless, the electrical energy generated by the PVT-RC collector varied between these locations as the monthly solar radiation intensity and the clear sky condition in the two locations were different.

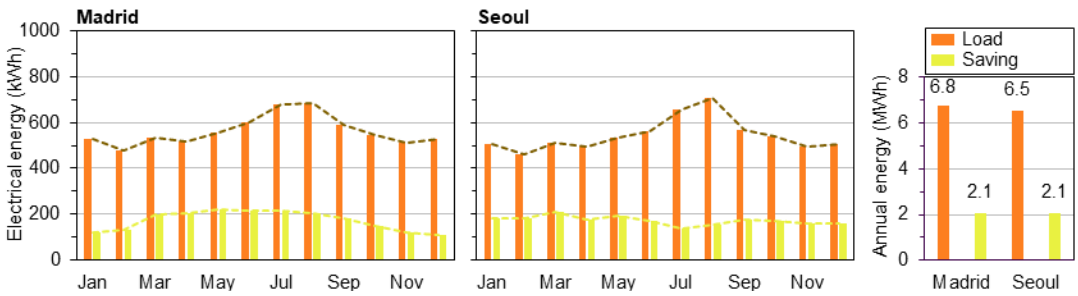

Figure 7-29 Monthly and annual electricity loads and savings of the building-integrated PVT-RC case study in Madrid and Seoul (A = 9.88 m^2).

The annual electrical load of the case study building in Madrid is around 6.8 MWh, and in Seoul is around 6.5 MWh. Yet, as previously shown in Section 7.6.2, the annual electrical energy generation of the PVT-RC collector in Madrid and Seoul shares a close value of around 2.1 MWh. This makes the percentage of electrical energy saving in Seoul larger than in Madrid with a respective value of 31.7% and 30.8%.

b. Water heating

The second function is water heating. The water heating load is calculated from the schedule of hot water usage, the hot water system used, and the ambient and hot water temperatures. This study used a gas water heater with 0.9 burner efficiency with the hot water temperature and load scheduling pattern following the data in the Energy Saving Trust (2008) report. The ambient water temperatures of Madrid and Seoul were set as 20°C and 18°C respectively.

Figure 7-30 displays the comparison between the water heating load and potential savings by the PVT-RC collector. In the EnergyPlus simulation to get the water heating load, the domestic gas water heater was used as the conventional heating supply for the water. Like the electrical energy, the two locations share an almost identical pattern of the monthly water heating load but are different in the amount of saved energy. This discrepancy is again due to the same reason as the electrical energy, which is the difference in monthly solar radiation intensity and the clear sky index.

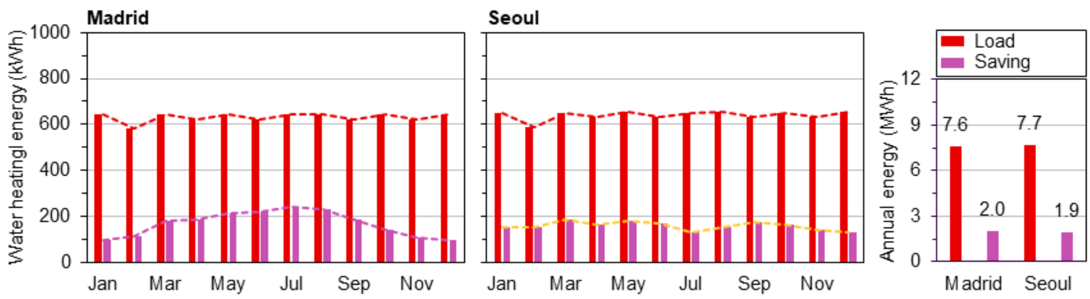

Figure 7-30 Monthly and annually water heating loads and savings of the building-integrated PVT-RC case study in Madrid and Seoul ($A = 9.88$ m^2, $\dot{m} = 0.035$ kg/s).

The energy saving from water heating in Madrid peaks in the summer, while in Seoul, it peaks in March. In terms of the total annual water heating load, Seoul demands more energy for water heating than Madrid, with a gap of 114 kWh. Whereas, in terms of energy saving provided by the PVT-RC collector, Madrid climate provides the better value with roughly 116 kWh more energy saved than Seoul. Hence, the building-integrated PVT-RC collector has more percentage of energy saving from water heating at 26.7% compared to Seoul with 24.8%.

c. Space heating and cooling

The third on the list is the energy saving from space heating and cooling. The method used in the calculation of energy saving for space heating and cooling is the same as the method used in Chapter 5, especially in Section 6.4.2. The heating and cooling load was calculated from an HVAC system with a gas heating coil with an efficiency of 0.9 and a direct expansion cooling coil (single speed) with a rated COP of 3.6 (ASHRAE, 2018). The set point temperatures for space heating and cooling were set at 21°C and

24°C., and the heating and cooling supply air temperatures were 40°C and 18°C respectively.

Figure 7-31 compares the heating load and the energy reduction offered by the PVT-RC collector in Madrid and Seoul. The figures reveal the expected pattern for the heating load that soars in the winter. The peak heating load in Seoul is almost double that in Madrid. In the annual energy load term, the case study building in Seoul needs 5.6 MWh for space heating while, in Madrid, it requires only 3.3 MWh.

Moreover, as the day is shorter during this heating season period, the heating energy provided by the PVT-RC collector is not as high as expected. Also, sometimes in the daytime, the room temperature might be warm enough to not need space heating, and thus the heated air from the PVT-RC is not always useful. For this reason, the potential energy savings from space heating become minuscule compared to the heating loads in both locations. In the annual term, the useful heating energy that contributes to the reduction in the space heating load is around 772 kWh (13.8 % saving) in Seoul and around 229 kWh (6.7%) in Madrid.

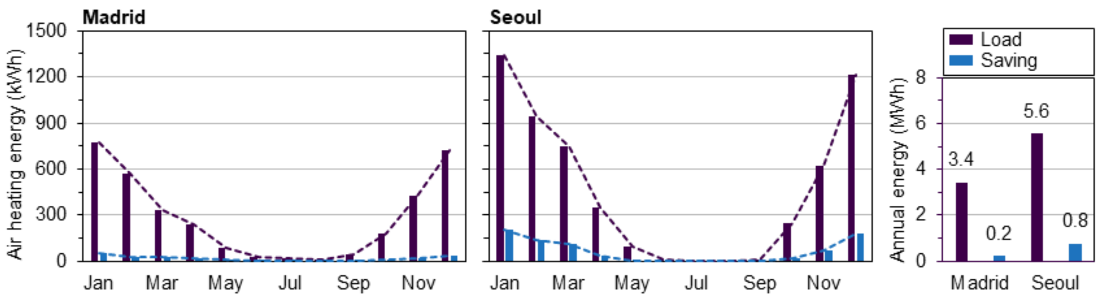

Figure 7-31 Monthly and annually space heating loads and savings of the building-integrated PVT-RC case study in Madrid and Seoul (A = 9.88 m^2, $\dot{m}$ = 0.023 kg/s).

In terms of energy saving from space cooling, Figure 7-32 summarises the cooling load and the useful cooling energy from the PVT-RC collector in the two climates. As seen in the figure, the cooling load peaks in the summer while the radiative cooling effect at night cannot catch up with the demand that mostly occurs during the day. This mismatch, along with the mismatch in the space heating load and yield, emphasises the importance of a cold storage mechanism for space cooling or heating to optimise the respective energy yield.

Madrid climate demands the case study building to be cooled down more frequently and thus makes the cooling load higher than in Seoul, as seen in the monthly and annual data in Figure 7-32. In Madrid, the cooling load is around 632.5 kWh annually, while in Seoul, it is 323.4 kWh. Nonetheless, the building-integrated PVT-RC collector also provides more useful energy for cooling in Madrid climate than in Seoul, with an annual gap of up to 57.4 kWh. The percentage of energy savings from space cooling for Madrid and Seoul annually is 15.4% and 12.3% respectively.

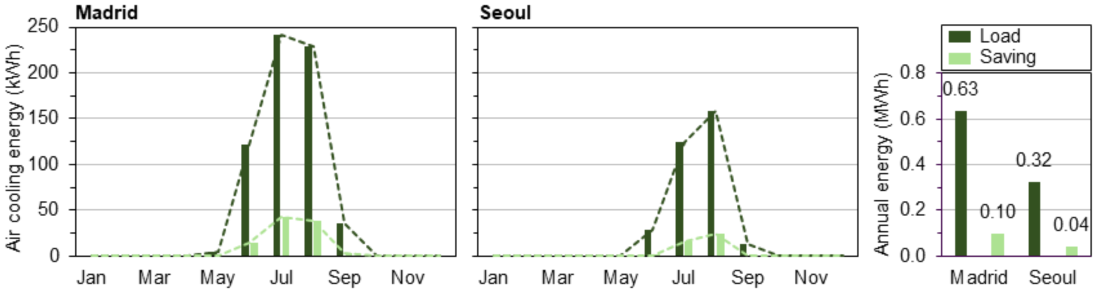

Figure 7-32 Monthly and annually space cooling loads and savings of the building-integrated PVT-RC case study in Madrid and Seoul (A = 9.88 m^2, $\dot{m}$ = 0.023 kg/s).

It is worth noting that, unlike the electricity and water heating loads that are required throughout the year, the space heating and cooling loads are seasonal. The flexibility to be used in both heating and cooling seasons is the advantage of the PVT-RC collector over the conventional PVT collector. It is especially remarked by the potential 15.4% and 12.3% energy savings from cooling in Madrid and Seoul, which would never be achieved with the conventional PVT collector.

7.7 Summary of Findings

The proof-of-concept of the most active proposed system in this thesis has been elaborated in this chapter. Experiments and simulations were conducted to evaluate the PVT-RC collector. The experiments have shown the ability of the PVT-Collector to collect heating and cooling during the day and night without intervening in the electrical performance of the modified PV module.

With the data from the experiments, a CFD model of the PVT-RC collector was validated and then used in parametric studies and performance evaluations. It is found that the mass flow rate positively correlates with the heating and cooling performance of the PVT-RC collector. Whereas the electrical efficiency is not affected much by the change in the air and water mass flow rates. The ambient temperature, however, negatively correlates with the heating, cooling, as well as electrical performance, *i.e.*, with the increase in ambient temperature, the collector performance deteriorates. In optimal conditions in the daytime, a total efficiency of 72% can be achieved by the bi-fluid PVT-RC collector. In optimal conditions at night, the bi-fluid PVT-RC collector can provide up to 45 W/m^2 cooling power.

One of the advantages of the bi-fluid PVT-RC collector compared to a conventional PV module or PVT collector is its ability to collect more thermal energy. On top of that, unlike the conventional PV module or PVT collector, the PVT-RC collector can also work at night to collect cooling energy. These advantages are shown in this chapter. For instance, the PVT-RC collector is found to be at least 25% more efficient in energy production than the PVT collector, and 65% more than the conventional PV. In terms of cooling power, the PVT-RC collector can provide up to 38.7 W/m^2 of cooling power, divided into 27.4 W/m^2 from air cooling and 11.3 W/m^2 from water cooling. The daytime efficiency can be converted into the power term and added with the cooling power to get the total power generated by the PVT-RC collector. Under the STC, one can expect 300 W/m^2 more power than the conventional PVT collector, and 700 W/m^2 more than the PV module.

Moreover, analysis of the building-integrated PVT-RC collector for the case study building shows the potential energy generation of the system. With 5 collectors attached to the gabled roof of a 10×10 m^2 residential building, the PVT-RC collector can deliver more than 600 kWh/m^2 of total energy annually in Madrid and Seoul climates. In Madrid climate, the building-integrated PVT-RC collector yields up to 20 kWh/m^2 more total energy annually than Seoul. Among the three different functions of the PVT-RC collector, the heating functions contribute the most to the total energy yield by 77%, compared to 17% contribution from cooling and 6% from electricity. Nonetheless, all the potentially generated energy shown in this chapter needs to be matched with the heating, cooling, and electricity demands of the building. Further studies need to be conducted to estimate the real savings from the building-integrated PVT-RC collector. In such a study, the involvement of thermal and electrical energy storage is required to overcome the mismatch between the supply and demand time.

Chapter 8 Conclusion and Future Study

8.1 Summary of the Thesis

Research on radiative sky cooling revives after the breakthrough in passive daytime radiative cooling. The research direction is now not only in the development of the radiative cooling emitter material but also in real-world applications. One research field that is particularly interested in the idea of using radiative cooling is the research in sustainable building. This thesis has attempted to contribute to the field by choosing a combination of solar energy technologies as the strategy to apply radiative cooling in buildings.

Chapter 2 of this thesis has reviewed the current research on the application of radiative cooling in buildings, specifically on how it is combined with solar energy technologies. There are at least three common themes of how radiative cooling is used. The first theme is the radiative cooling mechanism is used to enhance the performance of existing technologies. Secondly, radiative cooling is employed to extend the working time of existing solar energy technologies. Solar energy technologies are usually idle at night, and by using nocturnal radiative cooling, solar energy technologies can be made useful also during the night. The third theme is that most solar energy technologies are monofunctional (*e.g.*, for heating only), with some technologies even disadvantageous in the cooling season. Radiative cooling may fill in this gap by taking turns on the function in the cooling season. This third theme is possible with some kind of switchable mechanism applied for the solar absorption and radiative emitter material.

With those identified themes in the combination of radiative cooling with solar energy applications in buildings, four designs are proposed in this thesis. Discussion on proposed designs is organised systematically from the fully passive to fully active design. The first proposed design is a fully passive solar chimney-radiative cooling (SC-RC) ventilation, as discussed in Chapter 3. The SC-RC ventilation differs from conventional solar chimney ventilation in the ability to pre-cool the inlet and deliver ventilation at night. Performance evaluation of the SC-RC ventilation shows that the ventilation strategy can deliver up to 1.2 air change per hour (ACH), which is 0.2 more than conventional solar chimney ventilation. On top of that, the radiative cooling cavity in the SC-RC ventilation pre-cooled the inlet air to be more than 3 °C lower than the room air temperature. These findings show that radiative cooling can enhance the ventilation and cooling performance of solar chimney ventilation.

The abovementioned SC-RC ventilation design is then improved in Chapter 4. The fully passive ventilation may need to consume no electrical energy to operate, but its performance relies heavily on the weather conditions. Compared to fan-assisted ventilation, fully passive SC-RC ventilation has also lower efficiency. Thus, in Chapter 4, the improvement is made by introducing a modest active component in the form of a fan, and thus the SC-RC ventilation now becomes mechanical ventilation. In addition to that, to develop the ventilation strategy to be multifunctional, namely cater for cooling as well as heating, the switchable feature is introduced into the solar absorber/radiative cooling emitter.

A comparison of the Switchable SC-RC ventilation with one-functional SC and RC ventilations demonstrates the superiority of the Switchable SC-RC ventilation. Using Rome as the case study location, it is found that the Switchable SC-RC ventilation can provide warmer-than-ambient fresh air in winter and slightly cool down the inlet air in the summer. In the annual term, the Switchable SC-RC ventilation can reduce the total unmet hours, and thus provide a more thermally comfortable room than the conventional ventilation. Annually, the unmet hours of the Switchable SC-RC ventilation case are 429 hours fewer than the base case. Additionally, the Switchable SC-RC ventilation can also be improved using other passive heating and cooling techniques such as wall insulation, window-to-wall-ratio, shading devices, *etc*.

Proceed further to the more active design, in Chapter 5, the proposed photothermal-radiative cooling (PT-RC) collector is discussed. The PT-RC collector is a modified solar collector to make possible the radiative sky cooling of the absorber at night. The important change made is in the cover, in which the commonly used glass cover is changed into a PE cover to allow thermal radiation from the absorber to the sky. Besides delivering cooling at night, the PT-RC collector has the benefit of a multi-seasonal device rather than only used in the heating season. How the PT-RC collector is installed in buildings is also described in Chapter 5. The PT-RC collector is installed as part of an HVAC system to make the HVAC system more efficient. This involvement of the HVAC system makes this PT-RC collector design categorised as a fully active design.

The CFD simulation results comparing the performance of the conventional solar collector with the PT-RC collector display the superiority of the latter in delivering heating and cooling energy annually. The PT-RC collector has the potential to save up to 32.7% of energy from heating and cooling in the Mediterranean climate of Madrid. In other climates such as the cold desert climate of Isfahan and the humid subtropical climate of Tokyo, the PT-RC collector can save up to 14.0% and 25.5% respectively. Nevertheless, the annual energy saving potential figures can still be improved considering the mismatch between the time in which the heating and cooling are available with the loads.

Furthermore, the PT-RC collector design can be more developed into a PVT-RC collector. The difference between them is if the PT-RC collector is a modified solar collector, the PVT-RC, however, is a modified PV module. Hence, the PVT-RC has one additional function that PT-RC does not have, namely the ability to generate electricity. On top of that, the PVT-RC design uses two fluids (*i.e.*, water and air) to collect the heating and cooling energy. Therefore, this PVT-RC collector can be named a trifunctional bi-fluid PVT-RC collector.

Experiments and simulations were conducted to evaluate the PVT-RC collector. The experiments have shown the ability of the PVT-Collector to collect heating and cooling during the day and night without intervening in the electrical performance of the modified PV module. With the data from the experiments, a CFD model of the PVT-RC collector was validated and then used in performance evaluations. It is found that in optimal conditions in the daytime, a total efficiency of 72% can be achieved by the bi-fluid PVT-RC collector. In optimal conditions at night, the bi-fluid PVT-RC collector can provide up to 45 W/m^2 cooling power. When applied as a building-integrated PVT-RC collector, the proposed design can yield more than 600 kWh/m^2 of total energy annually in Madrid and Seoul climates. Among the three different functions of the PVT-RC collector, the heating functions contribute the most to the total energy yield by 77%, compared to 17% contribution from cooling and 6% from electricity.

8.2 Reflection on the Thesis Objective

Throughout this thesis, diverse proposed designs, different methods of investigation, and various findings are discussed. The summary of the thesis is also elaborated in the previous section. Nonetheless, it is important to reflect all of those back to the thesis objective. In Chapter 1, the research question or aim and steps to tackle that question have been formulated.

To the question of “how to best use the radiative cooling mechanism when combined with solar energy applications”, this thesis offers three approaches. Firstly, the radiative cooling mechanism can be used to enhance the performance of existing solar energy technologies. Secondly, radiative cooling can be employed to extend the working time of the existing technologies, *i.e.*, by using nocturnal radiative cooling to make use of the idle solar energy device during the night. Thirdly, radiative cooling can make the mono-functional, heating-only device to be a multi-functional heating/cooling device. This third theme is possible with some kind of switchable mechanism applied for the solar absorption and radiative emitter material.

Further, it is also found that the most suitable climate for the proposed concepts to work optimally are the dry climates such as the desert, steppe, or Mediterranean climates. On top of that, the thesis also has considerably proposed diverse ways of combining radiative cooling with solar energy technologies in buildings, namely from a fully passive to a fully active system. This variety in designs provide alternatives to the question of how to best use radiative cooling mechanism when combined with solar energy applications in buildings.

8.3 Outlook for Application of Radiative Cooling in Buildings

From the summary in the previous section, one may conclude that the application of radiative cooling in buildings by combining it with solar energy technologies is promising. Meanwhile, the radiative cooling emitter materials are being developed to be more powerful, durable, and affordable, this combination strategy is arguably the most convenient way to utilise the current available radiative cooling emitter material.

Nevertheless, to be widely adopted in buildings, the strategies to implement radiative cooling in buildings should be available from a fully passive to a fully active system. This variety in the strategies is necessary to attract more interest from different stakeholders of the building or construction industry. Passive strategies, for instance, are essential to be developed in the early stage of building design, where the architects play the dominant role. Imagine if all the applications of radiative cooling in buildings were active devices, it may only be the concern of the HVAC engineers.

Another point worth considering is the multi-seasonality of the proposed building-integrated radiative cooling. Throughout this thesis, this is often mentioned, sometimes in the terms of multifunctionality of the proposed concept. This is worth mentioning because most regions need both heating and cooling. Using the monofunctional device, either solar heating or radiative cooling only, can be costly for installation and maintenance because the device is useful only for half of the year. Therefore, a strategy that can combine radiative cooling with other technologies to make adaptable space heating and cooling from renewable resources would be more beneficial.

8.4 Limitations and Future Studies

Future studies are required either to address the limitations of this thesis or to expand the field of the studies. As with all research, this study also has some limitations. Firstly, in the study of SC-RC ventilation, excluding the wind effect on the ventilation may contribute a significant difference than when the wind-forced ventilation is involved. Secondly, in using the case study buildings, some chapters assume uniformly distributed internal heat gain for the case study buildings, and some even do not consider internal heat gain. This is acceptable to some limit for performance evaluation. However, to assess the performance of the radiative cooling system more robustly, internal heat gains that resemble the real condition with specifically located heat sources are necessary. This is especially crucial for the assessment of the effectiveness of the heating or cooling provided by strategies involving ventilations. In addition to that, the annual energy-saving potential from the proposed concepts can still be improved considering the mismatch between supply and demand. Studies on the use of energy storage mechanisms or heating and cooling load management can further improve the utility of this dual-functional PT-RC collector.

Furthermore, for future studies, the influence of other building design features may be analysed in some parametric studies, such as the roof shape, opening locations, building plan and geometry, number of floors, *etc.*, on the proposed strategies. Further studies on the effectiveness of the proposed concepts in various building types and functions according to an occupation schedule can also reveal additional advantages and disadvantages of the strategies. This is because this thesis only used a residential building as the case study with a similar plan and roof shape.

Moreover, there are currently more proofs-of-concept of various applications of radiative cooling in buildings being published in academic journals. However, the field of study still lacks some economic analysis of the concepts. Also, there is a need to do some kind of pilot study where the radiative cooling integration is applied in a real building and monitored for weeks or months. These aspects can also be the direction of future studies.

References

3M (2018) 3M™ Enhanced Specular Reflector (ESR).

Ahmad, M.I., Jarimi, H. and Riffat, S. (2019) Nocturnal Cooling Technology for Building Applications, SpringerBriefs in Applied Sciences and Technology. Singapore: Springer.

Ahmad, S.N. and Prakash, O. (2022) 'A review on modelling, experimental analysis and parametric effects of earth–air heat exchanger', Modeling Earth Systems and Environment. Springer Science and Business Media Deutschland GmbH, pp. 1535–1551. Available at: https://doi.org/10.1007/s40808-021-01229-x.

Ali, A.H.H. (2007) 'Passive cooling of water at night in uninsulated open tank in hot arid areas', Energy Conversion and Management, 48(1), pp. 93–100. Available at: https://doi.org/10.1016/j.enconman.2006.05.012.

Ali, A.H.H. (2013) 'Desiccant enhanced nocturnal radiative cooling-solar collector system for air comfort application in hot arid areas', Sustainable Energy Technologies and Assessments, 1(1), pp. 54–62. Available at: https://doi.org/10.1016/j.seta.2013.01.003.

Al-Masrani, S.M. et al. (2018) 'Design optimisation of solar shading systems for tropical office buildings: Challenges and future trends', Solar Energy. Elsevier Ltd, pp. 849–872. Available at: https://doi.org/10.1016/j.solener.2018.04.047.

Al-Masrani, S.M. and Al-Obaidi, K.M. (2019) 'Dynamic shading systems: A review of design parameters, platforms and evaluation strategies', Automation in Construction. Elsevier B.V., pp. 195–216. Available at: https://doi.org/10.1016/j.autcon.2019.01.014.

Al-Nimr, M.A., Kodah, Z. and Nassar, B. (1998) 'A Theoretical and Experimental Investigation of A Radiative Cooling System', Solar Energy, 63(6), pp. 367–373. Available at: https://doi.org/https://doi.org/10.1016/S0038-092X(98)00098-X.

Al-Sanea, S.A., Zedan, M.F. and Al-Hussain, S.N. (2013) 'Effect of masonry material and surface absorptivity on critical thermal mass in insulated building walls', Applied Energy, 102, pp. 1063–1070. Available at: https://doi.org/10.1016/j.apenergy.2012.06.016.

ANSI/ASHRAE (2019) ‘ANSI/ASHRAE Standard 62.1-2019 Ventilation for Acceptable Indoor Air Quality’. Atlanta, GA: ASHRAE.

Ansys® (2021) ‘Ansys Fluent 2021 R1, Help System, Fluent User’s Guide, Solution Mode, ANSYS, Inc.’

Ao, X. et al. (2019) ‘Preliminary experimental study of a specular and a diffuse surface for daytime radiative cooling’, Solar Energy Materials and Solar Cells, 191(October 2018), pp. 290–296. Available at: https://doi.org/10.1016/j.solmat.2018.11.032.

Argiriou, A. et al. (1992) ‘Potential Of Radiative Cooling In Southern Europe’, International Journal of Solar Energy, 13(3), pp. 189–203. Available at: https://doi.org/10.1080/01425919208909784.

Argiriou, A. (2013) ‘Radiative Cooling’, in D.A. Matheos Santamouris (ed.) Passive cooling of buildings. New York: Earthscan, pp. 424–454.

Argiriou, A., Santamouris, M. and Assimakopoulos, D.N. (1994) ‘Assessment of the radiative cooling potential of a collector using hourly weather data’, Energy, 19(8), pp. 879–888. Available at: https://doi.org/https://doi.org/10.1016/0360-5442(94)90040-X.

ASHRAE (2018) ‘ANSI/ASHRAE/IES Standard 90.2 2018 Energy-Efficient Design of Low-Rise Residential Buildings’. Atlanta, GA: ASHRAE.

ASHRAE (2020) ‘ANSI/ASHRAE Standard 55-2020 Thermal Environmental Conditions for Human Occupancy’. Atlanta, GA: ASHRAE.

Asim, N. et al. (2019) ‘Key factors of desiccant-based cooling systems: Materials’, Applied Thermal Engineering. Elsevier Ltd. Available at: https://doi.org/10.1016/j.applthermaleng.2019.113946.

Atzeri, A.M. et al. (2018) ‘Comfort and energy performance analysis of different glazing systems coupled with three shading control strategies’, Science and Technology for the Built Environment, 24(5), pp. 545–558. Available at: https://doi.org/10.1080/23744731.2018.1449517.

Baggenstos, A. et al. (2020) Existing PVT systems and solutions. Edited by T. Ramschak. SHC Task 60/Report A.

Bagiorgas, H.S. and Mihalakakou, G. (2008) ‘Experimental and theoretical investigation of a nocturnal radiator for space cooling’, Renewable Energy, 33(6), pp. 1220–1227. Available at: https://doi.org/10.1016/j.renene.2007.04.015.

Bahadori, M.N. (1985) ‘An improved design of wind towers for natural ventilation and passive cooling’, Solar Energy, 35(2), pp. 119–129. Available at: https://doi.org/10.1016/0038-092X(85)90002-7.

Bahaidarah, H. et al. (2013) ‘Performance evaluation of a PV (photovoltaic) module by back surface water cooling for hot climatic conditions’, Energy, 59, pp. 445–453. Available at: https://doi.org/10.1016/j.energy.2013.07.050.

Balaras, C.A. (1996) ‘The role of thermal mass on the cooling load of buildings . An overview of computational methods’, 24.

Bansal, N.K., Mathur, R. and Bhandari, M.S. (1993) ‘Solar chimney for enhanced stack ventilation’, Building and Environment, 28(3), pp. 373–377. Available at: https://doi.org/10.1016/0360-1323(93)90042-2.

Banu, D., Feldman, D. and Hawes, D. (1998) ‘Evaluation of thermal storage as latent heat in phase change material wallboard by differential scanning calorimetry and large scale thermal testing’, Thermochimica acta, 317(1), pp. 39–45.

Bao, H. et al. (2017) ‘Double-layer nanoparticle-based coatings for efficient terrestrial radiative cooling’, Solar Energy Materials and Solar Cells [Preprint]. Available at: https://doi.org/10.1016/j.solmat.2017.04.020.

Bartoli, B. et al. (1977) ‘Nocturnal and diurnal performances of selective radiators’, Applied Energy, 3(4), pp. 267–286.

Basit, A. et al. (2021) ‘Designing, Modelling and Experimental Investigation of Direct Evaporative Cooling System Coupled With Commercial Desiccant Dehumidifier’, Journal of Thermal Science and Engineering Applications, 14(7). Available at: https://doi.org/10.1115/1.4052378.

Bathgate, S.N. and Bosi, S.G. (2011) ‘A robust convection cover material for selective radiative cooling applications’, Solar Energy Materials and Solar Cells, 95(10), pp. 2778–2785. Available at: https://doi.org/10.1016/j.solmat.2011.05.027.

Belarbi, R., Ghiaus, C. and Allard, F. (2006) ‘Modeling of water spray evaporation: Application to passive cooling of buildings’, Solar Energy, 80(12), pp. 1540–1552. Available at: https://doi.org/10.1016/j.solener.2006.01.004.

Benlattar, M. et al. (2005) ‘Radiative properties of cadmium telluride thin film as radiative cooling materials’, Optics Communications, 256(1–3), pp. 10–15. Available at: https://doi.org/10.1016/j.optcom.2005.06.033.

Benlattar, M. et al. (2006) ‘Thin cadmium sulphide film for radiative cooling application’, Optics Communications, 267(1), pp. 65–68. Available at: https://doi.org/10.1016/j.optcom.2006.06.050.

Berdahl, P. and Martin, M. (1984) ‘Emissivity of clear skies’, Solar Energy, 32(5), pp. 663–664. Available at: https://doi.org/https://doi.org/10.1016/0038-092X(84)90144-0.

Bergman, T.L. (2018) ‘Active daytime radiative cooling using spectrally selective surfaces for air conditioning and refrigeration systems’, Solar Energy, 174, pp. 16–23. Available at: https://doi.org/10.1016/j.solener.2018.08.070.

Bevilacqua, P. et al. (2019) ‘Are Trombe walls suitable passive systems for the reduction of the yearly building energy requirements?’, Energy, 185, pp. 554–566. Available at: https://doi.org/10.1016/j.energy.2019.07.003.

Bhamare, D.K., Rathod, M.K. and Banerjee, J. (2019) ‘Passive cooling techniques for building and their applicability in different climatic zones—The state of art’, Energy and Buildings. Elsevier Ltd, pp. 467–490. Available at: https://doi.org/10.1016/j.enbuild.2019.06.023.

Bowman, N. et al. (1997) ‘Application of Passive Downdraught Evaporative Cooling (PDEC) to non-domestic buildings’, Renewable Energy, 10(2-3 SPEC. ISS.), pp. 191–196. Available at: https://doi.org/10.1016/0960-1481(96)00062-6.

Boyle, G. (1997) Renewable energy: power for a sustainable future. Taylor & Francis.

Brown, S.J. (2020) ‘Future changes in heatwave severity , duration and frequency due to climate change for the most populous cities’, Weather and Climate Extremes, 30(March), p. 100278. Available at: https://doi.org/10.1016/j.wace.2020.100278.

Bundgaard, E. and Krebs, F.C. (2007) ‘Low band gap polymers for organic photovoltaics’, Solar Energy Materials and Solar Cells, pp. 954–985. Available at: https://doi.org/10.1016/j.solmat.2007.01.015.

Butler, A. and Argyropoulos, C. (2022) ‘Mechanically tunable radiative cooling for adaptive thermal control’, Applied Thermal Engineering, 211. Available at: https://doi.org/10.1016/j.applthermaleng.2022.118527.

Calautit, J.K. et al. (2020) ‘Numerical and experimental investigation of the indoor air quality and thermal comfort performance of a low energy cooling windcatcher with heat pipes and extended surfaces’, Renewable Energy, 145, pp. 744–756. Available at: https://doi.org/10.1016/j.renene.2019.06.040.

Cao, Y. et al. (2021) ‘Innovative integration of solar chimney ventilator, solar panel and phase change material; under real transient weather condition of Hong Kong through different months’, Renewable Energy, 174, pp. 865–878. Available at: https://doi.org/10.1016/j.renene.2021.04.146.

Cascone, S. et al. (2019) ‘The evapotranspiration process in green roofs: A review’, Building and Environment. Elsevier Ltd, pp. 337–355. Available at: https://doi.org/10.1016/j.buildenv.2018.10.024.

Cesari, S. et al. (2020) ‘The Energy Saving Potential of Wide Windows in Hospital Patient Rooms, Optimizing the Type of Glazing and Lighting Control Strategy under Different Climatic Conditions’, Energies, 13(8), p. 2116. Available at: https://doi.org/https://doi.org/10.3390/en13082116.

Ben Cheikh, H. and Bouchair, A. (2004) ‘Passive cooling by evapo-reflective roof for hot dry climates’, Renewable Energy, 29(11), pp. 1877–1886. Available at: https://doi.org/10.1016/j.renene.2003.12.021.

Chen, J. and Lu, L. (2020) ‘Comprehensive evaluation of thermal and energy performance of radiative roof cooling in buildings’, Journal of Building Engineering, 33(February 2020), p. 101631. Available at: https://doi.org/10.1016/j.jobe.2020.101631.

Chen, P. et al. (2022) 'Performance of a solar ground source heat pump used for energy supply of a separated building', Geothermics, 105. Available at: https://doi.org/10.1016/j.geothermics.2022.102524.

Chen, Z. et al. (2016) 'Radiative cooling to deep sub-freezing temperatures through a 24-h day-night cycle', Nature Communications, 7, pp. 1–5. Available at: https://doi.org/10.1038/ncomms13729.

Chen, Z. D. et al. (2003) 'An experimental investigation of a solar chimney model with uniform wall heat flux', Building and Environment, 38(7), pp. 893–906. Available at: https://doi.org/10.1016/S0360-1323(03)00057-X.

Chen, Z D et al. (2003) 'An experimental investigation of a solar chimney model with uniform wall heat ux', 38, pp. 893–906. Available at: https://doi.org/10.1016/S0360-1323(03)00057-X.

Cheng, V., Ng, E. and Givoni, B. (2005) 'Effect of envelope colour and thermal mass on indoor temperatures in hot humid climate', 78, pp. 528–534. Available at: https://doi.org/10.1016/j.solener.2004.05.005.

Cheng, Z. et al. (2019) 'Effect of embedded polydisperse glass microspheres on radiative cooling of a coating', International Journal of Thermal Sciences, 140, pp. 358–367. Available at: https://doi.org/10.1016/j.ijthermalsci.2019.03.014.

Chenvidyakarn, T. (2013) Buoyancy effects on natural ventilation. Cambridge University Press.

Chotivisarut, N. and Kiatsiriroat, T. (2009) 'Cooling load reduction of building by seasonal nocturnal cooling water from thermosyphon heat pipe radiator', International Journal of Energy Research, 33(12), pp. 1089–1098. Available at: https://doi.org/10.1002/er.1543.

Chotivisarut, N., Nuntaphan, A. and Kiatsiriroat, T. (2012) 'Seasonal cooling load reduction of building by thermosyphon heat pipe radiator in different climate areas', Renewable Energy, 38(1), pp. 188–194. Available at: https://doi.org/10.1016/j.renene.2011.07.021.

Chua, K.J. et al. (2013) 'Achieving better energy-efficient air conditioning - A review of technologies and strategies', Applied Energy, 104, pp. 87–104. Available at: https://doi.org/10.1016/j.apenergy.2012.10.037.

Chun, T., Nyuk, W. and Kardinal, S. (2014) 'Landscape and Urban Planning Effects of vertical greenery on mean radiant temperature in the tropical urban environment', Landscape and Urban Planning, 127, pp. 52–64. Available at: https://doi.org/10.1016/j.landurbplan.2014.04.005.

Climate Change Committee (2020) 'The sixth carbon budget: the UK's path to net zero'.

Commons, W. (2020) Atmosfaerisk spredning. Available at: commons.wikimedia.org.

Cook, M.J. (1998) 'An evaluation of computational fluid dynamics for modelling buoyancy-driven displacement ventilation'.

Craig, S. et al. (2008) 'BioTRIZ Suggests Radiative Cooling of Buildings Can Be Done Passively by Changing the Structure of Roof Insulation to Let Longwave Infrared Pass', Journal of Bionic Engineering, 5(1), pp. 55–66. Available at: https://doi.org/10.1016/S1672-6529(08)60007-4.

Cuce, P.M. and Riffat, S. (2016) 'A state of the art review of evaporative cooling systems for building applications', Renewable and Sustainable Energy Reviews, 54, pp. 1240–1249. Available at: https://doi.org/10.1016/j.rser.2015.10.066.

Dai, Y.J. et al. (2003) 'Enhancement of natural ventilation in a solar house with a solar chimney and a solid adsorption cooling cavity', Solar Energy, 74(1), pp. 65–75. Available at: https://doi.org/https://doi.org/10.1016/S0038-092X(03)00106-3.

Darkwa, K. and Kim, J.S. (2004) 'Heat transfer in neuron composite laminated phase-change drywall', Proceedings of the Institution of Mechanical Engineers, Part A: Journal of Power and Energy, 218(2), pp. 83–87.

Dawood, N.I., Jalil, J.M. and Ahmed, M.K. (2022) 'Investigation of a novel window solar air collector with 7-moveable absorber plates', Energy, 257, p. 124829. Available at: https://doi.org/10.1016/j.energy.2022.124829.

Designed Research; X, G.P.A. (2022) 'Self-adaptive integration of photothermal and radiative cooling for continuous energy harvesting from the sun and outer space'. Available at: https://doi.org/10.1073/pnas.

Dharmasastha, K. et al. (2022) 'Impact of Indoor Heat Load and Natural Ventilation on Thermal Comfort of Radiant Cooling System: An Experimental Study', Energy and Built Environment [Preprint], (April). Available at: https://doi.org/10.1016/j.enbenv.2022.04.003.

Diatezua, D.M. et al. (1996) 'Silicon oxynitride multilayers as spectrally selective material for passive radiative cooling applications', Solar Energy Materials and Solar Cells, 40(3), pp. 253–259. Available at: https://doi.org/10.1016/0927-0248(95)00092-5.

Dimoudi, A. and Androutsopoulos, A. (2006) 'The cooling performance of a radiator based roof component', Solar Energy, 80(8), pp. 1039–1047. Available at: https://doi.org/10.1016/j.solener.2005.06.017.

Dong, M. et al. (2019) 'Nighttime radiative cooling in hot and humid climates', Optics Express, 27(22), p. 31587. Available at: https://doi.org/10.1364/OE.27.031587.

Duffie, J.A. and Beckman, W.A. (2013) 'Solar engineering of thermal processes, fourth edition'. John Wiley & Sons,.

Eicker, U. and Dalibard, A. (2011) 'Photovoltaic-thermal collectors for night radiative cooling of buildings', Solar Energy, 85(7), pp. 1322–1335. Available at: https://doi.org/10.1016/j.solener.2011.03.015.

Energy Saving Trust (2008) Measurement of Domestic Hot Water Consumption in Dwellings. Available at: www.est.org.uk/ (Accessed: 31 July 2023).

EnergyPlus (2021) Weather Data. Available at: energyplus.net/weather.

Erell, E. (2012) 'Radiative Cooling', in M. Santamouris (ed.) Advances in Passive Cooling. Sterling, USA: Earthscan, pp. 262–296.

Erell, E. and Etzion, Y. (1999) 'Analysis and Experimental Verification of an Improved Cooling Radiatior', Renewable Energy, 16(1), pp. 700–703. Available at: https://doi.org/https://doi.org/10.1016/S0960-1481(98)00255-9.

Etheridge, D. (2011) Natural ventilation of buildings: theory, measurement and design. John Wiley & Sons.

Etzion, Y. and Erell, E. (1991) 'Thermal storage mass in radiative cooling systems', Building and Environment, 26(4), pp. 389–394. Available at: https://doi.org/https://doi.org/10.1016/0360-1323(91)90065-J.

Eurostat (2022) Energy consumption in households. Available at: ec.europa.eu/eurostat/statistics-explained.

Evangelisti, L., Guattari, C. and Asdrubali, F. (2019) 'On the sky temperature models and their influence on buildings energy performance: A critical review', Energy and Buildings, 183, pp. 607–625. Available at: https://doi.org/10.1016/j.enbuild.2018.11.037.

Ezekwe, C.I. (1990) 'Performance of a heat pipe assisted night sky radiative cooler', Energy Conversion and Management, 30(4), pp. 403–408. Available at: https://doi.org/https://doi.org/10.1016/0196-8904(90)90041-V.

Fan, J., Fu, C. and Fu, T. (2020) 'Yttria-stabilized zirconia coating for passive daytime radiative cooling in humid environment', Applied Thermal Engineering, 165(October 2019), p. 114585. Available at: https://doi.org/10.1016/j.applthermaleng.2019.114585.

Fan, S. and Li, W. (2022) 'Photonics and thermodynamics concepts in radiative cooling', 16(March). Available at: https://doi.org/10.1038/s41566-021-00921-9.

Farahani, A.V. et al. (2021) 'Overheating risk and energy demand of nordic old and new apartment buildings during average and extreme weather conditions under a changing climate', Applied Sciences (Switzerland), 11(9). Available at: https://doi.org/10.3390/app11093972.

Farmahini Farahani, M., Heidarinejad, G. and Delfani, S. (2010) 'A two-stage system of nocturnal radiative and indirect evaporative cooling for conditions in Tehran', Energy and Buildings, 42(11), pp. 2131–2138. Available at: https://doi.org/10.1016/j.enbuild.2010.07.003.

Fei, J. et al. (2022) ‘Switchable Surface Coating for Bifunctional Passive Radiative Cooling and Solar Heating’, Advanced Functional Materials, 32(27). Available at: https://doi.org/10.1002/adfm.202203582.

Feldman, D., Banu, D. and Hawes, D.W. (1995) ‘Development and application of organic phase change mixtures in thermal storage gypsum wallboard’, Solar Energy Materials and Solar Cells, 36(2), pp. 147–157.

Feng, H. and Hewage, K. (2014) ‘Energy saving performance of green vegetation on LEED certified buildings’, Energy & Buildings, 75, pp. 281–289. Available at: https://doi.org/10.1016/j.enbuild.2013.10.039.

Feng, J. et al. (2022) ‘On the cooling energy conservation potential of super cool roofs’, Energy and Buildings, 264, p. 112076. Available at: https://doi.org/10.1016/j.enbuild.2022.112076.

Fernandez, N. et al. (2015) Energy Savings Potential of Radiative Cooling Technologies.

Fiorentini, M. et al. (2015) ‘Hybrid model predictive control of a residential HVAC system with PVT energy generation and PCM thermal storage’, in Energy Procedia. Elsevier Ltd, pp. 21–30. Available at: https://doi.org/10.1016/j.egypro.2015.12.192.

Fiorentini, M., Cooper, P. and Ma, Z. (2015a) ‘Development and optimization of an innovative HVAC system with integrated PVT and PCM thermal storage for a net-zero energy retrofitted house’, Energy and Buildings, 94, pp. 21–32. Available at: https://doi.org/10.1016/j.enbuild.2015.02.018.

Fiorentini, M., Cooper, P. and Ma, Z. (2015b) ‘Development and optimization of an innovative HVAC system with integrated PVT and PCM thermal storage for a net-zero energy retrofitted house’, Energy and Buildings, 94, pp. 21–32. Available at: https://doi.org/10.1016/j.enbuild.2015.02.018.

Frutos Dordelly, J.C. et al. (2019) ‘Experimental analysis of a PCM integrated solar chimney under laboratory conditions’, Solar Energy, 188, pp. 1332–1348. Available at: https://doi.org/10.1016/j.solener.2019.06.065.

Gabriel, P. et al. (2016) 'Thermal assessment of extensive green roofs as passive tool for energy savings in buildings', 85, pp. 1106–1115. Available at: https://doi.org/10.1016/j.renene.2015.07.074.

Gan, G. (2010) 'Impact of computational domain on the prediction of buoyancy-driven ventilation cooling', Building and Environment, 45(5), pp. 1173–1183. Available at: https://doi.org/10.1016/j.buildenv.2009.10.023.

Gao, Mengyu et al. (2019) 'Approach to fabricating high-performance cooler with near-ideal emissive spectrum for above-ambient air temperature radiative cooling', Solar Energy Materials and Solar Cells, 200(May), p. 110013. Available at: https://doi.org/10.1016/j.solmat.2019.110013.

Gao, Minmin et al. (2019) 'Solar absorber material and system designs for photothermal water vaporization towards clean water and energy production', Energy and Environmental Science. Royal Society of Chemistry, pp. 841–864. Available at: https://doi.org/10.1039/c8ee01146j.

García, M.P. and De Luis, F.J. (2002) 'Influence of site dependent effects on the assessment of the radiative cooling potential', International Journal of Solar Energy, 22(1), pp. 33–45. Available at: https://doi.org/10.1080/01425910212849.

Geetha, N.B. and Velraj, R. (2012) 'Passive cooling methods for energy efficient buildings with and without thermal energy storage–A review', Energy Education Science and Technology Part A: Energy Science and Research, 29(2), pp. 913–946.

Gentle, A.R. and Smith, G.B. (2015) 'A Subambient Open Roof Surface under the Mid-Summer Sun', Advanced Science, 2(9). Available at: https://doi.org/10.1002/advs.201500119.

Gilani, S., Montazeri, H. and Blocken, B. (2016) 'CFD simulation of stratified indoor environment in displacement ventilation: Validation and sensitivity analysis', Building and Environment, 95, pp. 299–313. Available at: https://doi.org/10.1016/j.buildenv.2015.09.010.

Givoni, B. (1977) 'Solar heating and night radiation cooling by a Roof Radiation Trap', Energy and Buildings, 1(2), pp. 141–145. Available at: https://doi.org/https://doi.org/10.1016/0378-7788(77)90026-3.

Givoni, B. (1993) ‘Semiempirical model of a building with a passive evaporative cool tower’, Solar Energy, 50(5), pp. 425–434. Available at: https://doi.org/10.1016/0038-092X(93)90064-U.

Gonome, H. et al. (2014) ‘Controlling the radiative properties of cool black-color coatings pigmented with CuO submicron particles’, Journal of Quantitative Spectroscopy and Radiative Transfer, 132, pp. 90–98. Available at: https://doi.org/10.1016/j.jqsrt.2013.02.027.

Granqvist, C.G. (2016) ‘Electrochromics and Thermochromics: Towards a New Paradigm for Energy Efficient Buildings’, in Materials Today: Proceedings. Elsevier Ltd, pp. S2–S11. Available at: https://doi.org/10.1016/j.matpr.2016.01.002.

Gregory, K. et al. (2008) ‘Effect of thermal mass on the thermal performance of various Australian residential constructions systems’, 40, pp. 459–465. Available at: https://doi.org/10.1016/j.enbuild.2007.04.001.

Haggag, M. and Hassan, A. (2017) ‘Energy and Economic Performance of Plant-Shaded Building Façade in Hot Arid Climate’. Available at: https://doi.org/10.3390/su9112026.

El Hammoumi, A. et al. (2018) ‘Low-cost virtual instrumentation of PV panel characteristics using Excel and Arduino in comparison with traditional instrumentation’, Renewables: Wind, Water, and Solar, 5(1). Available at: https://doi.org/10.1186/s40807-018-0049-0.

Han, D., Ng, B.F. and Wan, M.P. (2020) ‘Preliminary study of passive radiative cooling under Singapore’s tropical climate’, Solar Energy Materials and Solar Cells, 206(November 2019), p. 110270. Available at: https://doi.org/10.1016/j.solmat.2019.110270.

Harrison, A.W. and Walton, M.R. (1978) ‘Radiative cooling of TiO2 white paint’, Solar Energy, 20(2), pp. 185–188.

Hasse, C. et al. (2011) ‘Realization, test and modelling of honeycomb wallboards containing a Phase Change Material’, Energy and Buildings, 43(1), pp. 232–238.

Hay, H.R. and Yellott, J.I. (1969) ‘International aspects of air conditioning with movable insulation’, Solar Energy, 12(4), pp. 427–438. Available at: https://doi.org/10.1016/0038-092x(69)90065-6.

He, J. (2011) ‘A design supporting simulation system for predicting and evaluating the cool microclimate creating effect of passive evaporative cooling walls’, Building and Environment, 46(3), pp. 584–596. Available at: https://doi.org/10.1016/j.buildenv.2010.09.005.

He, J. and Hoyano, A. (2010) ‘Experimental study of cooling effects of a passive evaporative cooling wall constructed of porous ceramics with high water soaking-up ability’, Building and Environment, 45(2), pp. 461–472. Available at: https://doi.org/10.1016/j.buildenv.2009.07.002.

He, W. et al. (2019) ‘Experimental study on the performance of a novel RC-PCM-wall’, Energy and Buildings, 199, pp. 297–310. Available at: https://doi.org/10.1016/j.enbuild.2019.07.001.

Heidarinejad, G., Farmahini Farahani, M. and Delfani, S. (2010) ‘Investigation of a hybrid system of nocturnal radiative cooling and direct evaporative cooling’, Building and Environment, 45(6), pp. 1521–1528. Available at: https://doi.org/10.1016/j.buildenv.2010.01.003.

Henninger, R.H., Witte, M.J. and Crawley, D.B. (2004) ‘Analytical and comparative testing of EnergyPlus using IEA HVAC BESTEST E100-E200 test suite’, in Energy and Buildings, pp. 855–863. Available at: https://doi.org/10.1016/j.enbuild.2004.01.025.

Hoffman, M. et al. (1983) ‘Solar heating using common building elements as passive systems’, Solar Energy, 30(3), pp. 275–287.

Hollick, J. (2012) ‘Nocturnal radiation cooling tests’, in Energy Procedia. Elsevier Ltd, pp. 930–936. Available at: https://doi.org/10.1016/j.egypro.2012.11.105.

Hossain, M.M. and Gu, M. (2016) ‘Radiative cooling: Principles, progress, and potentials’, Advanced Science [Preprint]. Available at: https://doi.org/10.1002/advs.201500360.

Hossain, M.M., Jia, B. and Gu, M. (2015) 'A Metamaterial Emitter for Highly Efficient Radiative Cooling', Advanced Optical Materials, 3(8), pp. 1047–1051. Available at: https://doi.org/10.1002/adom.201500119.

Hosseinzadeh, E. and Taherian, H. (2012) 'An experimental and analytical study of a radiative cooling system with unglazed flat plate collectors', International Journal of Green Energy, pp. 766–779. Available at: https://doi.org/10.1080/15435075.2011.641189.

Hu, M., Zhao, B., Ao, X., Zhao, P., et al. (2018) 'Field investigation of a hybrid photovoltaic-photothermic-radiative cooling system', Applied Energy, 231, pp. 288–300. Available at: https://doi.org/10.1016/j.apenergy.2018.09.137.

Hu, M., Zhao, B., Ao, X., Su, Y., et al. (2018a) 'Parametric analysis and annual performance evaluation of an air-based integrated solar heating and radiative cooling collector', Energy, 165, pp. 811–824. Available at: https://doi.org/10.1016/j.energy.2018.09.127.

Hu, M., Zhao, B., Ao, X., Su, Y., et al. (2018b) 'Parametric analysis and annual performance evaluation of an air-based integrated solar heating and radiative cooling collector', Energy, 165, pp. 811–824. Available at: https://doi.org/10.1016/j.energy.2018.09.127.

Hu, M. et al. (2019) 'Experimental study on a hybrid photo-thermal and radiative cooling collector using black acrylic paint as the panel coating', Renewable Energy, 139, pp. 1217–1226. Available at: https://doi.org/10.1016/j.renene.2019.03.013.

Hu, M. et al. (2020) 'Feasibility research on a double-covered hybrid photo-thermal and radiative sky cooling module', Solar Energy, 197(January), pp. 332–343. Available at: https://doi.org/10.1016/j.solener.2020.01.022.

Hu, M., Suhendri, et al. (2021a) 'Effect of the spectrally selective features of the cover and emitter combination on radiative cooling performance', Energy and Built Environment, 2(3), pp. 251–259. Available at: https://doi.org/10.1016/j.enbenv.2020.06.008.

Hu, M., Suhendri, et al. (2021b) 'Effect of the spectrally selective features of the cover and emitter combination on radiative cooling performance', Energy and Built

Environment, 2(3), pp. 251–259. Available at: https://doi.org/10.1016/j.enbenv.2020.06.008.

Hu, M., Zhao, B., et al. (2021) ‘Performance analysis of a novel bifacial solar photothermic and radiative cooling module’, Energy Conversion and Management, 236. Available at: https://doi.org/10.1016/j.enconman.2021.114057.

Hu, M., Zhao, B., Suhendri, Ao, X., et al. (2022) ‘Applications of radiative sky cooling in solar energy systems: Progress, challenges, and prospects’, Renewable and Sustainable Energy Reviews, 160(February), p. 112304. Available at: https://doi.org/10.1016/j.rser.2022.112304.

Hu, M., Zhao, B., Suhendri, Cao, J., et al. (2022a) ‘Extending the operation of a solar air collector to night-time by integrating radiative sky cooling: A comparative experimental study’, Energy, 251, p. 123986. Available at: https://doi.org/10.1016/j.energy.2022.123986.

Hu, M., Zhao, B., Suhendri, Cao, J., et al. (2022b) ‘Quantitative characterization of the effect of inclination angle on flat-plate radiative cooling performance in buildings’, Journal of Building Engineering, 59(May), p. 105124. Available at: https://doi.org/10.1016/j.jobe.2022.105124.

Hu, T., Kwan, T.H. and Pei, G. (2022) ‘An all-day cooling system that combines solar absorption chiller and radiative cooling’, Renewable Energy, 186, pp. 831–844. Available at: https://doi.org/10.1016/j.renene.2022.01.058.

Hu, Z. et al. (2016) ‘Numerical analysis on the cooling performance of a ventilated Trombe wall combined with venetian blinds in an office building’, Energy and Buildings, 126, pp. 14–27. Available at: https://doi.org/10.1016/j.enbuild.2016.05.016.

Hu, Z. et al. (2017) ‘A review on the application of Trombe wall system in buildings’, Renewable and Sustainable Energy Reviews. Elsevier Ltd, pp. 976–987. Available at: https://doi.org/10.1016/j.rser.2016.12.003.

Huang, Y. et al. (2018) ‘Broadband metamaterial as an “invisible” radiative cooling coat’, Optics Communications, 407(June 2017), pp. 204–207. Available at: https://doi.org/10.1016/j.optcom.2017.09.036.

Huang, Z. and Ruan, X. (2017) 'Nanoparticle embedded double-layer coating for daytime radiative cooling', International Journal of Heat and Mass Transfer, 104, pp. 890–896. Available at: https://doi.org/10.1016/j.ijheatmasstransfer.2016.08.009.

Humphreys, M.A. and Nicol, J.F. (2000) 'Outdoor temperature and indoor thermal comfort: raising the precision of the relationship for the 1998 ASHRAE database of field studies', Ashrae Transactions, 106(2), pp. 485–492.

Hunger, M. et al. (2009) 'The behavior of self-compacting concrete containing micro-encapsulated phase change materials', Cement and Concrete Composites, 31(10), pp. 731–743.

IEA (2016) Global air conditioner stock, 1990-2050. Paris.

Imroz Sohel, M. et al. (2014) 'A feasibility study of night radiative cooling of BIPVT in climatic conditions of major Australian cities', in Asia-Pacific Solar Research Conference 2014. Kensington. Available at: https://www.researchgate.net/publication/269398451.

Jeong, S.Y. et al. (2018) 'A numerical study of daytime passive radiative coolers for space cooling in buildings', Building Simulation, 11(5), pp. 1011–1028. Available at: https://doi.org/10.1007/s12273-018-0474-4.

Jeong, S. Y. et al. (2020) 'Daytime passive radiative cooling by ultra emissive bio-inspired polymeric surface', Solar Energy Materials and Solar Cells, 206(July 2019), p. 110296. Available at: https://doi.org/10.1016/j.solmat.2019.110296.

Jeong, Shin Young et al. (2020) 'Field investigation of a photonic multi-layered TiO2 passive radiative cooler in sub-tropical climate', Renewable Energy, 146, pp. 44–55. Available at: https://doi.org/10.1016/j.renene.2019.06.119.

Jia, Y. et al. (2021) 'Highly tunable thermal emitter with vanadium dioxide metamaterials for radiative cooling', Applied Optics, 60(19), p. 5699. Available at: https://doi.org/10.1364/ao.421977.

Joshi, S.S. and Dhoble, A.S. (2018) 'Photovoltaic -Thermal systems (PVT): Technology review and future trends', Renewable and Sustainable Energy Reviews. Elsevier Ltd, pp. 848–882. Available at: https://doi.org/10.1016/j.rser.2018.04.067.

Kamal, M.A. (2012) ‘An Overview of Passive Cooling Techniques in Buildings: Design Concepts and Architectural Interventions’, Civil Engineering & Architecture, 55(1), pp. 84–97.

Karaipekli, A., Sarı, A. and Biçer, A. (2016) ‘Thermal regulating performance of gypsum/(C18–C24) composite phase change material (CPCM) for building energy storage applications’, Applied Thermal Engineering, 107, pp. 55–62.

Katramiz, E., Ghaddar, N. and Ghali, K. (2020) ‘Daytime radiative cooling: To what extent it enhances office cooling system performance in comparison to night cooling in semi-arid climate?’, Journal of Building Engineering, 28(October 2019), p. 101020. Available at: https://doi.org/10.1016/j.jobe.2019.101020.

Ke, W. et al. (2021) ‘Annual performance analysis of a dual-air-channel solar wall system with phase change material in different climate regions of China’, Energy, 235. Available at: https://doi.org/10.1016/j.energy.2021.121359.

Kendrick, C. et al. (2012) ‘Thermal mass in new build UK housing : A comparison of structural systems in a future weather scenario’, Energy & Buildings, 48, pp. 40–49. Available at: https://doi.org/10.1016/j.enbuild.2012.01.009.

Khedari, J. et al. (2000) ‘Field investigation of night radiation cooling under tropical climate’, Renewable Energy, 20, pp. 183–193. Available at: www.elsevier.com/locate/renene.

Kim, H. and Lenert, A. (2018) ‘Optical and thermal filtering nanoporous materials for sub-ambient radiative cooling’, Journal of Optics (United Kingdom), 20(8). Available at: https://doi.org/10.1088/2040-8986/aacaa1.

Kim, M. et al. (2021) ‘Switchable diurnal radiative cooling by doped vo2’, Opto-Electronic Advances, 4(5). Available at: https://doi.org/10.29026/oea.2021.200006.

Kirimtat, A. et al. (2016) ‘Review of simulation modeling for shading devices in buildings’, Renewable and Sustainable Energy Reviews. Elsevier Ltd, pp. 23–49. Available at: https://doi.org/10.1016/j.rser.2015.08.020.

Kirimtat, A. et al. (2019) ‘Multi-objective energy and daylight optimization of amorphous shading devices in buildings’, Solar Energy, pp. 100–111. Available at: https://doi.org/10.1016/j.solener.2019.04.048.

Kishore, R.A., Booten, C. and Wijesuriya, S. (2022) ‘Effective properties of semitransparent radiative cooling materials with spectrally variable properties’, Applied Thermal Engineering, 205(December 2021), p. 118048. Available at: https://doi.org/10.1016/j.applthermaleng.2022.118048.

Klinger, B.A. and Ryan, S.J. (2022) ‘Population distribution within the human climate niche’, PLOS Climate, 1(11), p. e0000086.

Koschenz, M. and Lehmann, B. (2004) ‘Development of a thermally activated ceiling panel with PCM for application in lightweight and retrofitted buildings’, Energy and buildings, 36(6), pp. 567–578.

Kottek, M. et al. (2006) ‘World map of the Köppen-Geiger climate classification updated’, Meteorologische Zeitschrift, 15(3), pp. 259–263. Available at: https://doi.org/10.1127/0941-2948/2006/0130.

Kou, J. long et al. (2017) ‘Daytime Radiative Cooling Using Near-Black Infrared Emitters’, ACS Photonics, 4(3), pp. 626–630. Available at: https://doi.org/10.1021/acsphotonics.6b00991.

Kuczyński, T. et al. (2021) ‘Effect of thermal mass, night ventilation and window shading on summer thermal comfort of buildings in a temperate climate’, Building and Environment, 204(May). Available at: https://doi.org/10.1016/j.buildenv.2021.108126.

Kuznik, F. and Virgone, J. (2009) ‘Experimental assessment of a phase change material for wall building use’, Applied energy, 86(10), pp. 2038–2046.

Lai, C., Chen, R.H. and Lin, C.-Y. (2010) ‘Heat transfer and thermal storage behaviour of gypsum boards incorporating micro-encapsulated PCM’, Energy and Buildings, 42(8), pp. 1259–1266.

Lal, S. (2014) ‘Experimental, CFD simulation and parametric studies on modified solar chimney for building ventilation’, Applied Solar Energy (English translation of Geliotekhnika), 50(1), pp. 37–43. Available at: https://doi.org/10.3103/S0003701X14010125.

Launder, B.E. and Spalding, D.B. (1972) Lectures in Mathematical Models of Turbulence. London, England: Academic Press.

Lawrie, L.K. and Crawley, D.B. (2022) Development of Global Typical Meteorological Years (TMYx). Available at: http://climate.onebuilding.org.

Lebbi, M. et al. (2021) 'Energy performance improvement of a new hybrid PV/T Bi-fluid system using active cooling and self-cleaning: Experimental study', Applied Thermal Engineering, 182. Available at: https://doi.org/10.1016/j.applthermaleng.2020.116033.

Lee, G.J. et al. (2018) 'Colored, Daytime Radiative Coolers with Thin-Film Resonators for Aesthetic Purposes', Advanced Optical Materials, 6(22), pp. 1–8. Available at: https://doi.org/10.1002/adom.201800707.

Lee, L.S.H. and Jim, C.Y. (2018) 'Thermal-cooling performance of subtropical green roof with deep substrate and woodland vegetation', Ecological Engineering, 119(April), pp. 8–18. Available at: https://doi.org/10.1016/j.ecoleng.2018.05.014.

Li, D. et al. (2021) 'Scalable and hierarchically designed polymer film as a selective thermal emitter for high-performance all-day radiative cooling', 16(FebruarY). Available at: https://doi.org/10.1038/s41565-020-00800-4.

Li, D.H.W. and Lam, J.C. (2000) 'Solar heat gain factors and the implications to building designs in subtropical regions', Energy and Buildings, 32(1), pp. 47–55. Available at: https://doi.org/10.1016/S0378-7788(99)00035-3.

Li, J. et al. (2020) 'Review of Radiative Cooling Materials: Performance Evaluation and Design Approaches', Nano Energy, p. 105526. Available at: https://doi.org/10.1016/j.nanoen.2021.106259.

Li, M. and Coimbra, C.F.M. (2019) 'On the effective spectral emissivity of clear skies and the radiative cooling potential of selectively designed materials', International Journal of Heat and Mass Transfer, 135, pp. 1053–1062. Available at: https://doi.org/10.1016/j.ijheatmasstransfer.2019.02.040.

Li, N. et al. (2019) 'Selective spectral optical properties and structure of aluminum phosphate for daytime passive radiative cooling application', Solar Energy Materials and Solar Cells, 194(October 2018), pp. 103–110. Available at: https://doi.org/10.1016/j.solmat.2019.01.036.

Li, R. and Cui, G. (2022) ‘Comprehensive Performance Evaluation of a Dual-Function Active Solar Thermal Façade System Based on Energy, Economic and Environmental Analysis in China’, Energies, 15(11). Available at: https://doi.org/10.3390/en15114147.

Liggett, R. and Milne, M. (2021) ‘Climate Consultant 6’. UCLA Energy Design Tools Group.

Lin, W. et al. (2014) ‘Development and evaluation of a ceiling ventilation system enhanced by solar photovoltaic thermal collectors and phase change materials’, Energy Conversion and Management, 88, pp. 218–230. Available at: https://doi.org/10.1016/j.enconman.2014.08.019.

Liu, J. et al. (2020) ‘Research on the performance of radiative cooling and solar heating coupling module to direct control indoor temperature’, Energy Conversion and Management, 205(December 2019), p. 112395. Available at: https://doi.org/10.1016/j.enconman.2019.112395.

Liu, L. et al. (2022) ‘Solar Energy Materials and Solar Cells Super-amphiphobic coatings with sub-ambient daytime radiative cooling — Part 2 : Cooling effect under real conditions’, 241(April), pp. 1–9.

Liu, X. et al. (2020) ‘Tunable radiative cooling based on a stretchable selective optical filter’, Journal of the Optical Society of America B, 37(9), p. 2534. Available at: https://doi.org/10.1364/josab.394671.

Liu, Y. et al. (2019) ‘A pragmatic bilayer selective emitter for efficient radiative cooling under direct sunlight’, Materials, 12(8). Available at: https://doi.org/10.3390/ma12081208.

LLC, B.L.S. (2022) EnergyPlus Version 8.6 Documents. Available at: bigladdersoftware.com.

Long, T. et al. (2021) ‘Numerical investigation of the working mechanisms of solar chimney coupled with earth-to-air heat exchanger (SCEAHE)’, Solar Energy, 230, pp. 109–121. Available at: https://doi.org/10.1016/j.solener.2021.10.029.

Lu, S.-M. and Yan, W.-J. (1995) ‘Development and experimental validation of a full-scale solar desiccant enhanced radiative cooling system’, Renewable Energy, 6(7), pp. 821–827. Available at: https://doi.org/10.1016/0360-5442(95)00019-D.

Lu, X. et al. (2016) ‘Cooling potential and applications prospects of passive radiative cooling in buildings: The current state-of-the-art’, Renewable and Sustainable Energy Reviews. Elsevier Ltd, pp. 1079–1097. Available at: https://doi.org/10.1016/j.rser.2016.07.058.

Luo, M. et al. (2022) ‘Tunable Infrared Detection, Radiative Cooling and Infrared-Laser Compatible Camouflage Based on a Multifunctional Nanostructure with Phase-Change Material’, Nanomaterials, 12(13). Available at: https://doi.org/10.3390/nano12132261.

Lv, S. et al. (2021) ‘A novel strategy of enhancing sky radiative cooling by solar photovoltaic-thermoelectric cooler’, Energy, 219, p. 119625. Available at: https://doi.org/10.1016/j.energy.2020.119625.

Maerefat, M and Haghighi, A.P. (2010) ‘Natural cooling of stand-alone houses using solar chimney and evaporative cooling cavity’, Renewable Energy, 35(9), pp. 2040–2052. Available at: https://doi.org/10.1016/j.renene.2010.02.005.

Maerefat, M. and Haghighi, A.P. (2010) ‘Passive cooling of buildings by using integrated earth to air heat exchanger and solar chimney’, Renewable Energy, 35(10), pp. 2316–2324. Available at: https://doi.org/10.1016/j.renene.2010.03.003.

Mahdavinejad, M. and Javanrudi, K. (2012) ‘Assessment of Ancient Fridges: A Sustainable Method to Storage Ice in Hot-Arid Climates’, Asian Culture and History, 4(2). Available at: https://doi.org/10.5539/ach.v4n2p133.

Man, Y. et al. (2011) ‘Feasibility study on novel hybrid ground coupled heat pump system with nocturnal cooling radiator for cooling load dominated buildings’, Applied Energy, 88(11), pp. 4160–4171. Available at: https://doi.org/10.1016/j.apenergy.2011.04.035.

Mandal, J. et al. (2018) ‘Hierarchically porous polymer coatings for highly efficient passive daytime radiative cooling’, Science, 362(6412), pp. 315–319. Available at: https://doi.org/10.1126/science.aat9513.

Mandal, J. et al. (2020) ‘Paints as a Scalable and Effective Radiative Cooling Technology for Buildings’, Joule, 4(7), pp. 1350–1356. Available at: https://doi.org/10.1016/j.joule.2020.04.010.

Meerdink, S.K. et al. (2019) ‘The ECOSTRESS spectral library version 1.0’, Remote Sensing of Environment, 230(May), p. 111196. Available at: https://doi.org/10.1016/j.rse.2019.05.015.

Melchor V, C. (1982) ‘New formula for the equivalent night sky emissivity’, Solar Energy, 28(6), pp. 489–498.

Memon, S.A. (2014) ‘Phase change materials integrated in building walls: A state of the art review’, Renewable and sustainable energy reviews, 31, pp. 870–906.

Michalak, P. (2022) ‘Hourly Simulation of an Earth-to-Air Heat Exchanger in a Low-Energy Residential Building’, Energies, 15(5). Available at: https://doi.org/10.3390/en15051898.

Mihalakakou, G., Ferrante, A. and Lewis, J.O. (1998) The cooling potential of a metallic nocturnal radiator, Energy and Buildings.

Misiopecki, C. et al. (2018) ‘Thermal modeling and investigation of the most energy-efficient window position’, Energy and Buildings, 158, pp. 1079–1086. Available at: https://doi.org/10.1016/j.enbuild.2017.10.021.

Modest, M.F. (2003) ‘Fundamentals of Thermal Radiation’, Radiative Heat Transfer, pp. 1–29. Available at: https://doi.org/10.1016/b978-012503163-9/50002-3.

van Moeseke, G., Bruyère, I. and De Herde, A. (2007) ‘Impact of control rules on the efficiency of shading devices and free cooling for office buildings’, Building and Environment, 42(2), pp. 784–793. Available at: https://doi.org/10.1016/j.buildenv.2005.09.015.

Mojumder, J.C. et al. (2016) ‘An experimental investigation on performance analysis of air type photovoltaic thermal collector system integrated with cooling fins design’, Energy and Buildings, 130, pp. 272–285. Available at: https://doi.org/10.1016/j.enbuild.2016.08.040.

Mokhtari, R., Ulpiani, G. and Ghasempour, R. (2022) ‘The Cooling Station: combining hydronic radiant cooling and daytime radiative cooling for urban shelters’, Applied Thermal Engineering, 211(April), p. 118493. Available at: https://doi.org/10.1016/j.applthermaleng.2022.118493.

Moosavi, L. et al. (2020) 'New design for solar chimney with integrated windcatcher for space cooling and ventilation', Building and Environment, 181(February), p. 106785. Available at: https://doi.org/10.1016/j.buildenv.2020.106785.

Naghshine, B.B. and Saboonchi, A. (2018) 'Optimized thin film coatings for passive radiative cooling applications', Optics Communications, 410(July 2017), pp. 416–423. Available at: https://doi.org/10.1016/j.optcom.2017.10.047.

Nasa Earth Observatory (2022) Heatwaves and Fires Scorch Europe, Africa, and Asia. Available at: earthobservatory.nasa.gov.

Nicol, J.F. and Humphreys, M.A. (2002) 'Adaptive thermal comfort and sustainable thermal standards for buildings', Energy and buildings, 34(6), pp. 563–572. Available at: https://doi.org/10.1016/S0378-7788(02)00006-3.

Nwaigwe, K.N. et al. (2010) 'Review of Nocturnal Cooling Systems', International Journal of Energy for a Clean Environment, 11(1–4), pp. 117–143. Available at: https://doi.org/10.1615/InterJEnerCleanEnv.2011003225.

Oikonomou, A. and Bougiatioti, F. (2011) 'Architectural structure and environmental performance of the traditional buildings in Florina, NW Greece', Building and Environment, 46(3), pp. 669–689. Available at: https://doi.org/10.1016/j.buildenv.2010.09.012.

Okoronkwo, C.A. et al. (2014) 'An experimental investigation of the passive cooling of a building using nighttime radiant cooling', International Journal of Green Energy, 11(10), pp. 1072–1083. Available at: https://doi.org/10.1080/15435075.2013.829775.

Oliveti, G. et al. (2012) 'Experimental evaluations of the building shell radiant exchange in clear sky conditions', Solar Energy, 86(6), pp. 1785–1795. Available at: https://doi.org/10.1016/j.solener.2012.03.009.

Olsthoorn, D. et al. (2017) 'Abilities and limitations of thermal mass activation for thermal comfort , peak shifting and shaving : A review', Building and Environment, 118, pp. 113–127. Available at: https://doi.org/10.1016/j.buildenv.2017.03.029.

Omara, A.A.M. et al. (2021) 'Performance improvement of solar chimneys using phase change materials: A review', Solar Energy, 228(May), pp. 68–88. Available at: https://doi.org/10.1016/j.solener.2021.09.037.

Orel, B., Gunde, M.K. and Krainer, A. (1993) 'Radiative cooling efficiency of white pigmented paints', Solar Energy, 50(6), pp. 477–482.

Pacheco, R., Ordóñez, J. and Martínez, G. (2012) 'Energy efficient design of building: A review', Renewable and Sustainable Energy Reviews, pp. 3559–3573. Available at: https://doi.org/10.1016/j.rser.2012.03.045.

Pan, L. and Chu, L.M. (2016) 'Energy saving potential and life cycle environmental impacts of a vertical greenery system in Hong Kong : A case study', Building and Environment, 96, pp. 293–300. Available at: https://doi.org/10.1016/j.buildenv.2015.06.033.

Pan, L., Wei, S. and Chu, L.M. (2018) 'Energy & Buildings Orientation effect on thermal and energy performance of vertical greenery systems', 175, pp. 102–112. Available at: https://doi.org/10.1016/j.enbuild.2018.07.024.

Panayiotou, G.P., Kalogirou, S.A. and Tassou, S.A. (2016) 'Evaluation of the application of Phase Change Materials (PCM) on the envelope of a typical dwelling in the Mediterranean region', Renewable Energy, 97, pp. 24–32.

Parker, D.S. and Sherwin, J.R. (2008) Evaluation of the NightCool Nocturnal Radiation Cooling Concept: Annual Performance Assessment in Scale Test Buildings Stage Gate 1B CONTRACT REPORT.

Passipedia (2021) Internal heat gains in relation to living area. Available at: passipedia.org.

Pasupathy, A. and Velraj, R. (2008) 'Effect of double layer phase change material in building roof for year round thermal management', Energy and Buildings, 40(3), pp. 193–203.

Pech-May, N.W. and Retsch, M. (2020) 'Tunable daytime passive radiative cooling based on a broadband angle selective low-pass filter', Nanoscale Advances, 2(1), pp. 249–255. Available at: https://doi.org/10.1039/c9na00557a.

Pérez, G. et al. (2011) 'Behaviour of green facades in Mediterranean Continental climate', 52, pp. 1861–1867. Available at: https://doi.org/10.1016/j.enconman.2010.11.008.

Pérez-Lombard, L., Ortiz, J. and Pout, C. (2008) 'A review on buildings energy consumption information', Energy and buildings, 40(3), pp. 394–398.

Raman, A.P. et al. (2014) 'Passive radiative cooling below ambient air temperature under direct sunlight', Nature, 515(7528), pp. 540–544. Available at: https://doi.org/10.1038/nature13883.

Rasheed, S. et al. (2022) 'Experimental evaluation of indirect evaporative cooler with improved heat and mass transfer', Applied Thermal Engineering, 217(July), p. 119152. Available at: https://doi.org/10.1016/j.applthermaleng.2022.119152.

Roche, P. La and Milne, M. (2004) 'Effects of window size and thermal mass on building comfort using an intelligent ventilation controller', 77, pp. 421–434. Available at: https://doi.org/10.1016/j.solener.2003.09.004.

Rodrigues, L., Sougkakis, V. and Gillott, M. (2016) 'Investigating the potential of adding thermal mass to mitigate overheating in a super-insulated low-energy timber house', (March 2015), pp. 305–316. Available at: https://doi.org/10.1093/ijlct/ctv003.

Saitoh, T.S. and Fujino, T. (2001) ADVANCED ENERGY-EFFICIENT HOUSE (HARBEMAN HOUSE) WITH SOLAR THERMAL, PHOTOVOLTAIC, AND SKY RADIATION ENERGIES (EXPERIMENTAL RESULTS). Available at: www.elsevier.com/locate/solener.

Sameti, M. and Kasaeian, A. (2015) 'Numerical simulation of combined solar passive heating and radiative cooling for a building', Building Simulation, 8(3), pp. 239–253. Available at: https://doi.org/10.1007/s12273-015-0215-x.

Santamouris, M. (2012) Advances in passive cooling. Routledge.

Santamouris, M. and Feng, J. (2018) 'Recent progress in daytime radiative cooling: Is it the air conditioner of the future?', Buildings, 8(12). Available at: https://doi.org/10.3390/buildings8120168.

Santamouris, M. and Kolokotsa, D. (2013) ‘Passive cooling dissipation techniques for buildings and other structures: The state of the art’, Energy and Buildings, 57, pp. 74–94. Available at: https://doi.org/10.1016/j.enbuild.2012.11.002.

Sardarabadi, M. et al. (2017) ‘Experimental study of using both ZnO/ water nanofluid and phase change material (PCM) in photovoltaic thermal systems’, Solar Energy Materials and Solar Cells, 161, pp. 62–69. Available at: https://doi.org/10.1016/j.solmat.2016.11.032.

Sayed, A. et al. (2013) ‘Integration of evaporative cooling technique with solar chimney to improve indoor thermal environment in the New Assiut City , Egypt’, pp. 1–15.

Schweitzer, O. and Erell, E. (2014) ‘Evaluation of the energy performance and irrigation requirements of extensive green roofs in a water-scarce Mediterranean climate’, Energy & Buildings, 68, pp. 25–32. Available at: https://doi.org/10.1016/j.enbuild.2013.09.012.

Serageldin, A.A., Abdelrahman, A.K. and Ookawara, S. (2018) ‘Parametric study and optimization of a solar chimney passive ventilation system coupled with an earth-to-air heat exchanger’, Sustainable Energy Technologies and Assessments, 30, pp. 263–278. Available at: https://doi.org/10.1016/j.seta.2018.10.010.

Serra, V. et al. (2017) ‘A novel vertical greenery module system for building envelopes : The results and outcomes of a multidisciplinary research project’, Energy & Buildings, 146, pp. 333–352. Available at: https://doi.org/10.1016/j.enbuild.2017.04.046.

Seyam, S. (2019) ‘The impact of greenery systems on building energy: Systematic review’, Journal of Building Engineering, 26, p. 100887. Available at: https://doi.org/10.1016/j.jobe.2019.100887.

Sharifi, A. and Yamagata, Y. (2015a) ‘Roof ponds as passive heating and cooling systems: A systematic review’, Applied Energy. Elsevier Ltd, pp. 336–357. Available at: https://doi.org/10.1016/j.apenergy.2015.09.061.

Sharifi, A. and Yamagata, Y. (2015b) 'Roof ponds as passive heating and cooling systems: A systematic review', Applied Energy, 160, pp. 336–357. Available at: https://doi.org/10.1016/j.apenergy.2015.09.061.

Shaviv, E., Yezioro, A. and Capeluto, I.G. (2001) 'Thermal mass and night ventilation as passive cooling design strategy', 24, pp. 445–452.

Shen, D., Yu, C. and Wang, W. (2020) 'Investigation on the thermal performance of the novel phase change materials wall with radiative cooling', Applied Thermal Engineering, 176(May), p. 115479. Available at: https://doi.org/10.1016/j.applthermaleng.2020.115479.

Şirin, C., Goggins, J. and Hajdukiewicz, M. (2023) 'A review on building-integrated photovoltaic/thermal systems for green buildings', Applied Thermal Engineering. Elsevier Ltd. Available at: https://doi.org/10.1016/j.applthermaleng.2023.120607.

Sodha, M.S. et al. (1981) Experimental Validation of Thermal Model of Open Roof Pond, Building and Environment.

Sodha, M.S., Kaushik, S.C. and Nayak, J.K. (1981) 'Performance of trombe walls and roof pond systems', Applied Energy, 8(3), pp. 175–191. Available at: https://doi.org/10.1016/0306-2619(81)90016-7.

Sohel, M.I. et al. (2014) 'A feasibility study of night radiative cooling of BIPVT in climatic conditions of major Australian cities', in Proceedings of Asia-Pacific solar research conference.

SolarWall (2022) SolarWall Systems. Available at: www.solarwall.com.

Solovyev, A.K., Ruipu, B. and Phuong, N.T.K. (2021) 'PRELIMINARY ASSESSMENT OF THE ENERGY EFFICIENCY OF THE TROMBE WALLS IN BUILDINGS WITH PASSIVE USE OF SOLAR ENERGY.', Light & Engineering, 29(5).

Son, S. et al. (2020) 'Colored emitters with silica-embedded perovskite nanocrystals for efficient daytime radiative cooling', International Journal of Refractory Metals and Hard Materials, p. 105247. Available at: https://doi.org/10.1016/j.nanoen.2020.105461.

Son, S. et al. (2021) 'Colored emitters with silica-embedded perovskite nanocrystals for efficient daytime radiative cooling', Nano Energy, 79(October 2020), p. 105461. Available at: https://doi.org/10.1016/j.nanoen.2020.105461.

SpectralCal.com (2020) Blackbody calculator. Available at: www.spectralcalc.com.

Strachan, P., Svehla, K., Kersken, M., et al. (2016) 'Reliable building energy performance characterisation based on full scale dynamic measurements', Annex, 58, p. 5.

Strachan, P., Svehla, K., Heusler, I., et al. (2016) 'Whole model empirical validation on a full-scale building', Journal of Building Performance Simulation, 9(4), pp. 331–350. Available at: https://doi.org/10.1080/19401493.2015.1064480.

Sullivan, J., Krishna, A. and Lee, J. (2018) 'Porous Nickel as a Selective Emitter for Surface Cooling in Various Environments', Proceedings of the 17th InterSociety Conference on Thermal and Thermomechanical Phenomena in Electronic Systems, ITherm 2018, pp. 915–920. Available at: https://doi.org/10.1109/ITHERM.2018.8419542.

Swinbank, W.C. (1963) 'Long-wave radiation from clear skies', Quarterly Journal of the Royal Meteorological Society, 89(381), pp. 339–348. Available at: https://doi.org/10.1002/qj.49708938105.

Tagliabue, L.C., Buzzetti, M. and Arosio, B. (2012) 'Energy saving through the sun: Analysis of visual comfort and energy consumption in office space', in Energy Procedia. Elsevier Ltd, pp. 693–703. Available at: https://doi.org/10.1016/j.egypro.2012.11.079.

Tang, R., Etzion, Y. and Meir, I.A. (2004) 'Estimates of clear night sky emissivity in the Negev Highlands, Israel', Energy Conversion and Management, 45(11–12), pp. 1831–1843. Available at: https://doi.org/10.1016/j.enconman.2003.09.033.

Tartarini, F. et al. (2020) 'CBE Thermal Comfort Tool: Online tool for thermal comfort calculations and visualizations', SoftwareX, 12, p. 100563. Available at: https://doi.org/10.1016/j.softx.2020.100563.

Taurines, K. (2019) ‘Energy and thermal analysis of an innovative earth-to-air heat exchanger: Experimental investigations’, Energy and Buildings, 187, pp. 1–15. Available at: https://doi.org/10.1016/j.enbuild.2019.01.037.

Taylor, S. et al. (2020) ‘Spectrally-selective vanadium dioxide based tunable metafilm emitter for dynamic radiative cooling’, Solar Energy Materials and Solar Cells, 217. Available at: https://doi.org/10.1016/j.solmat.2020.110739.

Teo, H.G., Lee, P.S. and Hawlader, M.N.A. (2012) ‘An active cooling system for photovoltaic modules’, Applied Energy, 90(1), pp. 309–315. Available at: https://doi.org/10.1016/j.apenergy.2011.01.017.

Torgerson, E. and Hellhake, J. (2019) ‘Polymer solar filter for enabling direct daytime radiative cooling’, Solar Energy Materials and Solar Cells, (November), p. 110319. Available at: https://doi.org/10.1016/j.solmat.2019.110319.

al Touma, A. et al. (2016) ‘Solar chimney integrated with passive evaporative cooler applied on glazing surfaces’, Energy, 115(2016), pp. 169–179. Available at: https://doi.org/10.1016/j.energy.2016.09.020.

Tso, C.Y., Chan, K.C. and Chao, C.Y.H. (2017) ‘A field investigation of passive radiative cooling under Hong Kong’s climate’, Renewable Energy, 106, pp. 52–61. Available at: https://doi.org/10.1016/j.renene.2017.01.018.

USA Today (2022) Extreme heat waves may be our new normal, thanks to climate change. Is the globe prepared? Available at: phys.org/news/2022-08-extreme-climate-globe.html.

Valladares-Rendón, L.G., Schmid, G. and Lo, S.L. (2017) ‘Review on energy savings by solar control techniques and optimal building orientation for the strategic placement of façade shading systems’, Energy and Buildings. Elsevier Ltd, pp. 458–479. Available at: https://doi.org/10.1016/j.enbuild.2016.12.073.

Verbeke, S. and Audenaert, A. (2018) ‘Thermal inertia in buildings: A review of impacts across climate and building use’, Renewable and Sustainable Energy Reviews. Elsevier Ltd, pp. 2300–2318. Available at: https://doi.org/10.1016/j.rser.2017.08.083.

Villar-Ramos, M.M. et al. (2020) ‘Parametric analysis of the thermal behavior of a single-channel solar chimney’, Solar Energy, 209(September), pp. 602–617. Available at: https://doi.org/10.1016/j.solener.2020.08.072.

Voelker, C., Kornadt, O. and Ostry, M. (2008) ‘Temperature reduction due to the application of phase change materials’, Energy and Buildings, 40(5), pp. 937–944.

Wang, J. et al. (2023) ‘Emergy analysis and optimization for a solar-driven heating and cooling system integrated with air source heat pump in the ultra-low energy building’, Journal of Building Engineering, 63. Available at: https://doi.org/10.1016/j.jobe.2022.105467.

Wang, Q. et al. (2023) ‘4E Analysis of a novel combined cooling, heating and power system coupled with solar thermochemical process and energy storage’, Energy, 275. Available at: https://doi.org/10.1016/j.energy.2023.127498.

Wang, W. et al. (2018a) ‘Performance assessment of a photonic radiative cooling system for office buildings’, Renewable Energy, 118, pp. 265–277. Available at: https://doi.org/10.1016/j.renene.2017.10.062.

Wang, W. et al. (2018b) ‘Performance assessment of a photonic radiative cooling system for office buildings’, Renewable Energy, 118, pp. 265–277. Available at: https://doi.org/10.1016/j.renene.2017.10.062.

Watmuff, J., Charters, W. and Proctor, D. (1977) ‘Solar and wind induced external coefficients - Solar collectors’, Cooperation Mediterraneenne pour l’Energie Solaire, 1, p. 56.

Williamson, T.J. (2011) ‘ASSESSING THE EFFECTIVENESS FOR THERMAL MASS IN THE BUILDING ENVELOP The School of Architecture , Landscape Architecture & Urban Design The University of Adelaide , Adelaide , Australia Q c’, pp. 14–16.

Wu, S.Y., Wu, L.F. and Xiao, L. (2023) ‘Effects of aspect ratio and inlet wind velocity on thermal characteristics of Trombe wall channel under different ventilation strategies: An indoor experiment’, Experimental Thermal and Fluid Science, 141. Available at: https://doi.org/10.1016/j.expthermflusci.2022.110800.

Wu, T. and Lei, C. (2016) ‘A review of research and development on water wall for building applications’, Energy and Buildings. Elsevier Ltd, pp. 198–208. Available at: https://doi.org/10.1016/j.enbuild.2015.12.003.

Xu, X. et al. (2005) ‘Modeling and simulation on the thermal performance of shape-stabilized phase change material floor used in passive solar buildings’, Energy and Buildings, 37(10), pp. 1084–1091.

Yang, L. and Li, Y. (2008) ‘Cooling load reduction by using thermal mass and night ventilation’, 40, pp. 2052–2058. Available at: https://doi.org/10.1016/j.enbuild.2008.05.014.

Yang, Y., Cui, G. and Lan, C.Q. (2019) ‘Developments in evaporative cooling and enhanced evaporative cooling - A review’, Renewable and Sustainable Energy Reviews. Elsevier Ltd. Available at: https://doi.org/10.1016/j.rser.2019.06.037.

Yi, Z. et al. (2020) ‘A Transparent Radiative Cooling Film for Building Energy Saving’, Energy and Built Environment [Preprint]. Available at: https://doi.org/10.1016/j.enbenv.2020.07.003.

Yong, C., Yiping, W. and Li, Z. (2015) ‘Performance analysis on a building-integrated solar heating and cooling panel’, Renewable Energy, 74, pp. 627–632. Available at: https://doi.org/10.1016/j.renene.2014.08.076.

You, W. and Ding, W. (2015) ‘Building façade opening evaluation using integrated energy simulation and automatic generation programs’, Architectural Science Review, 58(3), pp. 205–220.

Yu, C. et al. (2021) ‘Parametric analysis of the phase change material wall combining with micro-channel heat pipe and sky radiative cooling technology’, Renewable Energy, 178, pp. 1057–1069. Available at: https://doi.org/10.1016/j.renene.2021.07.001.

Yu, C. et al. (2022) ‘Numerical study on the thermal performance of phase change materials wall by radiative cooling’, Applied Thermal Engineering, 215(July), p. 119013. Available at: https://doi.org/10.1016/j.applthermaleng.2022.119013.

Yu, W. et al. (2022) ‘Modeling and assessing earth-air heat exchanger using the parametric performance design method’, Energy Sources, Part A: Recovery, Utilization, and Environmental Effects, 44(3), pp. 7873–7894. Available at: https://doi.org/10.1080/15567036.2022.2116504.

Yuan, J. et al. (2022) ‘On daytime radiative cooling using spectrally selective metamaterial based building envelopes’, Energy, 242, p. 122779. Available at: https://doi.org/10.1016/j.energy.2021.122779.

Zeinelabdein, R., Omer, S. and Gan, G. (2018) ‘Critical review of latent heat storage systems for free cooling in buildings’, Renewable and Sustainable Energy Reviews. Elsevier Ltd, pp. 2843–2868. Available at: https://doi.org/10.1016/j.rser.2017.10.046.

Zeyghami, M., Goswami, D.Y. and Stefanakos, E. (2018) ‘A review of clear sky radiative cooling developments and applications in renewable power systems and passive building cooling’, Solar Energy Materials and Solar Cells, 178(January), pp. 115–128. Available at: https://doi.org/10.1016/j.solmat.2018.01.015.

Zhang, J. et al. (2021) ‘Cover shields for sub-ambient radiative cooling: A literature review’, Renewable and Sustainable Energy Reviews, 143(February), p. 110959. Available at: https://doi.org/10.1016/j.rser.2021.110959.

Zhang, J. and Zhu, T. (2022) ‘Systematic review of solar air collector technologies: Performance evaluation, structure design and application analysis’, Sustainable Energy Technologies and Assessments, 54(409), p. 102885. Available at: https://doi.org/10.1016/j.seta.2022.102885.

Zhang, K. et al. (2018) ‘Energy saving and economic analysis of a new hybrid radiative cooling system for single-family houses in the USA’, Applied Energy, 224, pp. 371–381. Available at: https://doi.org/10.1016/j.apenergy.2018.04.115.

Zhang, S. and Niu, J. (2012) ‘Cooling performance of nocturnal radiative cooling combined with microencapsulated phase change material (MPCM) slurry storage’, Energy and Buildings, 54, pp. 122–130. Available at: https://doi.org/10.1016/j.enbuild.2012.07.041.

Zhang, Y. et al. (2006) ‘Experimental study on the thermal performance of the shape-stabilized phase change material floor used in passive solar buildings’.

Zhao, B. et al. (2017) ‘Conceptual development of a building-integrated photovoltaic–radiative cooling system and preliminary performance analysis in Eastern

China', Applied Energy, 205, pp. 626–634. Available at: https://doi.org/10.1016/j.apenergy.2017.08.011.

Zhao, B. et al. (2018) 'Comprehensive photonic approach for diurnal photovoltaic and nocturnal radiative cooling', Solar Energy Materials and Solar Cells, 178, pp. 266–272. Available at: https://doi.org/10.1016/j.solmat.2018.01.023.

Zhao, B., Hu, M., Ao, X., Chen, N., Xuan, Q., et al. (2019a) 'A novel strategy for a building-integrated diurnal photovoltaic and all-day radiative cooling system', Energy, 183, pp. 892–900. Available at: https://doi.org/10.1016/j.energy.2019.06.166.

Zhao, B., Hu, M., Ao, X., Huang, X., et al. (2019) 'Conventional photovoltaic panel for nocturnal radiative cooling and preliminary performance analysis', Energy, 175, pp. 677–686. Available at: https://doi.org/10.1016/j.energy.2019.03.106.

Zhao, B., Hu, M., Ao, X., Chen, N., Xuan, Q., et al. (2019b) 'Performance analysis of a hybrid system combining photovoltaic and nighttime radiative cooling', Applied Energy, 252(January), p. 113432. Available at: https://doi.org/10.1016/j.apenergy.2019.113432.

Zhao, B., Hu, M., Ao, X. and Pei, G. (2019) 'Performance evaluation of daytime radiative cooling under different clear sky conditions', Applied Thermal Engineering, 155(April), pp. 660–666. Available at: https://doi.org/10.1016/j.applthermaleng.2019.04.028.

Zhao, B., Hu, M., Ao, X., Chen, N. and Pei, G. (2019) 'Radiative cooling: A review of fundamentals, materials, applications, and prospects', Applied Energy, 236, pp. 489–513. Available at: https://doi.org/10.1016/j.apenergy.2018.12.018.

Zhao, B. et al. (2020) 'A spectrally selective surface structure for combined photothermic conversion and radiative sky cooling', Frontiers in Energy, 14(4), pp. 882–888. Available at: https://doi.org/10.1007/s11708-020-0694-z.

Zhao, B. et al. (2021) 'Is it possible for a photovoltaic-thermoelectric device to generate electricity at night?', Solar Energy Materials and Solar Cells, 228(December 2020), p. 111136. Available at: https://doi.org/10.1016/j.solmat.2021.111136.

Zhao, B. et al. (2022) ‘Tunable thermal management based on solar heating and radiative cooling’, Solar Energy Materials and Solar Cells, 235. Available at: https://doi.org/10.1016/j.solmat.2021.111457.

Zhao, D. et al. (2019) ‘Roof-integrated radiative air-cooling system to achieve cooler attic for building energy saving’, Energy and Buildings, 203. Available at: https://doi.org/10.1016/j.enbuild.2019.109453.

Zhao, D. et al. (2019) ‘Subambient Cooling of Water: Toward Real-World Applications of Daytime Radiative Cooling’, Joule [Preprint]. Available at: https://doi.org/10.1016/j.joule.2018.10.006.

Zhao, X. et al. (2022) ‘Dynamic glazing with switchable solar reflectance for radiative cooling and solar heating’, Cell Reports Physical Science, 3(4). Available at: https://doi.org/10.1016/j.xcrp.2022.100853.

Zhou, L. et al. (2019) ‘A polydimethylsiloxane-coated metal structure for all-day radiative cooling’, Nature Sustainability, 2(8), pp. 718–724. Available at: https://doi.org/10.1038/s41893-019-0348-5.

Zhou, Y., Zheng, S. and Zhang, G. (2020) ‘A review on cooling performance enhancement for phase change materials integrated systems—flexible design and smart control with machine learning applications’, Building and Environment, 174(January), p. 106786. Available at: https://doi.org/10.1016/j.buildenv.2020.106786.

Zhu, L. et al. (2009) ‘Detailed energy saving performance analyses on thermal mass walls demonstrated in a zero energy house’, 41, pp. 303–310. Available at: https://doi.org/10.1016/j.enbuild.2008.10.003.

Ziming, C. et al. (2020) ‘Low-cost radiative cooling blade coating with ultrahigh visible light transmittance and emission within an “atmospheric window”’, Solar Energy Materials and Solar Cells, 213(February), p. 110563. Available at: https://doi.org/10.1016/j.solmat.2020.110563.

Ziming, C. et al. (2021) ‘Influences of atmospheric water vapor on spectral effective emissivity of a single-layer radiative cooling coating’, AIMS Energy, 9(1), pp. 96–116. Available at: https://doi.org/10.3934/energy.2021006.

Appendices

Appendix A: Validating Ansys Fluent model for various radiative cooling cases

PART 1: ANSYS Simulation of Conventional Solar Heating

A. Geometry

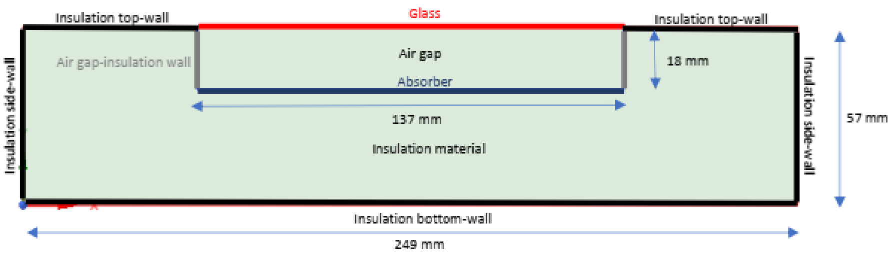

B. Material properties

Glass Density (ρ_g): 2203 kg/m³ Specific heat capacity ($c_{p\,glass}$): 703 J/kg.K Thermal conductivity (k_g): 1.38 W/m.K Thickness (d_g): 0.0028 m Absorptivity of the glass in the solar band (α_g): 0.03 Transmissivity of the glass in the solar band (τ_g): 0.9 Reflectivity of the glass in the solar band (ρ_g): 0.07 Emissivity of the glass in the LWIR (ε_g): 0.88
Absorber plate Density (ρ_p): 2719 kg/m³ Specific heat capacity ($c_{p\,abs}$): 871 J/kg.K Thermal conductivity (k_p): 202.4 W/m.K Thickness (d_p): 0.0004 m Absorptivity in the solar band (α_p): 0.92 Emissivity of the plate in the LWIR (ε_p): 0.05
Insulation Density (ρ_{ins}): 30 kg/m³ Specific heat capacity ($c_{p\,ins}$): 1400 J/kg.K Thermal conductivity (k_{ins}): 0.04 W/m.K Emissivity of the insulation in the LWIR (ε_i): 0.2

C. Heat transfer for each wall

1. Glass cover

Heat balance of the glass cover:

$$\underbrace{\alpha_g G}_{(i)} + \underbrace{h_{amb,g}(T_{amb} - T_g)}_{(ii)} + \underbrace{\varepsilon_{s,g}\sigma(T_s^4 - T_g^4)}_{(iii)} + \underbrace{h_{ag}(T_a - T_g)}_{(iv)} + \underbrace{q_{sur,g-rad}}_{(v)} = 0$$

i. $\alpha_g G$ is solar radiation absorbed by the glass, where α_g is absorptivity of the glass in the solar band and G is total solar irradiance. This was translated into the model using user's input tabular data to the "Heat Generation Rate" (W/m^3) (Figure 1, number (i)). The equation is converted to $\alpha_g G/d_g$, where d_g is the thickness of the glass.

ii. Convective heat transfer coefficient $h_{\mathrm{amb,g}}$ is calculated from.[1]

$$h_{\mathrm{amb,g}} = 2.8 + 3.0u_{\mathrm{amb}}$$

The u_{amb} is the ambient wind speed, and the data was taken from [2]. T_{amb} is ambient temperature, taken from the recorded data in the experiment, and T_{g} is glass temperature. Input for convection to ambient is indicated by Figure 1, number (ii).

iii. Radiation between the glass is calculated by $\varepsilon_{\mathrm{s,g}}\sigma\left(T_{\mathrm{s}}^4 - T_{\mathrm{g}}^4\right)$ where $\varepsilon_{\mathrm{s,g}}$ is the effective emissivity of the sky and the glass in the atmospheric window band, based on this relationship: $\varepsilon_{\mathrm{s,g}}$=$\varepsilon_{\mathrm{g}}\varepsilon_{\mathrm{g}}$. The value of sky emissivity ε_{s} calculated from empirical formula by [3,4] as shown below, and glass emissivity is as stated in the material propeties, while the sky temperature T_s is calculated using empirical formula from [4,5] as displayed below. The input in Fluent is indicated by Figure 1, (iii).

$$\varepsilon_{\mathrm{s}} = 1 - \left(0.261e^{-7.77\times10^{-4}\left(273.15 - T_{\mathrm{amb}}^2\right)}\right)$$

$$T_s = 0.0552T_{\mathrm{amb}}^{1.5}$$

iv. $h_{\mathrm{ag}}\left(T_{\mathrm{a}} - T_{\mathrm{g}}\right)$ is convective heat transfer between the glass and the air gap, where h_{ag} is the convective heat transfer coefficient, T_{a} is the average temperature in the air gap and $h_{\mathrm{ag}}\left(T_{\mathrm{a}} - T_{\mathrm{g}}\right)$. It is calculated by the ANSYS Fluent.[1]

v. $q_{\mathrm{sur,g-rad}}$ is radiative heat transfer between the glass with the surrounding walls in the computational domain. In this case the radiation model used was "surface to surface radiation model" with the following governing equation. The $F_{\mathrm{g},j}$ implies the view factor of surrounding walls j to the glass, and $q_{\mathrm{sur-rad},j}$ radiation leaving the surrounding walls [6].

$$q_{\mathrm{sur,g-rad}} = \varepsilon_{\mathrm{g}}\sigma\, T_{\mathrm{g}}^4 + \rho_{\mathrm{g}} \sum_{j=1}^{N} F_{\mathrm{g},j}\, q_{\mathrm{sur-rad},j}$$

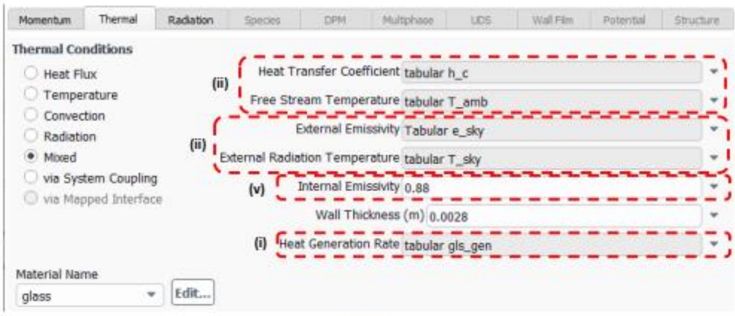

Figure 1

[1] I am still learning the detail equations used by Fluent for this part.

2. **Absorber plate**

Heat balance of the absorber plate

$$(\tau\alpha)_{\mathrm{p}}G + h_{\mathrm{ap}}(T_{\mathrm{a}} - T_{\mathrm{p}}) + U_{\mathrm{bp}}(T_{\mathrm{b}} - T_{\mathrm{p}}) + q_{\mathrm{sur,p-rad}} = 0$$

i. $(\tau\alpha)_{\mathrm{p}}G$ is solar radiation absorbed by the absorber plate after passing through the glass cover. Calculated by [7,8]:

$$(\tau\alpha)_{\mathrm{p}} = \frac{\tau_{\mathrm{g}}\alpha_{\mathrm{p}}}{1 - (1 - a_{\mathrm{p}})\rho_{\mathrm{g}}}$$

where τ_{g} is transmissivity of the glass in the solar band, α_{p} is the absorptivity of the plate in the solar band, ρ_{g} is reflectivity of the glass, and G is total solar irradiance. This was translated into the model using user's input tabular data to the "Heat Generation Rate" (W/m^3) (Figure 2, number (i)). The equation is converted to $(\tau\alpha)_{\mathrm{p}}G/d_{\mathrm{p}}$, where d_{p} is the thickness of the glass.

ii. $h_{\mathrm{ap}}(T_{\mathrm{a}} - T_{\mathrm{p}})$ and $U_{bp}(T_b - T_p)$ are convective heat transfer between the absorber and the air gap and conduction between the absorber with the insulation. It is "coupled" and calculated by ANSYS Fluent.

iii. $q_{\mathrm{sur,p-rad}}$ is radiative heat transfer between the absorber with the surrounding walls in the computational domain. In this case the radiation model used was "surface to surface radiation model" with the following governing equation. $F_{p,j}$ is the view factor of surrounding walls j to the absorber plate, and $q_{\mathrm{sur-rad},j}$ radiation leaving the surrounding walls.

$$q_{\mathrm{sur,p-rad}} = \varepsilon_{\mathrm{p}}\sigma\, T_{\mathrm{p}}^{4} + \rho_{\mathrm{p}} \sum_{j=1}^{N} F_{\mathrm{p},j}\, q_{\mathrm{sur-rad},j}$$

We defined the ε_{p} as the input.

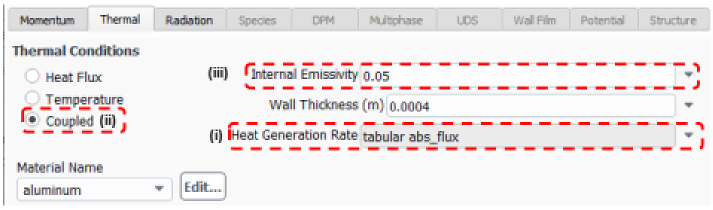

Figure 2

3. **Insulation**

a. Air gap side insulation wall

Side walls of the air gap is an insulation that set to have heat balance equations as follows:

$$h_{\mathrm{ai}}(T_{\mathrm{a}} - T_{\mathrm{i}}) + U_{\mathrm{i}}(T_{\mathrm{o}} - T_{\mathrm{i}}) + q_{\mathrm{sur,i-rad}} = 0$$

With the first two terms is calculate by ANSYS Fluent, while:

$$q_{\mathrm{sur,ins-rad}} = \varepsilon_{\mathrm{i}}\sigma\, T_{\mathrm{i}}^{4} + \rho_{\mathrm{ins}} \sum_{j=1}^{N} F_{\mathrm{i},j}\, q_{\mathrm{sur-rad},j}$$

We defined the emissivity of the interior of the insulation (ε_{i}) as the input.

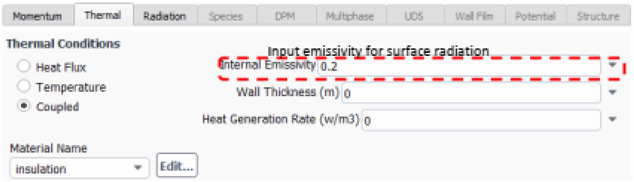

Figure 3

b. Top and side walls of the insulations

The top and side walls of the insulations that adjacent to ambient condition is accounted only for the convective heat transfer to the ambient and conduction to the interior domain. The heat balance equation becomes:

$$h_{\mathrm{amb,o}}(T_{\mathrm{amb}} - T_{\mathrm{o}}) + U_{\mathrm{ins}}(T_{\mathrm{i}} - T_{\mathrm{o}}) = 0$$

where $h_{\mathrm{amb,o}}$ is convection coefficient between ambient and the top side of the insulation calculated from the equation below, T_{o} is the temperature of the outer side of the insulation, T_{i} is the temperature of the inner side of the insulation, and U_{ins} is the thermal transmittance of the insulation.

$$h_{\mathrm{amb,o}} = 2.8 + 3.0u_{\mathrm{amb}}$$

The u_{amb} is the ambient wind speed, and the data was taken from [2].

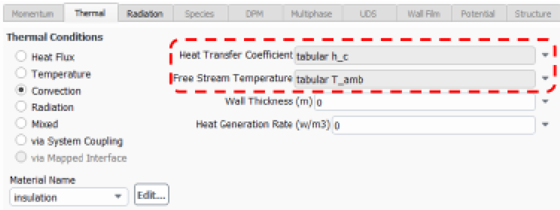

Figure 4

c. Bottom wall of the insulation is assumed to be adiabatic.

Figure 5

Note: Wall thicknesses in the insulation wall settings are inputted as zero because the walls are not thin layers or plates. They are directly the walls of the insulation material. Different case with the glass and the absorber in which it is a thin wall between two or more zones (i.e., outside-inside or air gap-insulation).

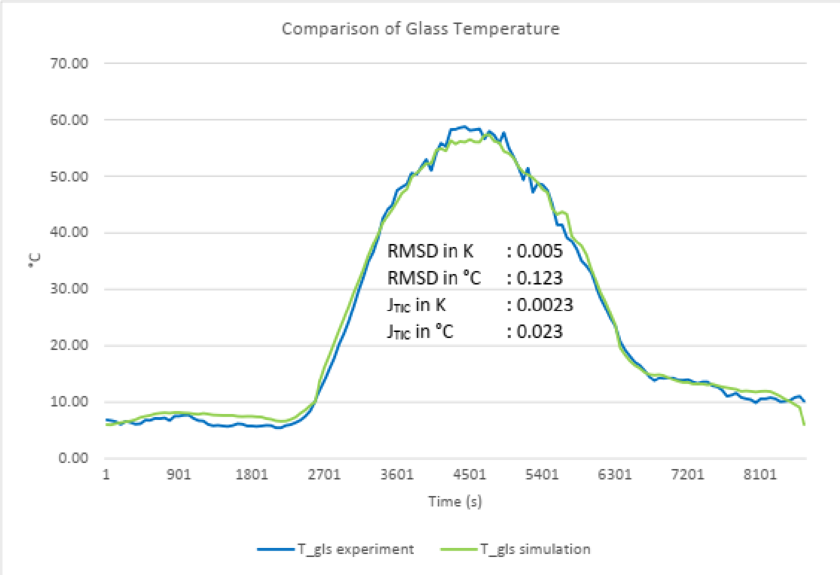

(a)

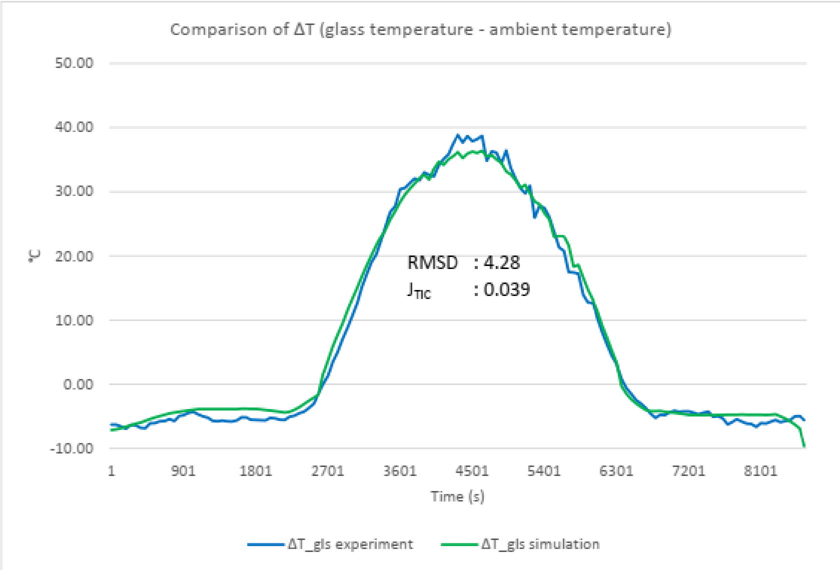

(b)

Figure 6 Glass temperature

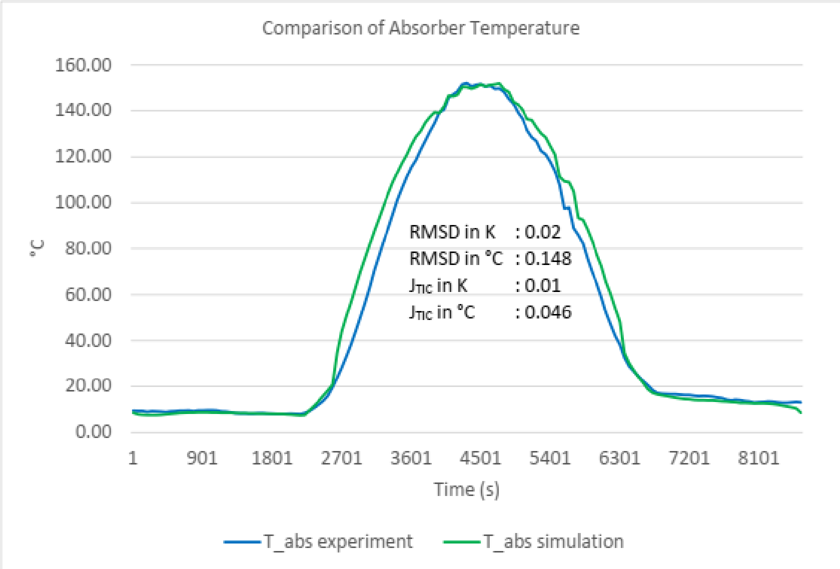

(a)

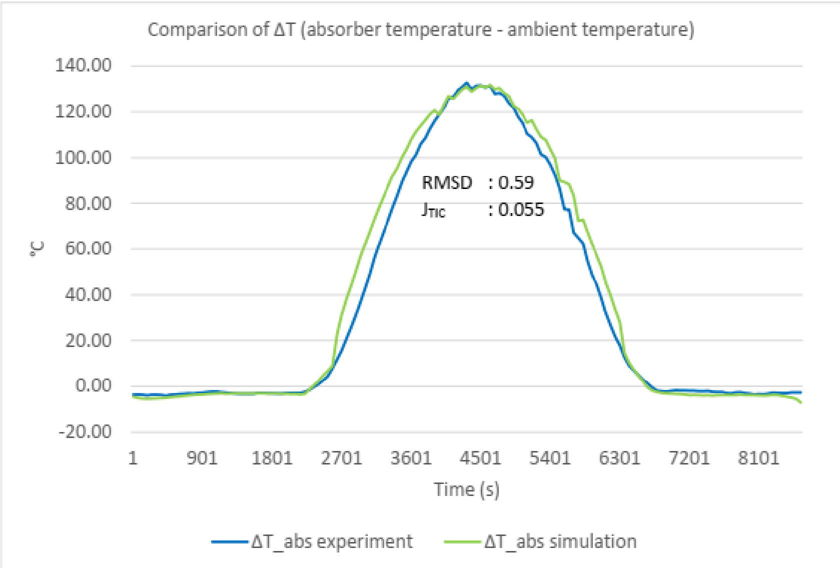

(b)

Figure 7 Absorber temperature

PART 2: ANSYS Simulation of Solar Air Collector & Radiative Cooling (SC-RC) at Night

A. Geometry

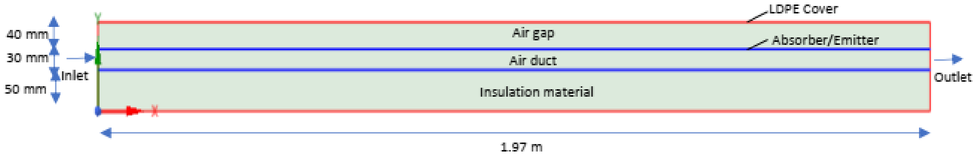

B. Material properties

LDPE Cover Density (ρ_g): 920 kg/m^3 Specific heat capacity ($c_{p\,glass}$): 2260 J/kg.K Thermal conductivity (k_g): 0.33 W/m.K Thickness (d_g): 0.000006 m Absorptivity of the glass in the solar band (α_g): 0.05 Transmissivity of the glass in the solar band (τ_g): 0.92 Reflectivity of the glass in the solar band (ρ_g): 0.03 Emissivity of the glass in the LWIR (ε_g): 0.05
Absorber plate Density (ρ_p): 2700 kg/m^3 Specific heat capacity ($c_{p\,abs}$): 917 J/kg.K Thermal conductivity (k_p): 202.4 W/m.K Thickness (d_p): 0.0004 m Absorptivity in the solar band (α_p): 0.92 Emissivity of the top surface of the plate in the 8-13 µm (ε_p): 0.88 Emissivity of the plate in the LWIR for the bottom side of the plate ($\varepsilon_{p,bottom}$): 0.1
Insulation Density (ρ_{ins}): 50 kg/m^3 Specific heat capacity ($c_{p\,ins}$): 2475 J/kg.K Thermal conductivity (k_{ins}): 0.028 W/m.K Emissivity of the insulation in the LWIR (ε_i): 0.2

C. Heat transfer for each wall

1. LDPE cover

Heat balance of the LDPE cover:

$$\underbrace{\alpha_c G}_{(i)} + \underbrace{h_{amb,c}(T_{amb} - T_c)}_{(ii)} + \underbrace{\varepsilon_{s,c}\sigma(T_s^4 - T_c^4)}_{(iii)} + \underbrace{h_{ac}(T_a - T_c)}_{(iv)} + \underbrace{q_{sur,c-rad}}_{(v)} = 0$$

vi. $\alpha_c G$ is solar radiation absorbed by the cover, where α_c is absorptivity of the cover in the solar band and G is total solar irradiance. This was translated into the model using user's input tabular data to the "Heat Generation Rate" (W/m^3) (Figure 4, number (i)). The equation is converted to $\alpha_c G/d_c$, where d_c is the thickness of the cover.

vii. Convective heat transfer coefficient $h_{\mathrm{amb,c}}$ is calculated from.

$$h_{\mathrm{amb,c}} = 2.8 + 3.0u_{\mathrm{amb}}$$

The u_{amb} is the ambient wind speed, and the data was taken from [2]. T_{amb} is ambient, taken from the recorded data in the experiment, meanwhile T_c is the cover temperature. Input for convection to ambient is indicated by Figure 4, number (ii).

viii. Radiation between the cover is calculated by $\varepsilon_s\sigma(T_s^4 - T_c^4)$. The value of sky emissivity ε_s calculated from empirical formula by [3,4] as shown below, while the sky temperature T_s is calculated using empirical formula from [4,12] as displayed below. The input in Fluent is indicated by Figure 4, (iii).

$$\varepsilon_s = 1 - (0.261e^{-7.77\times10^{-4}(273.15 - T_{\mathrm{amb}}^2)})$$

$$T_s = T_{\mathrm{amb}} - 20$$

ix. $h_{\mathrm{ac}}(T_a - T_c)$ is convective heat transfer between the cover and the air gap. It is calculated by the ANSYS Fluent.

x. $q_{\mathrm{sur,c-rad}}$ is radiative heat transfer between the cover with the surroundings computational domain. In this case the radiation model used was "surface to surface radiation model" with the following governing equation. The $F_{c,j}$ implies the view factor of surrounding walls j to the cover, and $q_{\mathrm{sur-rad},j}$ radiation leaving the surrounding walls.

$$q_{\mathrm{sur,c-rad}} = \varepsilon_c\sigma\, T_c^4 + \rho_g \sum_{j=1}^{N} F_{c,j}\, q_{\mathrm{sur-rad},j}$$

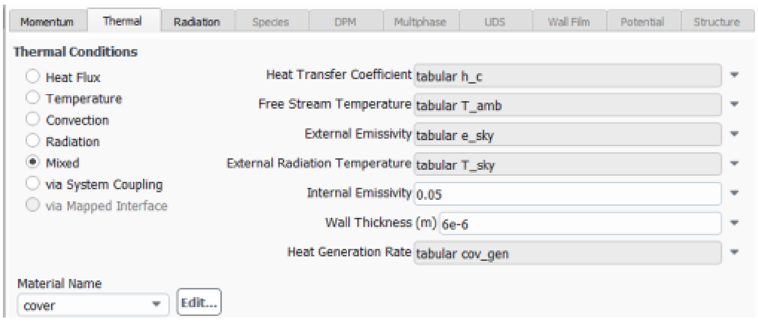

Figure 8

2. Absorber/emitter plate (roughness)

Heat balance of the absorber plate

$$(\tau\alpha)_p G + h_{\mathrm{ap}}(T_a - T_p) + h_{\mathrm{dp}}(T_d - T_p) + q_{\mathrm{sur,p-rad}} = 0$$

i. $(\tau\alpha)_p G$ is solar radiation absorbed by the absorber plate after passing through the glass cover. Calculated by [7,8]:

$$(\tau\alpha)_{\mathrm{p}} = \frac{\tau_{\mathrm{g}}\alpha_{\mathrm{p}}}{1-(1-a_{\mathrm{p}})\rho_{\mathrm{g}}}$$

where τ_{g} is transmissivity of the glass in the solar band, α_{p} is the absorptivity of the plate in the solar band, ρ_{g} is reflectivity of the glass, and G is total solar irradiance. This was translated into the model using user's input tabular data to the "Heat Generation Rate" (W/m^3). The equation is converted to $(\tau\alpha)_{\mathrm{p}}G/d_{\mathrm{p}}$, where d_{p} is the thickness of the glass.

ii. $h_{\mathrm{ap}}(T_{\mathrm{a}} - T_{\mathrm{p}})$ and $h_{\mathrm{dp}}(T_{\mathrm{d}} - T_{\mathrm{p}})$ are convective heat transfer between the absorber/emitter and the air gap and airduct, where h_{ap} is the convection coefficient between the plate and the airgap, T_{a} is the air temperature in the air gap, T_{p} is the plate temperature, h_{dp} is the convection coefficient between the air duct and the plate (mass flow rate of the inlet air is 0.03 kg/s), and T_{d} is the temperature of the air in the duct. It is "coupled" and calculated by ANSYS Fluent.

iii. $q_{\mathrm{sur,p-rad}}$ is radiative heat transfer between the absorber with the surrounding walls in the computational domain. In this case the radiation model used was "surface to surface radiation model" with the following governing equation. $F_{p,j}$ is the view factor of surrounding walls j to the absorber plate, and $q_{\mathrm{sur-rad},j}$ radiation leaving the surrounding walls.

$$q_{\mathrm{sur,p-rad}} = \varepsilon_{\mathrm{p}}\sigma\, T_{\mathrm{p}}^{4} + \rho_{\mathrm{p}}\sum_{j=1}^{N} F_{\mathrm{p},j}\, q_{\mathrm{sur-rad},j}$$

We defined the ε_{p} as the input.

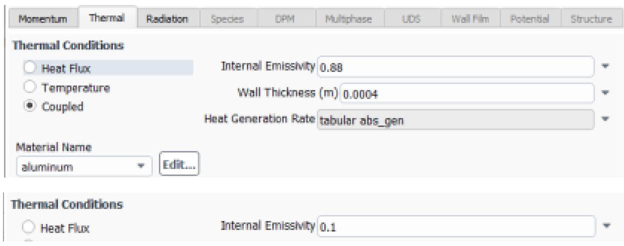

Figure 9

To enhance the contact between the air and the absorber/emitter, a rough structure is added on the bottom part of the plate. The roughness is modeled in ANSYS by using the roughness height and roughness constant as shown in Figure 9. I assumed the height of the roughness to be 0.5 mm.

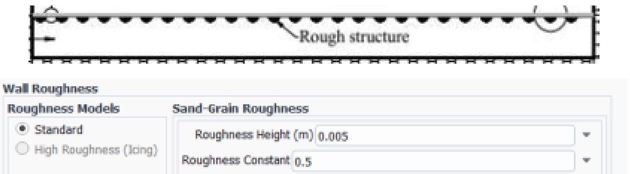

Figure 10

3. Insulation

Insulation walls is set to be adiabatic, meanwhile the eat balance for the inner side of the insulation is as follows.

$$h_{\mathrm{di}}(T_{\mathrm{d}} - T_{\mathrm{i}}) + U_{\mathrm{i}}(T_{\mathrm{o}} - T_{\mathrm{i}}) + q_{\mathrm{sur,i-rad}} = 0$$

with the first two terms is calculate by ANSYS Fluent, where h_{di} is the convection coefficient between the air duct and the insulation wall, T_{d} is the temperature of the air in the duct, U_{i} is the thermal transmittance of the insulation, and T_{o} is the temperature of the outer side of the insulation. The radiation exchange between the insulation and the bottom side of the absorber plate is as follows.

$$q_{\mathrm{sur,ins-rad}} = \varepsilon_{\mathrm{i}}\sigma\, T_{\mathrm{i}}^4 + \rho_{\mathrm{ins}} \sum_{j=1}^{N} F_{\mathrm{i},j}\, q_{\mathrm{sur-rad},j}$$

We defined the emissivity of the interior of the insulation (ε_{i}) as the input.

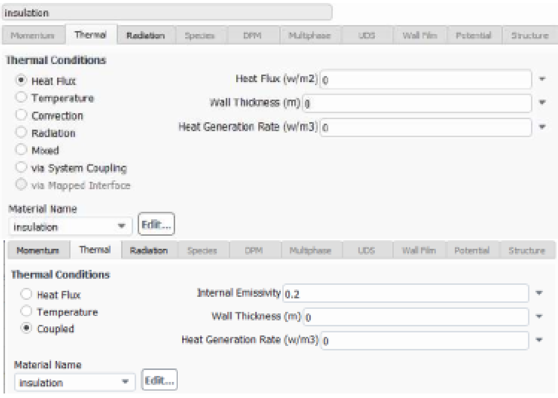

Figure 11

D. Comparison of the ANSYS simulation results with Mingke's simulation in MATLAB

Similar to the previous assessment in Part 1, this comparison also compares two values of temperature. The temperatures are outlet air temperature, i.e., the absolute value and relative value (differences between outlet temperature and inlet temperature). Root Mean Square Deviation (RMSD) and Theil's Inequality Coefficient (TIC) is in. The RMSD formula is stated below, as cited from [9,10].

$$RMSD = \sqrt{\frac{1}{n}\sum_{i=1}^{n}\left[\frac{(X_{\mathrm{sim},i} - X_{\mathrm{exp},i})}{X_{\mathrm{exp},i}}\right]^2}$$

The Theil's Inequality Coefficient (TIC) formula is as follows [11].

$$J_{\mathrm{TIC}} = \frac{\sqrt{\frac{1}{n}\sum_{i=1}^{n}(X_{\mathrm{sim},i} - X_{\mathrm{exp},i})^2}}{\sqrt{\frac{1}{n}\sum_{i=1}^{n} X_{\mathrm{sim},i}^2} + \sqrt{\frac{1}{n}\sum_{i=1}^{n} X_{\mathrm{exp},i}^2}}$$

Both methods are calculated in different units of temperature, °C and K, to see the sensitivity of them for different units. The comparison of the simulation and experimental data are shown in the following figures.

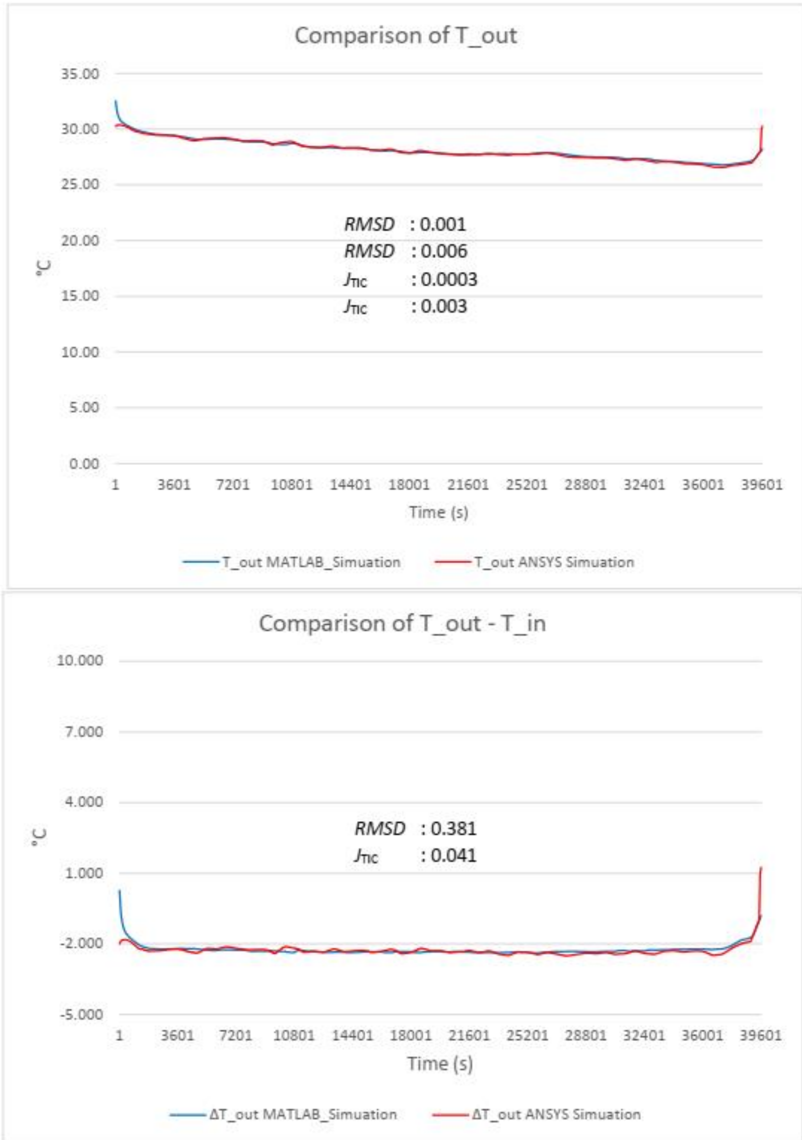

Figure 12

The problem arises for the quantitative assessment of the model has been mentioned previously.

ANSYS Simulation for solar heating (SH) and radiative cooling (RC) in a double-covered SH-RC

A. Geometry

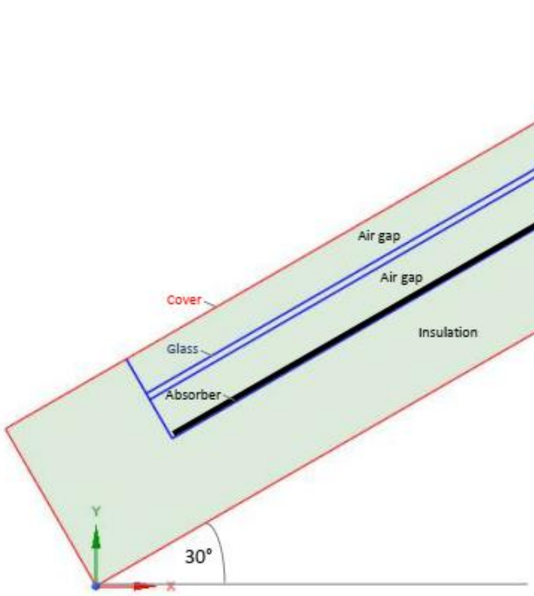

This double-covered PT-RC system has three layers, i.e., a wind cover made of low-density polyethylene film (6μm thick); a glass layer (2.8 mm thick), and an absorber (0.4 mm thick). The glass and the absorber are surrounded by insulation material. The panel is tilted 30° from horizontal, facing the south. Solar radiation data is adjusted to the tilt angle and solar position in the sky during the day. The solar position model was calculated using the model provided by Duffie and Beckman [1] in their book, which was summarised into a step-by-step calculation by Prof. Siddig Omer in his lecture notes for the K14RE2 module [2].[1]

Moreover, to see the range of the simulated surface temperatures resulting from uncertain wind speed magnitude and hourly variation, this simulation used five fixed wind speed values based on the data provided by the Wunderground website [3]. The five values ranged and distributed evenly from the minimum (around 1 m/s) and maximum wind speed (around 5m/s) data. Thus, the wind speed values are $u_1 = 1\ \mathrm{m/s}$; $u_2 = 2\ \mathrm{m/s}$; $u_3 = 3\ \mathrm{m/s}$; $u_4 = 4\ \mathrm{m/s}$; and $u_5 = 5\ \mathrm{m/s}$.

B. Material properties

LDPE cover
Density (ρ_c): 920 kg/m³
Specific heat capacity ($c_{p_{cover}}$): 2260 J/kg.K
Thermal conductivity (k_c): 0.3 W/m.K
Thickness (d_c): 6 μm
Absorptivity of the cover in the solar and atmospheric window band (α_c): 0.05
Transmissivity of the cover in the solar and atmospheric window band (τ_c): 0.92

[1] I took the module in 2015 during my master degree, and the solar radiation assessment was part of the coursework.

Reflectivity of the cover in the solar and atmospheric window band (ρ_c): 0.03
Glass Density (ρ_g): 2203 kg/m³ Specific heat capacity ($c_{p_{glass}}$): 703 J/kg.K Thermal conductivity (k_g): 1.38 W/m.K Thickness (d_g): 0.0028 m Absorptivity of the glass in the solar band (α_g): 0.03 Transmissivity of the glass in the solar band (τ_g): 0.87 Reflectivity of the glass in the solar band (ρ_g): 0.1 Emissivity of the glass in the 8-13 μm band (ε_g): 0.88
Absorber plate Density (ρ_p): 2719 kg/m³ Specific heat capacity ($c_{p_{abs}}$): 871 J/kg.K Thermal conductivity (k_p): 202.4 W/m.K Thickness (d_p): 0.0004 m Absorptivity in the solar band (α_p): 0.92 Emissivity of the plate in the 8-13 μm band (ε_p): 0.05
Insulation Density (ρ_{ins}): 30 kg/m³ Specific heat capacity ($c_{p_{ins}}$): 1400 J/kg.K Thermal conductivity (k_{ins}): 0.04 W/m.K Emissivity of the insulation in the 8-13 μm band (ε_{ins}): 0.2

C. Heat transfer for each wall

1. Wind Cover

The wind cover is set as diffuse semi-transparent material. The heat balance of the wind cover includes radiation to ($q_{c,in}$) and from the cover ($q_{c,out}$), convection with the ambient air, and convection with the top air gap. The heat balance equation is shown in Equation 1.

$$q_{c,in} - q_{c,out} + h_{amb,c}(T_{amb} - T_c) + h_{a_1,c}(T_{a_1} - T_c) = 0 \quad (1)$$

i. The $q_{c,in}$ consists of radiation from outside of the computational domain such as solar radiation and sky radiation, and from the inside of the computational domain. Thus, the $q_{c,in}$ can be written as in the Equation 2, where G is total solar irradiation, ε_{sky} and T_{sky} are emissivity and temperature of the sky, σ is Stefan-Boltzmann constant, and $q_{w,c}$ is radiation from the interior walls to the cover.

$$q_{c,in} = G + \varepsilon_{sky}\sigma T_{sky}{}^4 + q_{w,c} \quad (2)$$

In Equation 2, The value of sky emissivity ε_{sky} calculated from empirical formula by Jackson [4,5] as shown below, while the sky temperature T_{sky} is calculated using empirical formula from Swinbank [5,6] as displayed below, with T_{amb} as the ambient temperature.

$$\varepsilon_{sky} = 1 - \left[0.261e^{-7.77\times10^{-4}(273.15 - T_{amb}^2)}\right]$$

$$T_{sky} = 0.0552T_{amb}^{1.5}$$

ii. Moreover, $q_{c,out}$ also has three components, i.e., reflected & transmitted radiation to the top and bottom part of the cover, as well as thermal emission from the cover. Equation 3 formulated the $q_{c,out}$, where $I_{c,top}$ and $I_{c,bottom}$ radiation leaving the top and bottom surface of the cover. The term $a_c n_c^2 \frac{\sigma T_c^4}{\pi}$ is the thermal radiation from the cover, based on the DO radiation model for semi-transparent material, where a_c is the absorption coefficient of the cover, n_c is the refraction index of the cover, and T_c is the temperature of the cover [7].

$$q_{\mathrm{c,out}} = I_{\mathrm{c,top}} + I_{\mathrm{c,bottom}} + a_{\mathrm{c}} n_{\mathrm{c}}^2 \frac{\sigma T_c^4}{\pi} \tag{3}$$

Detail equation for the top and bottom surface of the cover are as follows.

$$I_{\mathrm{c,top}} = \frac{\rho_{\mathrm{c}}(G + \varepsilon_{\mathrm{sky}} \sigma T_{\mathrm{sky}}{}^4) + \tau_{\mathrm{c}} q_{\mathrm{w,c}}}{\pi} \tag{4}$$

$$I_{\mathrm{c,bottom}} = \frac{\rho_{\mathrm{c}} q_{\mathrm{w,c}} + \tau_{\mathrm{c}}(G + \varepsilon_{\mathrm{sky}} \sigma T_{\mathrm{sky}}{}^4)}{\pi} \tag{5}$$

Thus, the $q_{\mathrm{c,out}}$ equation can be reformulated as follows.

$$q_{\mathrm{c,out}} = \frac{(\rho_{\mathrm{c}} + \tau_{\mathrm{c}})(G + \varepsilon_{\mathrm{sky}} \sigma T_{\mathrm{sky}}{}^4 + \tau_{\mathrm{c}} q_{\mathrm{w,c}}) + a_{\mathrm{c}} n^2 \sigma T_c^4}{\pi} \tag{6}$$

or,

$$q_{\mathrm{c,out}} = \frac{(\rho_{\mathrm{c}} + \tau_{\mathrm{c}}) q_{\mathrm{c,in}} + a_{\mathrm{c}} n^2 \sigma T_c^4}{\pi} \tag{7}$$

Where ρ_{c} and τ_{c} are reflectivity and transmissivity of the cover, respectively, $q_{\mathrm{w,c}}$ is radiation from the interior walls to the cover, and $q_{\mathrm{c,in}}$ is radiation to the cover as in Equation 2.

In Equation 3, absorption coefficient is derived from empirical formula by Hassanien [8] as follows.

$$a = \left(\frac{1}{t}\right) \ln \left[\frac{(1-\rho)^2}{2\tau} + \sqrt{\frac{(1-\rho)^4}{4\tau^2} + \rho^2} \right] \tag{8}$$

iii. The $h_{\mathrm{amb,c}}(T_{\mathrm{amb}} - T_{\mathrm{c}})$ term is the convective heat transfer between ambient air with the cover. The convective heat transfer coefficient $h_{\mathrm{amb,c}}$ in the term is calculated from Watmuff et al. [9,10].

$$h_{\mathrm{amb,c}} = 5.7 + 3.8u \tag{9}$$

The u is the ambient wind speed, and as mentioned previously, there were five wind speed values use in the calculation, ranging from 1 to 5 m/s. T_{amb} is ambient temperature, taken from the recorded data in the experiment, and T_{c} is the cover temperature.

iv. Convective heat transfer in $h_{\mathrm{a_1,c}}(T_{\mathrm{a_1}} - T_{\mathrm{c}})$ term is the natural convection between the top air gap with the cover, where $h_{\mathrm{a_1,c}}$ is the convective heat transfer coefficient, and $T_{\mathrm{a_1}}$ is the average temperature of the top air gap.

2. Glass cover

The heat balance of the glass cover is as follows.

$$q_{\mathrm{g,in}} - q_{\mathrm{g,out}} + h_{\mathrm{a_1,g}}(T_{\mathrm{a_1}} - T_{\mathrm{g}}) + h_{\mathrm{a_2,g}}(T_{\mathrm{a_2}} - T_{\mathrm{g}}) = 0 \tag{10}$$

In Equation 10, $q_{\mathrm{g,in}}$ and $q_{\mathrm{g,out}}$ are the radiation to and from the glass, whereas the other two terms $h_{\mathrm{a_1,g}}(T_{\mathrm{a_1}} - T_{\mathrm{g}})$ and $h_{\mathrm{a_2,g}}(T_{\mathrm{a_2}} - T_{\mathrm{g}})$ are the convection heat transfer between the glass with the top and bottom air gap. $h_{\mathrm{a_1,g}}$ and $T_{\mathrm{a_1}}$ are heat transfer coefficient and temperature of the top air gap, $h_{\mathrm{a_2,g}}$ and $T_{\mathrm{a_2}}$ heat transfer coefficient and temperature for the bottom air gap, and T_{g} is the glass temperature.

i. Incoming radiation to the glass consists of radiation reflected and transmitted by the wind cover ($I_{c,bottom}$), the thermal radiation emitted by the cover, and radiation emitted by all interior walls that surround the glass cover (see Equation 18).

$$q_{g,in} = I_{c,bottom} + a_c n_c^2 \frac{\sigma T_c^4}{\pi} + q_{w,g} \tag{11}$$

ii. As in the case of the wind cover (from Equation 7), the emitted radiation from the glass, $q_{g,out}$, can be reformulated as the following.

$$q_{g,out} = I_{g,top} + I_{g,bottom} + a_g n^2 \frac{\sigma T_g^4}{\pi} \tag{12}$$

$$I_{g,top} = \frac{\rho_g \left(I_{c,bottom} + a_c n_c^2 \frac{\sigma T_c^4}{\pi} \right) + \tau_g q_{w,g}}{\pi} \tag{13}$$

$$I_{g,bottom} = \frac{\rho_c q_{w,g} + \tau_c \left(I_{c,bottom} + a_c n_c^2 \frac{\sigma T_c^4}{\pi} \right)}{\pi} \tag{14}$$

iii.

$$q_{g,out} = \frac{(\rho_g + \tau_g)\, q_{g,in} + a_g {n_g}^2 \sigma T_g^4}{\pi} \tag{15}$$

The reflectivity, the transmissivity, and the absorption coefficient of the glass are represented in ρ_g, τ_g, and a_g. Meanwhile, $q_{g,in}$ is all radiation received by the glass, n_g is the glass refractive index, and T_g is glass temperature. The $a_g {n_g}^2 \sigma T_g^4 / \pi$ term is the thermal radiation from the glass based on DO radiation model for semi-transparent material.

iv. $h_{a_1 g}(T_{a_1} - T_g)$ is convective heat transfer between the glass and the top air gap, where $h_{a_1 g}$ is the convective heat transfer coefficient of the top air gap, T_{a_1} is the average temperature in the top air gap and T_g is the glass temperature. Similarly, for the bottom air gap, convection with the glass is accounted in $h_{a_2 g}(T_{a_2} - T_g)$, where $h_{a_2 g}$ is the convective heat transfer coefficient of the bottom air gap, T_{a_2} is the average temperature in the bottom air gap.

3. **Absorber plate**

The heat balance of the absorber plate is as the following. It consists of incoming and outcoming radiation, convection with the bottom air gap and conduction with backside insulation material.

$$q_{p,in} - q_{p,out} + h_{a_2,p}(T_{a_2} - T_p) + U_{bp}(T_b - T_p) = 0 \tag{16}$$

i. $q_{p,in}$ is the radiation received by the absorber plate, following the Kirchoff's law where emissivity equals the absorptivity, the formula for $q_{p,in}$ is as the following.

$$q_{p,in} = \varepsilon_p \left(q_{w,p} + I_{g,bottom} + a_g n^2 \frac{\sigma T_g^4}{\pi} \right) \tag{17}$$

In Equation 17 ε_p is emissivity of the absorber plate, $q_{w,p}$ is radiation from the surrounding interior walls to the plate, $I_{g,bottom}$ is part of radiation comes from the bottom part of the glass layer as in the Equation 14, and $a_g n^2 \frac{\sigma T_g^4}{\pi}$ is the thermal radiation from within the glass layer as explained in the Equation 15.

ii. The outward radiation from the plate, $q_{\mathrm{p,out}}$, is a combination of reflected part of the $q_{\mathrm{p,in}}$ and the thermal radiation from the absorber plate itself. Reflectivity is calculated from $1-\varepsilon_{\mathrm{p}}$, while the thermal radiation from the plate is calculated from $\varepsilon_{\mathrm{p}}\sigma T_{\mathrm{p}}^{4}$, with ε_{p} is the emissivity of the plate, T_{p} represents the plate temperature, and σ is Stefan-Boltzmann constant.

$$q_{\mathrm{p,out}} = (1-\varepsilon_{\mathrm{p}})\left(q_{\mathrm{w,p}} + I_{\mathrm{g,bottom}} + a_{\mathrm{g}}n^{2}\frac{\sigma T_{\mathrm{g}}^{4}}{\pi}\right) + \varepsilon_{\mathrm{p}}\sigma T_{\mathrm{p}}^{4} \qquad 18$$

iii. $h_{\mathrm{a_2,p}}(T_{\mathrm{a_2}}-T_{\mathrm{p}})$ and $U_{bp}(T_b-T_p)$ are convective heat transfer between the absorber and the bottom air gap and conduction between the absorber with the insulation.

4. Insulation

The insulation receives convection from the ambient air on all its surfaces (top, bottom, side). The heat balance equation becomes:

$$h_{\mathrm{amb,o}}(T_{\mathrm{amb}}-T_{\mathrm{o}}) + U_{\mathrm{ins}}(T_{\mathrm{i}}-T_{\mathrm{o}}) = 0$$

where $h_{\mathrm{amb,o}}$ is convection coefficient between ambient and the outer side of the insulation calculated from the equation below, T_{o} is the temperature of the outer side of the insulation, T_{i} is the temperature of the inner side of the insulation, and U_{ins} is the thermal transmittance of the insulation.

$$h_{\mathrm{amb,o}} = 5.7 + 3.8u$$

The u is the ambient wind speed and varied accordingly.

D. Comparison of simulation results with experimental data

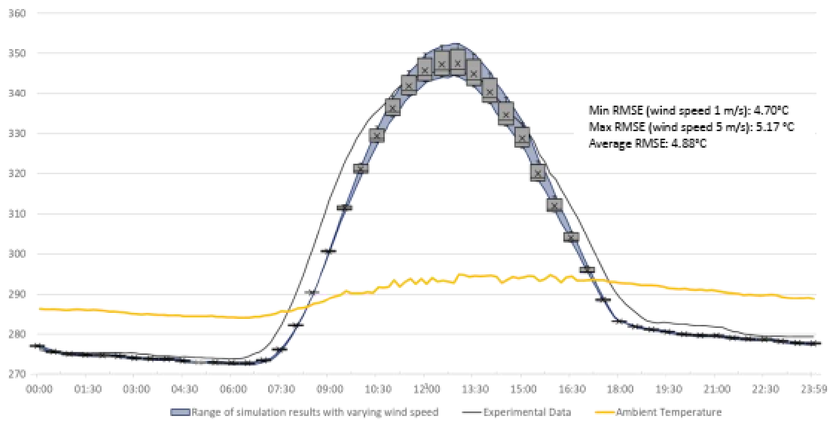

Figure 1 Glass temperature

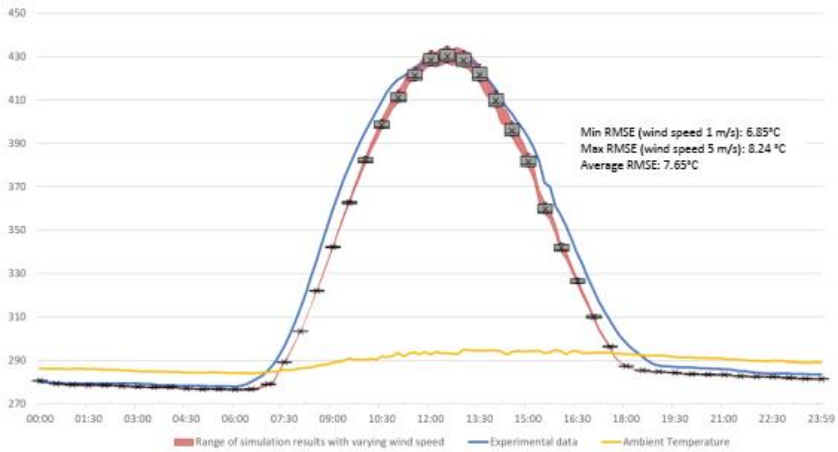

Figure 2 Absorber temperature

At 12 am	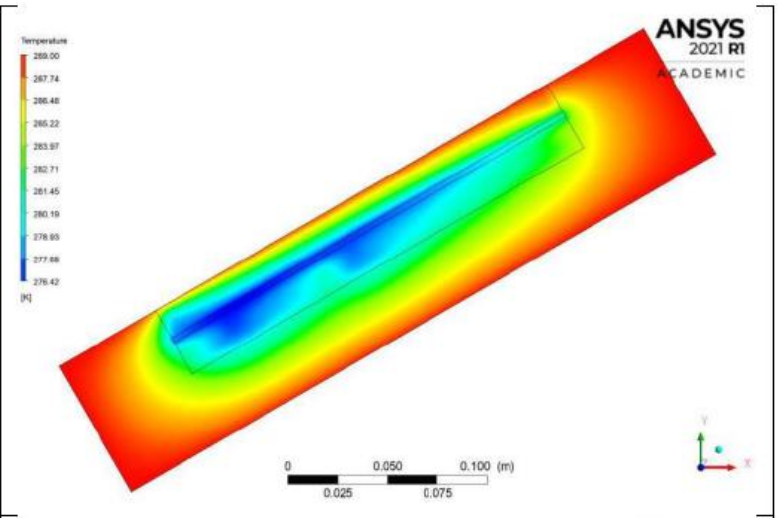
At 1 pm	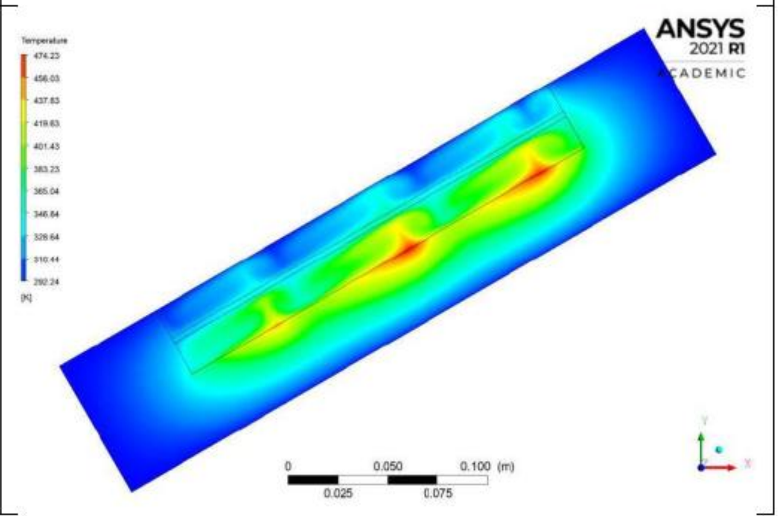

Appendix B: Examples of Ansys Fluent Settings for Radiative Cooling from Chapter 3

1. Geometry & Meshing size

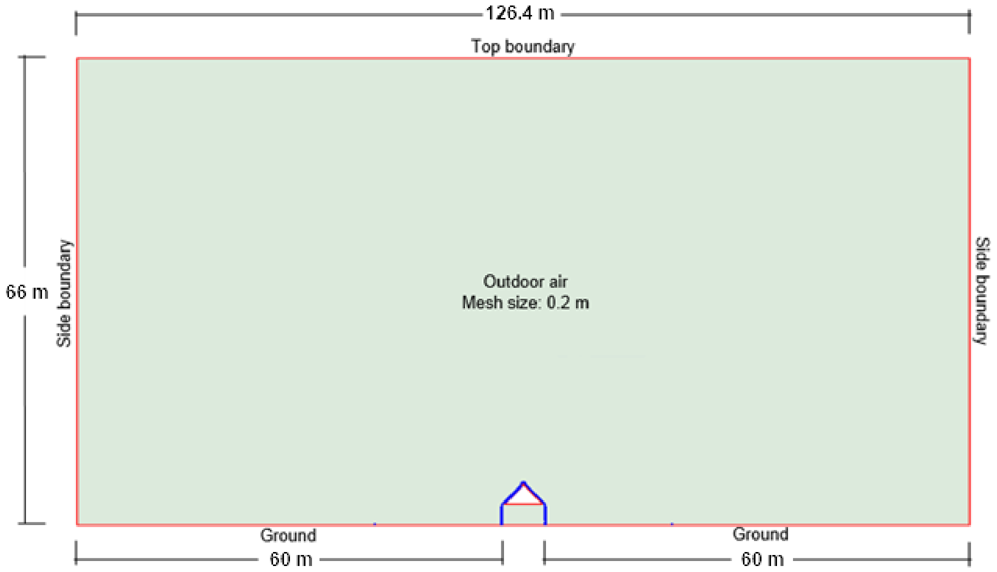

Figure 1 Geometry with the extended domain with dimension and boundary name

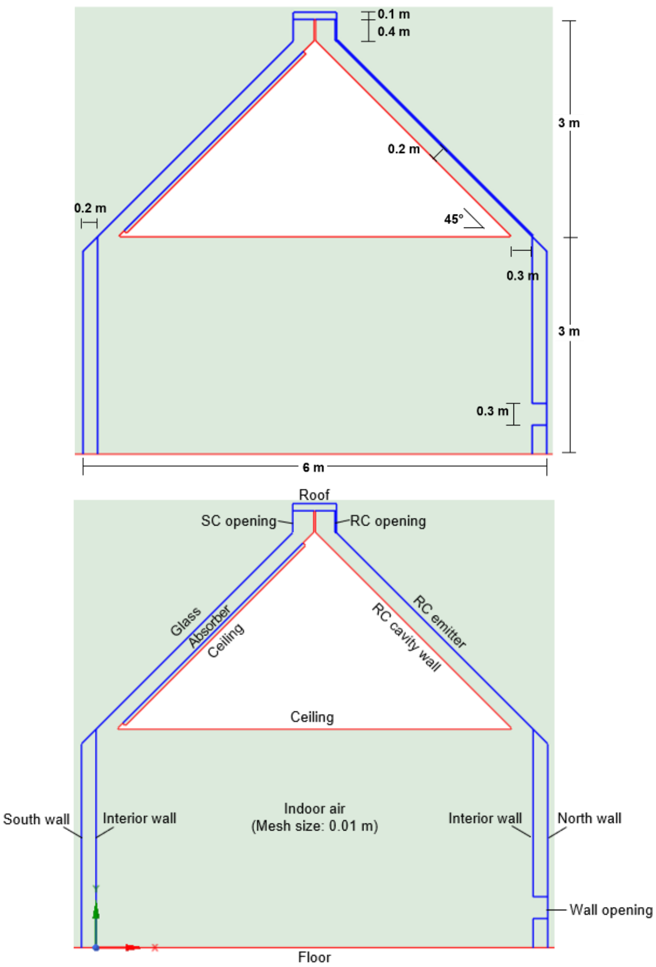

Figure 2 Building geometry with its (a) dimension and (b) boundary name

2. Simulation settings

- General: Pressure-based solver, transient simulation
- Energy: On
- Viscous model: Standard $k - \varepsilon$ turbulence model with standard wall function
- Radiation model: Discrete ordinates with 4 radiation bands (Band 0: 0.2-3 µm; Band 1:3-8 µm; Band 2: 8-13 µm; Band 3: 13-25 µm)
- Materials

Material	Thermal properties		
	Thermal conductivity (W·m-1·K-1)	**Density (kg·m-3)**	**Specific heat capacity (J·kg-1·K-1)**
Air	Piecewise linear 250 K: 0.0223 300 K: 0.0263 350 K: 0.03 400 K: 0.0338	Incompressible ideal gas law	Piecewise linear 250 K: 1006 300 K: 1007 350 K: 1009 400 K: 1014
Ground	0.364	1600	800
Brick	0.72	1920	840
Ceramic tile	0.8	1700	850

Insulation board	0.033	38	1400
Roof tile	0.8	1890	880
Timber	0.16	720	1260
Absorber	202.4	2719	871
Glass	1.38	2203	703
Emitter	202.4	2719	871

- Cell Zone Conditions:
  - Operating pressure: 101325 Pa
  - Gravity in Y direction: -9.81 m/s²
  - Operating temperature: Ambient temperature
  - Outdoor air condition: Ambient temperature

- Boundary conditions

Boundary name	Type (Material)	Thermal Boundary conditions	Radiation Boundary Conditions
External domain			
Top boundary	Pressure outlet	Total temperature: T_{amb}	0
Side boundary	Pressure outlet	Total temperature: T_{amb}	0
Ground	Wall (Ground)	Mixed Heat transfer coefficient: h_{amb} Free stream temperature: T_{amb} External emissivity: ε_{sky} External radiation temperature: T_{sky}	Internal emissivity Band 0: 0.7 Band 1: 0.87 Band 2: 0.97 Band 3: 0.98
Building domain			
SC opening, RC opening, and Wall opening	Internal	-	-
Roof	Two-sided Wall (Roof tile)	Coupled; External heat sources in Equation (2), namely $q_{\text{sol}} + q_{\text{rad}} + h_{\text{amb}}(T_{\text{amb}} - T_{\text{surf}})$, are inputted in the Heat Generation Rate entry-box*	Internal emissivity Band 0: 0.87 Band 1: 0.93 Band 2: 0.95 Band 3: 0.95
Glass	Two-sided Wall (Glass)	Coupled; External heat sources in Equation (2), namely $q_{\text{sol}} + q_{\text{rad}} + h_{\text{amb}}(T_{\text{amb}} - T_{\text{surf}})$, are inputted in the Heat Generation Rate entry-box*	Internal emissivity Band 0: 0.05 Band 1: 0.88 Band 2: 0.88 Band 3: 0.88
RC emitter	Two-sided Wall (Aluminium)	Coupled; External heat sources in Equation (2), namely $q_{\text{sol}} + q_{\text{rad}} + h_{\text{amb}}(T_{\text{amb}} - T_{\text{surf}})$, are inputted in the Heat Generation Rate entry-box*	Internal emissivity Band 0: 0.05 Band 1: 0.05 Band 2: 0.95 Band 3: 0.05
RC cavity wall	Two-sided Wall (Aluminium)	Coupled	Internal emissivity Band 0: 0.05 Band 1: 0.05 Band 2: 0.95

			Band 3: 0.05
Absorber	Two-sided Wall (Aluminium)	Coupled; External heat sources in Equation (7), namely $q_{\text{sol\_glass}} + q_{\text{rad\_abs}}$, are inputted in the Heat Generation Rate entry-box*	Internal emissivity Band 0: 0.95 Band 1: 0.95 Band 2: 0.95 Band 3: 0.95
South wall	Two-sided Wall (Brick)	Coupled; External heat sources in Equation (2), namely $q_{\text{sol}} + q_{\text{rad}} + h_{\text{amb}}(T_{\text{amb}} - T_{\text{surf}})$, are inputted in the Heat Generation Rate entry-box*	Internal emissivity Band 0: 0.79 Band 1: 0.77 Band 2: 0.93 Band 3: 0.93
North wall	Two-sided Wall (Brick)	Coupled; External heat sources in Equation (2), namely $q_{\text{sol}} + q_{\text{rad}} + h_{\text{amb}}(T_{\text{amb}} - T_{\text{surf}})$, are inputted in the Heat Generation Rate entry-box*	Internal emissivity Band 0: 0.79 Band 1: 0.77 Band 2: 0.93 Band 3: 0.93
Floor	Wall (Ceramic tile)	Heat Flux: 0	Internal emissivity Band 0: 0.34 Band 1: 0.94 Band 2: 0.93 Band 3: 0.93
Ceiling	Wall (Timber)	Heat Flux: 0	Internal emissivity Band 0: 0.46 Band 1: 0.9 Band 2: 0.94 Band 3: 0.96

**Because the Heat Generation Rate entry-box uses a volumetric unit, W/m³, we need to convert the external heat source equation of the surfaces to have the required unit. We did this by dividing the heat equation by the thickness of the wall and inputting that thickness in the Wall Thickness entry-box. For thin walls like the glass, absorber, and emitter, the heat equations are divided by the thickness of the material, i.e., 3 mm for the glass and 1 mm for the absorber and emitter. Whereas for the roof and walls, we used the thickness of its coating, i.e., 0.2 mm.*

- Solution Methods
  - Pressure-Velocity Coupling Scheme: PISO
  - Spatial Discretization:
    - Pressure: PRESTO!
    - Momentum: Second Order Upwind
    - Turbulent Kinetic Energy: First Order Upwind
    - Turbulent Dissipation Rate: First Order Upwind
    - Energy: Second Order Upwind
    - Discrete Ordinates: First Order Upwind
    - Transient Formulation: First-Order Implicit
- Monitors
  - Residual checking:

continuity	1×10^{-6}
x-velocity	1×10^{-6}
y-velocity	1×10^{-6}
energy	1×10^{-6}
k	1×10^{-6}

epsilon	1×10^{-6}
DO-intensity	1×10^{-6}

- Reported parameters for convergence checking
  - Glass, absorber, and emitter temperatures
  - Indoor air temperature
  - Indoor air velocity
  - Volume flow rate through each opening

- Running simulation
  - Time step size: 450 s
  - Number of time step: 1344 or until the reported parameters converged